VISIBLE BIDIRECTIONAL-REFLECTANCE MEASUREMENTS FOR ROUNDED GRAIN AND SURFACE HOAR SNOW CRYSTAL MORPHOLOGIES

by

Brad Thomas Stanton

A thesis submitted in partial fulfillment
of the requirements for the degree

of

Master of Science

in

Civil Engineering

MONTANA STATE UNIVERSITY
Bozeman, Montana

May 2013

©COPYRIGHT

by

Brad Thomas Stanton

2013

All Rights Reserved

APPROVAL

of a thesis submitted by

Brad Thomas Stanton

This thesis has been read and each member of the thesis committee and has been found to be satisfactory regarding content, English usage, format, citations, bibliographic style, and is ready for submission to The Graduate School.

Dr. Daniel Miller

Approved for the Department of Civil Engineering

Dr. Jerry Stephens

Approved for The Graduate School

Dr. Ronald W. Larsen

STATEMENT OF PERMISSION TO USE

In presenting this thesis in partial fulfillment of the requirements for a master's degree at Montana State University, I agree that the Library shall make it available to borrowers under rules of the Library.

If I have indicated my intention to copyright this thesis by including a copyright notice page, copying is allowable only for scholarly purposes, consistent with "fair use" as prescribed in the U.S. Copyright Law. Requests for permission for extended quotation from or reproduction of this thesis in whole or in parts may be granted only by the copyright holder.

Brad Thomas Stanton

May 2013

ACKNOWLEDGEMENTS

I would like to thank the Department of Civil Engineering at Montana State University, National Aeronautics and Space Administration (NASA), the Montana Space Grant Consortium, and the Murdock Charitable Trust for their continued support. I would also like to thank my committee, Dr. Dan Miller and Dr. Ed Adams for their invaluable advice and guidance in the world of snow science and Dr. Joe Shaw for answering my unending questions concerning optics. Additionally, I would like to thank Dr. Ladean McKittrick for keeping the lab in excellent working order, Dr. Andrew Slaughter for his initial work growing surface hoar in a lab setting, and David Walters for his incredible brilliance in all things science. Finally, I would like to thank my wife, Dr. Christine Stanton, for her unwavering patience and support.

TABLE OF CONTENTS

1. INTRODUCTION 1

2. BACKGROUND 7

The Physics of Snow 8
Crystal Growth in the Atmosphere 8
Crystal Growth in the Snowpack 15
Crystal Growth at the Surface 19
Energy Balance and Mass Flux Equations 23
Optics 31
Solid Angle and Projected Solid Angle 31
Radiometry 35
Bidirectional-Reflectance Distribution Function 42
Additional Reflectance Terminology 45
Literature Review of Snow Optics Studies 49
Radiative Transfer Models 49
Field Studies Concerning the BRDF/BRF of Snow 54

3. METHODOLOGY 59

Development of Varying Snow Morphologies in the Lab Setting 65
Documenting Crystal Habit 68
Crystal Types Grown for Optical Testing 70
Optics 71
Light Source Considerations 74
Field of View Considerations 78
Geometric Considerations 80
Spectralon Reference Panel and BRF 82

4. RESULTS AND DISCUSSION 84

Surface Hoar Growth Results 85
Surface Hoar Growth Discussion 90
Mass Flux Results 90
Mass Flux Discussion 96
Specific Surface Area Results 99
Specific Surface Area Discussion 100
Optical Properties Results and Discussion 102
Results: Figure 42 to Figure 44 and Table 9 to Table 11 103
Discussion: Figure 42 to Figure 44 and Table 9 to Table 11 108
Results: Figure 46 to Figure 51. 113
Discussion: Figure 46 to Figure 51 121
Final Considerations 125

TABLE OF CONTENTS - CONTINUED

5. CONCLUSIONS AND RECOMMENDATIONS 128

Surface Hoar Growth 128
Significant Findings: Surface Hoar Growth 128
Suggestions for Future Work: Surface Hoar Growth 129
Optical Properties of Snow 130
Significant Findings: Optical Study..... 130
Suggestions for Future Work: Optical Study..... 131

REFERENCES CITED..... 134

APPENDICES 143

APPENDIX A: Analysis of Stellarnet Black Comet-HR Spectrometer..... 144
APPENDIX B: Field of View and Shadow Geometery Equations 163
APPENDIX C: Mass Flux Matlab Code 166
APPENDIX D: Examination of The Directional Growth of Surface Hoar..... 174
APPENDIX E: Meteorlogical Conditions During Surface Hoar Growth 192
APPENDIX F: BRF Values and geometries 219

LIST OF TABLES

Table Page

1. Test Matrix showing dominant axial growth a crystal habit tested as well as listing tables or figures where results can be found. 64

2. List of meteorlogical data collected during surface hoar growth. The Agilent data logger recorded values for meterological data every 30 seconds. The only exception was wind speed which was measured approximately 2-3 times during the course of a experiment. 70

3. List of computed tomography data collected at the start and end of each surface hoar growth period as well as 1-2 times in between. 70

4. List of all lighting and observer angles from which BRF data were obtained. θr = reflected/observer zenith angle. ϕr = reflected/observer azimuth angle. θi = incident zenith angle. ϕi = incident azimuth angle (i.e. $180°$ in all cases). 72

5. Mean environmental chamber parameters for test 1. Corresponding images can be seen in Figure 32 to Figure 34. $\Delta Time$ represents time elapsed from the initial start of the experiment (i.e. $\Delta T = 0$). An explination of the symbols used is provided in the text at the beginning of the section titled *Mass Flux Results*. The boxed terms reprsents calculated values. 93

6. Mean environmental chamber parameters for test 2. Corresponding images can be seen in Figure 35 to Figure 37. $\Delta Time$ represents time elapsed from the initial start of the experiment (i.e. $\Delta T = 0$). An explination of the symbols used is provided in the text at the beginning of the section titled *Mass Flux Results*. The boxed terms represents calculated values. 94

7. Mean environmental chamber parameters for test 3. Corresponding images can be seen in Figure 38 to Figure 40. $\Delta Time$ represents time elapsed from the initial start of the experiment (i.e. $\Delta T = 0$). An explination of the symbols used is provided in the text at the beginning of the section titled *Mass Flux Results*. The boxed terms reprsents calculated values. 95

LIST OF TABLES - CONTINUED

Table Page

8. CT Data: Specific Surface Area (SSA). Scan 0 represents the SSA of the rounded grains before surface hoar growth. The Remaining scans represent the SSA of only the deposited surface hoar. The tests 0-4 correspond to the CT images (left to right) in Figure 32 to Figure 40. $r_{optical}$ is the optically equivialant grain radius for the final SSA measurement. 100

9. Test 3a. Descriptive statistics for BRF values across all geometries at 510 nm. See also Appendix F. 105

10. Test 3b. Descriptive statistics for BRF values across all geometries at 510 nm. See also Appendix F. 106

11. Test 3c. Descriptive statistics for BRF values across all geometries at 510 nm. See also Appendix F. 107

12. The range of BRF values for each test and the percent change in range between initial form (I.F.) and final form (F.F.). Note that surface hoar tends to have a wider range of BRF values than rounded grains. 110

13. Mean BRF values from tests 3a, 3b, and 3c and percent change from initial form (I.F.) to final form (F.F.) at 510 nm. Note the data indicates a slight decrease in mean BRF (essentially albedo). 112

14. Standard deviation and percent change in standard deviation of BRF values from rounded grains to surface hoar in each of the three tests at 510 nm. 112

15. Maximum BRF for each test as well as corresponding BRF value and percent change between initial form and final form. A positive sign on the % change indicates an increase in BRF. 121

16. Minimum BRF for each test as well as corresponding BRF value and percent change between initial form and final form. A negative sign on the % change indicates an decrease in BRF. 121

LIST OF TABLES - CONTINUED

Table Page

17. Mean BRF values for nadir illumination angle θi showing darking at grazing observation angles (i.e larger values of θr). Initial forms (rounded grains) are shown on the left while finial forms (surface hoar) is shown on the right. 123

18. Mean directional scatter along a in the solar principle plan across all solar zenith angles. In general the trend is for more forward-scatter than backward-scatter with the exception being Test 3c Final Form in which there is almos no difference between forward and backward-scatter. 124

LIST OF FIGURES

Figure Page

1. Left, buried surface hoar layer (photo Aspen Expeditions) and, right, surface hoar (photo David Walters).....4

2. Plot of Equation (4) and (5), showing that the vapor pressure over liquid water is higher than over ice. 11

3. Example of rimed and unrimed hexagonal plate (left) (Reproduced from Libbrecht, 1999). Conceptual illustration of the Bergeron process (left) (Reproduced from PicsWeb). 12

4. Conceptual illustration of a water molecule and the hexagonal latticework of ice (Reproduced from Libbrecht, 2001).....13

5. Illustration of the relationship between temperature, supersaturation, and crystal habit (adapted from Nakaya, 1954) 13

6. Conceptual illustration of additional contact in flat vs. curved surface. The extra bonds in the flat surface tend to limit the amount that can escape thereby lowering the vapor pressure over a flat (or concave) surface relative to a curved surface. 16

7. Sintering (right) and rounding (left) [Reproduced from McClung and Schaerer, 2006] of new snow due to curvature induced vapor pressure gradients. 17

8. Depth hoar chains showing simple crystal habit due to low supersaturation and preferential orientation along the temperature gradient (photo David Walters).....18

9. Energy balance of a snowpack. Note that the conductive term q can represent heat conduction from the soil to the snowpack or from snow sublayer to the snow surface depending on the choice of control volume (Adapted from Armstrong, 2008). 24

10. Electromagnetic spectrum (Incropera and Dewitt, 2007, Figure 12.3).....26

11. Example illustrating solid angle ω. Note that, as seen from the Earth, the Sun and Moon share the same solid angle during a perfect eclipse. 32

LIST OF FIGURES - CONTINUED

Figure Page

12. The relationship between solid angle and polar coordinates (Mobley, 2006). 33

13. Radiance [$W\ m-2\ sr-1$] as calculated from Plank's equation for perfect black body emission showing the temperature and wavelength dependence. Note the log-log scale. For reference the sun is ~6000K and terrestrial objects ~300K. 36

14. Incident light geometry. Power on the differential surface area dAi can be calculated by integrating the radiance $Li\cos\theta i$ of the source collected by a differential solid angle $d\omega i$ (solid angle of source as seen from reflective surface) with respect to solid angle and area as shown in Equation (29)....39

15. Left: Equivalent throughputs using notation in Equation (30). Right: Using general subscripts it becomes clear that area A_1 or A_2 could act as sources, reflective surfaces, or detectors. In any case throughput would be could be calculated by either $A1 \cdot \Omega 1$ or the equivalent$A2 \cdot \Omega 2$....40

16. Top: For a point source, solid angle $d\omega$ can be used to calculate power at the detector $d\phi = Ls \cdot dAS \cdot d\omega$ for all view angles. Bottom: For a flat extended source, as θ changes, the view area changes. Multiplying by cosine of theta corrects for this phenomenon, $d\phi = Ls \cdot \cos\theta \cdot d\omega \cdot dAS = Ls \cdot d\Omega s, det \cdot dAS$. 42

17. Illustration of geometry and terminology associated with multi-angle optical studies (reproduced from Nicodemus, 1977). 43

18. Hemispherical reflectance of Spectralon as a function of wavelength showing nearly Lambertian reflectance in the UV/VIS/NIR (figure from Labsphere Inc. website). 49

19. Reproduction of Figure 5 with the snow surface temperatures used in each experiment and expected snow morphology shown. 63

LIST OF FIGURES - CONTINUED

Figure Page

20. Experimental set up. The box on the lower left provides humidity-controlled airflow through a ducting system over the snow surface in the upper right. The temperature-controlled cold ceiling above provides the longwave radiation interaction. 66

21. A) Detail of experimental set up and instrumentation. B) Functional diagram of experimental set up. 67

22. A) Wild optical microscope with digital imaging, B) SkyScan 1173 CT Scanner adapted for cold room use, C) $34cm3$ sample holder with surface hoar growth. The vertical rod is used for image rotational indexing. 69

23. Left) Goniometer and Spectrometer Configuration. Right) Sun angle θi was varied by tilting the snow surface with respect to the fixed light source. 72

24. Left: Relative power incident at snow surface with clean lamp. Right: Before cleaning. 75

25. ModTran Model of transmittance for a 2m Path in Bozeman, Mt. 76

26. The spectrum produced by the light as measured in the lab using a spectrometer. 77

27. Depiction of the solar spectrum as measured at the top of the atmosphere and at sea level after attenuation in the atmosphere. Additionally, the solid line represents Planck's curve for a blackbody at $5250°C$ 78

28. Response of spectrometer as a function of incident solar angle. Note that solid angle field of view half angle of 15 degrees captures nearly 100% of incident light. 80

29. Viewing Geometry showing the *upper bound* of viewer zenith angle to be 75 degrees for a 4cm probe height. Equations for labels shown in the figure are provided in Appendix B. 80

LIST OF FIGURES - CONTINUED

Figure Page

30. Viewing geometry showing the *lower bound* is controlled by the shadow from the gantry. Negative values of B indicate the shadow of the gantry is captured within the field of view of the spectrometer. Equations for labels shown in the figure are provided in Appendix B. 81

31. Illustration of forward and backscatter direction based on a fixed incident azimuth angle of $\phi i = 180°$. 82

32. Test 1a 3/27/12. Snow surface temperature during first 7 hours of growth started at ~-26.8°C and steadily approached a constant -31.5°C. During the final 17-hour growth period, surface temperature data failed to record; however, it is speculated the snow surface temperature remained close to -31.5°C during periods of actual surface hoar growth. CT Images at times: 0, 7, 24 (hrs) (Sample Area: 389.59 mm^2) and corresponding microscopic images (2 mm grid). 85

33. Test 1b 3/28/12. Snow Surface Temperature Range: -13.6 to -21.1°C. Mean Snow Surface Temperature: -15.5°C with a standard deviation of 1.9°C. CT Images at times: 0, 6.5, 22 (hrs) (Sample Area: 501.08 mm^2) and corresponding microscopic images (2 mm grid). 86

34. Test 1c 3/29/12. Snow Surface Temperature Range: -1.8 to -11.8°C. Mean Snow Surface Temperature: -8.3°C with a standard deviation of 1.0°C. CT Images at times: 0, 6.5, 22.5 (hrs) (Sample Area: 551.92 mm^2) and corresponding microscopic images (2 mm grid). 86

35. Test 2a 6/19/12. Snow Surface Temperature Range: -26.5 to -31.1°C. Mean Snow Surface Temperature: -29.7°C with a standard deviation of 1.2°C. CT Images at times: 0, 5, 8.5, 12.5, 25 (hrs) (Sample Area: 505.22 mm^2) and select microscopic images (2 mm grid) at time 0, 12.5, 25 (hrs). Note: during the initial 12.5 hours, the snow surface temperature dropped as the snow equilibrated with the chamber air temperature. Significant growth did not occur until the snow surface temperature dropped below this chamber air temperature, due to the longwave loss to the cold ceiling, around hour 10. 87

LIST OF FIGURES - CONTINUED

Figure Page

36. Test 2b 6/21/12. Snow Surface Temperature Range: -12.4 to -16.5°C. Mean Snow Surface Temperature: -15°C with a standard deviation of 0.4°C. CT Images at times: 0, 7, 12.5, 24 (hrs) (Sample Area: 469.7 mm^2) and select microscopic images (2 mm grid) at times 0, 12.5, 24 (hrs).....87

37. Test 2c 6/26/12. Snow Surface Temperature Range: -5.5 to -12.7°C. Mean Snow Surface Temperature: -8.3°C with a standard deviation of 0.76°C. CT Images at times: 0, 7, 11, 13.5, 23.5 (hrs) and (Sample Area: 550.68 mm^2) select microscopic images (2 mm grid) at times 0, 11, 23.5 (hrs). 88

38. Test 3a 10/25/12. Snow Surface Temperature Range: -12.2 to -16.1°C. Mean Snow Surface Temperature: -15.2°C with a standard deviation of 0.85°C. CT Images at times: 0, 12, 23.5 (hrs) and (Sample Area: 447.65 mm^2) select microscopic images (2 mm grid) at times 0, 7.5, 13, 23.5 5 (hrs). Note: less surface hoar growth was observed in front of the left ducting (where the CT sample was located) compared to the right ducting (where optical tests and regular microscopic photographs were taken. 88

39. Test 3b 11/15/12. Snow Surface Temperature Range: -15.3 to -17.3°C. Mean Snow Surface Temperature: -16.4°C with a standard deviation of 0.26°C. CT Images at times: 0, 10.4, 21 (hrs) and (Sample Area: 367.31 mm^2) select microscopic images (2 mm grid) at times 0, 10.4, 21 (hrs).....89

40. Test 3c 11/29/12. Snow Surface Temperature Range: -13.7 to -15.6 °C. Mean Snow Surface Temperature: -14.6°C with a standard deviation of 0.36°C. CT Images at times: 0, 6.5,12, 24 (hrs) and (Sample Area: 414.23 mm^2) select microscopic images (2 mm grid) at times 0, 6.26, 11.98, 23.94 (hrs).....89

41. The needle like hoar frost that formed on the cold ceiling at a temperature of $\sim -50°C$ and fell onto the snow surface was often readily apparent compared to the surface hoar due to its different grain morphology. 97

LIST OF FIGURES - CONTINUED

Figure Page

42. Test 3a. BRF as a function of wavelength. Each line represents a different lighting and viewing geometry. Initial rounded form (left) and surface hoar (right). Red line marks 510 nm. 105

43. Test 3b. BRF as a function of wavelength. Each line represents a different lighting and viewing geometry. Initial rounded form (left) and surface hoar (right). Red line marks 510 nm. 106

44. Test 3c. BRF as a function of wavelength. Each line represents a different lighting and viewing geometry. Initial rounded form (left) and surface hoar (right). Red line marks 510 nm. 107

45. Figure reproduced from Wiscombe and Warren (1980) showing direct beam albedo as a function of wavelength for various grain radii. Note decreasing albedo with increasing grain size in the NIR as well as the nominal effect of grain size in the visible. 111

46. Tests 3a 10-24-12. Initial form BRF results at a wavelength of 510 nm. Radial value represents BRF while angular value represents viewer azimuth angle. 115

47. Test 3a 10-24-12. Final form BRF results at a wavelength of 510 nm. Radial value represents BRF while angular value represents viewer azimuth angle.....116

48. Test 3b 11-15-12. Initial form BRF results at a wavelength of 510 nm. Radial value represents BRF while angular value represents viewer azimuth angle. 117

49. Test 3b 11-16-12. Final form BRF results at a wavelength of 510 nm. Radial value represents BRF while angular value represents viewer azimuth angle. 118

50. Test 3c 11-28-12. Initial form BRF results at a wavelength of 510 nm. Radial value represents BRF while angular value represents viewer azimuth angle. 119

51. Test 3c 11-30-12. Final form BRF results at a wavelength of 510 nm. Radial value represents BRF while angular value represents viewer azimuth angle.....120

LIST OF SYMBOLS

Symbols

$\mathcal{A}, \mathcal{B}, \mathcal{C}$	Antoine parameters
A	surface area
a	albedo
$\mathbb{A}$	anisotropy factor
C	bulk transfer coefficient (heat, H; momentum, D; mass, Q)
c	speed of light in a vacuum ($2.998x10^8\ m\ s^{-1}$)
$c_{p,i}$	specific heat capacity of ice ($2.1 \times 10^3\ J\ kg^{-1}\ K^{-1}$)
Φ	power or radiant flux [W]
E	irradiance, incident flux density; $\equiv d\Phi/dA$[W m-2]
ε	emissivity
F_m	mass flux
$F_{ss,obj}$	sky view factor of the snow surface looking skyward
f_{r}	bidirectional reflection distribution-function [sr-1]
H	internal energy
h	Planck's constant ($6.626x10^{-34}\ J\ s$)
$\mathcal{H}_{\mathrm{S,L,P}}$	heat flux (sensible, S; latent, L; precipitation, P)
L	radiance; $\equiv d^2\Phi/(dA \cdot cos\theta \cdot d\omega)$ [W m-2 sr-1]
L_{mn}	latent heat of phase change from phase m to n
$\mathcal{L}$	longwave radiation
M	radiant exitance, exitent flux density; $d\Phi/dA$ [W m-2]
$\mathcal{M}_{CT}, \mathcal{M}_{calc}$	new mass (CT scanner results/predicted from mass flux calculations)
R	reflectance factor; $d\Phi_r/d\Phi_i$ [dimensionless]
ρ_k	density of material k

LIST OF SYMBOLS - CONTINUED

Symbols

q	conductive heat flux (Wm^{-2})
R_F	rate of freezing
R_M	rate of melting
R_{vap}	gas constant for water vapor ($= 461.50\ J\ kg^{-1}\ K^{-1}$)
RH	relative humidity [dimensionless]
$\mathcal{R}_{\text{total}}$	total radiative contribution from both long- and shortwave
$r_{optical}$	radius of an optically equivalent sphere
σ	Stefan-Boltzman constant ($5.6696x10^{-8}$ [$W\ m^{-2}K^{-4}$])
σ_{mn}	interfacial surface tension between phases m and n
S	distribution of direction of radiation
$\mathcal{S}$	shortwave radiation
T	temperature
u	wind speed
θ	zenith angle, in a spherical coordinate system [rad]
Φ	power [W]
ϕ	azimuth angle, in a spherical coordinate system [rad]
ω	solid angle; $\equiv \int d\omega \equiv \iint sin\theta \cdot d\theta \cdot d\phi$ [sr]
Ω	projected solid angle; $\equiv \int \cos\theta \cdot d\omega \equiv \iint cos\theta \cdot sin\theta \cdot d\theta \cdot d\phi$
λ	wavelength of radiation [nm]
k	Boltzmann's constant ($1.381x10^{-23}\ J\ K^{-1}$)
k_{eff}	effective thermal conductivity ($W\ m^{-2}K^{-1}$)
P_{actual}	total pressure exerted by all gasses in a mixture
P_{air}	total pressure exerted by all gasses the air

LIST OF SYMBOLS - CONTINUED

Symbols

$\mathcal{p}_k$	partial pressure of component k in the system (does not imply equilibrium/saturation)
$\mathcal{p}_{H2O}$	vapor pressure[1] (a.k.a. partial pressure) of $H2O$ in the system
$p_{eqm.vap.,m,k}$	equilibrium vapor pressure over a flat surface with respect to phase m of component k in a mixture (if subscript k is not present assume $k = H2O$)
$p'_{eqm.vap.,m,k}$	equilibrium vapor pressure over a curved surface with respect to phase m of component k in a mixture (if subscript k is not present assume $k = H2O$)
p_{mn}	equilibrium vapor pressure difference between phase m and n for a curved surface
x_k	molar mass of component k
y_k	mole fraction of component k $[e.g.\ y_{H2O} = x_{H2O}/(x_{H2O} + x_k)]$

Sub- and superscripts

atm	atmospheric
D	momentum
diff	diffuse
dir	direct
H	heat
i	incident
id	ideal (lossless) and diffuse (isotropic or Lambertian)
k	component of a mixture (i.e. H2O, salt, etc.)
m, n	phase of substance (liquid, solid, or gas)

[1] This usage of the term vapor pressure to refer to non-equilibrium vapor pressure is consistent with many meteorological sources (see Stull (1995) page 83). Alternately, many chemistry and thermodynamic sources use the term vapor pressure to refer exclusively to equilibrium vapor pressure (see Atkins (1990) page 132).

LIST OF SYMBOLS - CONTINUED

Sub- and superscripts

obj	object
Q	mass
r	reflected
rs	reflective surface
s	surface
ss	snow surface
vap	vapor
liq	liquid
m, n	non-vapor phase (solid/ice or liquid)

Abbreviations

BCRDF	BiConical-Reflectance Distribution Function
BHR	BiHemispherical Reflectance
BRDF	Bidirectional-Reflectance Distribution Function
BRF	Bidirectional-reflectance factor
DHR	Directional-Hemispherical Reflectance
FOV	Field of View
HDRF	Hemispherical-Directional Reflectance Factor
NIR	Near-Infrared
SSA	Specific Surface Area
UV	Ultraviolet
VIS	Visible

ABSTRACT

An understanding of the optical properties of snow is vital to accurately quantifying the effect of snow cover on the Earth's radiative energy balance. Existing radiative transfer models often simplify complex crystal habits by utilizing spheres of equivalent specific surface area (SSA). While these models have had some success in accurately predicting snow albedo, more complex models strive to predict the directional reflectance properties of snow. These models require accurate bidirectional reflectance values for various snow crystal habits against which to compare their results. However, few studies in this area exist and none focus specifically on surface hoar—a well-known surface crystal type often responsible for avalanches once buried by subsequent snows.

In this study, it is hypothesized that microstructural changes due to near surface metamorphism, traced by crystal size and type, will alter snow's solar bidirectional reflectance. Specifically, it is postulated that the bidirectional reflectance distribution of the snow's surface before and after surface hoar growth will be predictably and quantifiably different when viewed in the visible wavelengths, thereby allowing the remote detection of surface hoar presence.

To test this hypothesis, a methodology for reliably growing surface hoar in a lab setting was developed. Temporal changes in crystal mass and specific surface area were documented using computed tomography and visible microscopic imaging while a suite of meteorological instrumentation recorded environmental chamber conditions. A spectrometer was used to measure bidirectional-reflectance factors (BRF) both before growth (rounded grains) and after growth (surface hoar) from 42 different incident lighting and viewing geometries. These BRF values provide an accurate data set for comparison to modeling studies.

Analysis of the result revealed three primary conclusions: 1) In the transition from rounded grains to surface hoar, mean BRF values (essentially albedo) decrease slightly ($\leq 2.9\%$) likely due to an increase in grain size; 2) Accompanying surface hoar growth is an increase in SSA and a departure from Lambertian scattering. That is, surface hoar has significantly brighter peak values and significantly darker minimum values than rounded grains; 3. Incident lighting and viewing geometries at which these maximum and minimum BRF values occur show no discernible pattern.

CHAPTER 1

INTRODUCTION

For the listener, who listens in the snow,
And, nothing himself beholds
Nothing that is not there and the nothing that is.—Wallace Stevens

With snow covering as much as 30% of the Earth's surface (Frei and Robinson, 1999), an understanding of its reflectance, absorption, and transmittance properties is important to quantifying its contribution to the planetary radiation budget (Warren, 1982). In addition, advances in satellite remote sensing capabilities have introduced the need for accurate multi-angle reflectance studies at a high temporal and spatial resolution (Brugge et al., 2000). A central challenge faced in researching the optical properties of snow is the extensive diversity of possible crystal habits. Mango and Lee (1966) published a classification system that details 81 categories for crystals grown in the atmosphere, each of which has the potential to display different optical properties once deposited on the snow surface. As explained in *Chapter 2: The Physics of Snow* (page 8), a myriad of environmental factors are constantly conspiring to reshape the predominant crystal type, size, orientation, and interconnectivity both within the snowpack and on its surface. These microstructural changes not only affect the optical response of the snowpack but greatly alter its mechanical properties as well. Thus, in addition to contributing to the scientific community's understanding of climate change, the ability to remotely detect specific snow morphologies will greatly enhance avalanche forecasting capabilities.

To address the challenge presented by so many crystal habit possibilities, a common simplification in radiative transfer models is to utalize an *optically equivalent grain*—a mathematical construct that approximates the complex shape and size of an actual snow crystal by defining a spherical grain with an equivalent surface area to volume ratio (Wiscombe and Warren, 1980; Nolin and Dozier, 2000; Li and Zhou, 2004; Painter and Dozier, 2004). While necessary for models using Mie scatter theory, the optically equivalent sphere neglects many of the crystal features that affect its directional scattering properties and is primarily useful in hemispherically averaged radiative quantities such as irradiance or albedo (Jin et al., 2008).

As examined in *Chapter 2: Bidirectional-Reflectance Distribution Function* (page 42), a more appropriate approach for capturing the effects of crystal habit on the angular distribution of reflected light is a comprehensive multi-angle study using various incident and observer angles. Multi-angle studies often report results in terms of a *bidirectional reflection distribution function* (BRDF, f) or a *bidirectional-reflectance factor* (BRF, R). As the name implies, a BRDF "describes the scattering of a parallel beam of incident light from one direction in the hemisphere into another direction in the hemisphere" (Brugge et al., 2000). Mathematically, it is the ratio of incident irradiance E (W m^{-2}) from a single direction to the radiance L (W m^{-2} sr^{-1}) exiting the surface in a single direction. This ratio is therefore a function of reflectance azimuth (θ_r) and zenith (ϕ_r) angle as well as incident zenith (θ_i) and azimuth (ϕ_i) angle and, finally, wavelength (λ). Results in this thesis are reported in terms of a BRF value. Closely related to the BRDF, the term BRF describes the ratio of radiance L_r reflected from the snow surface to the

radiance L_{rid} reflected from a commercially available reference surface (e.g. Spectralon-discussed in *Chapter 3: Spectralon Reference Panel and BRF*—page 82).

For anyone who has walked through a field of newly fallen snow on a sunny day, the term BRDF should have an intuitively obvious meaning as it allows the observer to characterize the intense sparkles of light that emanate from the snow surface and appear to twinkle with changing viewer angle.

The myriad of factors involved in the birth and development of various snow crystal habits is discussed in *Chapter 2: Crystal Growth in the Atmosphere* (page 8). It is shown that there are nearly unlimited possibilities for crystal habit. An exhaustive examination of the bidirectional reflectance properties of every possible crystal habit is not possible within the constraint of this thesis and is likely unnecessary, as the snow surface is rarely made up of exactly identical grain types within the field of view of most optical instrumentation. Certainly within the field of view of satellite-based sensors such as MISR (Multi-angle Imaging SpectroRadiometer), a sensor that is mounted on NASA's EOS satellite and is commonly used for multi-angle optical measurements (Dozier and Painter, 2004), the observed snow field will not contain exactly identical crystal size, type, and arrangement. Nevertheless, it is not uncommon to find that crystals within a snow field that share generally related features.

A more general classification system than Mango and Lee's 81 categories, *The International Classification for Season Snow on the Ground* (Fierz et al., 2009) provides a useful system for recording terrestrial snow observations at the scale likely to be encountered in remote sensing studies. In this system there are 7 basic categories

important for recording snow surface crystal type: precipitation particles, decomposing fragmented precipitation particles, rounded grains, faceted crystals, surface hoar, melt forms, and ice formations. This paper further focuses on the optical properties of rounded grains as well as surface hoar, a common surface crystal morphology that, once buried by subsequent snows, acts as a weak layer leading to avalanching.

The growth of surface hoar is explored in detail in *Chapter 2: Crystal Growth at the Snow Surface* (page 19). Surface hoar is a faceted crystal known to form on cold, clear nights when the air temperature drops below the frost point, at which point vapor in the saturated air deposits directly on the snow surface (Figure 1). Shea and Jamieson (2011) state that 34% of all avalanche fatalities between 1972 and 1991 that occurred in the Canada Mountains initiated on a surface hoar layer. The critical nature of this particular crystal habit to avalanche occurrence makes it an obvious choice for study in this thesis.



Figure 1. Left, buried surface hoar layer (photo Aspen Expeditions) and, right, surface hoar (photo David Walters)

In a preliminary study at Montana State University's (MSU) Subzero Science and Engineering Research Facility (SSERF), a Resonon Inc. Hyperfire visible hyperspectral camera was used to take images of rounded grains and surface hoar snow with nadir solar simulator illumination and a single off-axis view angle. The reflected radiation averaged over an small area ($\sim 25\ cm^2$), showed a change in visible BRF values after the surface hoar had developed. Since visible albedo has been shown to be largely insensitive to grain size, the observed changes are likely attributable to grain type. These early results potentially reveal surface hoar's optical signature. To address the lacunae in this early work, the study conducted for this thesis expands the solar illumination and viewing geometry to include a variety of forward- and backward-scattering observation angles.

This study's hypothesis is that microstructural changes due to the deposition of faceted surface hoar crystals at the snow's surface, will alter visible bidirectional reflectance as compared to rounded grains. Specifically, it is postulated that the bidirectional-reflectance factor of the snow's surface before and after surface hoar growth will be predictably and quantifiably different, thereby allowing the remote detection of surface hoar presence. Recent theoretical studies found in the literature support this assertion but physical verification is necessary.

To test this hypothesis, it was first necessary to develop a methodology (explored in Chapter 3) for growing surface hoar in a lab setting as well as accurately documenting crystal growth parameters such as size, type, rate of mass deposition, and orientation. Once various surface hoar morphologies were predictably and reliably grown in the lab, protocols for optical testing were developed and carried out on two distinct crystal

morphologies: rounded grains and c-axis dominated surface hoar. The resulting BRF values for both grain types are presented in *Chapter 4: Optical Properties Results* (page 102).

While the growing of the surface hoar was developed as a necessity to test its optical properties, the unique methodology developed has scientific relevance in its own right. While Adams and Miller (2003) have grown surface hoar in a lab setting, until this study none had accurately simulated the radiative energy loss to the clear night sky that occurs at the snow surface and is the driving mechanism for creating necessary temperature gradients and subsequent deposition of water vapor. Not only does MSU's climate control chamber allow the growth of surface hoar, but it also enables careful selection of atmospheric conditions to develop particular surface hoar morphologies. Consistent with Kobayashi (1961), the predominant axis of growth could be controlled by varying snow surface temperature.

For this reason, chapters are divided into two sections—the first dealing with surface hoar growth and the second with its optical properties. Chapter 2 provides background on the relevance of surface hoar in snow science as well as previous optical studies of various snow morphologies. Chapter 3 details the methodology developed both to grow surface hoar in a lab setting and test its optical properties. Chapter 4 provides an examination of the results and discussion of possible implications. Finally, Chapter 5 gives closing remarks and recommendations for future study.

CHAPTER 2

BACKGROUND

How full of the creative genius is the air in which these (crystals) are generated! I should hardly admire them more if real stars fell and lodged on my coat.—H. D. Thoreau

The following chapter looks first at how crystals growth in the atmosphere, then at how they morph once deposited on the ground and, finally, how the interplay of energy fluxes at the surface of the snowpack form surface hoar, a layer that once buried creates a potential weak layer on which an avalanche can occur. The necessary equations for an energy audit at the snow surface are provided as well as the means for calculating mass flux during surface hoar growth. In subsequent chapters, lab data are used to predict the amount of mass added during surface hoar growth and the results are compared to data from computed tomography scans.

The optics section of this chapter examines the nomenclature particular to bidirectional reflectance studies. Care is taken to provide units with all terms in order to avoid confusion with the myriad of non-standard uses of optics jargon. Time is spent examining solid angle, projected solid angle, and throughput, as well as other terms whose subtle distinctions, if not well understood at the outset, will perpetually hamper understanding. Finally, previous studies in snow optics are surveyed and the state-of-the-art explained.

The Physics of Snow

Crystal Growth in the Atmosphere

Vapor Pressure. The growth of snow crystals in the atmosphere (and in the snowpack) is primarily driven by vapor pressure gradients. As a thought experiment, imagine a pot of liquid water at a given temperature. A lid is placed on the pot creating a closed system. At the air-water interface water molecules are constantly in motion and, if excited enough, will break free of the surface tension and form vapor in the air above the water. The warmer the water, the more excited the water molecules and the easier it is to break free and form vapor. The vapor, in turn, presses against the water surface. This pressure acts to slow additional water molecules from leaving the surface and is termed *vapor pressure*[2] $\wp_{H2O}$. Given enough time at a fixed water temperature, the system will reach a dynamic equilibrium in which the number of molecules leaving the surface is exactly balanced by the number of molecules that rejoin the surface. At this point the vapor is said to be in equilibrium with respect to the water surface and the pressure it exerts is termed the *equilibrium vapor pressure* (a.k.a. *saturation*[3] *vapor pressure*). Succinctly, equilibrium vapor pressure is the pressure exerted by a vapor that is in equilibrium with its non-vapor phase; thus, we can now expand our thought experiment

[2] This usage of the term vapor pressure to refer to non-equilibrium vapor pressure is consistent with many meteorological sources (see Stull (1995) page 83). Alternately, many chemistry and thermodynamic sources use the term vapor pressure to refer exclusively to equilibrium vapor pressure (see Atkins (1990) page 132). The later definition is consistent with Raoult's Law of Vapor Pressure.

[3] Equilibrium vapor pressure is also often referred to as saturation vapor pressure. This term originated before the 18th century during which time scientist erroneously believed air dissolved water vapor (Babin, 2000). Saturation vapor pressure was used to indicate the maximum amount of water that air could dissolve. Today it is used to indicate equilibrium vapor pressure.

to include any material (not just an air-water interface) in either its liquid or its solid phase (Perrot, 1998).

Partial Pressure. Air is a mixture of gasses, each of which contributes to the total pressure of the system. According to Stull (1995), "the pressure associated with any one gas in a mixture is called the partial pressure." Dalton's Law of Partial Pressure (1808) states,

$$P_{actual} = \sum_{k} \wp_k \tag{1}$$

where, P_{actual} is the total pressure of the gas in the system and $\wp_k$ represents the partial pressure of each component of the system (Pauling, 1970). Water vapor is a gas component in an air mixture. Vapor pressure may now be more precisely defined as the partial pressure of water vapor in air mixture (Stull, 1995).

Clausius-Clapeyron. The equilibrium vapor pressure over a flat, liquid or solid surface can be calculated using the *Clausius-Clapeyron equation*,

$$\frac{dp_{eqm.vap,m}}{dT} = \frac{L_{mn}}{T(V_n - V_m)}, \tag{2}$$

where m and n are the two phases, T is temperature in Kelvin, V is the volume per unit mass of the phase, and L is the latent heat between two phases. For reference, at $0°C$ the latent heat of fusion ($L_{ice,liq}$), evaporation ($L_{liq,vap}$), and sublimation ($L_{ice,vap}$) for water are, respectively, $3.335 \times 10^5, 2.505 \times 10^6, and\ 2.838 \times 10^6\ J\ kg^{-1}$ (Armstrong and

Brun, 2008). A common and convenient alternative is the *Antoine equation*, which provides a 3-parameter fit to experimental pressure data[4],

$$p_{eqm.vap.,m} = \exp\left(\mathcal{A} - \frac{\mathcal{B}}{T + \mathcal{C}}\right) \qquad (3)$$

where $p_{eqm.vap.,m}$ is the equilibrium vapor pressure over a flat surface with respect to phase m, T is the temperature in Kelvin, and $\mathcal{A}, \mathcal{B},$ and $\mathcal{C}$ are Antoine parameters discussed below (Perry and Green, 1997; Tester and Modell, 1997).

Continuing our thought experiment, as the temperature of the water in the pot decreases, the water molecules become less excited and fewer molecules break free from the surface. In turn, the equilibrium vapor pressure decreases since there are now less vapor molecules in the air above the surface. Ice, with its rigid latticework and lethargic molecules, always has a lower equilibrium vapor pressure than liquid water. This is true even for *supercooled* droplets (liquid water cooled below freezing that has yet to change phase). Buck (1981) provides empirically derived Antoine parameters for Equation (3)). In a generally metastable state with respect to flat, liquid water between the temperatures of $-40°C$ and $0°C$ Buck suggests

$$p_{eqm.vap.,liq} = [1.0007 + (3.46 \times 10^{-6} P_{air})]6.1121 \exp\left(\frac{17.966T}{247.15 + T}\right) \qquad (4)$$

and with respect to ice between the temperatures of $-50°C$ and $0°C$,

$$p_{eqm.vap.,ice} = [1.0003 + (4.18 \times 10^{-6} P_{air})]6.1115 \exp\left(\frac{17.966T}{272.55 + T}\right), \qquad (5)$$

[4] While not generally of concern in crystal growth, assumptions used in deriving the Clausius-Clapryeon make it unsuitable at high pressures and near the critical point (Perry, 1997).

where P_{air} is the atmospheric air pressure (hPa) and T is in Celsius. A plot of Equations (4) and (5) is provided in Figure 2, illustrating a higher vapor pressure over liquid water than ice.

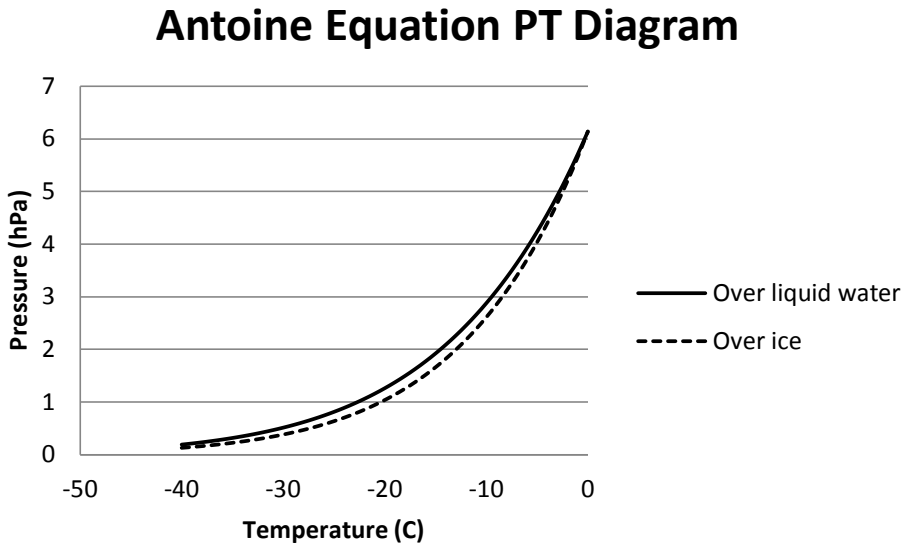


Figure 2. Plot of Equation (4) and (5), showing that the vapor pressure over liquid water is higher than over ice.

Equations (4) and (5) predict the growth of ice crystals at the expense of supercooled water droplets in the atmosphere—a process known as the *Bergeron process* (Ahrens, 2007). That is, a vapor pressure gradient will develop that directs a mass flow of evaporated water molecules from over the liquid water drops to areas of lower vapor pressure over the surface of the ice crystals. As crystals grow in mass, they are no longer supported by updrafts in the clouds and fall to earth. Collision with supercooled particles can causes *riming* or *accretion*—the freezing of water droplets from the liquid phase onto the surface of the crystal (Figure 3). A collection of crystals intertwined is often called a *snowflake* (Libbrecht, 2001). With an explanation of how snow crystals form in the

atmosphere now in place, attention is turned to examining the shape of crystal that develops during growth.

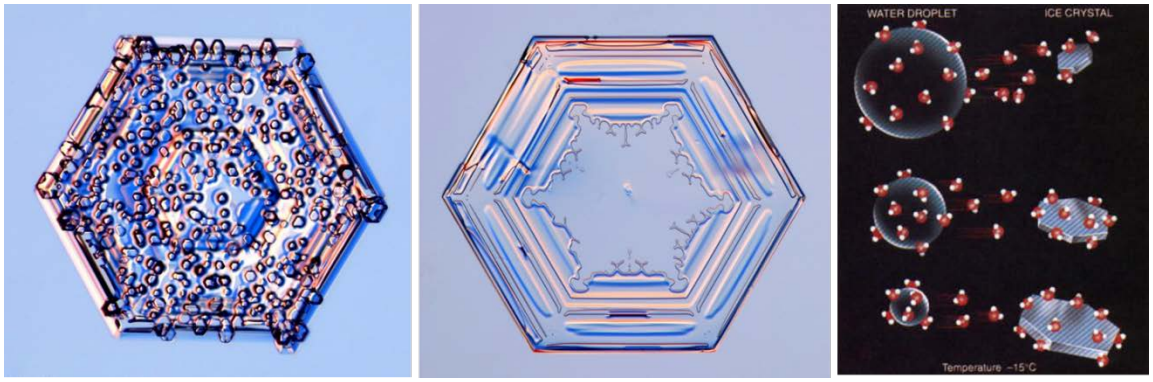


Figure 3. Example of rimed and unrimed hexagonal plate (left) (Reproduced from Libbrecht, 1999). Conceptual illustration of the Bergeron process (left) (Reproduced from PicsWeb).

Relative Humidity. With vapor pressure defined, we can now define *relative humidity* (%) as the ratio of the partial pressure of water vapor in the system (e.g. the vapor pressure) to that of the equilibrium vapor pressure relative to a *flat* (liquid or ice) surface at a given temperature,

$$RH = \frac{\mathcal{P}_{H2o}}{p_{eqm.vap,m,H2O.}} \qquad (6)$$

Because relative humidity is defined relative to a flat surface, in the atmosphere—where liquid water drops have convexly curved surfaces—a relative humidity of greater than 100% is possible and is termed *supersaturation*. The effects of curvature are discussed in a subsequent section.

Crystal Habit. It is well known that the oxygen and two hydrogen atoms that form water create a hexagonal latticework. This molecular level geometry is reflected in

the structure of ice, which consists of six prism faces bounded by two basal planes (Figure 4). Nakaya (1954) published an early study concerning habit of atmospherically grown crystals. By nucleating crystals on rabbit hair, he determined that preference for growth of prism faces (c-axis growth) or for growth of basal faces (a-axis growth) was primarily a function of air temperature. Further, secondary features were controlled by the degree of supersaturation (Figure 5). Hallett and Mason (1958) and Kobayashi (1961) confirmed these results.

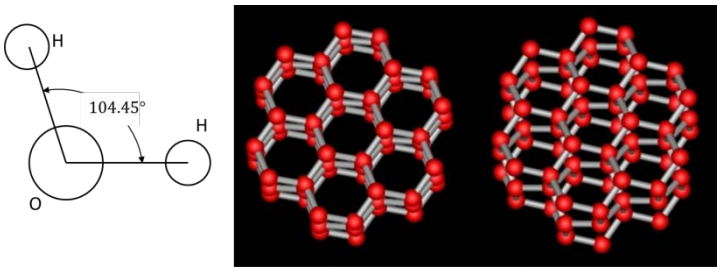


Figure 4. Conceptual illustration of a water molecule and the hexagonal latticework of ice (Reproduced from Libbrecht, 2001)

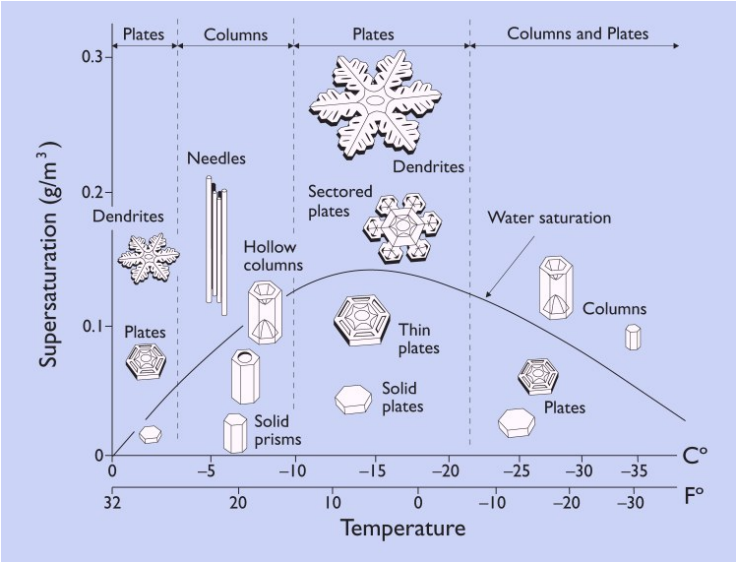


Figure 5. Illustration of the relationship between temperature, supersaturation, and crystal habit (adapted from Nakaya, 1954)

Of note in Figure 5 is the alternating transition between c-axis dominated growth and a-axis dominated growth as a function of temperature. That is, plate growth occurs between $0°C\ to\ -4°C$, column growth between $-4°C\ to\ -10°C$, plate growth between $-10°C\ to\ -22°C$, columns and plates below -22°C. Below $-22°C$, supersaturation plays a significant role in determining plate vs column growth (Kurdoda, 1983). Additionally, increasing supersaturation increases the complexity of the crystal habit that develops. For example, the thick, solid plates that form at low supersaturation transition to skeletal plates and finally to dendrites as supersaturation increases. Solid prismatic columns become hollow prisms and finally needles as supersaturation increases. As Kuroda (1986) explains, "the surfaces of polyhedral ice crystals become morphologically unstable by way of preferred growth of edges and corners of the crystals with increasing supersaturation."

The development of the complex shapes at high supersaturation can be largely explained by Mullins-Sekerka instabilities, random perturbations that develop on prism faces (due to impurities in water) and act as concentration points for diffusing molecules (Mullins and Sekerka, 1963). In the case of ice crystals, the convexities at the corner of the hexagon act as instability points growing more rapidly than the flat faces. In turn, these new growths can develop their own Mullins-Sekerka instabilities causing further branching of the crystal and the complex dendritic forms popularly associated with snow crystals (Libbrecht, 2005).

Crystal Growth in the Snowpack

Equilibrium Growth. While the physics governing crystal growth does not change for crystals in the snowpack, the thermodynamic conditions in which the crystal is grown change considerably. The tangled mass of newly fallen snow forms a network of capillary spaces filled primarily with air, water vapor, and possibly liquid water. Within this porous medium, "the thermodynamic relationships among the three water phases determine the grain growth and metamorphism of snow" (Armstrong and Brun, 2008). Unlike crystals grown in the highly supersaturated atmosphere, supersaturation values within the snowpack generally much lower—on the order of 1% (McClung and Schaerer, 2006). In this environment even slight vapor pressure gradients can dictate crystal morphology. In fact, in the absence of any temperature gradient in the snowpack, surface curvature plays a vital role in determining how a crystal will morph with time. At the ice/air interface, the pressure difference ($p_{m,n}$) between phases m and n is a function of surface radius ($\mathbb{r}_{m,n}$),

$$p_{mn} = \frac{2\sigma_{mn}}{\mathbb{r}_{mn}}, \tag{7}$$

where σ_{mn}can represent either, $\sigma_{vap,ice}$, or $\sigma_{vap,liq}$ and is the interfacial surface tension. Accordingly, tight curvatures produce higher pressure differences. The Gibbs-Duhem equation, a more general form of Clausius-Clapeyron equation, is useful for curved surfaces (Defay et al., 1966, Colbeck 1980, Adams and Brown, 1983),

$$\frac{V_{ice}dp_{eqm.vap.,ice}}{dT} - \frac{V_m dp_{eqm.vap.,m}}{dT} = \frac{L_{mn}}{T}. \tag{8}$$

Armstrong and Brun (2008) states, "Relating the phase pressure through Equation (7), Gibbs-Duhem's equation integrates to Kelvin's expression for the equilibrium vapor pressure $p'_{vap,sat,m}$ over a curved surface,"

$$p'_{eqm.vap,m} = p_{eqm.vap.,m} \exp\left(\frac{2\sigma_{m,vap}}{\mathbb{r}_{m,vap}} \frac{1}{R_{vap}\rho_m T}\right), \qquad (9)$$

where the subscript m can be replaced with either *ice* or *liq*, $p_{eqm.vap.,m}$ can be calculated from either Equation (4) or (5), ρ_m is the density of liquid water or ice, R_{vap} is the gas constant for water vapor ($= 461.50\ J\ kg^{-1}\ K^{-1}$), and T is temperature in Kelvin. Equation (9) predicts the vapor pressure above the sharply curved convexities of newly fallen snow will be higher than above concavities (Armstrong and Brun, 2008). The physical reasoning for this phenomenon is illustrated in Figure 6.

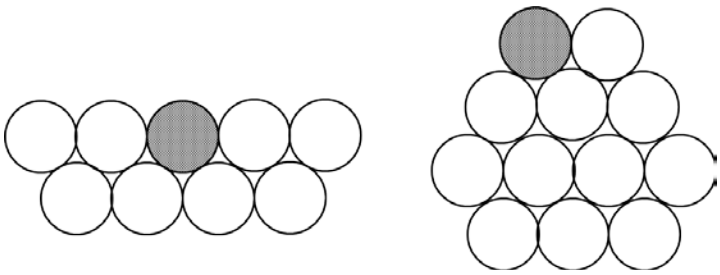


Figure 6. Conceptual illustration of additional contact in flat vs. curved surface. The extra bonds in the flat surface tend to limit the amount that can escape thereby lowering the vapor pressure over a flat (or concave) surface relative to a curved surface.

This slight vapor pressure gradient will tend to erode newly fallen snow, sublimating dendritic arms and depositing mass in concavities. It also encourages *sintering* (the bonding of adjacent snow grains) at points of grain-to-grain contact where concavities often occur (Figure 7). Growth due to curvature effects is sometimes termed e*quilibrium growth* and results in *rounded* grains (Colbeck, 1980). However, this is

something of a misnomer since lab studies of single crystal growth suggest that the equilibrium form for snow is a hexagonal plate at temperatures below $-10°C$ and rounded forms at higher temperatures (McClung and Schaerer, 2006). Nevertheless, equilibrium growth is commonly used to describe the growth of rounded forms. Left unchecked, equilibrium growth will also grow larger rounded forms at the expense of smaller grains (again, due to the sharper radius of smaller grains). In a permanent snowpack, where temperature gradients at depth are small, this rounding process, in conjunction with the overburden pressure, can transform snow into *neve*, *firn snow*, and finally glacier ice.

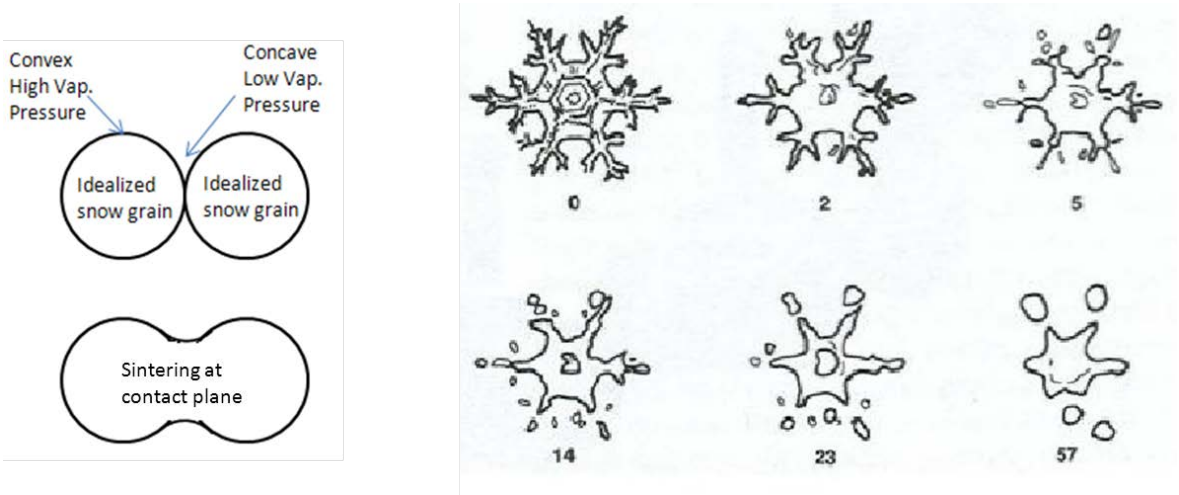


Figure 7. Sintering (right) and rounding (left) [Reproduced from McClung and Schaerer, 2006] of new snow due to curvature induced vapor pressure gradients.

Kinetic Growth. In contrast to the equilibrium growth discussed above, it is quite possible to have strong temperature gradients within a snowpack that render curvature effects negligible. Throughout the winter the ground surface remains close to freezing (due to geothermal heating) while the air temperature above the snow can be

considerably colder. The resulting temperature gradient induces a vapor pressure gradient in the snowpack that competes with the curvature effects. At a critical threshold of $\sim 10°C\ m^{-1}$ temperature gradient effects begin to dominate and *kinetic growth* occurs (Akitaya, 1974; Colbeck 1982; Armstrong, 1985; McClung and Schaerer, 2006).

In a supersaturated environment in the atmosphere, kinetic growth leads the diverse crystal shapes shown in Nakaya's table (Figure 5). However, within the snowpack, the confining nature of the pore space as well as low supersaturation tends to limit growth of crystals to simple prismatic forms. Further, the faceted crystals that develop within a snowpack often reflect the direction of the temperature gradient in the snowpack, growing into the flow of vapor being transported by the temperature induced pressure gradient. While faceting in the snow pack can take place anywhere the temperature gradient is strong enough, *depth hoar* is an often-cited example of kinetic growth forms. It often forms near the base of a shallow snowpack where moisture from the ground coupled with strong temperature gradients cause faceting (Figure 8).

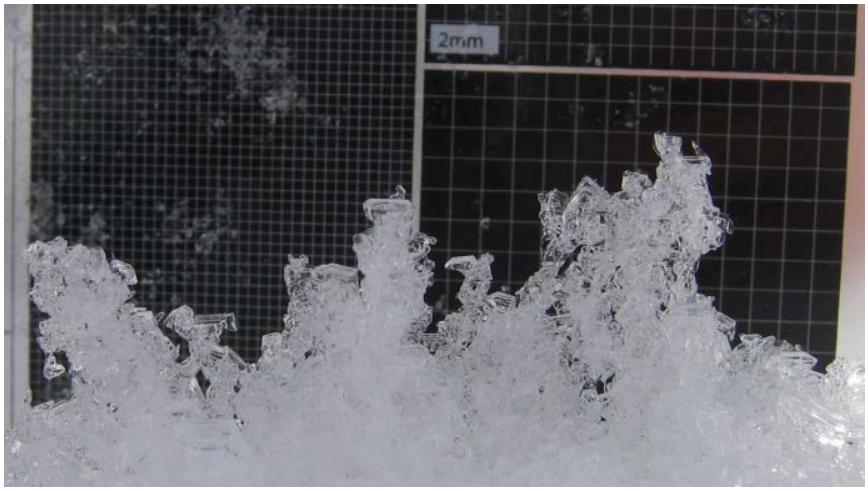


Figure 8. Depth hoar chains showing simple crystal habit due to low supersaturation and preferential orientation along the temperature gradient (photo David Walters)

Thus, within the snowpack, one observes nearly continuous metamorphism in response to the myriad variations in growth conditions. In a shallow homogeneous snowpack, the daily variations in air temperature and cloud cover produce temperature gradients that come and go. Each new snow storm brings another layer of snow with its own temperature, density, and predominant crystal shape. Thus, temperature gradients can develop between adjacent snow layers. Ice crusts buried in the snow pack often produce strong localize gradients above and below the frozen surface causing faceting (Adams and Brown 1988 and 1990). Even in an *isothermal* snowpack—that is, in the absence of any temperature gradient—the crystal morphology continues to change due to curvature effects, slowly rounding and growing the grains.

Crystal Growth at the Surface

The surface layer of the snowpack is also subject to the ever-changing thermodynamic conditions. In fact, energy balance calculations at the snow surface have to account for long- and shortwave energy, latent heat flux due to phase change, and convective heat flux both from the air above and the snow below (see following section). Further, the surface of the snow has the potential to experience widely ranging supersaturation. A wide variety of crystal habits are thus possible.

Crystals are often categorized by the processes which formed them regardless of the specifics of crystal habit. Near the surface, five distinct process typically drive crystal formation or metamorphism: melt-layer recrystallization, radiation recrystallization, diurnal recrystallization, equilibrium growth and surface hoar. 1) *Melt-layer recrystallization* occurs when crusts, formed from rain or melt-freeze events. This layer

acts as impervious dam for moisture creating high supersaturation below the crust. In addition, large temperature gradients can be found in the vicinity of the crusts. The combination encourages faceted crystal growth (Fukuzawa, T. and E. Akitaya, 1993). 2) *Radiation recrystallization* occurs during clear days when strong solar radiation penetrates the first few centimeters of the snowpack and warms the snow just below the surface. At the same time, the surface of the snow is radiating its energy to the clear sky and cooling. A gradient forms in the first few centimeters of the snowpack morphing the crystals into a faceted form (LaChapelle and Armstrong, 1977). 3) *Diurnal recrystallization* occurs as a result of the strong temperature gradient reversal that occurs between night and day in the top few centimeters of the snow. As with any temperature gradient that is strong enough, faceted crystals can form (Birkeland, 1998). 4) *Equilibrium growth*, occurs when no distinct vapor pressure gradient is created by atmospheric conditions. Similar to equilibrium growth conditions within the snowpack, in the absence of any gradient, curvature effects dominate and newly fallen snow will begin to round. This is a typical process seen on cloudy, warm days. 5) *Surface hoar*, being the focus of the research in this thesis, is addressed in detail in the follow section.

Surface Hoar. A 1965 study by Gow noted a faceted crystal (later termed surface hoar) that grew on the surface of the snow. He speculated that it developed through metamorphism of crystals at the snow surface. Linkletter and Warburton (1975) determined that, in fact, surface hoar is created by deposition of water vapor under cold, clear atmospheric conditions. In fact, many avalanche safety books provide an introductory explanation of surface hoar as simply frozen dew (Tremper, 2001). While a

reasonable definition to a first approximation, frozen dew may erroneously be interpreted to mean that the water vapor first condenses onto the snow surface as liquid water and then freezes in situ. In fact, surface hoar is a result of direct deposition from the vapor phase. Under calm, clear night skies, an energy loss due to longwave radiation cools the snow, creating a sharp temperature gradient in the first few millimeters above the snow surface (Lang and Brown (1984). When the snow surface temperature drops below the frost point temperature, the air directly above the surface becomes supersaturated (relative humidity greater than 100%). The resulting vapor pressure gradient causes *deposition*—the direct gas to solid transition of water vapor to ice—on the snow surface; the resulting crystals are known as surface hoar and are distinct from *rime*, which forms from *condensation*—the direct liquid to solid transition of supercooled water droplets to ice (McClung and Schaerer 2006).

A complete understanding of surface hoar growth conditions requires the examination of the feedback processes of water vapor in the atmosphere as well as the effects of wind. Water vapor in the atmosphere tends to absorb and emit radiant energy efficiently (high emissivity and absorptivity) at terrestrial wavelengths, and clouds (i.e. water in its liquid state) are even more efficient, essentially acting as a blackbody radiators (Arya, 2001). Therefore, clouds (and water vapor to a lesser extent) act as an insulating layer, constantly absorbing and reemitting longwave radiation back to the snow surface. While high absolute humidity provides needed moisture for surface hoar growth, the water vapor also acts as insulation, hampering the cooling of the snow surface. Colbeck (1988) suggests that, in the absence of any air movement, when the air directly

above the snow surface finally supersaturates, fog inevitably forms negating further cooling and the possibility of surface hoar growth. Additionally, he states that, even if no fog formed, the temperature gradients just above the snow surface resulting from radiative cooling alone could not produce the crystal growth rates seen in field observations by Lang et al. (1984). He argues some air movement is needed to prevent the formation of fog, bring needed moisture to the snow surface, and to steepen the temperature gradient.

In regard to the latter assertion, Nyberg (1939) found temperature gradients in the first millimeter above the snow surface of $1.25°C\ mm^{-1}$ and $0.63°C\ mm^{-1}$ in the next 4 mm, suggesting a laminar sublayer in the first 1 mm above the snow surface (Colbeck, 1988). The gradients in this sublayer are significantly larger than the expected $0.035°C\ mm^{-1}$ from pure diffusion. Colbeck argues that warm, well mixed air currents above the interfacial layer, likely from very light gravitational winds, are responsible for the steeper than expected gradient. Conversely, turbulent transfer of energy caused by wind speed in excess of $2\ m\ s^{-1}$ destroys the sublayer temperature gradient and any chance of surface hoar growth. Succinctly, Colbeck states, "Apparently some wind is necessary to provide the turbulent transfer necessary to bring the vapor to the interfacial sublayer, but more wind transfers enough heat to prevent the degree of cooling necessary for condensation."

Lending credit to the above observations, Hachikubo and Akitaya (1997) found large crystal hoar developed at wind speeds of 1 to $2\ m\ s^{-1}$. Further, condensation rates increased linearly with the product of wind speed and vapor pressure gradient indicating

both are necessary. Interestingly, they found the bulk transfer coefficient was nearly constant when the surface hoar was small, but increased as the surface hoar grew to more than a few millimeters. They suggest that these larger crystals extended beyond the interfacial sublayer, interacting with the turbulent air above, resulting in an increase in bulk transfer.

Energy Balance and Mass Flux Equations

The complex interplay of various heat fluxes experienced by the surface of the snow is illustrated in Figure 9 and can be quantified by considering all of the radiative, convective, and conductive processes involved—namely: shortwave radiation ($\mathcal{S}_{net}$) between 200 and 4000 nm, net longwave radiation ($\mathcal{L}_{net}$) 4000 nm and longer, sensible heat ($\mathcal{H}_s$), latent heat ($\mathcal{H}_L$), and energy flux carried by precipitation and blowing snow ($\mathcal{H}_P$). In this context, sensible heat is a direct application of the heat flux equation (Wetly et al., 2008, p302). If considering an energy balance on an infinitesimally thin surface interface between the air and the snow, (q) represents the conductive heat flux from the snow layer below the surface, whereas if the entire snowpack is included in the control volume, (q) represents the conductive heat flux from the soil underlying the snow pack (Morstad, 2004; Armstrong, 2008).

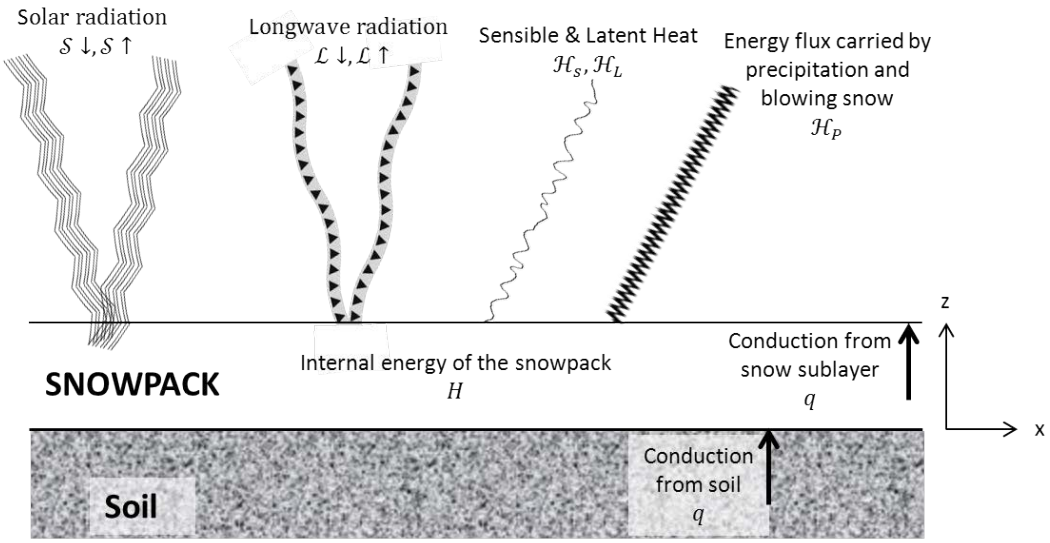


Figure 9. Energy balance of a snowpack. Note that the conductive term (q) can represent heat conduction from the soil to the snowpack or from snow sublayer to the snow surface depending on the choice of control volume (Adapted from Armstrong, 2008).

Mathematically, the energy balance may be expressed,

$$\frac{dH}{dt} = \mathcal{S}_{net} + \mathcal{L}_{net} + \mathcal{H}_S + \mathcal{H}_L + \mathcal{H}_P + \mathcal{G} \qquad (10)$$

where,

dH/dt $= net\ rate\ of\ change\ of\ snowpack\ internal\ energy$
$\mathcal{S}_{net}$ $= shortwave\ radiation$
$\mathcal{L}_{net}$ $= longwave\ radiation$
$\mathcal{H}_S = sensible\ heat\ flux\ from\ the\ atmoshere$
$\mathcal{H}_L = latent\ heat\ due\ to\ phase\ change$
$\mathcal{H}_p = energy\ carried\ with\ blowing\ or\ precipitating\ snow$
q $= conductive\ heat\ flux\ from\ soil\ or\ snow\ surface\ sublayer$

The value of $\mathcal{H}_p$ is generally small, except in the case of warm rain, and is neglected in the following development (Armstrong and Brun, 2008). Energy gain by the snowpack ($dH/dt > 0$) is positive, while energy loss by the snowpack ($dH/dt < 0$) is negative. Each term in Equation (10) will be considered individually with special

attention given to the latent heat ($\mathcal{H}_L$) accompanying phase change during surface hoar growth.

Internal Energy. The term dH/dt represents the thermal component of the snowpack. It is dependent on either the latent heat of ice melting or freezing as well as the *snowpack's cold content*, where cold content is defined as the integral term in the following equation,

$$\frac{dH}{dt} = L_{liq,ice}(R_M - R_F) - \int_{z=0}^{HS} \left[\frac{d}{dt}\left(\rho_{snow}(z) c_{p,i} T_{snow}(z)\right)\right] dz. \quad (11)$$

Here R_M and R_F are the rate of melting and freezing respectively, $L_{liq,ice}$ is the latent heat of fusion of ice ($3.34 \times 10^5\ J\ kg^{-1}$), and $c_{p,i}$ is the specific heat capacity of ice ($2.1 \times 10^3\ J\ kg^{-1}\ K^{-1}$). Snow density ρ_{snow} and snow temperature T_{snow} are both functions of height z above the soil/snow interface and are integrated between $z = 0$ and the height of the snowpack (HS).

Radiative Heat Transfer. Electromagnetic radiation is examined in more depth in the optics section of this paper. At this juncture it is enough to say that vibrating atoms or molecules (say on the surface of the sun) emit energy in the form of waves or photons. Radiation can travel through a vacuum and can warm the surface of objects it strikes if absorbed. The wavelength emitted by an object is a function of its temperature. Figure 10 shows the electromagnetic spectrum with common terminology labeled. In physics, all radiation, regardless of whether it can be seen with the human eye or not, is termed *light* (i.e. radiation and light can be used synonymously).

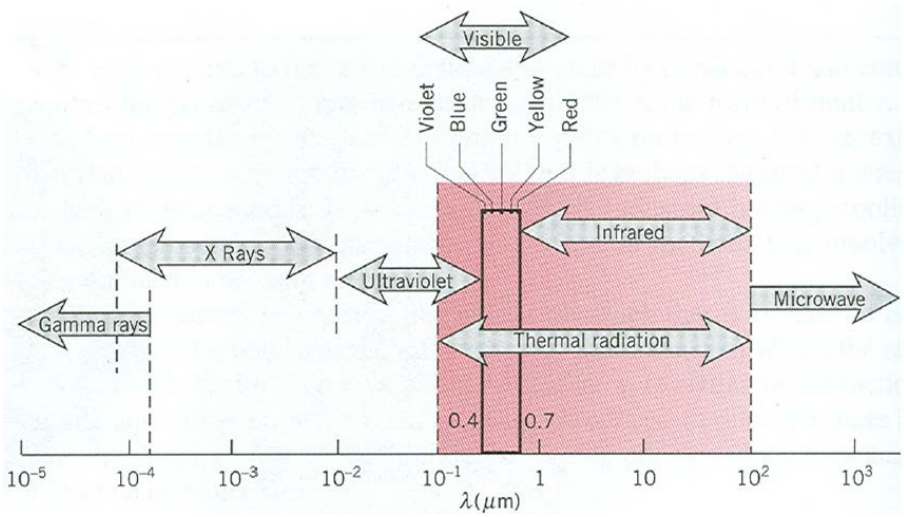


Figure 10. Electromagnetic spectrum (Incropera and Dewitt, 2007, Figure 12.3).

Radiative Heat Transfer: Ultraviolet/Visible/Near Infrared Radiation. The sun, at approximately 5788K, radiates over 99% of its energy in the bandwidth between 200 to $4000nm$ and is termed *shortwave radiation*, *insolation*, or solar *radiation* (Petty, 2006). Wavelengths longer than 4000 nm are termed *longwave radiation*. Further subdividing, *ultraviolet* (UV), *visible* (Vis), and *near infrared* (NIR) radiation have spectral bandwidths from 200 to 400 nm, 400 to 700 nm, and 700 to $4000\ nm$ respectively[5].

Much of the energy that strikes the top of the Earth's atmosphere is absorbed by the atmosphere or reflected back to space. Of the percentage that reaches the snow's surface, nearly all is reflected due to snow's high *albedo* a in the UV/VIS. The energy available to warm the snow ($\mathcal{S}_{net}$) is given by,

$$\mathcal{S}_{net} = \mathcal{S}\downarrow + \mathcal{S}\uparrow = \mathcal{S}\downarrow(1-a). \qquad (12)$$

where $(1-a)$ represents the percent of insolation absorbed by the snowpack. Net radiation values greater than zero ($\mathcal{S}_{net} > 0$) represent a positive energy gain (warming

[5] The bandwidths delineated for each of the above terms are subjective and some variation occurs between publications.

of the snow). The expected solar contribution to surface hoar growth is negligible since surface hoar grows at night.

Radiative Heat Transfer: Longwave Radiation. The globally averaved temperature of the Earth is approximately $\sim 15°C$ $(288K)$ and thus radiates at significantly longer wavelengths than the sun. The longwave bandwidth (between 0.4 and $100\mu m$) accounts for nearly all wavelengths emitted by terrestrial objects and is sometimes called *terrestrial radiation* or *thermal radiation.* The snow surface (subscript SS) sees longwave radiation from all terrestrial objects within its field of view. The fractional area of each object within the snow's field of view is known as the object's *view factor* $F_{ss,obj}$, where the object can be the atmosphere itself, passing clouds, trees, adjacent hill sides, etc. Incoming longwave radiation can be calculated by summing the radiation from each object within the snow surface's field of view. The net flux of longwave radiation averaged over all wavelengths is given by

$$\mathcal{L}_{net} = F_{ss,sky}\left(\mathcal{L}_{i,sky} - \varepsilon_{ice}\sigma T_{ice}^4\right) + \sigma \sum_{obj=1}^{\#obj} F_{ss,obj}(\varepsilon_{obj}T_{obj}^4 - \varepsilon_{ice}T_{ice}^4) \qquad (13)$$

where ε_{obj} and ε_{ice} are the emissivity of the object and the snow surface respectively, σ is the Stefan-Boltzman constant ($5.6696x10^{-8}$ $[W\ m^{-2}K^{-4}]$), T_{obj} and T_{ice} (in K) are the temperature of objects in the snow's field of view and of the ice, respectively, $\mathcal{L}_{i,sky}$ is the incident longwave radiation from the sky, and $F_{ss,sky}$ and $F_{ss,obj}$ are the view factors from the snow to the sky and the snow to surrounding objects respectively (Adams et al., 2005). Net radiation values greater than zero ($\mathcal{L}_{net} > 0$) represent a

positive energy gain (warming of the snow). The first term on the right hand side accounts for the exchange of energy between the snow surface and the sky, while the right most term accounts for energy exchange to and from surrounding objects such as trees and rocks.

Convective Heat Transfer: Sensible Heat Flux. As used here, sensible heat is the energy transported to the snow pack by convective process in the turbulent air above the snow. It can be accounted for using Newton's Law of cooling,

$$\mathcal{H}_S = \overline{h_c}\left(T_a(z_{ref}) - T_{ss}\right) \tag{14}$$

where $\overline{h_c}$ is the average convective heat transfer coefficient,

$$\overline{h_c} = \rho_a c_{p,a} C_H u\left(z_{ref}\right). \tag{15}$$

In the above equations ρ_a is the density of air, $c_{p,a}$ is the specific heat of air at constant pressure ($1.01 \times 10^3\ J\ kg^{-1}\ K^{-1}$), $u(z_{ref})$ is the wind speed at a reference height z_{ref} above the snow surface, $T_a(z_{ref})$ is the temperature (K) of the air at reference height z_{ref}, C_H is the dimensionless heat transfer coefficient, and T_{ss} is the temeperature (K) of the snow surface (Adams et al., 2005; Armstrong and Brun, 2008). Armstrong provides a method for calculating the dimensionless heat transfer coefficient C_H based on surface layer similarity functions.

Latent Heat. Latent heat is the energy transferred to or removed from the snowpack during phase change. It is contrasted with sensible heat in that it does not produce a measurable change in the temperature of the system. Here, the discussion will be confined to deposition or sublimation, although evaporation and condensation are

possible if temperatures are above freezing. In the event that water vapor deposits directly on the snow surface forming surface hoar, energy is added to the snowpack, whereas if snow sublimates energy is removed from the snowpack. The heat flux due to phase change can be calculated from,

$$\mathcal{H}_L = L_{vap,ice} F_{m.} \tag{16}$$

where F_m is the mass flux due the phase change,

$$F_m = 0.622 \rho_a u_a(z_{ref}) C_Q \frac{(\wp_{vap} - p_{eqm.vap,ice})}{P_{air}}. \tag{17}$$

Here 0.622 is the ratio of the gas constant of dry air to that of water vapor (Sutton, 1953), $\wp_{vap}$ is the partial pressure of the water vapor in the air, P_{air} is the air pressure, and C_Q is dimensionless bulk transfer coefficient for water vapor, and $p_{eqm.vap,ice}$ is the equilibrium vapor pressure with respect to ice (Stull, 1988; Hachikubo and Akitaya, 1998; Adams et al., 2005). Positive values of F_m indicate mass being added to the snowpack and thus a positive energy gain (i.e. positive values of $\mathcal{H}_L$). Again, Armstrong and Brun (2008) suggests calculating C_Q from integrated forms of the surface layer similarity function. Alternately, two empirical estimates of C_Q are $C_Q = 2.9 \times 10^{-3}$ (Hachikubo and Akitaya, 1997) and $C_Q = 2.3 \times 10^{-3}$ (Morstad, 2004). As noted earlier, Hachikubo and Akitaya found an increase in C_Q with increasing surface hoar crystal size.

Conductive Heat Transfer. Conduction is a process whereby energy is transferred from warmer regions to colder regions through direct molecular contact. For a control volume that includes the entire snowpack, conductive heat transfer occurs between the soil and the snow. As shown in Figure 9 the soil generally stays warmer than the

snowpack (due to geothermal heating), thus a positive temperature gradient develops (e.g. a vector pointing from warm to cold points in the positive z direction), creating a positive flux of energy into the snowpack. This conductive process can be described with Fourier's Law (Incropera and Dewitt, 2007),

$$q = -k_{eff}\frac{dT}{dz}. \tag{18}$$

where q is the conductive heat flux from the soil (Wm^{-2}), k_{eff} is the effective thermal conductivity of the soil ($W\ m^{-2}K^{-1}$), and dT/dz is the temperature gradient in the z direction.

If a new control volume is considered that only includes the top most layer of the snowpack, k_{eff} can be defined as the effective thermal conductivity of the ice/air network underlying the surface. That is to say, it accounts for conduction through the ice lattice, conduction through the air mixture in the pore spaces and vapor diffusion across pore spaces due to vapor sublimation and deposition (Morstad, 2004). Since conduction in the air of pore spaces is significantly less than in the ice network, it is reasonable to neglect this effect. In his dissertation work, Shertzer (2011, Equation 3.34) develops an effective thermal conductivity tensor that utilizes a fabric tensor to account for bond direction and a bond radius to grain radius ratio to account for the extent of contact area between grains. A far less comprehensive method for calculating k_{eff} that still accounts for the intergranular bonding and microstructure in general is provided by Adams and Sato (1993).

Optics

Most of the fundamental ideas of science are essentially simple, and may, as a rule, be expressed in a language comprehensible to everyone.—Albert Einstein

A multi-directional optical study tries to glean information about a surface's physical properties by comparing the energy striking a reflective surface to the energy leaving the surface. As such, basic radiometry terms are needed to describe the energy of the light. Additionally, terms are needed to describe the geometry of light either traveling toward—or *incident* (subscript *i*) upon—the reflective surface and away—or *reflected* (subscript *r*) from—the surface. Finally, various terms are needed to describe the relationship between incident and reflected energy.

Despite early efforts by Nicodemus et al. (1977) to standardize the terminology associated with multi-angle studies, the rapid advancement of remote sensing in the past few decades has led to variations in nomenclature from working group to working group (Bruegge et al. 2000). To address this, Bruegge et al. (2000) and Shaepman-Strub et al. (2006) published suggested updates to Nicodemus's work. Except where noted, the radiometry terminology and symbols used in this paper are consistent with Schaepman-Strub et al. (2006). Further, much of the confusion relating to variation in terminology from one publication to the next can be mitigated by the inclusion of units with all relevant terms. Careful attention to units is suggested in the following development.

Solid Angle and Projected Solid Angle

Many of the most basic radiometric calculations make use of solid angle, a simple concept that, nevertheless, can provide no end to one's confusion in the following

development of terminology if not first addressed. Solid angle is perhaps best explained through a simple example; as seen from the Earth on a day when the moon perfectly eclipses the sun, one could say that the moon and sun share an equal solid angle in the sky (Figure 11). That is to say, both the moon and the sun subtend the same angle when measured from the point of view of an observer on the Earth's surface.

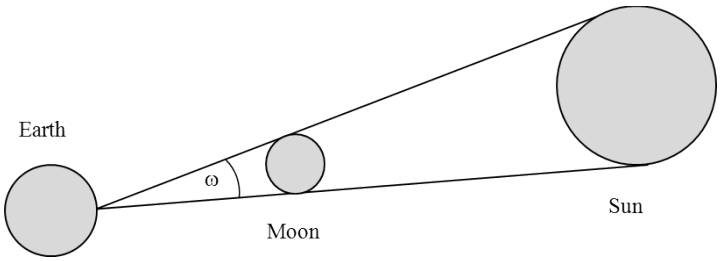


Figure 11. Example illustrating solid angle ω. Note that, as seen from the Earth, the Sun and Moon share the same solid angle during a perfect eclipse.

A solid angle's usefulness lies in its ability to translate an optical instrument's 2-dimensional Field of View (FOV) into an observed surface area. Formally, *solid angle* ω [sr] is defined as

$$d\omega = \sin\theta \, d\theta d\phi \quad [sr], \tag{19}$$

where θ and ϕ are polar angles as depicted in Figure 12 (Petty, 2006). The *zenith angle* θ is measured from the z-axis with $\theta = 0°$ representing nadir and the x, y plane represented by $\theta = 90°$. The *azimuth angle* ϕ lies in the x,y plane and is a measured positively in the counter clockwise direction from the x-axis. Two derivations of Equation (19) provide useful insight into the physical meaning of solid angle. First, integrating from 0 to 2π in the ϕ direction followed by 0 to π in the θ direction one finds that the solid angle of a complete sphere is 4π [sr]:

$$\omega = \int_0^{2\pi} \int_0^{\pi} \sin\theta \; d\theta d\phi = 2\pi \int_0^{\pi} \sin\theta \, d\theta = 4\pi \quad [sr]. \qquad (20)$$

Many pyrometers collect down welling radiation from the atmosphere using full hemisphere or 2π [sr] FOV. Additionally, knowing that the solid angle of a sphere is 4π [sr] provides a useful reference in the same way that knowing 2π [rad] describes a full circle is a useful reference. Another useful derivation of Equation (19) pertains to instruments with conical FOV directed normal to the detector surface (e.g. most optical systems). In that case, solid angle can be calculated:

$$\omega = \int_{\phi=0}^{2\pi} \int_{\theta=0}^{\Theta} \frac{\mathbb{r}^2 \sin\theta \, d\theta \, d\phi}{\mathbb{r}^2} = [2\pi - cos]_0^{\Theta} = 2\pi(1 - \cos\Theta), \qquad (21)$$

where Θ represent the half angle FOV of the instrument.

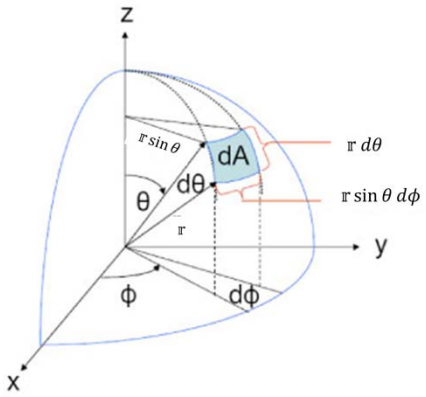


Figure 12. The relationship between solid angle and polar coordinates (Mobley, 2006).

A less stringent definition, applicable only when the solid angles involved are small (as is often true with optical instruments), helps depict the relationship between steradians and area:

$$\omega \cong \frac{A}{\mathbb{r}^2} \quad [sr]. \tag{22}$$

In this form it is easier to see the similarity between "regular" angle and its counterpart solid angle. That is—in the same manner in which $\theta = s/\mathbb{r}$ described the relationship between arc length S, radius $\mathbb{r}$, and regular angle θ—Equation (22) describes the relationship between area A, radius squared $\mathbb{r}^2$, and a solid angle ω.

Finally, as can be seen in Figure 12, the area of consideration in Equation (22) is the curved area projected onto a sphere of radius $\mathbb{r}$. When considering a flat surface, such as charge-coupled device (CCD) detectors, it is useful to calculate the *projected solid angle* Ω $[sr]$. This is accomplished by simply multiplying both Equation (19) and Equation (22) by the $\cos\theta$,

$$\Omega \cong \frac{A\cos\theta}{\mathbb{r}^2} \quad or \quad d\Omega = \sin\theta\cos\theta\, d\theta d\phi \quad [sr]. \tag{23}$$

The projected solid angle equivalents to Equations (20) and (21) can then be developed as follows,

$$\begin{aligned} \Omega &= \int_0^{2\pi}\int_0^{\pi} \sin\theta\ \cos\theta\ d\theta d\phi = 2\pi\int_0^{\pi}\cos\theta\sin\theta\, d\theta \\ &= 2\pi \quad [sr]. \end{aligned} \tag{24}$$

and

$$\begin{aligned} \Omega &= \int_{\phi=0}^{2\pi}\int_{\theta=0}^{\Theta}\cos\theta\sin\theta\, d\theta\, d\phi = [2\pi - cos]_0^{\Theta} \\ &= 2\pi(1-\cos\Theta) \quad [sr]. \end{aligned} \tag{25}$$

In practice, very few occasions arise in which solid angle ω is a useful description (as compared to projected solid angle Ω). The exception to this caveat is theoretical point

sources, which can be described as projecting energy into a give solid angle ω. Almost without exception, any practical application involves sensors with flat surfaces and projected solid angle Ω is the appropriate descriptor. Thus, the use of the term solid angle to mean projected solid angle is ubiquitous in academic publications. A mathematical explanation of this practice is most easily understood in relationship to calculating power incident on a reflecting surface and is detailed in the following section (Figure 16). While this thesis adopts the convention of using solid angle in place of projected solid angle, effort is made to use the symbol ω or Ω in places where context does not provide adequate understanding.

Radiometry

A convenient starting point for exploring radiometric terminology is the concept of radiance L $[W\ m^{-2}\ sr^{-1}\ m^{-1}]$. Due to random, thermally induced motion of molecules, all objects above absolute zero produce electromagnetic radiation. The term radiance is used to describe the electromagnetic radiation reflected or emitted by a surface. The *spectral* (per unit wavelength) distribution of thermal radiation is given by the Plank Function (Shaw, 2012),

$$L_{\lambda}^{BB} = \frac{2c^2h}{\lambda^5}\frac{1}{e^{\frac{hc}{\lambda kT}} - 1} \quad [W\ m^{-2}\ sr^{-1}\ m^{-1}] \qquad (26)$$

where c = the speed of light in a vacuum ($2.998x10^8\ \frac{m}{s}$), h = Planck's constant ($6.626x10^{-34}\ J\ s$), k = Boltzmann's constant ($1.381x10^{-23}\ J\ K^{-1}$), T = absolute temperature in Kelvin (K), and λ = wavelength (m). The superscript BB indicates black body exitance and the subscript λ indicates the radiance given by this equation is on a

spectral basis. An object whose radiance is perfectly predicted by Equation (26)—that is to say, it emits the maximum energy possible at a given wavelength—is said to be a perfect *black body* and is seldom realized in nature (Petty, 2006). An examination of Equation (26) reveals that the power emitted from an object is primarily a function of temperature and the wavelength. Plots of perfect black body emission, as described by Planck's equation, are presented in Figure 13. Of practical note in Figure 13 is the realization that the power detected from an object by an actual sensor will be greatly affected by the *bandwidth* (range of wavelengths) over which the sensor operates. Since real sensors cannot measure instantaneously small bandwidths, the power of a single wavelength can never actually be measured. Radiance integrated across more than one wavelength is reported in $W\ m^{-2} sr^{-1}$.

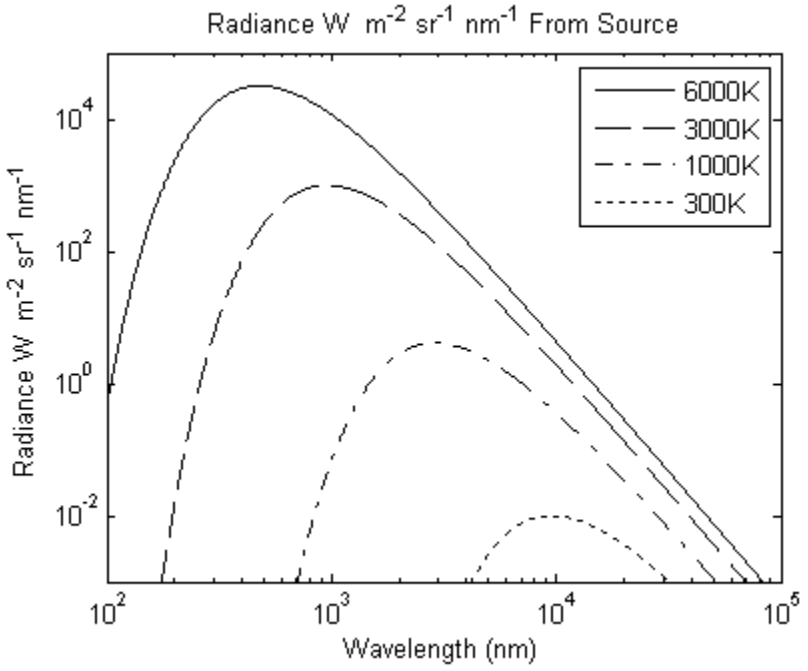


Figure 13. Radiance [$W\ m^{-2}\ sr^{-1}$] as calculated from Plank's equation for perfect black body emission showing the temperature and wavelength dependence. Note the log-log scale. For reference the sun is ~6000K and terrestrial objects ~300K.

Integrating Equation (26) across *all* wavelengths and multiplying by a hemispherical solid angle ($\pi\ steradians$) yields the *Stefan-Boltzman Law:*

$$M = \varepsilon\sigma T^4 \quad [W\ m^{-2}], \tag{27}$$

where M is defined as *exitance* $[W\ m^{-2}]$, T is temperature in Kelvin [K], σ is the Stefan-Boltzman constant ($5.6696x10^{-8}$ $[W\ m^{-2}K^{-4}]$), and ε is emissivity, a measure of an objects departure from perfect black body exitance. Mathematically, *emissivity* ε is the ratio of actual emitted radiance by a given surface to that of a perfect black body at a given wavelength (Petty, 2006). Equation (27) calculates the area under the curve shown in Figure 13—that is, the total exitance $[W\ m^{-2}]$ from a radiating object as a function of temperature. As a last note on Figure 13, it is clear that, for any given temperature there is a wavelength corresponding to maximum exitance. The wavelength of this peak emission (for a temperature given in Kelvin) can be calculated from *Wien's Displacement Law*:

$$\lambda_{max} = \frac{2897}{T} \quad [\mu m]. \tag{28}$$

Bodies that emit easily at a given wavelength also tend to absorb energy easily at that wavelength as well. In fact, in thermal equilibrium absorption equals emissivity. Conservation of energy requires that $a + \rho + T_r = 1$ where a is *absorption*, ρ is *reflectance*, and T_r is *transmittance*. If we lump absorption and transmittance this equation requires the energy entering the snow and the energy reflected from the snow to equal unity. It is important to note that each of these terms is a function of wavelength λ. At wavelengths where snow absorbs well reflection will be low. For example, a snowpack can be considered semi-infinite in the NIR when depth exceeds 3cm due to its

high absorption (Dozier and Painter, 2004). Conversely, at wavelengths where it does not absorb or transmit, reflection will the large. If we take, for example, the average temperature of snow to be 263K ($-10°C$) its peak exitance will occur at $1.1 \times 10^{-5}\mu m$ ($0.011nm$). At this wavelength (and all long wavelengths in general) snow is nearly a perfect black body ($\varepsilon \cong a \cong 1$) and reflectance is quite low. Conversely at short wavelengths (particularly in the visible wavelengths), snow is a nearly perfect reflector ($\rho \cong 1$). In the UV/VIS, snow is a poor absorber and light in this wavelength can travel to depths of 10cm before extinction (Armstrong and Brun, 2008).

As indicated by its units, radiance provides a measure of the *power* Φ $[W]$ projected into a given solid angle ω $[sr]$ per unit surface area A [m^2]. Knowing the radiance of a source, allows the calculation of power incident on a reflective surface. Consider an element of reflecting surface dA_i, as depicted in Figure 14, with a surface normal z that is illuminated by radiant energy (Nicodemus et al., 1977). The radiance L_i falling into a differential solid angle $d\omega_i$ [sr] can be thought of as a ray originating from an infinitesimal point source and striking a differential surface element dA_i [m^2] located at (x_i, y_i). This *incident* ray can be described in spherical coordinates based on the angle it forms with the z-axis (*incident zenith angle*, θ_i) and the angle it forms with the x-axis (*incident azimuth angle*, ϕ_i). Radiance is, therefore, a function of position, $L_i = L_i(\theta_i, \phi_i)$.

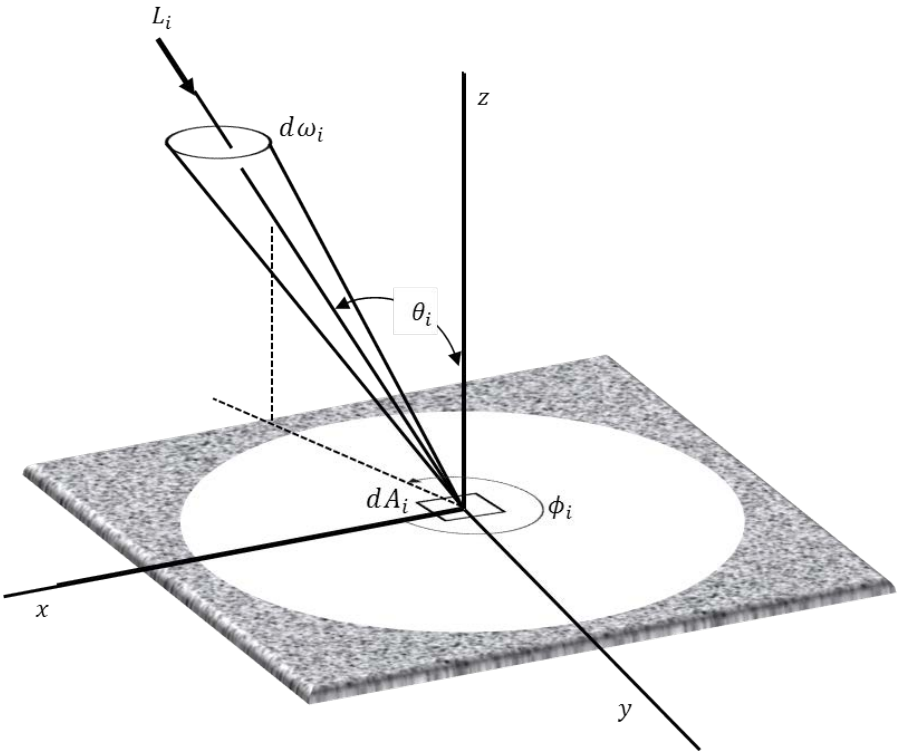


Figure 14. Incident light geometry. Power on the differential surface area dA_i can be calculated by integrating the radiance $L_i \cos\theta_i$ of the source collected by a differential solid angle $d\omega_i$ (solid angle of source as seen from reflective surface) with respect to solid angle and area as shown in Equation (29).

Power incident on dA_i can calculate by,

$$\begin{aligned} d\Phi_i &= L_i \cdot \cos\theta_i \cdot d\omega_i \, dA_i \\ &= L_i \cdot \mathrm{d}\Omega_i \, dA_i \\ &= dE_i \cdot dA_i \quad [W], \end{aligned} \tag{29}$$

where dE_i $[= L_i \cdot \cos\theta_i \cdot d\omega_i = L_i \cdot \mathrm{d}\Omega_i]$ is defined as *irradiance* $[W\ m^{-2}]$, e.g. the incident light collected in the solid angle element as depicted in Figure 14 (Nicodemus,1977). Irradiance $[W\ m^{-2}]$ is typically associated with light incident on a surface whereas radiance $[W\ m^{-2}\ sr^{-1}]$ is typically associated with light leaving a source.

Integrating Equation (29) yields:

$$\Phi_{\mathrm{i}} = L_i \cdot A_s \cdot \Omega_{\mathrm{rs,s}} = L_i \cdot A_{rs} \cdot \Omega_{\mathrm{s,rs}} \quad [W] \tag{30}$$

where $\mathrm{A} \cdot \Omega$ $[m^{-2}\ sr^{-1}]$ is known as the system's *throughput*. Additionally, $\Omega_{s,rs}$ indicates the solid angle of the source as seen from the reflective surface and $\Omega_{rs,s}$ indicates the solid angle of the reflective surface as seen from the source. Figure 15 illustrates the physical meaning of two throughput terms in Equation (30). While both methods are equivalent, they represent a conceptual shift between considering the problem from the perspective of the radiant surface verses the perspective of the detector. The right hand figure depicts the versatility of throughput; if we now blur the line between a source and a reflective surface (after all, from the point of view of the detector there is no distinction) and the line between reflective surface and detector (both are surfaces on which light is incident), we see that A_1 or A_2 are free to act as detectors, reflective surfaces, or sources.

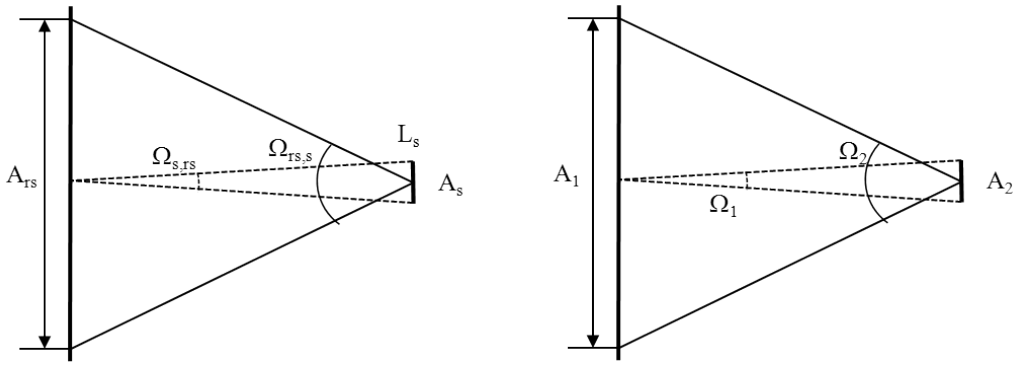


Figure 15. Left: Equivalent throughputs using notation in Equation (30). Right: Using general subscripts it becomes clear that area A_1 or A_2 could act as sources, reflective surfaces, or detectors. In any case throughput would be could be calculated by either $A_1 \cdot \Omega_1$ or the equivalent$A_2 \cdot \Omega_2$.

Conceptually, this distinction is important in understanding many of the figures both in this thesis and in other academic works. However, as a practical consideration, when calculating power on a detector, where the optical system has a fixed FOV, the most covenant throughput option is $A_{det} \cdot \Omega_{\mathrm{det}}$ where Ω_{det} represents the solid angle of the instrument's FOV and A_{det} is the surface area of the detector. It is also helpful to remember that, when calculating throughput, the solid angle Ω_1 always opens *away* from the area A_1.

With a method for calculating power now defined, a more complete understanding of the difference between solid angle and projected solid angle can be elucidated. As illustrated in Figure 16, power at a detector viewing a point source with uniform radiance from a fixed radius, will not be effected by any change view angle θ. However, for a flat, extended, diffuse source area dA_s—as the detector moves through angle θ it will see a greater portion of surface and power will thus appear to increase (violating the law of conservation of energy). To correct for this, it is necessary to use projected solid angle $d\phi = L_s \cdot \cos\theta \cdot d\omega \cdot dA_S = L_s \cdot d\Omega_{s,det} \cdot dA_S$. In considering the interchangeable definition of throughput provided in Equation (30), it can be seen that, in all cases in which non-spherical source or detector surfaces are used, projected solid angle is needed.

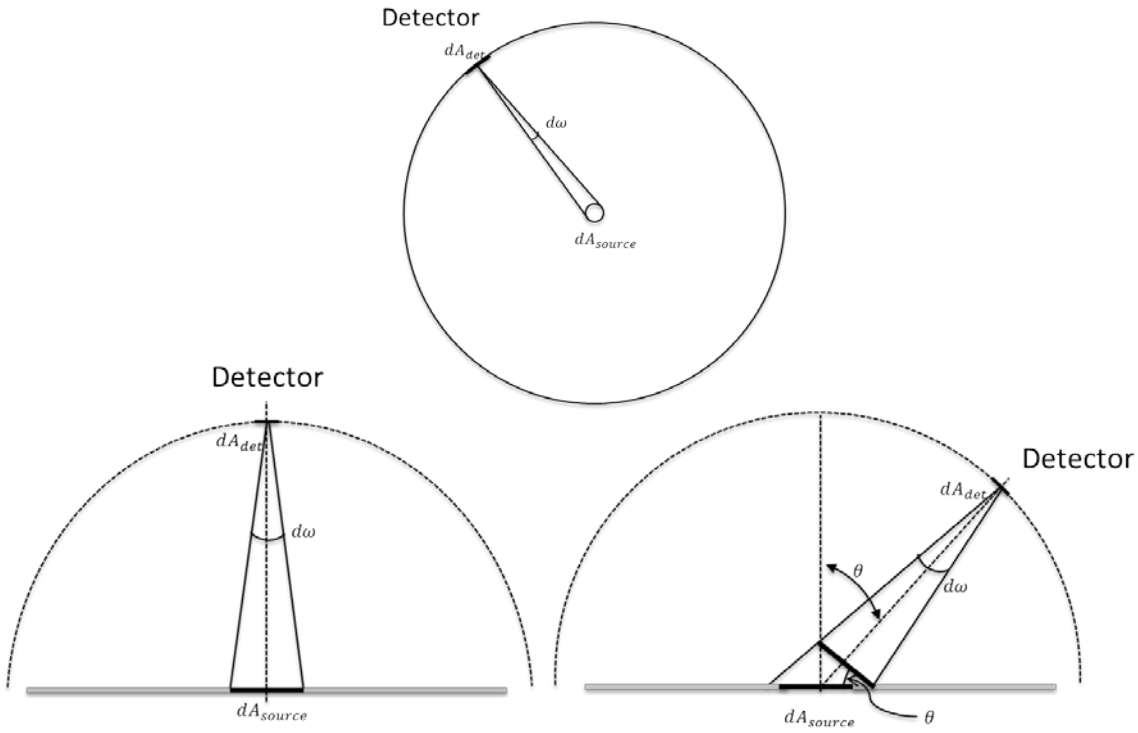


Figure 16. Top: For a point source, solid angle $d\omega$ can be used to calculate power at the detector $d\phi = L_s \cdot dA_S \cdot d\omega$ for all view angles. Bottom: For a flat extended source, as θ changes, the view area changes. Multiplying by cosine of theta corrects for this phenomenon, $d\phi = L_s \cdot \cos\theta \cdot d\omega \cdot dA_S = L_s \cdot d\Omega_{s,det} \cdot dA_S$.

Bidirectional-Reflectance Distribution Function

Due to subsurface scattering, the point where the reflected ray emerges from surface A does not have to be equivalent to the point of entry. The reflected ray leaves surface A at point (x_r, y_r) and is described by its reflectance zenith angle (θ_r) and its reflectance azimuth angle (ϕ_r), that is, $L_r = L_r(\theta_r, \phi_r)$. In the course of this thesis illumination angle, sun angle, or source angle will be use synonymously with incident angle to indicate both azimuth and zenith lighting geometry. Similarly, observer angle, viewer angle, or sensor angle will be used synonymously with reflectance angle to indicate both azimuth and zenith viewing geometry.

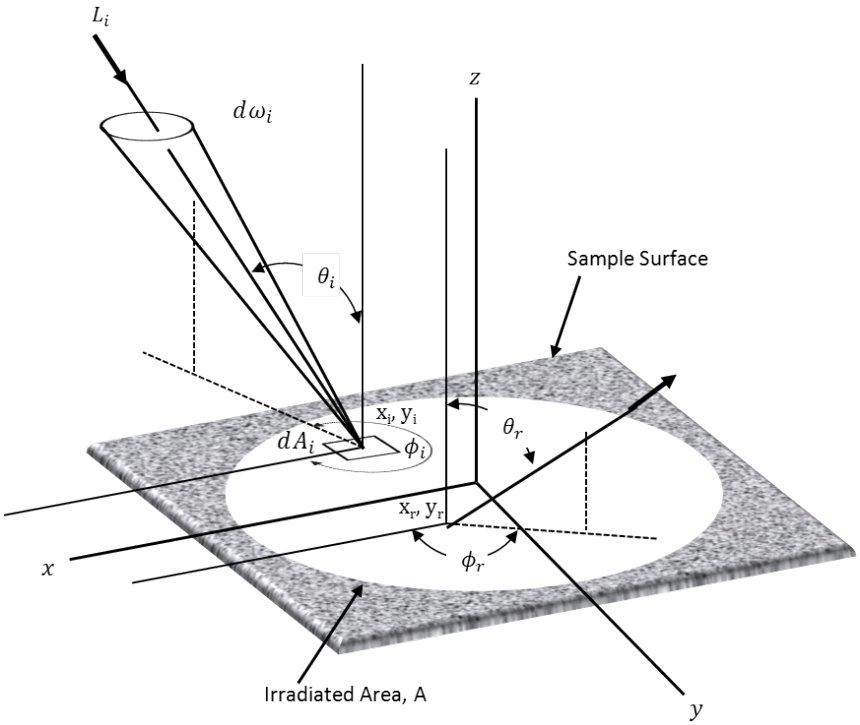


Figure 17. Illustration of geometry and terminology associated with multi-angle optical studies (reproduced from Nicodemus, 1977).

The reflected radiance dL_r (W m^{-2} sr^{-1}) is proportional to the *incident flux* $d\Phi_i$ (W) falling on area dA_i (m^2) through the proportionality constant S,

$$dL_r = S \cdot d\Phi_i \quad [W\ m^{-2}\ sr^{-1}] \tag{31}$$

where S is known as *bidirectional scattering-surface reflectance-distribution function* (BSSRDF),

$$S(\theta_i, \phi_i, x_i, y_i; \theta_r, \phi_r, x_r, y_r) \quad [\mathrm{m}^{-2}\ \mathrm{sr}^{-1}]. \tag{32}$$

If we assume the area A is uniformly irradiated and that the reflecting surface has isotropic scattering properties, we can exclude the x and y dependence in Equation (32). Substituting $d\phi_i = dE_i \cdot dA_i$ (Equation (29)) into Equation (31) and integrating yields,

$$dL_r = dE_i \int_{A_i} S \cdot dA_i$$
$$= dE_i \cdot f_r(\theta_i, \phi_i, \theta_r, \phi_r) \quad [W\ m^{-2}\ sr^{-1}] \tag{33}$$

where

$$f_r(\theta_i, \phi_i, \theta_r, \phi_r) = \int_{A_i} S \cdot dA_i \quad [sr^{-1}]. \tag{34}$$

The term f_r is known as a *bidirectional reflectance distribution function* (BRDF). It characterizes (geometrically) the reflecting properties of a uniformly irradiated surface with uniform and isotropic properties (Nicodemus et al., 1977) and is the ratio of reflected radiance L_r $[W\ m^{-2}\ sr^{-1}]$ to the incident irradiance E_i $[W\ m^{-2}]$,

$$f_r(\theta_i, \phi_i, \theta_r, \phi_r) = \frac{L_r(\theta_i, \phi_i, \theta_r, \phi_r)}{E_i(\theta_i, \phi_i)} \quad [sr^{-1}]. \tag{35}$$

It is important to note that, as defined, the BRDF does not provide any explanation of the mechanisms involved in reflectance. It simply provides a ratio of incoming and outgoing light (Nicodemus et al., 1977).

Further, as defined, BRDF cannot be directly measured in practice since it contains instantaneous solid angles. In fact, the term *directional* is used to indicate that light is projected into or collected from an infinitely small differential solid angle. More specifically, *bidirectional* indicates that both incident and reflected light area measured by an instantaneous solid angle. Real measurements of radiance and irradiance contain average values across some finite solid angle (i.e. a finite FOV), across some average bandwidth, and over some finite area (Nicodemus et al., 1977). Nevertheless, BRDF is a useful concept underpinning many of the related terms defined in the following section.

Two other terms often appear in radiometry studies and warrant address: albedo and anisotropy factor. *Albedo* $\alpha(\theta_i)$ is defined as the integration of all BRDF values across the entire hemisphere and is thus the ratio of all incident light to all exiting light across the entire hemisphere,

$$\alpha(\theta_i) = \int_0^{2\pi} \int_0^{\frac{\pi}{2}} f_r(\theta_i, \phi_i, \theta_r, \phi_r) \cos\theta_r \sin\theta_r d\theta_r d\phi_r. \qquad (36)$$

The *anisotropy* $\mathcal{A}$ factor is similar to the BRDF in that it provides a sense of the amount of light exiting the snow compared to that leaving the snow. The difference is that the anisotropy factor is the ratio of a BRDF (at a particular geometry) to the albedo of the snow as a whole,

$$\mathbb{A} = \frac{f_r(\theta_i, \phi_i, \theta_r, \phi_r)}{\alpha(\theta_i)}. \qquad (37)$$

Additional Reflectance Terminology

A wide variety of nomenclature has been developed by the remote sensing community to describe variations in the geometry and solid angle of incident and reflected light. As defined above, the BRDF is the ratio of radiance $[W\ m^2\ sr^{-1}]$ incident upon a surface to the exitance $[W\ m^2]$ reflected into an infinitely small solid angle, specified by the directional term. Since truly directional light cannot be measured with a real sensor, a more accurate term for field studies of this nature would be *bi-conical reflectance distribution function* BCRDF (Bourgeois, 2006). However, the term directional, in practice, is loosely used to mean light captured by a small, finite, conical FOV. At the other extreme, if radiance is measured with a full $2\pi\ [sr]\ solid\ angle$ (e.g. π [sr] projected solid angle) FOV, it is termed *hemispherical*.

In describing incident and reflected light, standard nomenclature dictates that the angular characteristic of the illumination is mentioned first, followed by the angular characteristic of the reflected radiance. Thus, *hemispherical-directional* implies hemispherically integrated incident light and reflected light measured with an infinitesimal FOV at a given reflectance geometry (θ_r, ϕ_r) while *directional-hemispherical* implies incident light from an infinitely small point source and reflected light measured hemispherically.

In practice, field studies using the sun as the illumination source have both a direct and diffuse (due to Rayleigh scattering in the atmosphere) component. These studies often report a *hemispherical-directional reflectance factor* (HDRF) to indicate the result includes incident light scattered by the atmosphere. HDRF values, which depend on daily atmospheric conditions, are of limited use in comparison to BRDF.

As a convenient alternative to the BRDF, it is also common practice to report the unitless ratio of reflected radiance $[W\ m^{-2}\ sr^{-1}]$ from the target surface to the reflected radiance from a calibration standard with known properties. As with any reference standard, the use of a reflectance panel allows easy comparison of results between research groups. In cases where a reference panel is used, the reported value is appended with the term *factor*. Thus, it is possible to speak of a dimensionless *bidirectional-reflectance factor* R (BRF),

$$R = \frac{d\Phi_{r,snow}}{d\Phi_{r,id}}. \tag{38}$$

where $d\Phi_{r,snow}$ is the power [W] reflected from the snow surface and $d\Phi_{r,id}$ is the power [W] reflected from the ideal reference panel. Both terms can be calculated from

Equation (29) by noting that light reflected from the surface is incident on the detector. Thus, in Equation (29), A_i is the area of the detector, $d\omega_i$ is the solid angle of the sample surface as seen from the detector, and L_i is the radiance $[W\ m^{-2}sr^{-2}]$ leaving the reflectance surface. It is also possible to speak of a hemispherical-directional factor or a directional-hemispherical factor, etc.

The SSERF lab utilizes a metal-halide solar simulation lamp that produces a spectral distribution comparable to the sun (in the range of 280 – 2480 nm). Minimal Rayleigh scattering occurs in the lab setting and the light can be considered direct allowing measurements independent of atmospheric conditions. Further, a Labsphere Spectralon reference panel was utilized to normalize collected data by a universally used standard. Thus, this study reports its results in terms of R, the bidirectional-reflectance factor (BRF).

Because the BRF utilizes Spectralon to normalize the snow sample, it is constructive to examine the theoretical behavior of Spectralon. The surface of an object can demonstrate a perfectly *specular reflection* (from the Latin word for "mirror"), meaning that the light is reflected only at a definite angle. On the other end of the continuum, an object can demonstrate perfectly *Lambertian reflection*, in which *radiance* $[W\ m^{-2}s^{-1}]$ is constant from any view angle. That is to say, to the human eye, a Lambertian surface appears to have the same brightness from all observer angles. For this reason, Lambertian surfaces are sometimes called diffuse surfaces. Note that the ratio of incident irradiance $[W\ m^{-2}]$ to outgoing radiance $[W\ m^{-2}sr^{-1}]$—that is the BRDF—for a Lambertian surface is$1/\pi[sr]$ regardless of viewing geometry.

Alternately, in apparent contradiction to the above definition, Lambertian surfaces are sometimes called *cosine reflectors*. In this case, however, the cosine term is referring to the fact that *intensity* [$W\ sr^{-1}$] is proportional to the cosine of the angle between the surface normal and the observer; this relationship between *intensity* and observer angle θ is known as *Lamberts Cosine Law*. The physical reason that intensity is proportional to θ involves the concept of throughput as discussed previously. While power detected from a reflective surface falls off by the cosine of the observer angle θ, the area observed by the detector increases by the cosine of the observer angle. Thus, the two effects cancel each other out.

While idealized Lambertial scatter is not realized in nature, the Spectralon sample used in this study is close with reflectance values of 99% in the visible wavelengths for observer zenith angles of less than 8° according to Labsphere (Figure 18). Labsphere suggests that, for polarized light, reflectance values fall to considerable less than 99% at observer zenith angles greater than $\sim 60°$. While not explicitly stated, it is likely this effect will be evident with non-polarized light as well. This breakdown in the Lambertian properties of Spectralon at observer grazing angles is easily corrected for by simply sampling the Spectralon from the same incident/viewing geometries as the snow, thereby assuring a consistent normalized BRF value. A BRF greater than one indicates the snow has a greater radiance than Spectralon at a particular wavelength and incident/viewing geometry; the converse is true as well.

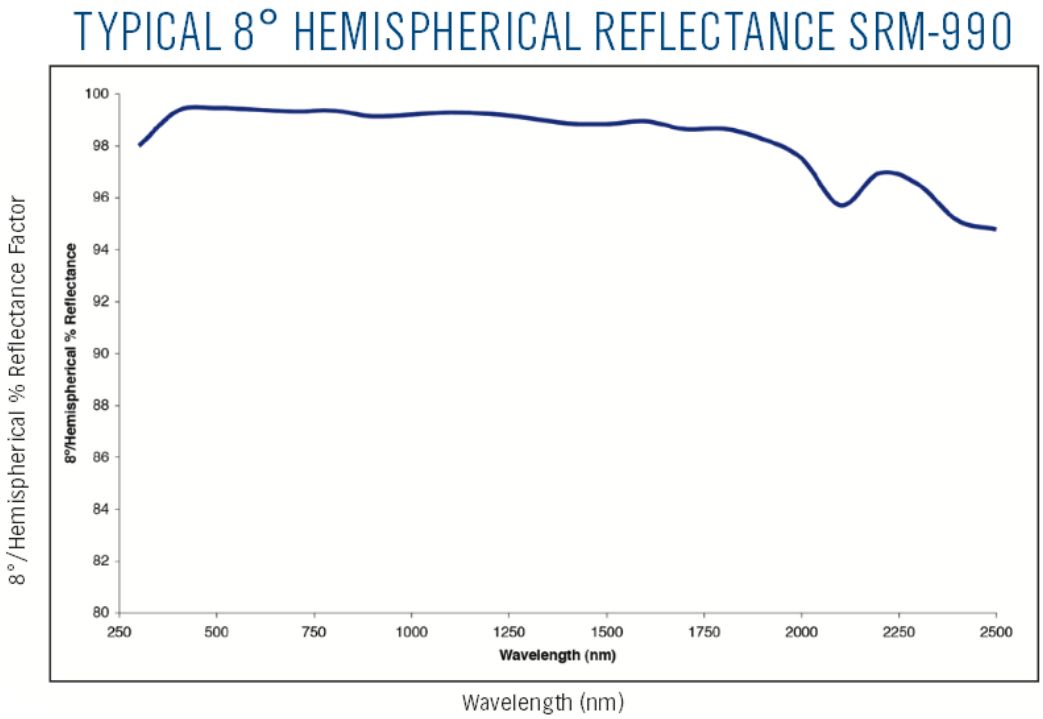


Figure 18. Hemispherical reflectance of Spectralon as a function of wavelength showing nearly Lambertian reflectance in the UV/VIS/NIR (figure from Labsphere Inc. website).

Literature Review of Snow Optics Studies

Radiative Transfer Models

Energy in the form of radiance (light[6]) entering the snowpack can be either absorbed, transmitted, or scattered. The light that is absorbed can, in turn, be reemitted (though typically not at the same wavelength). Thus, the change in radiance along a path through the snowpack can be characterized by the summation of emission, absorption, and scatter of photons. Radiative transfer models of the light through the snowpack must mathematically account for these terms (Petty, 2006). Some of the earliest work in optical modeling of snow was done by Dunkle and Beavans (1956). This early model

[6] In the vernacular usage light is often associated with radiance in the visible bandwidth; however, in physics light and radiance can be used interchangeable and is not restricted to a particular bandwidth.

treated the snow pack as layers of uniform sheets of ice of different thickness rather than distinct grains. Further, the model only considered normal incident light, Fresnel reflectivity, and used the simplest possible analytical solution method for solving the radiative transfer equation: the *two-stream method*. The two-stream method assumes that upwelling radiance from an ice layer is hemispherically uniform. Likewise, down welling radiance from the ice layer is also hemispherically uniform. Thus, it is not suitable for remote sensing purposes where bidirectional data is needed (Petty, 2006).

One of the first treatments of the snowpack using single-scattering theory, where ice grains were treated as spherical particles, was completed by Barkstrom (1972). This model, like all single scatter models, required three key parameters to describe the scatter and absorption of radiation by a single ice crytal: *extinction efficiency* (essentially describing the likelihood of a photon being absorbed by the ice crystal), *single-scatter albedo* (the ratio of scattering efficiency to extinction efficiency, providing a sense of the relative importance of scattering vs. extinction), and the *phase function* (a mathematical description of the probability of a scattered photon exiting in a given direction). The assumption of spherical ice grains allowed the simplification of the phase function to a cosine relationship between the incident and scattered beam. The study further assumed isotropic scattering—that is, the simplest possible treatment of the phase function as a constant. Barkstrom and Querfeld (1975), considered anisotropic scatter, but were unable to make their model work without using unrealistic values for the phase function.

A more accurate model for calculating albedo was formulated by Bohren and Barkstrom (1974) using geometric optics. They determined that scattered light was

mostly due to refraction rather than reflection. However, this model was limited to use in the UV/VIS length. Berger (1979) adapted this model for use with longer wavelength by assuming 100% absorption by ice grains, arguably a reasonable approximation for wavelengths longer than $1 \times 10^5\, nm$. O'Brien and Munis (1975) performed BRDF studies on snow, providing a valuable reference for future modeling studies. Wiscombe and Warren (1980) presented a model using direct Mie scatter calculations and a delta-Eddington approximation to handle anisotropic phase functions across a wide range of wavelengths and incorporating various solar incident angles.

Warren (1982) suggests that *specific surface area* (SSA)—the crystal surface area to volume ratio (m^{-1}).[7]—can provide a reasonably accurate method for approximating the optical diameter of the equivalent spheres in Mie scattering studies. This optically equivalent grain is primarily a mathematical construct and may share little resemblance to the crystal type observed in the field. Nevertheless, it has been shown that the use of SSA can adequately describe the albedo (e.g. the hemispherically integrated BRDF) of snow in bandwidths greater than 1300 nm (Grenfell and Warren, 1999; Domine et al., 2006). However, they noted that it fails to capture the bidirectional nature of snow at a given geometry. Warren et al. (1998) emphasized this issue, pointing out the importance of accurately modeling the phase function in order to calculate the snow BRDF.

The ease with which SSA can be used in Mei theory calculations means it is incorporated into many of the models discussed subsequently, despite being a difficult parameter to measure. Picard et al. (2009) argued that the techniques required to measure

[7] Note SSA has two definitions. In addition to the one mentioned in the text, studies that use methane absorption to determine SSA often report the surface area to mass ratio (with units of m^2/kg) as SSA. To convert this value simply multiply by the density of ice (~$0.9167\ g/m^3$).

SSA—methane absorption, photography using coaxial reflected illumination and stereology principles, or microtomography—are time-consuming, with the consequence that it is rarely measured in field campaigns. He goes on to say there are few examples of temporal evolution of SSA in the natural setting though recent studies have been conducted relating SSA evolution to snow metamorphism (Legagneux et al., 2004; Legagneux and Domine, 2005; Flanner and Zender, 2006; Taillander et al., 2007).

Legagneux et al (2002) used a methane absorption method to determine the SSA for a variety of crystal habits. It was found that SSA decreases with the age of the snow. Newly fallen dendritic forms had the highest SSA (88.2 ± 28)[8]. New plates, needles, and columns had an average SSA of (57.7 ± 22). Decomposing snow that still showed recognizable particles generally had smaller SSA values with dendrites averaging (49.4 ± 11) and plates, needles, and columns averaging(34.2 ± 11). Finally, aged snow typically demonstrated the lowest SSA values with mostly rounded grains averaging(22.8 ± 7). Interestingly, the smallest SSA values were for depth hoar and faceted crystals ((14.9 ± 4) and (13.8 ± 5) respectively. Surface hoar was found to have an average SSA of (36.1 ± 12), but it was noted that additional samples were needed to confirm this number. Note that the large plus/minus values indicate a wide range of SSA is possible for a given crystal type. Nevertheless, Domine et al. (2006), found similar trends. He reported SSA values of 62.6 for fresh dendrites, 41.0 for needles and dendrites, and 11.4 for rounded grains.

[8] Note that Legagneux reported SSA values in units of cm^2/g. The values shown here have been converted by multiplying by the density of ice.

An optically equivalent spherical grain radius can be calculated from the above SSA values by noting that the surface area of a sphere ($4\pi r^2$) divided by its volume ($(4/3)\pi r^3$) reduces to $3/r$. Thus, $r_{optical} = 3/SSA$. The optically equivalent radius for the above SSA values ranges from $r_{optical} = 0.034\ mm$ for fresh dendrites to $r_{optical} = 0.22\ mm$ for faceted crystals.

Advanced models of radiative transfer have also been developed. Painter and Dozier (2004) used DISORT transfer code as well as the added-doubling method, noting that it was critical to precisely define single-scatter albedo and phase function in order to accurately model BRDF. DISORT (Chandrasekhar, 1960; Stamnes et al., 1988) uses a discrete ordinates system, "as a generalization of the two-stream method to an arbitrarily large number of discrete 'streams' of radiation in each hemisphere (upward and downward hemisphere from the snow layer) each one representing a different direction" (Petty 2006). The added-doubling method starts with an assumed thin layer of snow allowing reflectance and transmission to be calculated using single scattering phase function. Subsequent layers are added by successively combining layers until the desired optical thickness is achieved (van de Hulst, 1963; Petty. 2008). Kokhanovsky and Zege (2004) attempted to simulate optical grains using fractal theory, concluding it was more accurate for predicting BRDF behavior. As computational power of computers increases the possibility of Monte-Carlo approaches, which numerically trace individual rays, is becoming possible. For example, Picard et al. (2008) used photon ray tracing in the NIR to look at the relationship between BRDF and SSA.

Dumont et al. (2010) concludes that the studies presented above, "lead to the conclusion that spectral albedo can be accurately modeled but that theoretical difficulties linked with the non sphericity of snow grains still remain and limit accurate modeling of snow BRDF." Field studies looking at the SSA of various crystal morphologies as well as the development of BRDF/BRF values for individual crystals habits are needed.

Field Studies Concerning the BRDF/BRF of Snow

While practical for modeling snow albedo (as demonstrated in the above models), the use of a spherically equivalent grain disregards the complex crystal features present in nature (Dumont et al. 2010). A more complete understanding of the relationship between grain size as well as shape requires the development of bidirectional reflectance data (i.e. BRDF or BRF values) for various snow surface morphologies. Bidirectional studies are characterized by their efforts to record directionally dependent reflectance characteristics and to relate them to physical characteristics of the observed surface. Accurate bidirectional studies provide empirical data against which optical models can be compared. The following details the state of the art in bidirectional reflectance field studies.

Leroux et al. (1998) performed ground measurements in the long and NIR wavelengths of HDRF values for clustered rounded grains, faceted and fine particles, and faceted crystal and surface hoar. The values were then corrected to account for atmospheric scattering, thereby converting them to BRDF. The study then compared these results to a radiative transfer model they created, finding that hexagonal particles provided the best fit to real data. Though not specified in the discussion of their

measured results, observation of their reflectance data suggests that, at 1650 nm, the BRDF of rounded grains varies significantly less than the BRDF of surface hoar.

Similarly, Aoki et al. (2000), measured HDRF data in the 350 to 2500 nm range for new snow, granular snow, and faceted crystals but does not indicate whether the faceted crystals were surface hoar. The study concludes that BRDF showed significant anisotropy in the NIR but was generally insensitive to grain shape in the visible range.

Painter and Dozier (2004) measured HDRF values for fine grained decomposed dendritic forms and medium sized clustered grains after a melt-freeze cycle. The noticed the fine grain faceted snow "exhibited a local backscattering peak at the view zenith near the solar zenith angle, whereas (the HDRF) for medium grain, clustered snow did not have a local backscattering peak." Further, an increase in grain radius from 8×10^4 to $280 \times 10^3 nm$ was accompanied by a decrease in the HDRF for all wavelengths.

Li and Zhou (2004), performed HDRF measurements (and later translated the results into BRF values) in the 350-1050 nm range on rounded, sintered, composite coarse grains overlain by broken fine particles and solid, faceted, coarse particles overlain by fine grains. They looked at large solar zenith angles ($65°$ and $85°$). The results showed these snow types had a strong forward-scattering peak under large solar incidence angles.

Similarly, Bourgeois et al. (2006) performed HDRF (350-1050 nm) studies in Greenland on wind-broken small grained snow and a surface covered with rime causing a higher surface roughness. They found a wide range of HDRF values (from 0.6 to 13) depending on the solar zenith angle. It varied from nearly isotropic at nadir illumination

angles to highly forward-scattering at solar zenith angle of 85°. Additionally, surfaces covered with rime exhibited less forward-scattering than smooth surfaces.

In a study that uses similar methodology to that of this thesis, directional dependence on grain type for 4 different grains (dendritic fragments, clustered rounded grains, melt freeze crusted grains, new wet snow) over a wide range of lighting and viewing geometries was conducted by Dumont, et al. (2010). They concluded that both grain size and shape have an effect on the reflectance distribution (primarily in the NIR and longer wavelengths) but their effects are difficult to predict. Further, they were able to distinguish a recognizable reflectance pattern for elongated or faceted shapes. Specifically, they noted darking at viewer grazing angles in situations of near nadir illumination as well as strong forward-scatter peak in the NIR wavelengths for all grain types. However, Dumont's study did not specifically address surface hoar.

Several distinct themes can be seen in these studies: 1) snow in the UV/VIS length appears far more Lambertian than snow in longer wavelengths; 2) albedo decreases with increasing grain size; 3) snow tends to demonstrate a strong forward-scatter peak at large incident light angles. 4) Grain habit plays a role but is not well understood. Several prominent works by S. G. Warren provide theoretical rational for these observations (Warren and Wiscombe, 1980; Warren, 1982 and 1984).

The Lambertian appearance of snow in the UV/VIS can be attributed to its low absorption in that bandwidth. UV/VIS light entering the snow is transmitted thus encountering many scattering surfaces. With each scatter the probability of ejection from the snowpack increases. Thus, one sees high reflective values in the UV/VIS. Further,

the light ejected after multiple scatters is equally likely to be scattered in any given direction, thus contributing to the Lambertian effect.

The decrease in albedo with increasing grain size is due to the fact that a photon in a large grain must transverse more ice before escaping thus increasing the probability of absorption. This effect is more pronounced in the NIR and longer wavelengths were ice is highly absorptive, whereas in the UV/VIS wavelengths the low attenuation of means a lower statistical probability of being absorbed before the photon is ejected from the snowpack. Finally, the strong forward-scatter peak is likely due to the higher probability of single scatter for photons arriving from grazing angles as compared to those arriving from nadir incident angles, which are more likely to enter the snowpack and experience multiple scattering events. Dumont et al. (2010) uses this argument to suggest the darkening observed with nadir incident light and large viewing zenith angles was due to the lower probability of photons emerging from deep within the snowpack at large reflectance zenith angle angles.

While many of the above studies conclude that grain shapes as well as optically equivalent grain size play a role in the reflectance properties of snow, few studies directly address crystal habit specifically. Conspicuously absent from the studies presented above is a comprehensive bidirectional study of surface hoar. Further, most of the above studies were performed outside where diffuse lighting had to be accounted for before HDRF values could be reported independent of atmospheric conditions. The focus of the following thesis is a multi-angle investigation of the BRF values in the visible bandwidth of two distinctly different crystal morphologies: rounded grains and surface hoar. The

study is performed in a lab setting to minimize atmospheric scattering effects. Additionally, addressing the lacuna in SSA research alluded to by Picard et al. (2009), temporal evolution of SSA of surface hoar is documented using computed tomography and the result presented in Chapter 4.

CHAPTER 3

METHODOLOGY

You boil it in sawdust; you salt it in glue;
You condense it with locusts and tape;
Still keeping one principal object in view,
To preserve its symmetrical shape.—Lewis Carroll

This study hypothesizes that microstructural changes due to near surface metamorphism, traced by crystal type, will alter snow's solar albedo. Specifically, it is postulated that the bidirectional-reflectance factor of the snow's surface before and after surface hoar growth will be predictably and quantifiably different, thereby allowing the remote detection of surface hoar presence. To test this hypothesis it was necessary to examine the reflectance of light in the solar wavelengths from two distinct grain types—rounded grains (i.e. before growth) and surface hoar (i.e. after growth)—from a variety of lighting and viewing geometries. As explained in Chapter 2, surface hoar can take on a variety of crystal habits depending on temperature and supersaturation. These forms can be generalized as c-axis dominated growth (broadly referred to as needle like growth) or a-axis dominated growth (broadly referred to as plate like or feathery growth). Feathery surface hoar is ubiquitous in the mountains of central Montana where conditions for plate like growth—clear nights with temperatures between $-10°C$ to $-22°C$—are common. For this reason, it was selected as the principle surface hoar crystal for this study.

While surface hoar is common in Montana, the difficultly of forecasting the meteorological conditions necessary for growth makes it difficult to study in a natural setting. Further, optical studies performed outside are subject to hemispherically diffuse

lighting due to Rayleigh scattering in the atmosphere. To assure the necessary control of the meteorological conditions affecting both the habit of surface hoar growth as well as the lighting conditions, the experiments in this study were conducted in a walk-in environmental chamber at Montana State University's Snow Science Engineering Research Facility (SSERF). As detailed in the section entitled *Development of Varying Snow Morphologies in the Lab Setting* (page 65), this chamber allowed control of meteorological conditions such that surface hoar could be grown on a 30x30cm snow surface. This study capitalized on a surface hoar growth methodology developed previously by Andrew Slaughter and others, refining it to the point where specific surface hoar crystal types could be predictably and reliable grown (see *Crystal Types Grown for Optical Testing* on page 70). In addition, a built in solar simulator eliminated excess atmospheric scatter allowing the reporting of directional (as opposed to hemispherical-directional) data.

Since the study presented here hypothesizes that crystal shape plays an important role in how snow reflects, a method for documenting crystal type was necessary. Two methods for documenting crystal type were utilized: microscopic still photographs and computed tomography (CT) images. The microscopic images provided a picture of disaggregate grains from a variety of locations across the 30x30 cm test surface, whereas the CT images provided a detailed look at the microstructure of a few specific grains before and after surface hoar growth. In addition, the software accompanying the CT scanner provided a wealth of additional microstructural data including specific surface

area. The details of these methods are discussed in the section entitled *Documenting Crystal Habit* (page 68).

With a method in place for growing and documenting specific grain types, attention was turned to collecting optical data. As discussed in the section entitled *Optics*, a spectrometer was purchased covering the solar spectrum and a custom hemispherical gantry was designed and built to allow the sampling of spectral data from a variety of observer azimuth and zenith angles. A solar simulation lamp, built into the ceiling of the environmental chamber, provided lighting. Since the light source could not be moved, the snow surface was tilted to simulate various incident geometries. An analysis of the properties of the light source is provided in the section entitled *Light Source Characterization* (page 74).

As discussed in Chapter 2, a complete multi-angle study of the bidirectional reflectance of snow requires knowledge of the snows BRF from an infinite number of viewing and lighting geometries. While not achievable in reality, careful selection of a finite number of viewer and illumination geometries allows interpolation to other points in the hemisphere. The selection of viewer and illumination geometries is dependent on the limitations of the spectrometer and the goniometer used in the experiments. That is, it is necessary that the spectrometer's FOV remain on the snow surface for all given viewing angle. In addition, the gantry's arm casts shadows on the snow surface or physically touched the snow at certain geometries. Careful reviews of these issues are provided in the sections entitled *Field of View Considerations* (page 78) and *Geometric Considerations* (page 80).

Chapter 2 provided a plethora of terms often used in reporting optical data. This study present bidirectional-reflectance factors (BRF). As the term implies, the data is bidirectional (incident and reflected light are collected from a small conical FOV) and not effected by diffuse lighting. Further, as the term factor implies, the data is normalized to a Lambertian reference panel, the commercially available Spectralon. BRF data is therefore referenced to a scientific standard commonly available and is widely applicable (unlike HDRF) due to its independence from atmospheric conditions. The details of producing a BRF from recorded data are presented in the section entitled *Spectralon Reference Panel and BRF* (page 82).

As detailed in Table 1, nine experiments (labeled Test 1a, b, c; 2a, b, c; 3a, b, c) were performed in total. Experiment 1 and 2 were designed to examine changes in specific surface area and mass flux during growth of surface hoar crystal morphologies grown at 3 different snow surface temperatures and do *not* include optical data. As shown in Figure 19, each subtest a, b, c explored surface hoar morphologies grown at different snow surface temperatures: below $-22°C$ (test 1a and 2a), -22 to $-10°C$ (test 1b and 2b), $-10$to $-4°C$ (test 1c and 2c). In addition to providing valuable data on SSA and mass flux, these initial tests assured that specific surface morphologies could be reliably reproduced. With a validated method for growing surface hoar in place, Test 3 added an optical component to the methodology developed in tests 1 and 2. Test 3 focused on the optical properties of plate like surface hoar growth (grown at temperatures between -10 and $-22°C$).

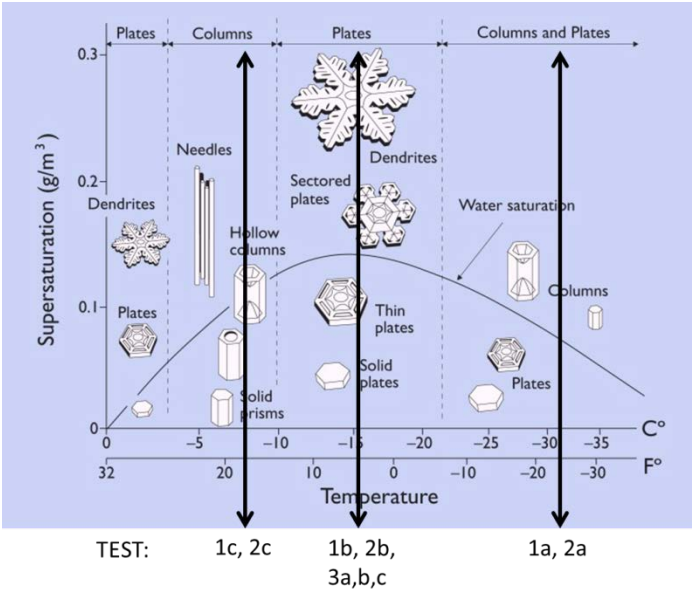


Figure 19. Reproduction of Figure 5 with the snow surface temperatures used in each experiment and expected snow morphology shown.

The final methodology used in test 3, consisted of sampling rounded grains from 42 different viewing geometries—21 forward-scattering angle and 21 backscattering angles. Each sample was normalized by the Spectralon reference panel across all wavelengths (200 to 1100 nm) via Equation (38). Microscopic images and CT scans were made of the rounded snow. After optical sampling, surface hoar was grown. Environmental conditions in the chamber were monitored continuously as detailed below. Growth was allowed to continue for approximately 24 hours, during which time 1-2 additional CT scans and as many microscopic images were recorded. The cold ceiling, at $-50°C$, was the coldest point in the chamber and inevitably collected hoar frost that could potentially fall from the ceiling and contaminate the snow surface. To mitigate this problem, the snow surface was covered and the ceiling was swept clean with a broom ever 3-4 hours during the course of growth. At the end of the growth period a final CT

scan and microscopic images were acquired. The surface hoar was sampled optically, again from 42 different viewing geometries. In total, 3 of these experiments were conducted, resulting in 3 optical samples on rounded grains and 3 samples on feather like surface hoar.

Table 1. Test Matrix showing dominant axial growth a crystal habit tested as well as listing tables or figures where results can be found.

Test #	**Mean Snow Surface Temp. °C**	**Dominate Axial Growth**	**Optical Properties Tested**	**Microscopic and CT Images**	**Meteorological and Mass Flux Data**	**SSA Data**
1a	~-31.5	C	No	Figure 32	Table 5	Table 8
1b	-15.5	A	No	Figure 33	Table 5	Table 8
1c	-8.3	C	No	Figure 34	Table 5	Table 8
2a	-29.7	C	No	Figure 35	Table 6	Table 8
2b	-15.0	A	No	Figure 36	Table 6	Table 8
2c	-8.3	C	No	Figure 37	Table 6	Table 8
3a	-15.2	A	Yes	Figure 38	Table 7	Table 8
3b	-16.4	A	Yes	Figure 39	Table 7	Table 8
3c	-14.6	A	Yes	Figure 40	Table 7	Table 8

In summary, the following chapter examines the methodology for both growing surface hoar in a lab setting and the subsequent testing of its optical properties. The first section, entitled *Development of Varying Snow Morphologies in the Lab Setting* (page 65), looks at the instrumentation and lab set up for growing surface hoar as well as the various tools used to document grain size and habit and collect data on mass flux rates. The second section, entitled *Optics* (page 71), focuses on optical methods including light source and spectrometer specifications as well as the method used to develop a BRF. While not presented in this thesis, extensive Matlab routines were developed to organize data, calculate results, and produce the plots and tables in the results section.

Development of Varying Snow Morphologies in the Lab Setting

To eliminate the challenge presented by the unpredictable nature of weather and snow surface conditions in the natural environment, preliminary work was devoted to protocols for growing various snow morphologies in the lab setting. Capitalizing on preliminary work by Andrew Slaughter, a walk-in environmental chamber at Montana State University's SSERF was used to prescribe the atmospheric conditions necessary to grow surface hoar. As discussed in Chapter 2, surface hoar forms when the water-vapor pressure in the air exceeds the equilibrium vapor pressure of ice at the surface. Two conditions are necessary for its formation in a lab setting: 1) a large temperature gradient above a snow surface cooled below the ice point and 2) sufficient supply of water vapor (Lang and Brown, 1984; Colbeck, 1988; McClung et al. 2006). In nature, the driving mechanism for developing a strong temperature gradient at the snow surface is longwave radiation loss to clear night sky. This longwave coupling was simulated in the lab through independent temperature controlled ceiling panels, which could be cooled to temperatures as low as -50°C. Necessary water vapor was supplied via fans directing moist air through ducting and across the snow sample's surface (Figure 20).

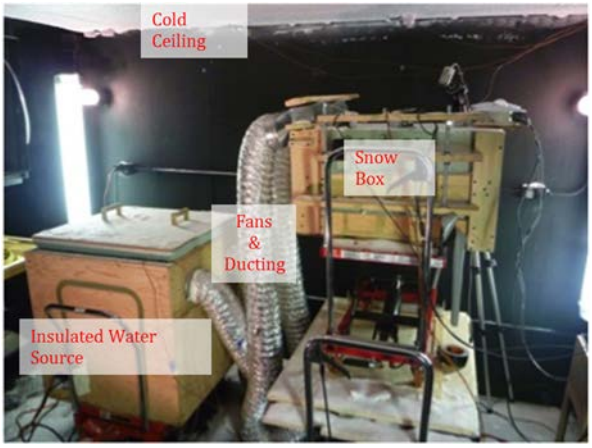


Figure 20. Experimental set up. The box on the lower left provides humidity-controlled airflow through a ducting system over the snow surface in the upper right. The temperature-controlled cold ceiling above provides the longwave radiation interaction.

The continuous sampling of environmental conditions in the lab every 30 seconds by a variety of instruments connected to an Agilent data logger (Figure 21) provided the necessary data to analyses growth conditions. Preliminary work was spent changing parameters one at a time until crystal growth occurred. The initial plastic shroud covering the water source was replaced by an insulated wooden box to facilitate more accurate control of the water temperature. The size of the fans as well as the length of the ducting and shape of the ducting outlet where experimented with until growth was uniform across the surface of the snow sample. Once surface hoar could be grown consistently, the air temperature of the room was varied to produce various crystal habits. Finally the environmental data was used in conjunction with Equation (17) to predict mass deposition rates and the result compared to CT scan data.

Long- and shortwave radiation at the snow surface were measured using Eppley Laboratories: Precision Spectral Pyranometer (PSP) (0.285–2.8 μm) and a Precision Infrared Radiometer (PIR) (3.5–50 μm). Note, however, that the surface hoar was grown

in the dark (simulating night) and the contribution of UV/VIS energy is expected to be negligible. An Everest Interscience Model 4000-4ZL non-contact infrared sensor provided continuous surface temperature measurement. Relative Humidity was monitored using Campbell Scientific, Inc CS215 Relative Humidity and Temperature Probe and/or a Vaisala INTERCAP Humidity and Temperature Probe HMP60. An array of thermocouples, buried at 1 cm intervals, captured the temperature profile within the top 7 cm of the snowpack. Additional thermocouples monitored the air temperature 1 and 2 cm above the snow surface and at the entrance and outlet to the ducting. Cold ceiling and surrounding wall temperatures were recorded via built in thermocouples incorporated into the environmental chamber. Finally, wind speed was held constant (~0.75 to 1.5 m/s) and was measured approximately 2 to 3 times during the course of each experiment using a hand held Omega Engineering, Inc. Digital Anemometer.



Figure 21. A) Detail of experimental set up and instrumentation. B) Functional diagram of experimental set up.

Documenting Crystal Habit

To ensure accurate, high quality documentation of surface crystal type as well as to document changes in microstructural parameters that might affect optical results, computed tomography (CT) images were taken before each optical test. To facilitate in-situ CT scans of growing surface hoar, a cylindrical sample holder with a cross sectional area of $706mm^2$ and a height of 51mm was buried with its top edge flush with the snow surface (Figure 21 and Figure 22). An ASTM #8 soil sieve (mesh size: 2.36 mm) was used to both fill the sample container and sift a uniform, level layer of rounded grains onto the snow surface. Before, during, and after each experiment, the sample holder was carefully removed, scanned using a SkyScan 1173 CT scanner at a resolution of 14.8 μm, and then returned to its original position and orientation. A 0.5 mm diameter graphite cylinder was inserted into the sample container as an index reference so the CT scans could be properly oriented for comparison at different time steps (Figure 22). Specific surface area (SSA) data as well data concerning the change in mass during growth was obtained by selecting a volume of interest of cross sectional area $\sim 700mm^2$ containing the top few millimeters of the snow sample including new growth. The three-dimensional images depicted in the results section were created using a smaller subregion of the original volume of interest due to the extensive computational time needed to reconstruct larger images. All data presented in the results section includes cross sectional area data where appropriate.

As shown in Figure 21, the CT sample container represents only a small portion of the total surface area on which the surface hoar was grown. In order to account for

variability of crystal habit across the entire 30x30cm snow surface, microscopic still photographs of disaggregate grains were taken at locations away from the CT sample. Images were taken at magnifications ranging from 6x to 50x in order to document general grain shape across many grains as well as a detailed view of individual grains.

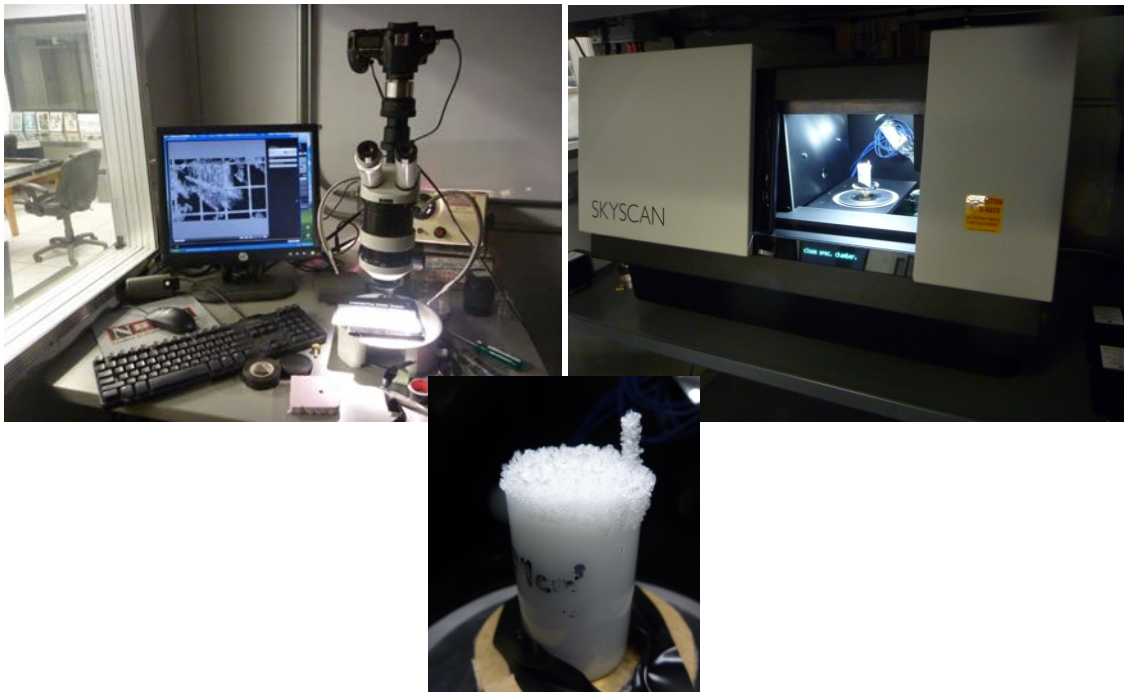


Figure 22. A) Wild optical microscope with digital imaging, B) SkyScan 1173 CT Scanner adapted for cold room use, C) $34cm^3$ sample holder with surface hoar growth. The vertical rod is used for image rotational indexing.

Table 2. List of meteorlogical data collected during surface hoar growth. The Agilent data logger recorded values for meterological data every 30 seconds. The only exception was wind speed which was measured approximately 2-3 times during the course of a experiment.

Meteorological Data	**Units**	**Symbol**
Time	s	t
Air Pressure	Pa	$\boldsymbol{P_{air}}$
Air Density	$g\ cm^{-3}$	ρ_{air}
Wind Speed	$m\ s^{-1}$	u
Relative Humidity	%	R.H.
Air Temperature	$°C$	T_{air}
Snow Surface Temperature	$°C$	T_{SS}
Water Temperature	$°C$	T_{water}
Long Wave Irradiance	$W\ m^{-2}$	E_{LW}
Short Wave Irradiance	$W\ m^{-2}$	E_{SW}

Table 3. List of computed tomography data collected at the start and end of each surface hoar growth period as well as 1-2 times in between.

Computed Tomography Data	**Units**	**Symbol**
Cross Section Area of CT Sample	mm^2	A_{samp}
Object Volume	mm^3	V_{obj}
Object Surface Area	mm^2	SA_{obj}
Specific Surface Area (V_obj/SA_obj)	mm^{-1}	SSA
Thermocouple Array Temperatures	$°C$	T_{probe_n}

Crystal Types Grown for Optical Testing

In an effort to assure that consistent crystal morphologies could be reproduced reliably in the lab setting, a plethora of tests where run varying parameters such as temperature of water source (and therefore humidity of air flow through ducting), wind speed, chamber temperature, sky view factor (controlled by varying position of snow surface relative to the cold ceiling), and positioning of airflow. In addition, various configurations of instrumentation were examined to determine optimal positioning of sensors. The data collected from these early tests, while not linked to any optical properties, provided interesting insight into changes in crystal specific surface area during

growth due to mass deposition. Data for surface hoar crystals grown at three separate chamber temperatures is shown in the results section. Consistent with Kobayashi (1961), the results from these early tests, demonstrated that surface hoar, like crystals grown in the atmosphere, develop morphologies based primarily on snow surface temperature while secondary features develop as a result of supersaturation values. Finally, equations were developed in an effort to predict mass flux from observed environmental data.

Optics

In the SSERF cold chamber, a Stellarnet Inc. Black Comet-HR spectrometer with a holographic concave grating covering 200-1100 nm ranges was used to capture spectral data from the snow surface. A technical analysis of the instrument is provided in Appendix A. A custom, hemispherical gantry was designed and built to support the spectrometers probe (Figure 23). This goniometer allowed the probe to be positioned at viewer zenith (θ_r) and azimuth (ϕ_r) ranging from $\sim 0^{\circ}$ to 75° and a full $360°$ respectively. Since the light source was built into the ceiling and could not be moved, sun geometry was controlled by tilting the snow surface with respect to the light as illustrated in Figure 23. Incident zenith angles utilized in this study were $15°$, $30°$, and $45°$. Finally, the common convention of defining a solar incident plane such that the sun is always at an incident azimuth angle of $180°$ was used in this thesis. This Table 4 shows the incident/observer geometries tested.

At each geometry, the raw counts striking the spectrometer's CCD was recorded on a spectral basis (called an .SSM file). This value was then normalized by the raw

counts striking the CCD as reflected from a Spectralon panel utilizing the same geometry. The resulting value is known as a BRF (see Equation (38)).

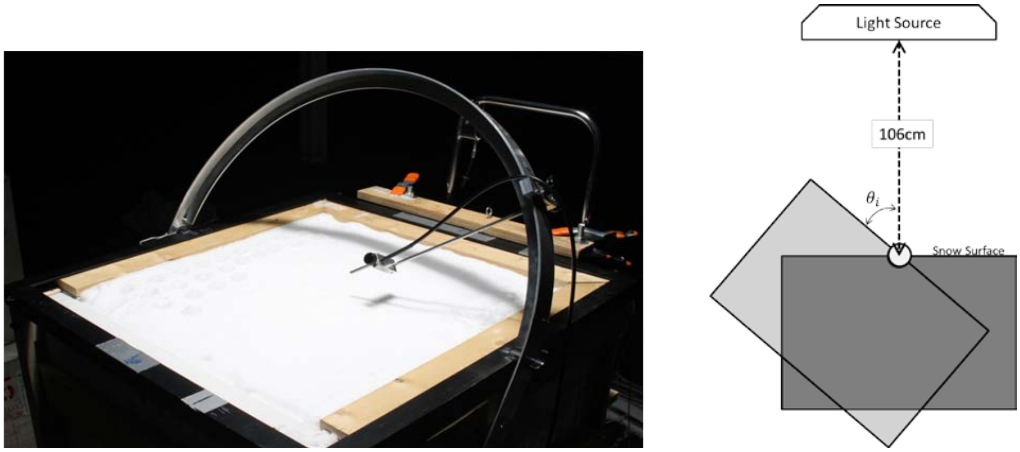


Figure 23. Left) Goniometer and Spectrometer Configuration. Right) Sun angle θ_i was varied by tilting the snow surface with respect to the fixed light source.

Table 4. List of all lighting and observer angles from which BRF data were obtained. θ_r = reflected/observer zenith angle. ϕ_r = reflected/observer azimuth angle. θ_i = incident zenith angle. ϕ_i = incident azimuth angle (i.e. 180° in all cases).

$\boldsymbol{\theta_r}$	$\boldsymbol{\phi_r}$	$\boldsymbol{\theta_i}$	$\boldsymbol{\phi_i}$
30	0	0	180
30	135	0	180
30	180	0	180
30	225	0	180
30	315	0	180
30	45	0	180
45	0	0	180
45	180	0	180
45	225	0	180
45	45	0	180
60	0	0	180
60	180	0	180
60	225	0	180
60	45	0	180
30	0	15	180
30	135	15	180
30	180	15	180
30	225	15	180

Table 4 Continued.

$\boldsymbol{\theta_r}$	$\boldsymbol{\phi_r}$	$\boldsymbol{\theta_i}$	$\boldsymbol{\phi_i}$
30	315	15	180
30	45	15	180
45	0	15	180
45	180	15	180
45	225	15	180
45	45	15	180
60	0	15	180
60	180	15	180
60	225	15	180
60	45	15	180
50	0	30	180
50	135	30	180
50	180	30	180
50	225	30	180
50	315	30	180
50	45	30	180
60	0	30	180
60	180	30	180
60	225	30	180
60	45	30	180
60	0	45	180
60	180	45	180
63	225	45	180
63	45	45	180

In test 3a, BRF values were obtained from 42 incident/observer geometries first on rounded grains and then again on surface hoar grown at an average snow surface temperature of $-15.2°C$. Tests 3b and 3c, repeated their procedure as closely as possible in an effort to assess reproducibility. As discussed in the section entitled *Spectralon Reference Panel and BRF* (page 82), a BRF value was obtained for each of the given geometries in Table 4 half of which represent forward-scatter and half of which represent backscatter.

The section titled *Light Source Considerations* (page 74) examines steps taken to ensure the light source produced a reliable spectrum similar to that of the sun. To assure that optical measurements did not capture unwanted light, the field of view of the spectrometer was carefully assessed and the results used to determine the optimal viewing/lighting geometry. This process is detailed in the sections titled *Field of View Considerations* (page 78) and *Geometric Considerations* (page 80). Finally, Spectralon and BRF considerations are explained in the section titled *Spectralon Reference Panel and BRF* (page 82).

Light Source Considerations

This study used a metal-halide solar simulation lamp that produces a spectral distribution comparable to the sun (in the range of 280 – 2480 nm) with programmable irradiance from 0−1200 [$W\ m^{-2}$]. The distribution of power incident on the snow surface was mapped over a 25 in^2 area. As can be seen in Figure 24, initial tests revealed areas of dust had gathered on the lamp surface causing uneven distribution of power at the snow surface. After cleaning, the lamp continued to demonstrate a “hot spot” at the snow surface.

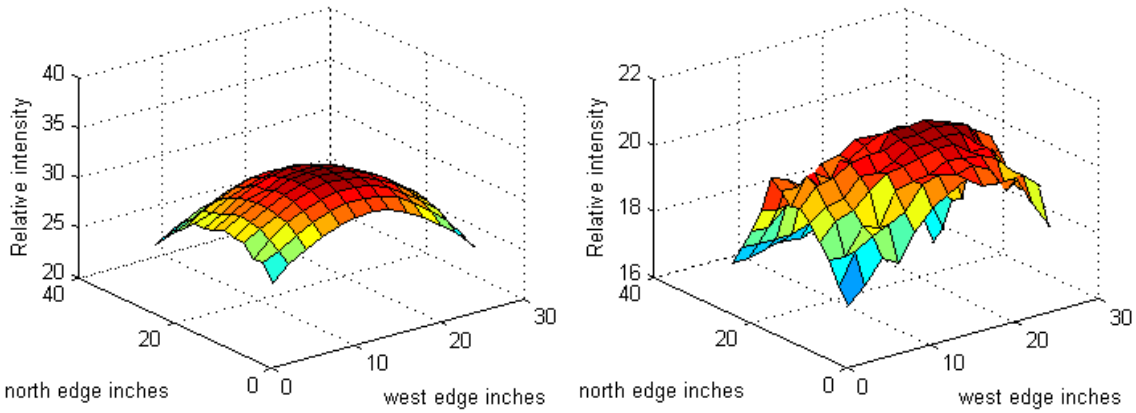


Figure 24. Left: Relative power incident at snow surface with clean lamp. Right: Before cleaning.

However, the uneven distribution of light at the snow surface provided no obstacle in measuring a BRF since the same lighting conditions and geometries were used in collecting both snow sample data and Spectralon data. Since a BRF is the ratio of the radiance $[W\ m^{-2}\ Sr^{-1}]$ from the snow surface divided by the radiance from the Spectralon (see Equation (38)), the effect of uneven power distribution cancels out in this normalizing process. This is true even if the light source was not clean.

In addition to mapping the power of the lamp as a function of position, the temporal consistency of the lamps power was also assessed using a pyronometer. As shown in Appendix B, the lamp reached full power in approximately 10 minutes and remained constant with time during the 1 hour test. For this reason, in all experiments the light was allowed to warm up for at least 10 minutes prior to use.

Light traveling through the atmosphere is subjected to scatter. Over a path length as thick as the atmosphere, the effect can be considerable. In a lab setting, where the path length between the source and the surface of snow is approximately two meters these losses are expected to be minimal. Nevertheless, a Modtran (MoDerate resolution

atmospheric TRANsmission) computer model was run using simulating the transmittance of radiation for the bandwidth of the Black Comet spectrometer used in this study. Modtran is a radiative transfer computer model that is commonly used in the remote sensing community (Anderson et al., 2009). The model accounted for typical humidity, air pressure, and atmospheric conditions in Bozeman Montana in the winter time. The model suggests that only O2 and H20 act as absorbers in this bandwidth. As expected for a 2 meter path, the atmospheric transmission is better than 97%. In fact, if we exclude H20 abortion between 875 and 1000 nm (this represents the edge of the spectrometers capability), the transmission jumps to better than 99% .

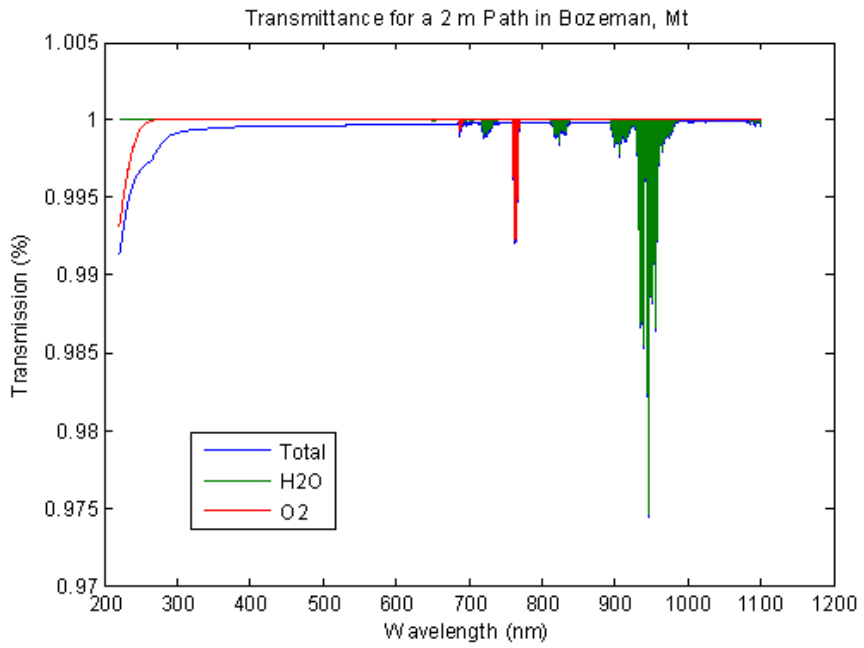


Figure 25. ModTran Model of transmittance for a 2m Path in Bozeman, Mt.

As a final consideration, the light source manufacturer claims it is an accurate simulation of the solar spectrum. Figure 26 depicts the spectrum produced by the light as

measured in the laboratory using a spectrometer in raw counts (a count of photons striking the CCD). This value can be calibrated using an integration sphere to return power [W], irradiance [$W\ m^{-2}$], or radiance [$W\ m^{-2}sr^{-1}$]. However, since the BRF values are unitless ratios of signal from the snow normalized by signal from the Spectralon, calibration is unnecessary for the purposes of this thesis. Figure 27 depicts the solar spectrum as measured at the top of the atmosphere as well as at sea level after attenuation in the atmosphere. Additionally, the solid line represents Planck's curve for a blackbody at $5250°C$. A comparison of the two figures shows the lamp provides an adequate spectral representation of the sun, especially top of atmosphere radiation, for the purposes of this thesis.

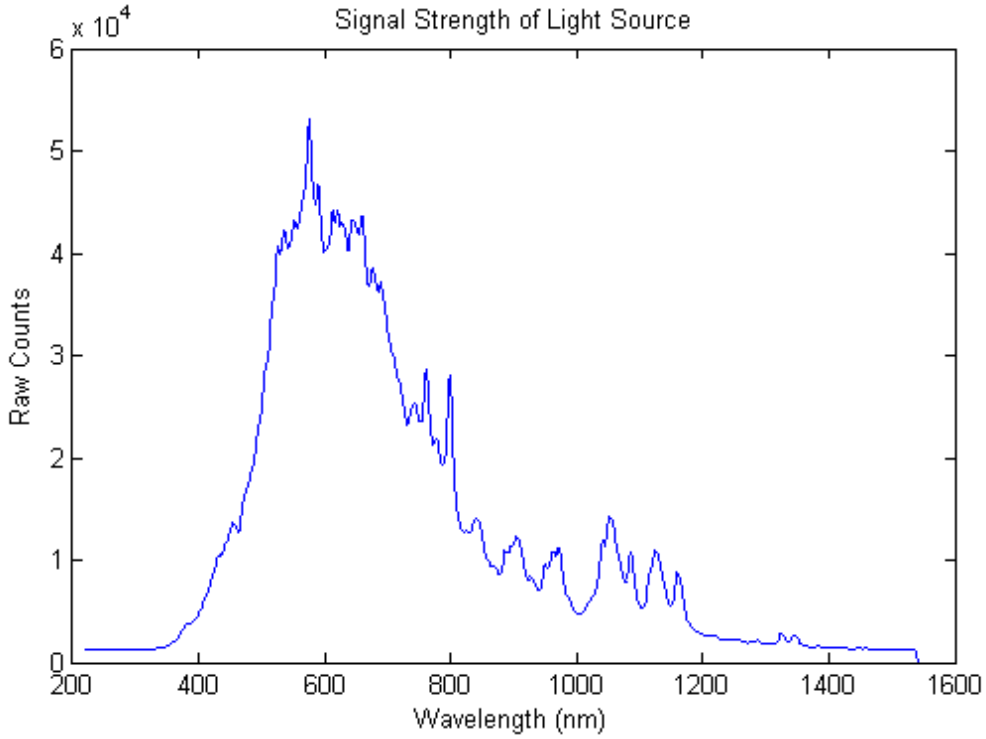


Figure 26. The spectrum produced by the light as measured in the lab using a spectrometer.

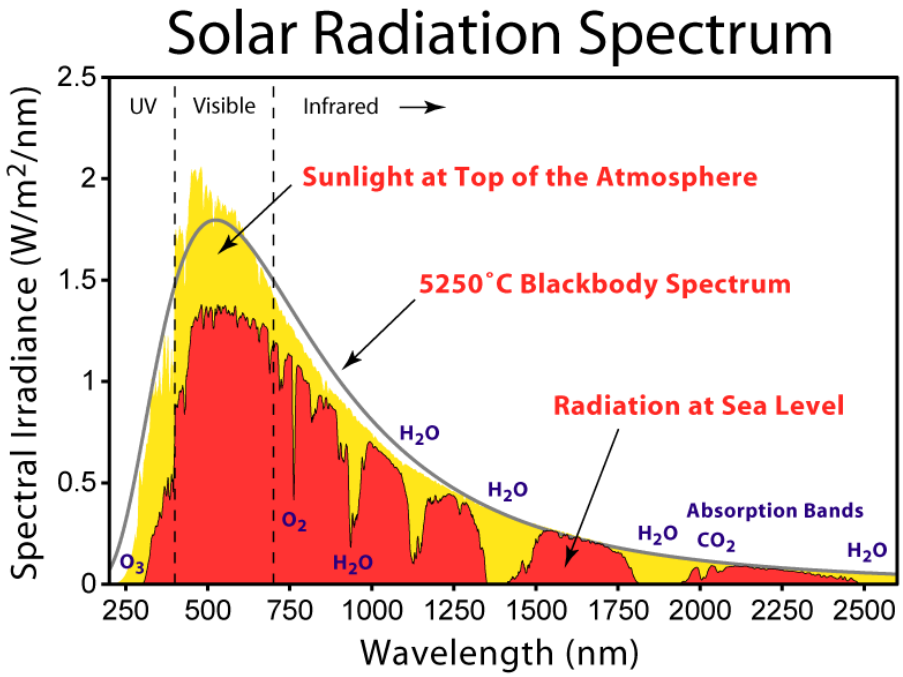


Figure 27. Depiction of the solar spectrum as measured at the top of the atmosphere and at sea level after attenuation in the atmosphere. Additionally, the solid line represents Planck's curve for a blackbody at $5250°C$.

Field of View Considerations

Due to subsurface scattering the point where incident light enters the snow does not have to be the same point where the beam exits the snow (see Figure 17). Conversely, Spectralon demonstrates very little subsurface scattering. Conveniently, a BRF captures the effect of subsurface scattering as normalized by a surface with little subsurface scatter rendering a detailed discussion of how subsurface scattering occurs unnecessary in reporting the observed results. Nevertheless, it is speculated that light striking the snow just outside of the edge of the field of view (FOV) might travel subsurface and reemerge within the FOV, thus adding to the power detected by the spectrometer. However, due to the symmetrical nature of the FOV, it is equally as likely that light striking within the FOV will emerge outside the field of view, thus subtracting

from the power detected at the spectrometer. The two effects are, therefore, expected to cancel out. In the lab, effort was made to assure that the area extent of the incident radiation on the snow's surface was much greater than the area viewed by the detector. This assured the effect of subsurface scattering near the edge of the area viewed by the receiver is consistent from test to test.

A possible source of error in performing BRF studies is the FOV of the spectrometer straying off the Spectralon or snow surface thus capturing of unwanted. This is easy to do as viewing angles, and thus, the viewing area, is changed. In this study, the FOV of spectrometer was carefully mapped by recording the signal response from a various lighting angles. To assure that as much reflected light was being captured, as possible as well as to minimize edge effects, a power cut off of approximately 100% was used to define limits of FOV rather than the more typical half-power value. The FOV of the spectrometer was determined to be 15 degrees half angle. A plot of signal strength as a function of illumination angle can be seen in Figure 28. Note that the raw fiber optic cable was used in all reported tests rather than an attached probe as per the manufacturer's recommendation (personal correspondence).

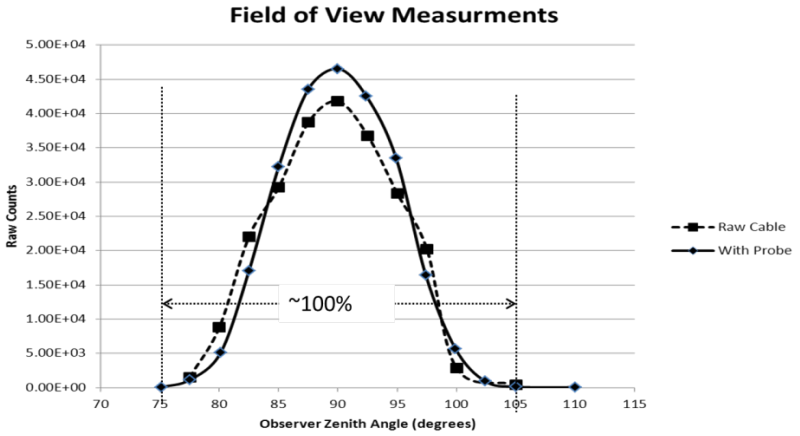


Figure 28. Response of spectrometer as a function of incident solar angle. Note that solid angle field of view half angle of 15 degrees captures nearly 100% of incident light.

Geometric Considerations

Equations were developed relating the spectrometer's FOV to its observational footprint, which changes from a perfect circle at nadir viewing angle to an ellipsoid at off nadir viewing angles. As illustrated in Figure 29, at viewer zenith angle of $\theta_r = 75°$ (for a 4cm probe height) the field of view paralleled the snow surface. The maximum viewer angle θ_r that still fell within the confines of the Spectralon's $30cm \times 30cm$ surface area was $\theta_r = 60°$.

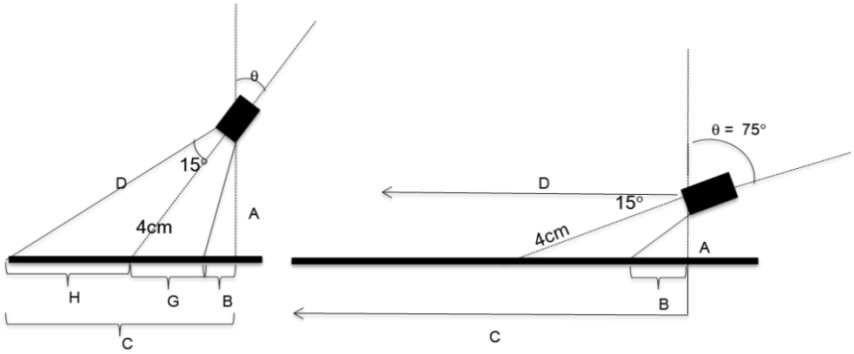


Figure 29. Viewing Geometry showing the *upper bound* of viewer zenith angle to be 75 degrees for a 4cm probe height. Equations for labels shown in the figure are provided in Appendix B.

While FOV determined the upper bound to viewer zenith angle, a shadow cast by the gantry's arm provided the primary limitation to capturing a full hemispherical data set and dictated the lower bound of viewer zenith angle to be $\theta_r = 10°$ (Figure 30).

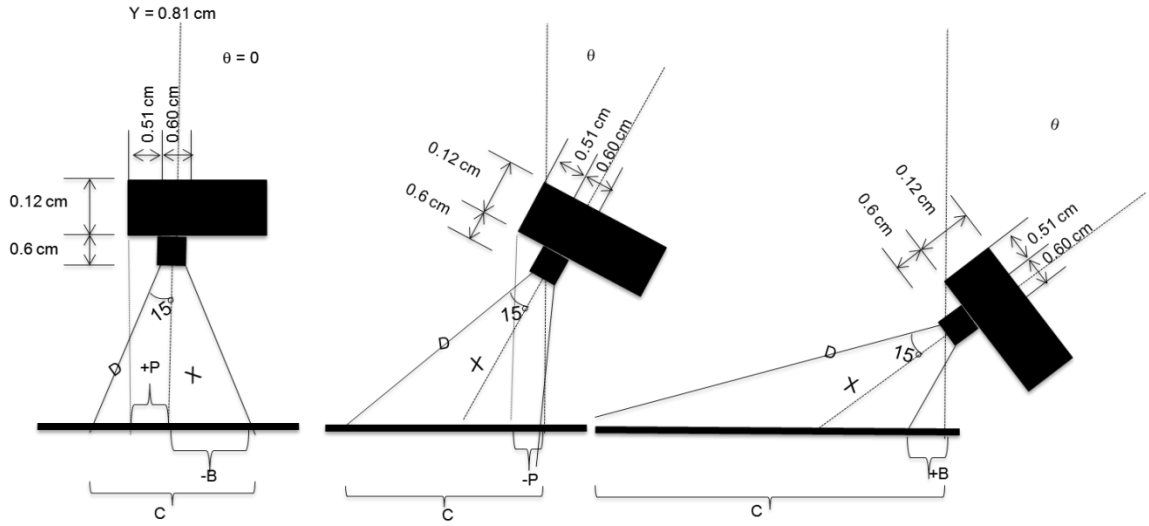


Figure 30. Viewing geometry showing the *lower bound* is controlled by the shadow from the gantry. Negative values of B indicate the shadow of the gantry is captured within the field of view of the spectrometer. Equations for labels shown in the figure are provided in Appendix B.

Observer azimuth angles were primarily limited by the possibility of the probe tip or its support touching the snow surface at large zenith angles. Additionally, the physical configuration of the gantry meant that measurements near $\phi = 90°$ and $\phi = 270°$ were not possible. Trial and error was used to select the final observer azimuth angles.

An incident azimuth angle of $\phi_i = 180°$ was used in all experiments. Thus, reflected light in this direction is backscatter, while light reflected into the hemisphere containing $\phi_r = 0°$ is forward-scatter (Figure 31). For reference, "the *solar principle plane* is defined in such a way that the azimuth angle of the incident radiation is equal to

180° and the azimuth angle of the forward-scattering is equal to zero (Bourgeois et al. 2006). Incident zenith angle's of 0° (nadir), 15°, 30°, and 45° were used in conjunction with various zenith angles defined above. Full data sets showing all recorded geometries are presented in Appendix F. Note that time constraints and the physical challenge of manually collecting the data meant that full hemispherical data sets were not collected. Rather it is assumed that the scatter is symmetric about the incident plane (the plane containing a ray of incoming light).

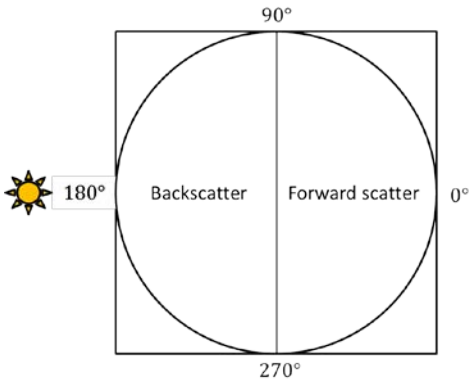


Figure 31. Illustration of forward and backscatter direction based on a fixed incident azimuth angle of $\phi_i = 180°$.

Spectralon Reference Panel and BRF

The uncalibrated spectrometer returned raw counts (the actual count of photons striking the charge-coupled device [CCD] detector within the spectrometer). The software accompanying the spectrometer allowed the user to sample Spectralon as the reference surface by which the future samples were normalized. Once referenced, the spectrometer returned a unitless BRF when pointed at a snow surface. However, this process required referencing the Spectralon each time the sun geometry was changed and proved impractical—primarily because the cumbersome process of switching between

the snow surface and the Spectralon surface for each of the 40+ samples taken during the course of an experiment was time prohibitive. In addition to being cumbersome, files saved in this format, could not be renormalized to a different Spectralon reference in the future. This caused the loss of several months' worth of data when it was discovered that the Spectralon reference was incorrectly sampled at certain sun geometries (see discussion in Chapter 5). Finally, as mentioned previously, Spectralon—while exceedingly close to being an idealize Lambertian surface—departs from 99% diffuse scatter at observer zenith angles greater than 8° and is even less diffuse at observer zenith angles greater than ~60°.

To overcome these challenges a more practical method was developed in which the Spectralon was first sampled from all necessary geometries (in raw counts); the snow was then sampled at these same geometries (again in raw counts) and a Matlab program was created to produce a BRF. This was advantageous in that it allowed the Spectralon to be tested once and all future snow samples normalized by these values, greatly increasing the efficiency of the testing process. Further, any angular dependence of Spectralon was corrected for in the normalizing process. However, it also required sun intensity settings and geometries (zenith/azimuth angles and the distance of the snow surface to the sun) as well as the internal settings of the spectrometer (detection integration time, Xtiming resolution control, etc.) to be consistent for all subsequent tests. Protocols were developed to assure consistency between tests.

CHAPTER 4

RESULTS AND DISCUSSION

Nothing is too wonderful to be true if it be consistent with the laws of nature.—Michael Faraday

As detailed in the test matrix (Table 1 of Chapter 3), a total 9 experiments were conducted: test 1a, b, c; 2a, b, c; 3a, b, c. Experiments 1 and 2 were designed to examine changes in specific surface area and mass flux during growth of surface hoar crystal morphologies grown at 3 different snow surface temperatures and do *not* include optical data. In conjunction with SSA and mass flux data, these test validate the surface hoar growing method. Test sequence 3 added an optical component to the methodology developed in tests 1 and 2. Test 3 focused on the optical properties of plate like surface hoar growth for 3 experiments. In all tests (1, 2 and 3), CT scans as well as microscopic images were taken before, during, and after surface hoar growth. CT and microscopic images are presented in the section titled *Surface hoar Growth Results* (page 85).

Additionally, environmental chamber conditions were logged every 30 seconds by a data logger and the results used to predict mass flux. The results of this analysis were compared to changes in crystal mass as recorded by the CT scanner. The comparisons are elaborated on in the section titled *Mass Flux Results* (page 90). Temporal changes in specific surface area (SSA) are presented in the section titled *Specific Surface Area Results* (page 99). Finally, the optical BRF values recorded in test 3 are presented and discussed in the section entitled *Optical Property Results* (page 102).

Surface Hoar Growth Results

Three-dimensional CT scans and select accompanying optical images are presented for each experiment in Figure 32 to Figure 40. All CT scans were taken at a resolution of $14.8 \times 10^3\ nm$. The initial image (left side) is the base surface snow that the surface hoar was allowed to develop upon. In the sequences of images, the development of surface hoar is evident in the CT and optical images.

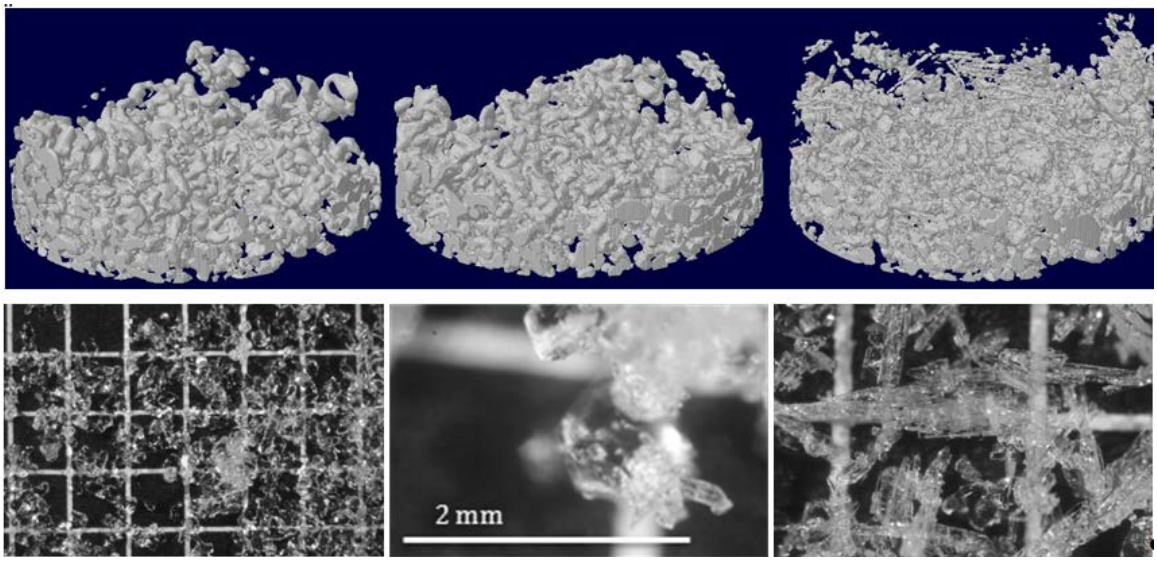


Figure 32. Test 1a 3/27/12. Snow surface temperature during first 7 hours of growth started at ~-26.8°C and steadily approached a constant -31.5°C. During the final 17-hour growth period, surface temperature data failed to record; however, it is speculated the snow surface temperature remained close to -31.5°C during periods of actual surface hoar growth. CT Images at times: 0, 7, 24 (hrs) (Sample Area: 389.59 mm^2) and corresponding microscopic images (2 mm grid).

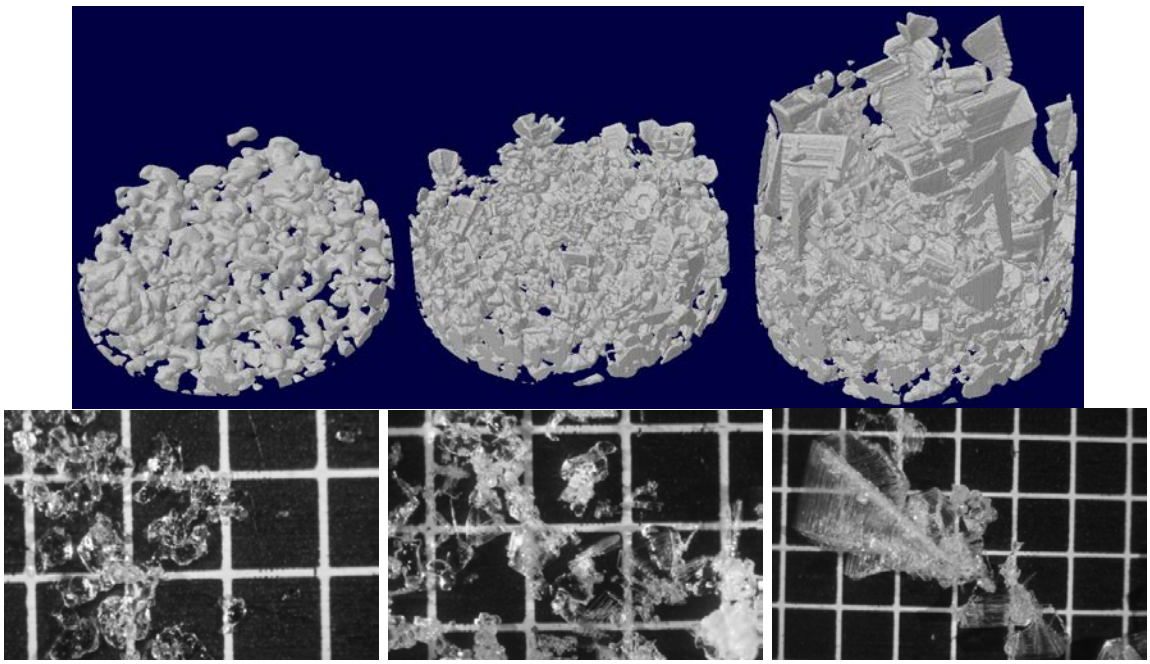


Figure 33. Test 1b 3/28/12. Snow Surface Temperature Range: -13.6 to -21.1°C. Mean Snow Surface Temperature: -15.5°C with a standard deviation of 1.9°C. CT Images at times: 0, 6.5, 22 (hrs) (Sample Area: 501.08 mm^2) and corresponding microscopic images (2 mm grid).

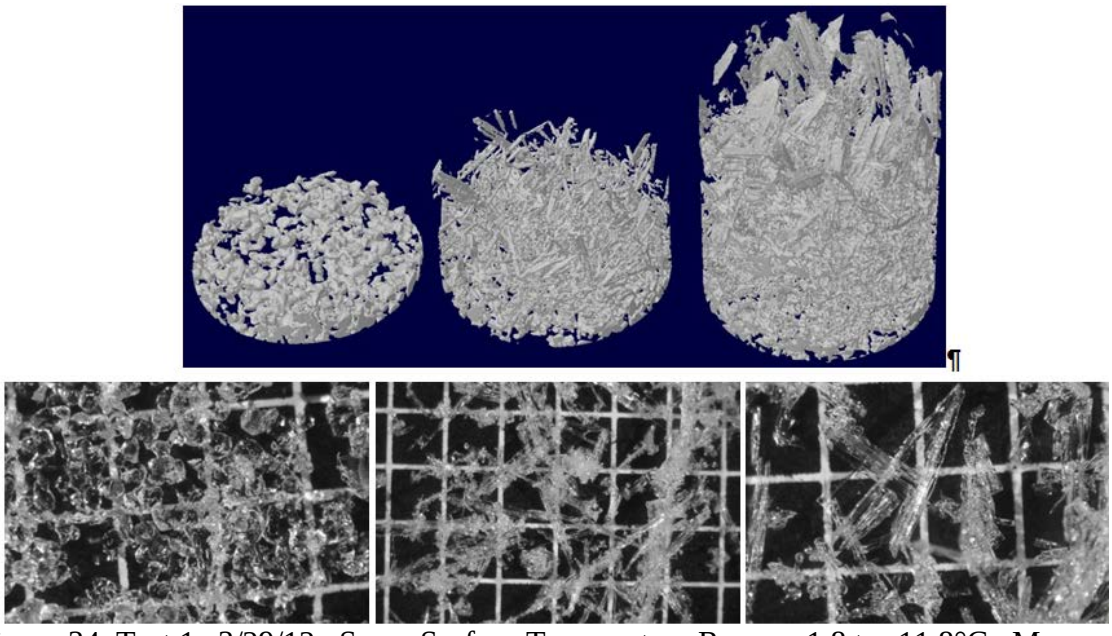


Figure 34. Test 1c 3/29/12. Snow Surface Temperature Range: -1.8 to -11.8°C. Mean Snow Surface Temperature: -8.3°C with a standard deviation of 1.0°C. CT Images at times: 0, 6.5, 22.5 (hrs) (Sample Area: 551.92 mm^2) and corresponding microscopic images (2 mm grid).

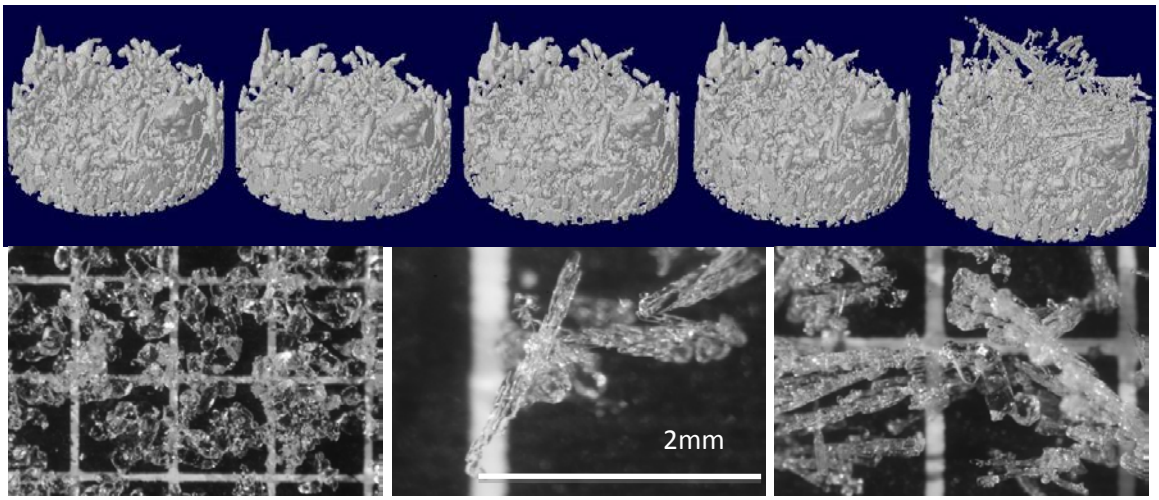


Figure 35. Test 2a 6/19/12. Snow Surface Temperature Range: -26.5 to -31.1°C. Mean Snow Surface Temperature: -29.7°C with a standard deviation of 1.2°C. CT Images at times: 0, 5, 8.5, 12.5, 25 (hrs) (Sample Area: 505.22 mm^2) and select microscopic images (2 mm grid) at time 0, 12.5, 25 (hrs). Note: during the initial 12.5 hours, the snow surface temperature dropped as the snow equilibrated with the chamber air temperature. Significant growth did not occur until the snow surface temperature dropped below this chamber air temperature, due to the longwave loss to the cold ceiling, around hour 10.

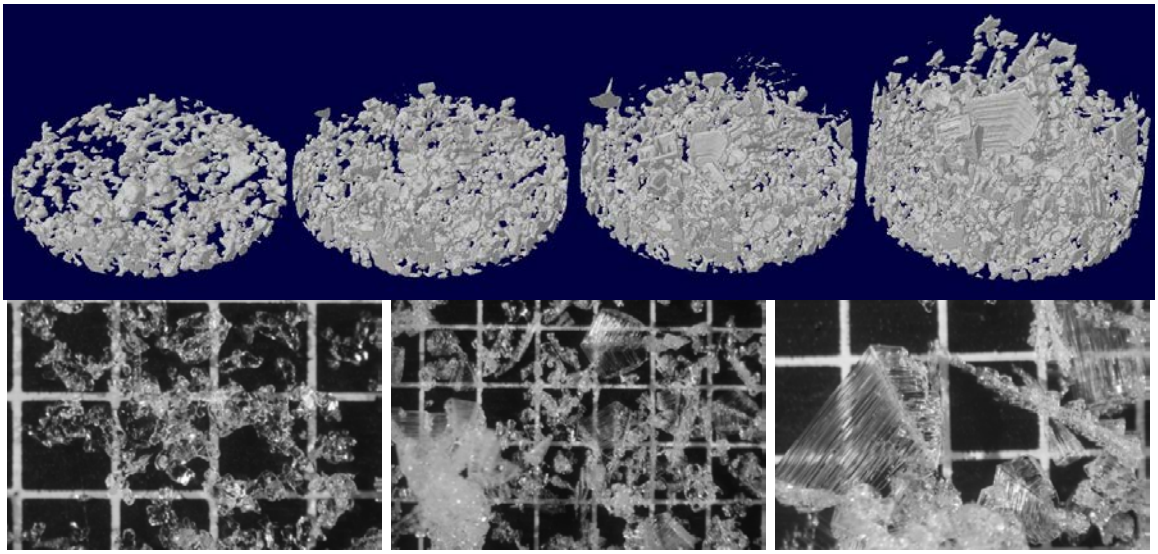


Figure 36. Test 2b 6/21/12. Snow Surface Temperature Range: -12.4 to -16.5°C. Mean Snow Surface Temperature: -15°C with a standard deviation of 0.4°C. CT Images at times: 0, 7, 12.5, 24 (hrs) (Sample Area: 469.7 mm^2) and select microscopic images (2 mm grid) at times 0, 12.5, 24 (hrs).

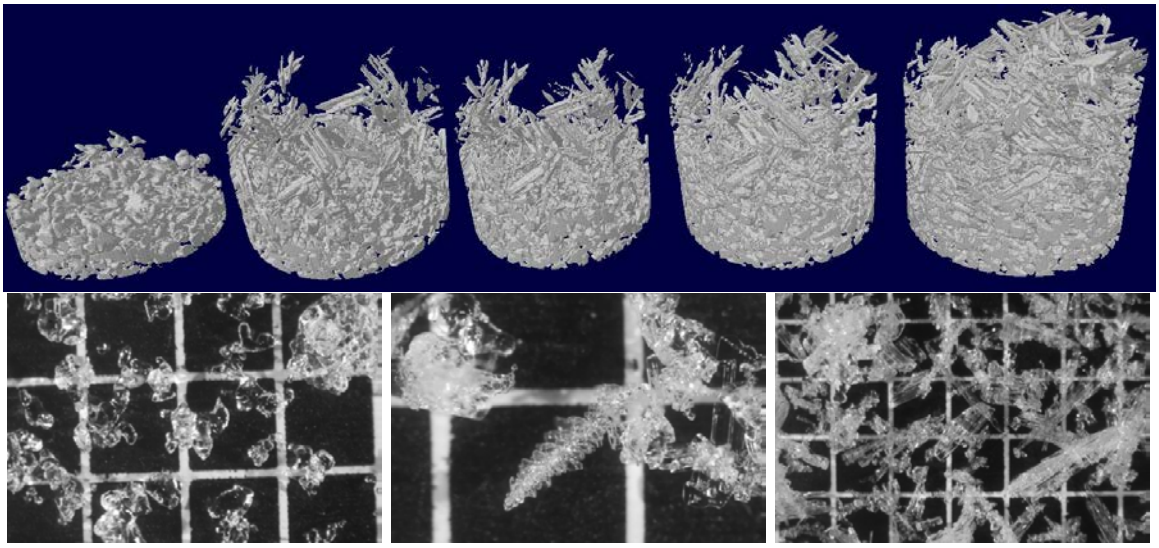


Figure 37. Test 2c 6/26/12. Snow Surface Temperature Range: -5.5 to -12.7°C. Mean Snow Surface Temperature: -8.3°C with a standard deviation of 0.76°C. CT Images at times: 0, 7, 11, 13.5, 23.5 (hrs) and (Sample Area: 550.68 mm^2) select microscopic images (2 mm grid) at times 0, 11, 23.5 (hrs).

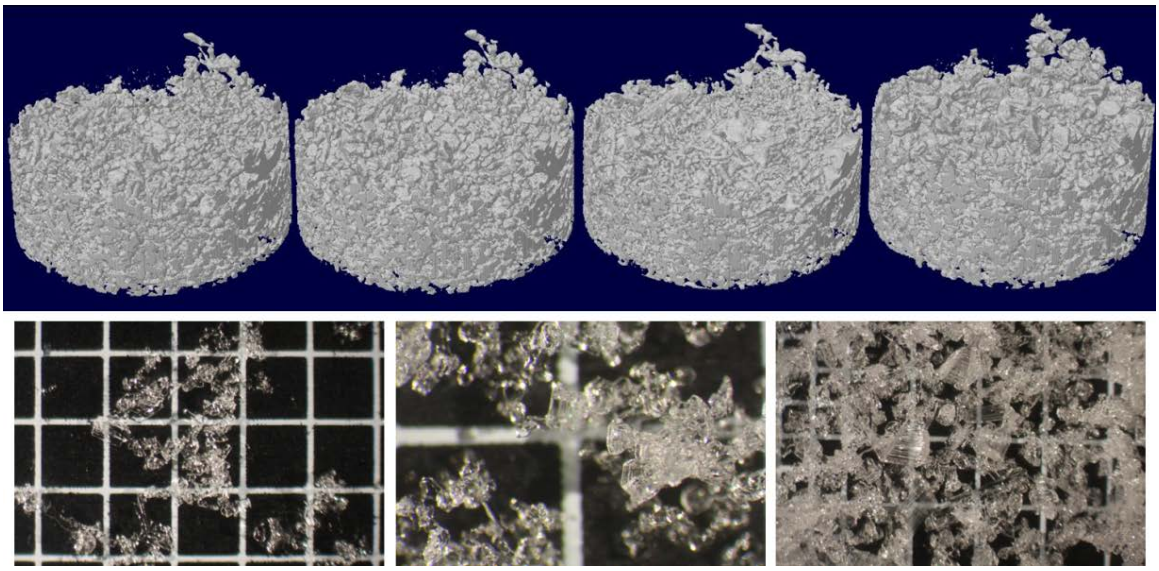


Figure 38. Test 3a 10/25/12. Snow Surface Temperature Range: -12.2 to -16.1°C. Mean Snow Surface Temperature: -15.2°C with a standard deviation of 0.85°C. CT Images at times: 0, 12, 23.5 (hrs) and (Sample Area: 447.65 mm^2) select microscopic images (2 mm grid) at times 0, 7.5, 13, 23.5 5 (hrs). Note: less surface hoar growth was observed in front of the left ducting (where the CT sample was located) compared to the right ducting (where optical tests and regular microscopic photographs were taken.

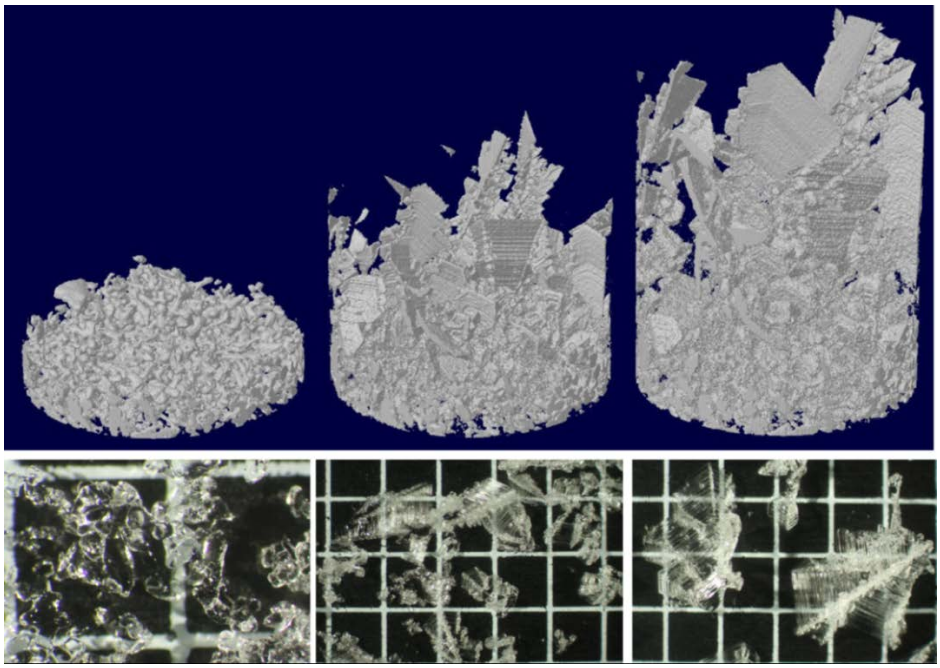


Figure 39. Test 3b 11/15/12. Snow Surface Temperature Range: -15.3 to -17.3°C. Mean Snow Surface Temperature: -16.4°C with a standard deviation of 0.26°C. CT Images at times: 0, 10.4, 21 (hrs) and (Sample Area: 367.31 mm^2) select microscopic images (2 mm grid) at times 0, 10.4, 21 (hrs).

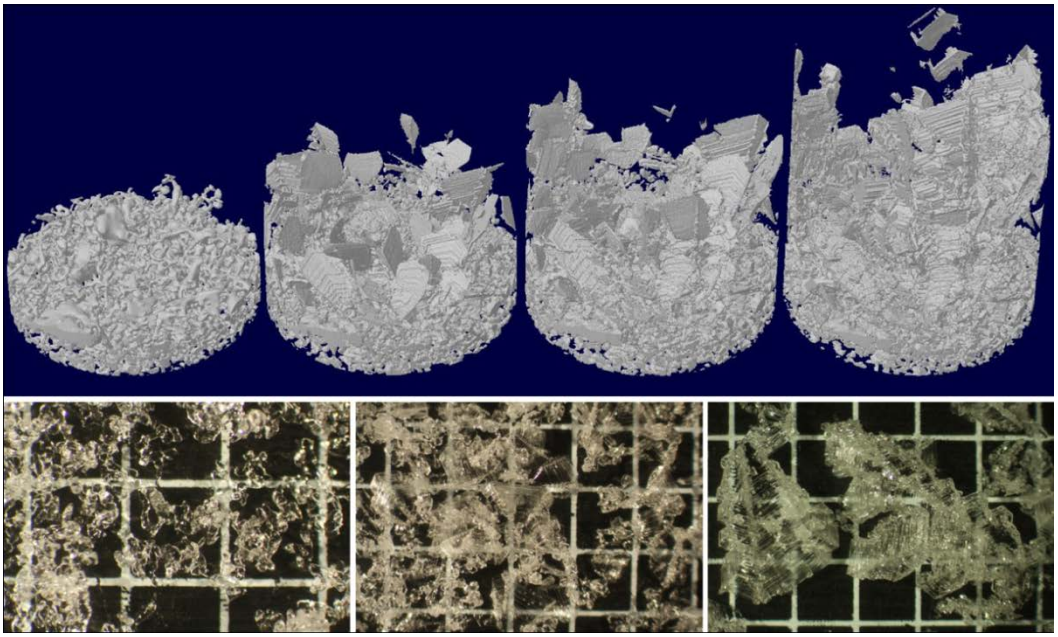


Figure 40. Test 3c 11/29/12. Snow Surface Temperature Range: -13.7 to -15.6 °C. Mean Snow Surface Temperature: -14.6°C with a standard deviation of 0.36°C. CT Images at times: 0, 6.5,12, 24 (hrs) and (Sample Area: 414.23 mm^2) select microscopic images (2 mm grid) at times 0, 6.26, 11.98, 23.94 (hrs).

Surface Hoar Growth Discussion

By controlling the air temperature, wind speed, humidity and longwave radiation exchange, surface hoar was consistently produced in a lab setting. The approach simulated the natural processes believed to be dominant in surface hoar development. Consistent with the findings of Nakaya, 1954, Hallet and Mason, 1958, and Kobayashi, 1961 discussed previously in Chapter 2: Crystal Growth in the Atmosphere and detailed again in the methodology chapter (see Figure 19), the surface hoar grown in this study displayed c-axis dominant growth in tests 1a and 2a (Figure 32 and Figure 35) where snow surface temperatures, during growth, were approximately -31°C as well as in tests 1c and 2c (Figure 34 and Figure 37) where average snow surface temperatures were approximately -8°C.

Likewise, crystals grown in tests 1b, 2b, 3a, 3b, 3c , at average surface temperatures of approximately -15°C, demonstrated a-axis dominant growth. These cupped and feathery crystals can be seen in Figure 33, Figure 36, and Figure 38 to Figure 40. These results provide further confirmation that primary crystal habit temperature dependence of atmospheric snow crystals applies to surface hoar.

Mass Flux Results

Table 5 through Table 7 present the mean environmental parameters recorded by the data logger during the course of each experiment. Those parameters are: test number $Test\ \#$, change in time $\Delta Time$, cross-sectional area of the snow sample used in calculations A_{sample}, wind speed u, air pressure P_{air}, relative humidity R.H., air

temperature T_{air}, and snow surface temperature T_{ss}. The remaining parameters were calculated using this data and are delineated with a bold outline. They include: air density ρ_{air}, equilibrium vapor pressure with respect to liquid water in the air above the snow $p^{air}_{eqm.vap.,liq}$, partial pressure of water vapor in the air above the snow $\wp_{vap}$, equilibrium vapor pressure with respect to ice at the snow surface $p^{ss}_{eqm.vap.,ice}$, and mass flux in $g\ m^{-2}\ s^{-1}$ as calculated using Equation (17) F_m. The value $\mathcal{M}_{calc}$ represent total accumulated mass up to the time shown in $\Delta Time$. The value $\mathcal{M}_{CT}$ represents the mass flux as calculated using CT scan data: the change in object volume times the density of ice ($916.7\ Kg\ m^{-3}$).

As discussed in Chapter 2, mass flux F_m $[g\ m^{-2}s^{-1}]$ can be calculated from Equation (17). Of the terms in this equation, only air pressure and wind speed were recorded directly. The remaining values were calculated based on recorded meteorological parameters. Wind speed was measured periodically and varied between 0.75 and 1.5 m/s. Thus, 1 m/s was used as a representative constant in calculating mass flux. The dimensionless mass transfer coefficient was taken to be $C_Q = 2.9 \times 10^{-3}$ based on Hachikubo (1997) work as discussed below. Air density was calculated from the ideal gas law $\rho_{air} = P_{air}/(R_s T_{air})$, where R_s is the ideal gas constant for water vapor ($0.2870\ kJ\ kg^{-1}K^{-1}$).

The equilibrium vapor pressure with respect to liquid water above the snow surface $p^{air}_{eqm.vap.,liq}$ was calculated using the Antoine equation (Equation (4)) where the air pressure P_{air} and air temperature T_{air} value were recorded directly by the data logger. The term $p^{air}_{eqm.vap.,liq}$ represents the equilibrium vapor pressure in the air above snow

given its temperature. To find the actual partial pressure of the water vapor (a.k.a. the vapor pressure[9] $\wp_{H2O}$) in the air this value must be multiplied by the relative humidity (R.H.), a value recorded directly during each experiment, $\wp_{H2O} = p^{air}_{eqm.vap.,liq} * R.H.$. Finally, the value of $p^{ss}_{eqm.vap.,ice}$ can be calculated from the Antoine equation (Equation (5)). With these terms defined Equation (17) can be used to find mass flux F_m in units of $g\ m^{-2}s^{-2}$. An analysis of these units shows that multiplying mass flux by an area (in this case A_{sample}) returns a value of mass deposited per unit time. Therefore, this term can be integrated over time (the length of the experiment) to determine the total mass added or subtracted from the snow surface. This value is given by $\square_{calc}$ and was calculated numerically using the Matlab script (Appendix C) which assumes a linear interpolation between the 30 second time intervals recorded by the data logger (i.e. a simply application of the trapezoid rule). Plots of meteorological conditions, including mass flux, are presented in Appendix E.

[9] As mentioned previously, the term vapor pressure is sometimes used to exclusively mean equilibrium vapor pressure. Here vapor pressure does not imply equilibrium; rather, it represents the partial pressure of the water vapor in the system.

Table 5. Mean environmental chamber parameters for test 1. Corresponding images can be seen in Figure 32 to Figure 34. $\Delta Time$ represents time elapsed from the initial start of the experiment (i.e. $\Delta T = 0$). An explination of the symbols used is provided in the text at the beginning of the section titled *Mass Flux Results*. The boxed terms reprsents calculated values.

$\boldsymbol{Test\ \#}$	$\boldsymbol{\Delta Time}$ $(\boldsymbol{hour})$	$\boldsymbol{A}_{\boldsymbol{samp}}$ (mm^2)	$\boldsymbol{u}$ $(\boldsymbol{m/s})$	$\boldsymbol{P_{air}}$ $(\boldsymbol{hPa})$	$\boldsymbol{R.H.}$ (%)	$\boldsymbol{T_{air}}$ $(°\boldsymbol{C})$	$\boldsymbol{T_{ss}}$ $(°\boldsymbol{C})$	$\boldsymbol{\rho_{air}}$ $\boldsymbol{g/cm^3}$	$\boldsymbol{p^{air}_{eqm.vap,liq}}$ $(\boldsymbol{hPa})$	$\boldsymbol{p_{vap}}$ $(\boldsymbol{hPa})$	$\boldsymbol{p^{ss}_{eqm.vap,ice}}$ $(\boldsymbol{hPa})$	$\boldsymbol{F_m}$ $\boldsymbol{g\ m^{-2}s^{-1}}$	$\boldsymbol{\mathcal{M}_{calc}}$ $(\boldsymbol{g})$	$\boldsymbol{\mathcal{M}_{CT}}$ $(\boldsymbol{g})$
1a	6.0167	389.59	1	Probe Failure			-29.864	Probe Failure						1.06e-2
1b	8.3333	501.08	1	900.23	84.60	-10.676	-17.289	1195.1	2.4604	2.0817	1.3632	1.72e-3	0.0259	0.0891
1b	20.850	501.08	1	900.23	85.99	-10.679	-15.474	1195.1	2.4587	2.1146	1.6115	1.20e-3	0.045	0.2523
1c	6.2250	551.92	1	900.24	93.63	-4.2887	-7.6900	1166.7	4.3034	4.0351	3.2196	1.91e-3	0.0236	0.0312
1c	21.750	551.92	1	900.24	92.47	-4.5042	-8.2588	1167.6	4.2180	3.9035	3.0551	1.98e-3	0.0857	0.1256

Table 6. Mean environmental chamber parameters for test 2. Corresponding images can be seen in Figure 35 to Figure 37. $\Delta Time$ represents time elapsed from the initial start of the experiment (i.e. $\Delta T = 0$). An explination of the symbols used is provided in the text at the beginning of the section titled *Mass Flux Results*. The boxed terms represents calculated values.

$Test\ \#$	$\Delta Time$ $(hour)$	A_{samp} (mm^2)	u (m/s)	P_{air} (hPa)	$R.H.$ (%)	T_{air} $(°C)$	T_{ss} $(°C)$	ρ_{air} g/cm^3	$p^{air}_{eqm.vap,liq}$ (hPa)	p_{vap} (hPa)	$p^{ss}_{eqm.vap,ice}$ (hPa)	F_m $g\ m^{-2}s^{-1}$	$\mathcal{M}_{calc}$ (g)	$\mathcal{M}_{CT}$ (g)
2a	4.333	505.22	1	900.22	73.25	-28.027	-28.808	1279.6	0.4695	0.3441	0.4331	-2.28e-4	-1.80e-3	-0.026
2a	8.050	505.22	1	900.22	71.09	-26.323	-29.273	1279.0	0.4750	0.3377	0.4131	-1.93e-4	-2.83e-3	0.0511
2a	11.883	505.22	1	900.22	70.039	-28.208	-29.73	1280.6	0.4611	0.3234	0.3946	-1.8e3-4	-3.64e-3	0.0692
2a	24.225	505.22	1	900.22	69.158	-28.486	-29.658	1282.0	0.4485	0.3109	0.3986	-2.25e-4	-9.91e-3	0.0224
2b	5.2	469.7	1	900.23	88.924	-10.586	-15.43	1194.6	2.481	2.207	1.5971	1.46e-03	0.0128	0.9259
2b	10.567	469.7	1	900.23	88.808	-11.099	-15.161	1197	2.3715	2.1075	1.6372	1.13e-03	0.0201	0.1407
2b	20.858	469.7	1	900.23	87.183	-11.487	-14.971	1198.8	2.2897	1.9984	1.666	7.97e-04	0.0281	0.2212
2c	7.0167	550.68	1	900.24	67.396	-4.4452	-9.0228	1167.3	4.2331	2.8563	2.8544	4.60e-06	6.71e-5	0.1356
2c	10.4	550.68	1	900.24	67.716	-4.375	-8.749	1167	4.2581	2.8859	2.9229	-8.63e-5	-1.77e-3	0.2185
2c	13.167	550.68	1	900.24	67.62	-4.3482	-8.6161	1166.9	4.2677	2.888	2.9565	-1.60e-4	-4.17e-3	0.2842
2c	21.758	550.68	1	900.24	66.063	-4.1983	-8.2974	116.3	4.3229	2.8557	3.0398	-4.30e-4	-0.0185	0.3551

Table 7. Mean environmental chamber parameters for test 3. Corresponding images can be seen in Figure 38 to Figure 40. $\Delta Time$ represents time elapsed from the initial start of the experiment (i.e. $\Delta T = 0$). An explination of the symbols used is provided in the text at the beginning of the section titled *Mass Flux Results*. The boxed terms reprsents calculated values.

$\boldsymbol{Test\ \#}$	$\boldsymbol{\Delta Time}$ $(\boldsymbol{hour})$	$\boldsymbol{A_{samp}}$ $(\boldsymbol{mm^2})$	$\boldsymbol{u}$ $(\boldsymbol{m/s})$	$\boldsymbol{P_{air}}$ $(\boldsymbol{hPa})$	$\boldsymbol{R.H.}$ (%)	$\boldsymbol{T_{air}}$ $(\boldsymbol{°C})$	$\boldsymbol{T_{ss}}$ $(\boldsymbol{°C})$	$\boldsymbol{\rho_{air}}$ $\boldsymbol{g/cm^3}$	$\boldsymbol{p^{air}_{eqm.vap,liq}}$ $(\boldsymbol{hPa})$	$\boldsymbol{p_{vap}}$ $(\boldsymbol{hPa})$	$\boldsymbol{p^{ss}_{eqm.vap,ice}}$ $(\boldsymbol{hPa})$	$\boldsymbol{F_m}$ $\boldsymbol{g\ m^{-2}s^{-1}}$	$\boldsymbol{\mathcal{M}_{calc}}$ $(\boldsymbol{g})$	$\boldsymbol{\mathcal{M}_{CT}}$ $(\boldsymbol{g})$
3a	6.2667	447.65	1	900.23	73.182	-10.328	-14.406	1193.5	2.5405	1.8731	1.7581	2.75e-4	2.78e-3	0.0151
3a	11.983	447.65	1	900.23	75.89	-10.94	-15.049	1196.3	2.4077	1.8237	1.6585	3.96e-4	7.65e-3	0.0353
3a	23.5	447.65	1	Data Logger Failed No Data										
3b	10.433	367.31	1	900.23	89.594	-13.596	-16.593	1208.5	1.8896	1.6932	1.4326	6.31e-4	8.70e-3	0.1413
3b	21.167	367.31	1	900.23	89.508	-13.545	-16.439	1208.3	1.8986	1.6998	1.4534	5.96e-4	0.0167	0.3028
3c	6.4	414.23	1	900.23	85.3	-11.487	-14.757	1198.8	2.2892	1.9552	1.6993	6.14e-4	5.86e-3	0.0788
3c	13	414.23	1	900.23	85.245	-11.552	-14.715	1199.1	2.2751	1.9412	1.7055	5.66e-4	0.011	0.1285
3c	23.942	414.23	1	900.23	85.375	-11.608	-14.597	1199.3	2.2461	1.9349	1.7243	5.06e-4	0.0181	0.2666

Mass Flux Discussion

The values calculated using the theoretical mass flux equation vary dramatically from the experimental mass flux values calculated from CT scans. The theoretical values consistently underestimate the mass flux and even occasionally predict mass loss when the CT scans and optical images demonstrate clear growth. Several possibilities may account for this error. The most pressing is the lack of detailed wind data. In Equation (17) mass flux is directly proportional to wind speed and is thus quite sensitive to even minor changes in wind speed. Available anemometers proved too bulky to attach to the lab set up (blocking long wave radiation loss from the snow surface) and where not sensitive enough to detect the low velocities at the fan exits. A hand held anemometer was used to take periodic readings of wind speed throughout the course of an experiment. Typical values were 0.75 to 1.5 $m\ s^{-1}$, but would vary as the fans iced up. An average value of 1 $m\ s^{-1}$ was used for the calculated values found in Table 5 through Table 7.

The snow surface presented to the cold ceiling, had an area extent of 30cm x 30cm. Two ducts directed moist air through a nozzle designed to spread the flow evenly across the snow surface. However, through the course of an experiment, the flow was not always perfectly uniform due to icing around the outlet and inside the piping. Consequently, areas of the snow surface would occasionally demonstrate higher growth rates than other areas. This can be seen in the meteorological data as well; the three temperature/relative humidity probes position as depicted in Figure 21 often recorded slightly different readings. Thus, it is possible the CT sample container was positioned such that it received less/more growth than near one of the sensors. This is clearly the

case in test 3a (Figure 38) where CT scans show very little growth, while the pictures show significant growth. Even small variations can cause significant variation in calculated values at the scale of 0.1 to 0.01 of a gram typical in Table 5 through Table 7.

As mentioned in the methodology chapter, the cold ceiling inevitably formed hoar frost on its surface during experiments. It was swept clean by hand approximately every three hours for the full 20 + hour duration of each experiment. Despite these efforts, it is possible small amounts of frost fell from the ceiling and contaminated the snow surface. Contamination is primarily a concern for gathering optical data as the snow from the ceiling often had a distinct appearance that would have been distinguishable to the naked eye had it fallen into the CT sample (Figure 41).

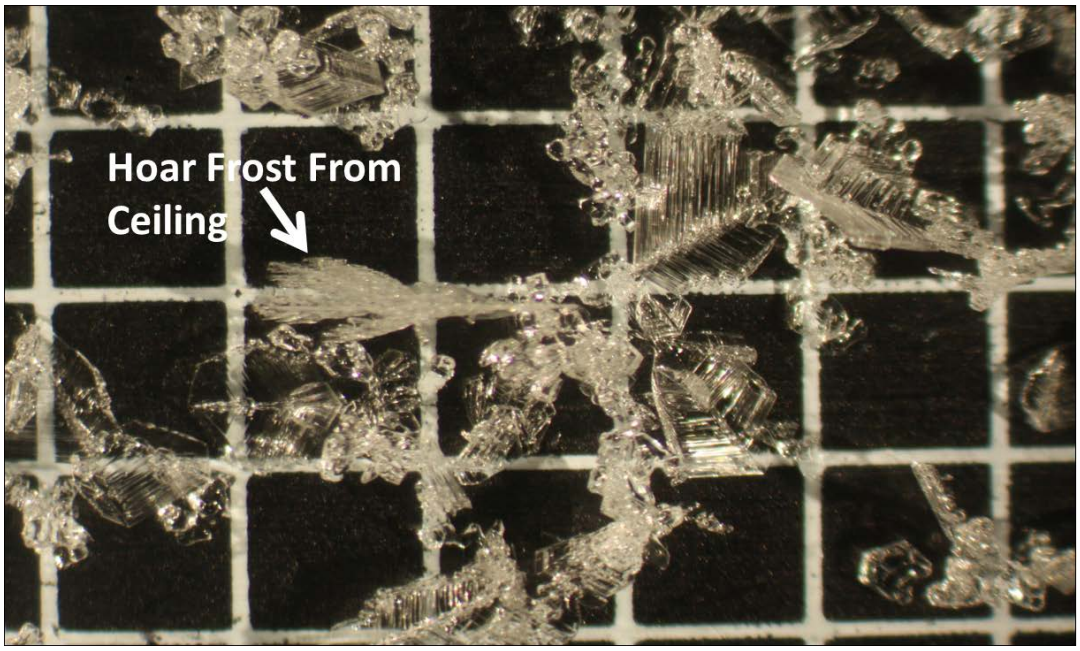


Figure 41. The needle like hoar frost that formed on the cold ceiling at a temperature of $\sim -50°C$ and fell onto the snow surface was often readily apparent compared to the surface hoar due to its different grain morphology.

On a more theoretical level, an additional source of error could lie in the mass transfer coefficient C_Q value. Mass flux is linearly proportional to C_Q and even small changes in it produce substantial differences in calculated mass flux. Of the two empirical estimates [$C_Q = 2.9 \times 10^{-3}$ (Hachikubo, 1997) and $C_Q = 2.3 \times 10^{-3}$ (Morstad, 2004)] presented in chapter 2, the larger value was used for calculations in this paper for the simple reason that it more closely approximated the CT results. Armstrong (2008) suggests calculating C_Q from integrated forms of the surface layer similarity function; however, this involved method required knowledge of a roughness length, values for which vary from study to study by as much as a full order of magnitude (Konstantinov, 1966; Harding, 1986). Finally, as noted earlier, Hachikubo found an increase in C_Q with increasing surface hoar crystal size, with growth occurring quickly once the crystal reached above the 1 mm laminar sublayer. Thus, a single value may not be an appropriate. Additional evidence supporting a changing C_Q value is presented in Appendix D, which examines the effects of parent grain orientation on surface hoar development.

The combined effect of varying wind speed and ambiguity in the mass transfer coefficient, both of which are directly proportional to mass flux, as well as the possibility of the CT sample holder experiencing slightly different atmospheric conditions than the relative humidity/temperature probe several centimeters away, may help explain the discrepancy between measured mass flux and calculated values.

Specific Surface Area Results

As explained in Chapter 2, SSA is the ratio of the surface area of the ice to the total volume of the ice. The well-developed theory of Mie scatter accurately predicts scatter in a medium that contains spherical particles. As such it is advantageous to reduce the complex features of snow crystals to a sphere with an SSA equivalent to that of the original snow grain (Domine et al., 2006). This primarily mathematically construct may share little physical resemblance to the original snow grain but can be used, with reasonable accuracy, to simulate albedo in the NIR and longer wavelengths (Warren 1982 and 1984). However, theoretical studies indicate that grain shape still plays a role in albedo calculations and further study is warranted (Grenfell and Warren, 1999).

Further, according to Picard et all. (2008), the difficulty of measuring SSA means that it is "not systematically measured during field campaigns…and there are only a few studies of the temporal evolution of SSA" (Tailandier et al., 2007). Table 8 presents the temporal change of the SSA of the various surface hoar morphologies depicted in Figure 32 to Figure 40 as calculated from CT scans. The dominant growth axis and snow surface temperature (being the primary factor in determining crystal habit) are presented as well.

Table 8. CT Data: Specific Surface Area (SSA). Scan 0 represents the SSA of the rounded grains before surface hoar growth. The Remaining scans represent the SSA of only the deposited surface hoar. The tests 0-4 correspond to the CT images (left to right) in Figure 32 to Figure 40. $r_{optical}$ is the optically equivialant grain radius for the final SSA measurement.

$\boldsymbol{Test\ \#}$	$\boldsymbol{SSA\ mm^{-1}\ 0}$	$\boldsymbol{SSA\ mm^{-1}\ 1}$	$\boldsymbol{SSA\ mm^{-1}\ 2}$	$\boldsymbol{SSA\ mm^{-1}\ 3}$	$\boldsymbol{SSA\ mm^{-1}\ 4}$	$\boldsymbol{T_{ss}}$ $(°\boldsymbol{C})$	$\boldsymbol{Growth\ Axis}$	$\boldsymbol{r_{optical}\ mm}$
1a	16.4	61.3	41.0			-29.9	C	0.073
1b	15.4	18.8	24.7			-15.5	A	0.121
1c	18.6	54.1	43.4			-8.3	C	0.069
2a	15.3	11.5	14.9	17.8	64.5	-29.7	C	0.047
2b	15.6	13.4	14.4	15.6		-15.0	A	0.192
2c	13.2	22.3	19.7	17.7	20.9	-8.3	C	0.144
3a	31.7	31.0	31.6	28.5		-15.2	A	0.105
3b	23.0	26.6	24.7			-16.4	A	0.121
3c	26.9	31.1	31.4	31.5		-14.6	A	0.095

Specific Surface Area Discussion

The range of values seen in Table 8 (from a minimum SSA of 13.2 to a maximum SSA of 64.5) is within the range of results obtained by Legagneux et al. (2002) and Domine et al. (2006) both of whom used methane gas absorption to predict SSA (see page 52). Further, it can be seen in Table 8 that c-axis dominated growth generally produced the highest SSA values, comparable to Legagneux et al.'s values for newly fallen plates, needles, and columns (57.7 ± 22). Values for SSA(0)—i.e. rounded forms—averaged 19.6 and are comparable to Legagneux et al.'s values for rounded grains which averaged (22.8 ± 7).

For crystals displaying c-axis dominant growth, the initial surface hoar SSA (1) is much greater than for the rounded base snow (0). As surface hoar growth progressed and

the crystals became larger, there was a marked decrease in SSA. The exception to the trend of decreasing SSA in c-axis dominant growth is test 2a. It is believed from environmental chamber data that during the first 12.5 hours of this experiment conditions were not favorable to growth; that is, the surface temperature of the snow never fell below the frost point. This is likely due to researchers entering and leaving the room, thus changing the room's temperature and relative humidity. In the latter half of the growth period (i.e. overnight) there was less activity in the cold chamber. Thus little growth is evident in the first 12.5 hours as evidenced by the CT and microscopic images in (Figure 7). Had growth begun immediately at the start of the experiment, it is expected that test 2a would also have shown a marked increase in SSA followed by decline.

Tests involving a-axis growths generally demonstrated increasing SSA with increasing crystal size. An exception to this is test 3a; however, as can be seen in Figure 38, very little growth occurred on the CT sample container and is not a representative sample. This is also confirmed in Table 7 which shows very small $\mathcal{M}_{CT}$ values. More vexing is test 3c which also bucks the trend for increasing SSA. No explanation is readily apparent for this deviation. A larger sample size might clarify the trends observed here.

The trend of decreasing SSA for c-axis growth and increasing SSA for a-axis growth is interesting and is likely attributed to the resulting crystal shapes. A-axis growth results in large plate like crystals, which have a correspondingly high SSA. Conversely, c-axis growth resulted in needle like crystals that have low SSA.

Optical Properties Results and Discussion

The BRF, obtained from optical tests in this study, is a function of 5 parameters: viewer azimuth ϕ_r and zenith θ_r angle, sun azimuth ϕ_i and zenith ϕ_s angle, and wavelength λ as well as varying for rounded vs. surface hoar grain type. Further, forty-two viewer/incident geometries were utilized during each optical test for each snow type creating a plethora of data. Thus, several methods are used to present the data. A table format with geometries and BRF values shown a wavelength near the center of the visible spectrum (e.g. green light, 510 nm) is provided in Appendix F.

In Figure 42 to Figure 44, plots of all forty-two geometries (each line representing a different lighting and viewing geometry) showing wavelength dependence of BRF values are shown. No legend is provided as it would be impractical for 42 values; however, a discussion follows the plots, which highlights important points.

The polar plots (Figure 46 to Figure 51) show BRF values at 510 nm for each of the three optical tests (3a, 3b, 3c) on a radial axis from BRF values of 0.80 to 0.98. The four plots in each figure represent four sun zenith angles (0, 15, 30, 45°) as detailed in the title of the plot. The angular coordinate represents the viewer azimuth angle while the legend presents observer zenith angle. The legend provides two symbols for 60°—that is $60°_1 \; and \; 60°_2$. This is because at a sun zenith angle of 45° and an observer zenith angle of 60° the spectrometer captured a shadow from the overhead gantry and is thus not directly comparable to the 60° observer zenith angle measurements in other plots. Nevertheless, the shadow affected data is presented as it is comparable between snow grain types and between each of the three tests (3a, 3b, 3c).

Eight primary conclusions are drawn from the data: 1) BRF values are highest in the UV/VIS and drop off in the NIR for all grain types; 2) There is distinct dip in BRF value at the known ice absorption line at 1030 nm for all grain types; 3) In the visible wavelengths the BRF values varied by less than ~17%; 4) There is a distinct increase in the range (and standard deviation) of BRF values between rounded grains and surface hoar, indicating departure from Lambertian scatter with the growth of surface hoar; 5) There is a slight decrease in mean BRF (essentially albedo[10]) in the transition from rounded grains to surface hoar; 6) No distinct pattern concerning the geometry of the maximum and minimum BRF value is evident; 7) There is darkening at large viewing angles and nadir incident angles; 8) Forward-scatter in the solar principal plane is brighter than backward-scatter. Conclusions 4, 5, and 6 provide new insight into the scattering properties of surface hoar, whereas the remaining conclusions serve primarily as a validation of previous optical studies. That these conclusions are congruent with previous studies lends credence to conclusions 4, 5, and 6.

Each of these conclusions is addressed in the following chapter. Lastly, the reader is referred back to Figure 38 through Figure 40 as well as Table 7 for image, mass flux, and SSA data specific to test sequence 3.

Results: Figure 42 to Figure 44
and Table 9 to Table 11

Figure 42 to Figure 44 show BRF as a function of wavelength for all 42 geometries tested. Each line represents a different viewing/lighting geometry. No legend

[10] As mentioned previously, albedo is calculated by integrating BRF values across all hemispherical azimuth and zenith angles. As such the mean BRF values serves as something of a proxy for albedo in that an increase in mean BRF means a proportional increase in albedo.

is provided as it would be impractical. However, the data are still instructive in that they demonstrate some of the basic reflectance features of snow (conclusions 1 through 3 above). Further they demonstrate a distinct spreading of data along the y-axis from rounded grains to surface hoar (conclusion 4). This unique feature indicates a departure from Lambertian scattering as surface hoar develops and is discussed at length following the figures.

Table 9 through Table 11 provide a statistical examination of BRF values at 510 nm (green light)—chosen as a representative wavelength since it is at approximately the center of the visible spectrum. This is a justifiable representative of the behavior of the BRF since values at a given viewer/incident geometry are similar across the visible bandwidth. That is, BRF lines in the plots below do not cross and are relatively flat in the visible spectrum. Therefore, any visible wavelength will demonstrate similar anisotropy in scatter. As discussed in detail following the tables, the distinct features in this set of data are the slight decrease in mean BRF and significant increase in standard deviation and range between initial form and final form (conclusion 6).

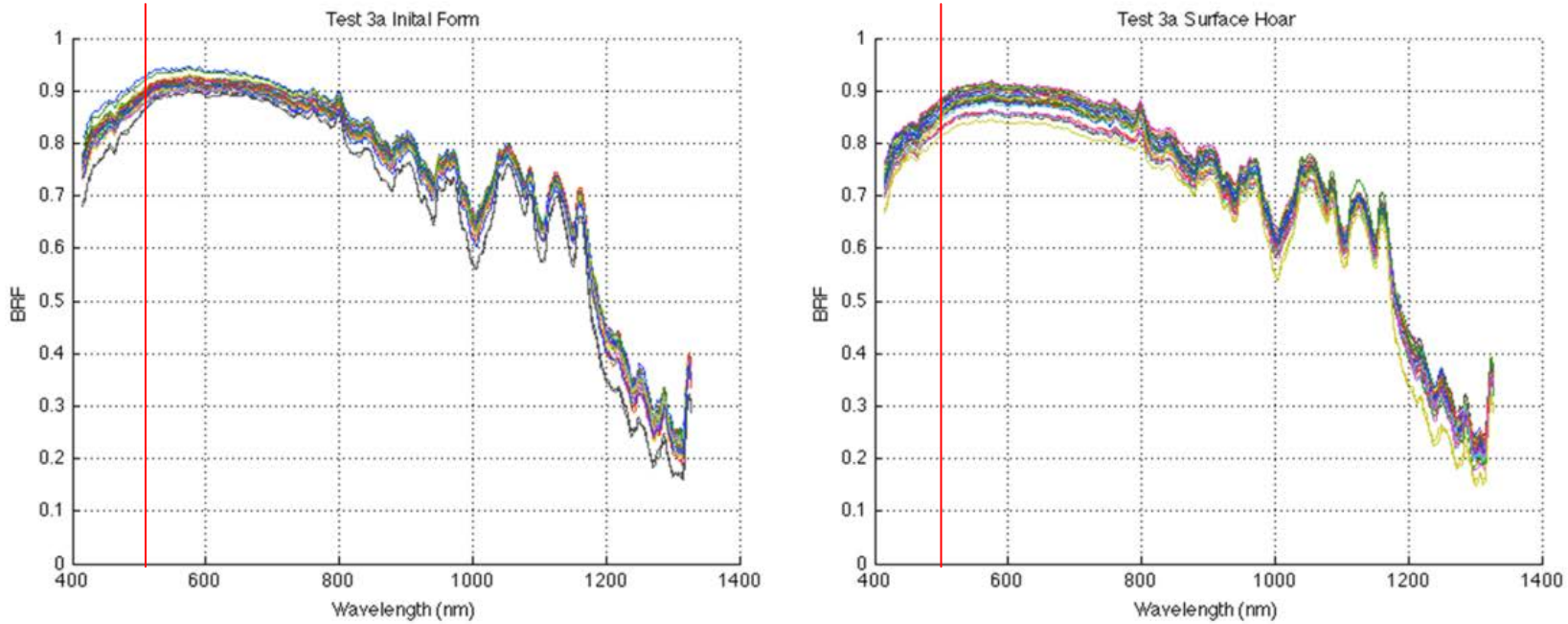


Figure 42. Test 3a. BRF as a function of wavelength. Each line represents a different lighting and viewing geometry. Initial rounded form (left) and surface hoar (right). Red line marks 510 nm.

Table 9. Test 3a. Descriptive statistics for BRF values across all geometries at 510 nm. See also Appendix F.

3a Initial Form	
Mean	0.892
Median	0.891
Standard Deviation	0.013
Range	0.064
Minimum	0.863
Maximum	0.927

3a Final Form	
Mean	0.867
Median	0.867
Standard Deviation	0.019
Range	0.072
Minimum	0.820
Maximum	0.892

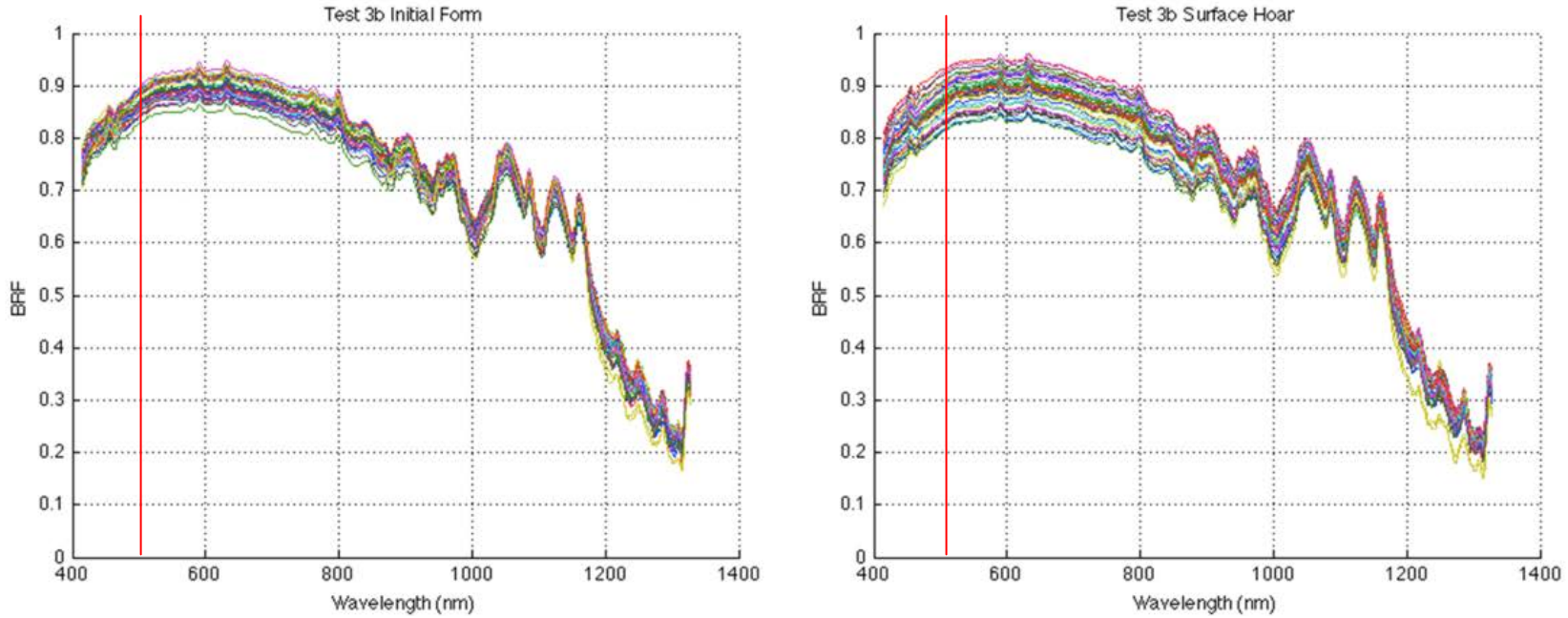


Figure 43. Test 3b. BRF as a function of wavelength. Each line represents a different lighting and viewing geometry. Initial rounded form (left) and surface hoar (right). Red line marks 510 nm.

Table 10. Test 3b. Descriptive statistics for BRF values across all geometries at 510 nm. See also Appendix F.

3b Initial Form	
Mean	0.873
Median	0.870
Standard Deviation	0.018
Range	0.070
Minimum	0.837
Maximum	0.907

3b Final Form	
Mean	0.872
Median	0.873
Standard Deviation	0.031
Range	0.116
Minimum	0.817
Maximum	0.933

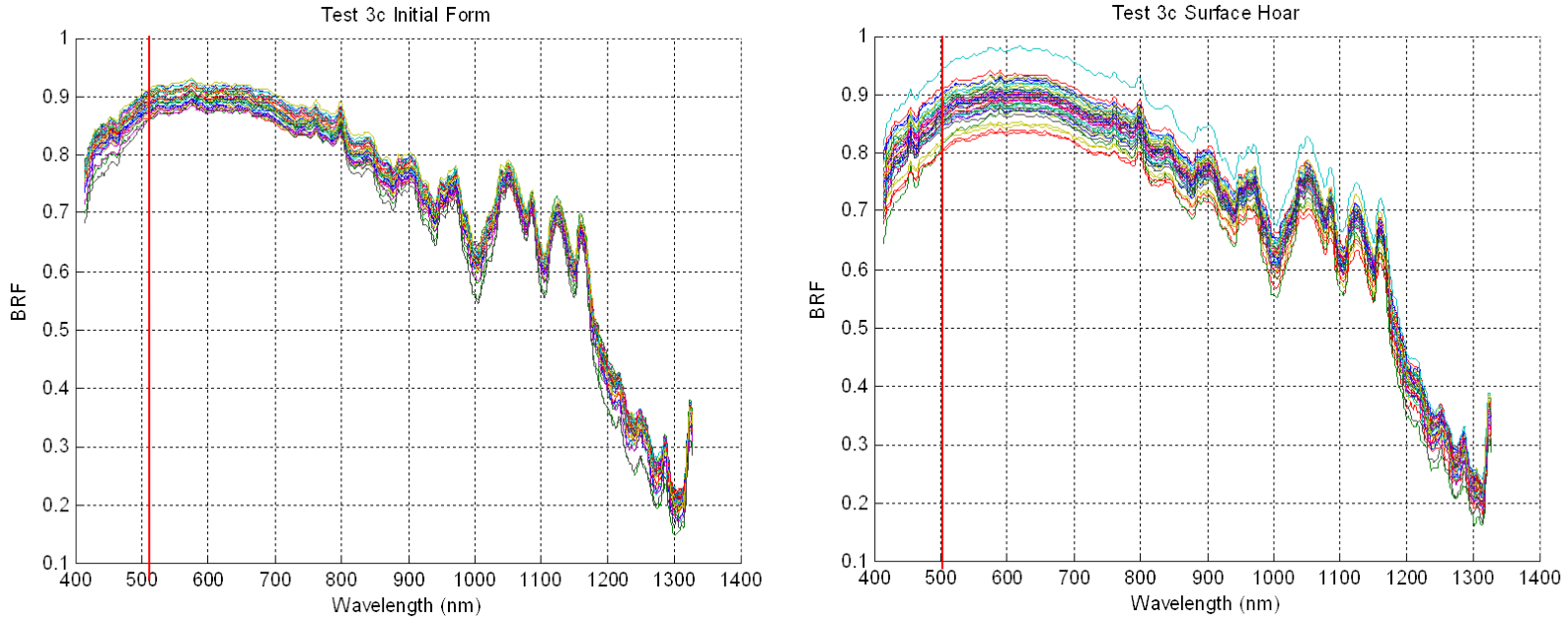


Figure 44. Test 3c. BRF as a function of wavelength. Each line represents a different lighting and viewing geometry. Initial rounded form (left) and surface hoar (right). Red line marks 510 nm.

Table 11. Test 3c. Descriptive statistics for BRF values across all geometries at 510 nm. See also Appendix F.

3c Initial Form	
Mean	0.884
Median	0.886
Standard Deviation	0.014
Range	0.052
Minimum	0.858
Maximum	0.911

3c Final Form	
Mean	0.870
Median	0.873
Standard Deviation	0.028
Range	0.142
Minimum	0.807
Maximum	0.949

Discussion: Figure 42 to Figure 44
and Table 9 to Table 11.

Conclusion 1 and 2. Lending credit to the validity of the measured optical data, Figure 42 to Figure 44 demonstrate high reflectivity in the visible bandwidth with BRF values dropping off distinctly as wavelength increases toward the NIR. This is to be expected since snow is known to be highly reflective in the visible and nearly a perfect absorber in the long wave (Warren and Wiscombe, 1980; Warren et al. 1982). Further, ice has a known absorption band at 1030 nm accounting for the sharp dip in BRF at that wavelength seen in all figures.

Conclusion 3. At 510 nm, the minimum and maximum of BRF values across all data sets/figures was 0.807 to 0.950, a range of 0.142. This corresponds to a 17% variation in BRF regardless of crystal type or viewer/incident geometry. While none of the studies reviewed in Chapter 2 tested the BRF of surface hoar specifically, this finding is consistent with Dumont et al. (2010) who found anisotropy factors (Equation (37)) varied less than 10% out to $1200nm$ for new and rounded snow alike. In comparison, the same study found anisotropy factors in the wavelengths longer than 1200 nm (beyond the range of the instrument used in this thesis) varied by as much as 400% depending on grain type. Likewise, Warren and Wiscombe, 1980 characterize the spectral albedo between 400 and 700 nm as fairly constant with a peak between 400 and 600 nm, consistent with the results in this study.

The predominate theory behind the relatively small variation in BRF in the UV/VIS as compared to the longwave (as described by Warren, 1982) is that the low

absorption of snow in the UV/VIS means that light will likely be scattered from crystal to crystal multiple times before leaving the snow pack at a random angle. In bulk, this causes a Lambertian appearance as the probability of a photon leaving at any given angle is the same for all directions. However, this theory is predicated on the idea that the reflections within the snowpack are random. For scatter from a surface hoar layer with distinct crystal habit, size, and possible preferred orientation, the assumption of random scatter might not hold. According to the data collected in this study, the larger grained surface hoar has far less Lambertian like scatter than the smaller rounded grains. Grain shape plays a critical role in determining the angular distribution of scattered light.

Conclusion 4. In fact, Figure 42 to Figure 44 also reveal that rounded grains and surface hoar have distinctly different BRF signatures at certain incident/viewer geometries. From the initial form (on the left) to the surface hoar form (on the right), there is a distinct spreading of the data along the y-axis. That is, when the data is looked at as a whole, we see a greater range of BRF values for surface hoar than for rounded grains. The range for rounded grains at 510 nm in test 3a was 0.0640 while the range for surface hoar was 0.0722 (a 13% increase). In test 3b it was 0.0699 for rounded grains and 0.1162 for surface hoar (a 66% increase). Finally, for test 3C it was 0.0522 for rounded grains and 0.1422 (a 172% increase). The results are summarized in Table 12.

Table 12. The range of BRF values for each test and the percent change in range between initial form (I.F.) and final form (F.F.). Note that surface hoar tends to have a wider range of BRF values than rounded grains.

Test	BRF Range	% Change
3a I.F.	0.064	12.8%
3a F.F.	0.072	
3b I.F.	0.070	66.3%
3b F.F.	0.116	
3c I.F.	0.052	172.1%
3c F.F.	0.142	

Note that test 3a, which demonstrated the smallest change in BRF range from rounded grains to surface hoar, also experienced very little change in SSA (see Table 8) and very little mass change (primarily evidenced by the CT images in Figure 38). This suggests a link between SSA and BRF values based on grain type in the visible spectrum. Increasing SSA is accompanied by an increase in the brightest points in the hemisphere and decrease in the darkest points in the hemisphere. More succinctly, increasing SSA is accompanied by increasing departure from Lambertian scatter.

Two questions arise: is it possible to distinguish the effects of grain shape and grain size in these plots and is there a discernible pattern in the geometry of surface hoar scatter? The former question is addressed in the following discussion. Subsequent sections address the geometric variation in BRF.

In all three tests, grain size increased between initial form and final from. Test 3b and 3c showed the greatest grain size increase (~5mm as measured by the longest axial length in the microscopic images in Figure 39 and Figure 40) while test 3a showed the smallest change in grain size (~2.5mm, Figure 38). As discussed in the methodology chapter, Warren (1982) suggests, in the NIR, larger gain size means that a photon must

transverse more ice before encountering a diffractive surface and the chance to be ejected from the snowpack. As such it has a higher chance of being absorbed than for small grains where the number of scattering events, and thus the probability of being ejected, is higher. Concisely stated, in the NIR, smaller grains are more reflective than larger grains (Figure 45). This effect is less pronounced in the UV/VIS, where the low abortion of ice makes it less sensitive to grain size.

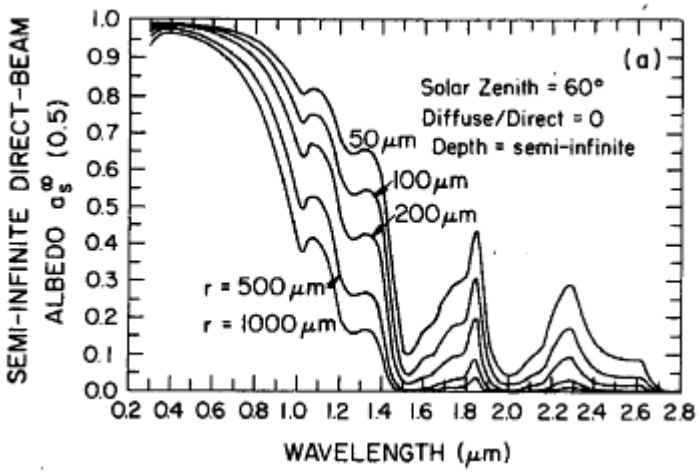


Figure 45. Figure reproduced from Wiscombe and Warren (1980) showing direct beam albedo as a function of wavelength for various grain radii. Note decreasing albedo with increasing grain size in the NIR as well as the nominal effect of grain size in the visible.

Accordingly, at 510 nm (the middle of the visible spectrum) grain size should have less of an effect on the reflectance than in the NIR. Xie et al. (2006) corroborates this conclusion using three different modeling approaches. The increase in range between rounded grains and surface hoar is, therefore, likely a result of crystal habit change rather than grain size.

Conclusion 5. Additionally, if grain size were the only factor determining the BRF values in Figure 42 to Figure 44, from the above theory, one would expect smaller BRF values for surface hoar (the physically larger grain) than for rounded snow (the physically smaller grain). In fact, there is a decrease in *mean* BRF (essentially albedo) between rounded grains and surface hoar. However, the change is generally small ($\leq$ 2.9%). Table 13 summarizes the change in mean BRF from rounded grains to surface hoar.

Table 13. Mean BRF values from tests 3a, 3b, and 3c and percent change from initial form (I.F.) to final form (F.F.) at 510 nm. Note the data indicates a slight decrease in mean BRF (essentially albedo).

Test	Mean BRF	% Change
3a I.F.	0.892	-2.9%
3a F.F.	0.867	
3b I.F.	0.873	-0.1%
3b F.F.	0.872	
3c I.F.	0.884	-1.6%
3c F.F.	0.870	

The decrease in mean BRF is likely accounted for by the increase in grain size. However, accompanying this slight decrease in mean, we see a large increase in the standard deviation—as much as 98.2% (Table 14).

Table 14. Standard deviation and percent change in standard deviation of BRF values from rounded grains to surface hoar in each of the three tests at 510 nm.

Test	Std. Dev.	% Change
3a I.F.	0.013	47.8%
3a F.F.	0.019	
3b I.F.	0.018	69.0%
3b F.F.	0.031	
3c I.F.	0.014	98.2%
3c F.F.	0.028	

Like the increase in range, this increase in standard deviation reflects spreading of the BRF data along the y-axis and cannot simply be accounted for by grain size increase.

In summary, the mean BRF (essentially albedo) is relatively unchanged by the growth of surface hoar demonstrating a slight decrease due to increase in grain size. This change in grain size does not account for the general increase in the range and standard deviation that occurs in the transition from rounded grains to surface hoar. More likely this is due to grain shape and indicates that the bright points get brighter and the dark areas get darker when viewing surface hoar as compared to rounded grains. That is, as surface hoar develops, SSA increases, and the reflected light departs from Lambertian scatter. Having distinguished the role of grain size in this effect, the question now becomes: do these bright points and dark points correspond to predictable viewing/incident geometry?

Results: Figure 46 to Figure 51.

The forgoing discussion examined BRF as a function of wavelength looking for general patterns in reflectance suggesting a broadening of BRF range in the transition from rounded grains to surface hoar with little change in overall albedo. This begs the question, at what geometries do we find the minimum and maximum values and how do they change? Figure 46 through Figure 51 address the lacunae in the previous figures, providing insight into the directional nature of the snow's reflectance. As with the data in Table 9 through Table 11, the plots below are for 510 nm (the center of the visible spectrum and a reasonable representative value for the BRF value in the bandwidth). As noted in the methodology chapter, sun azimuth angle was fixed at $\phi_i = 180°$ in all

experiments and, therefore, in all plots below as well. The upper left, upper right, lower left, and lower right graph in each figure represent, respectively, $\theta_i = 0$ (nadir), 15, 30, 45° sun angles. BRF values are displayed along the radial axis and azimuth angle in the plots represents the azimuth angle from which BRF data was collected.

As discussed following the data, the figures show no discernible geometric pattern in BRF (conclusion 6), darkening near the edges at nadir incident angle (conclusion 7), and a forward-scatter peak along the solar principle plane (conclusion 8).

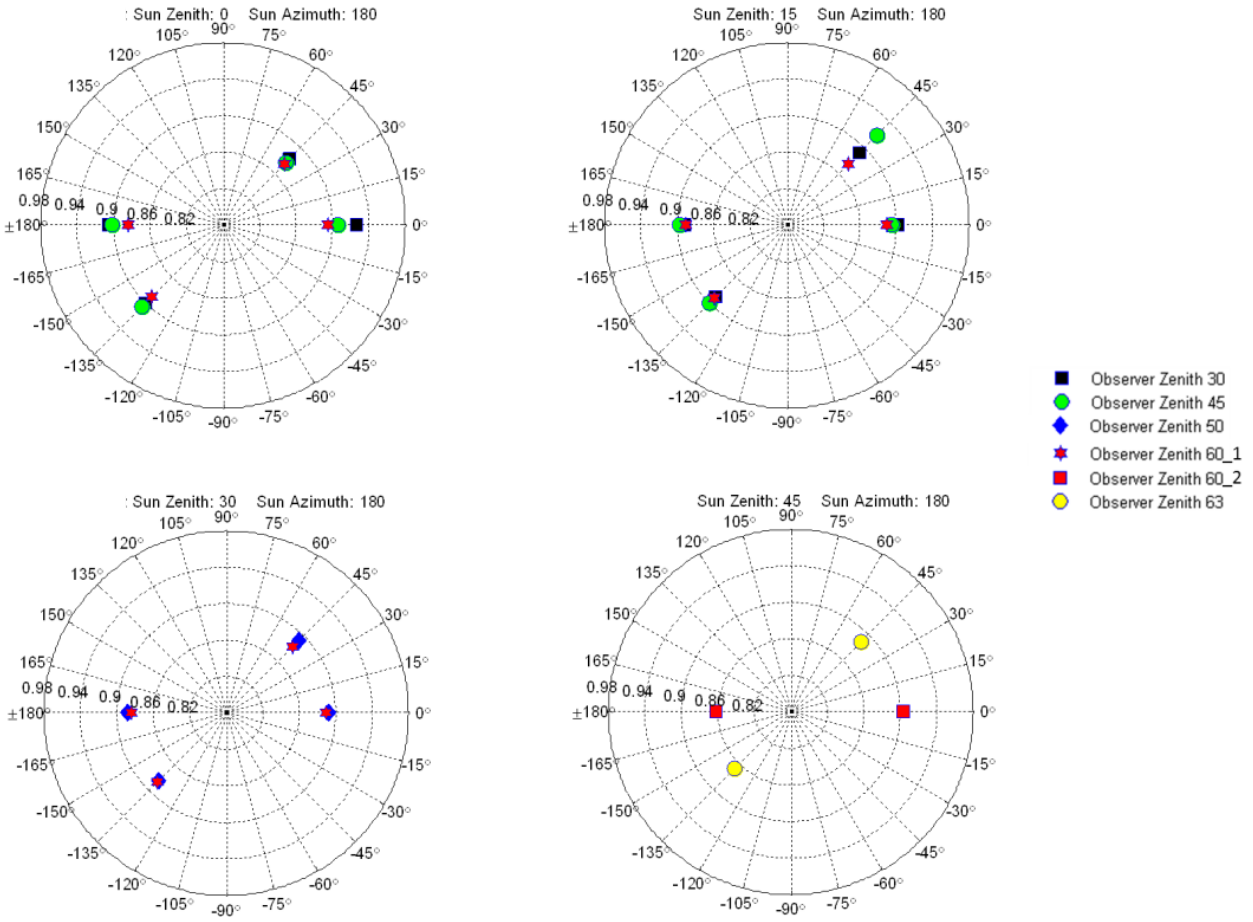


Figure 46. Tests 3a 10-24-12. Initial form BRF results at a wavelength of 510 nm. Radial value represents BRF while angular value represents viewer azimuth angle.

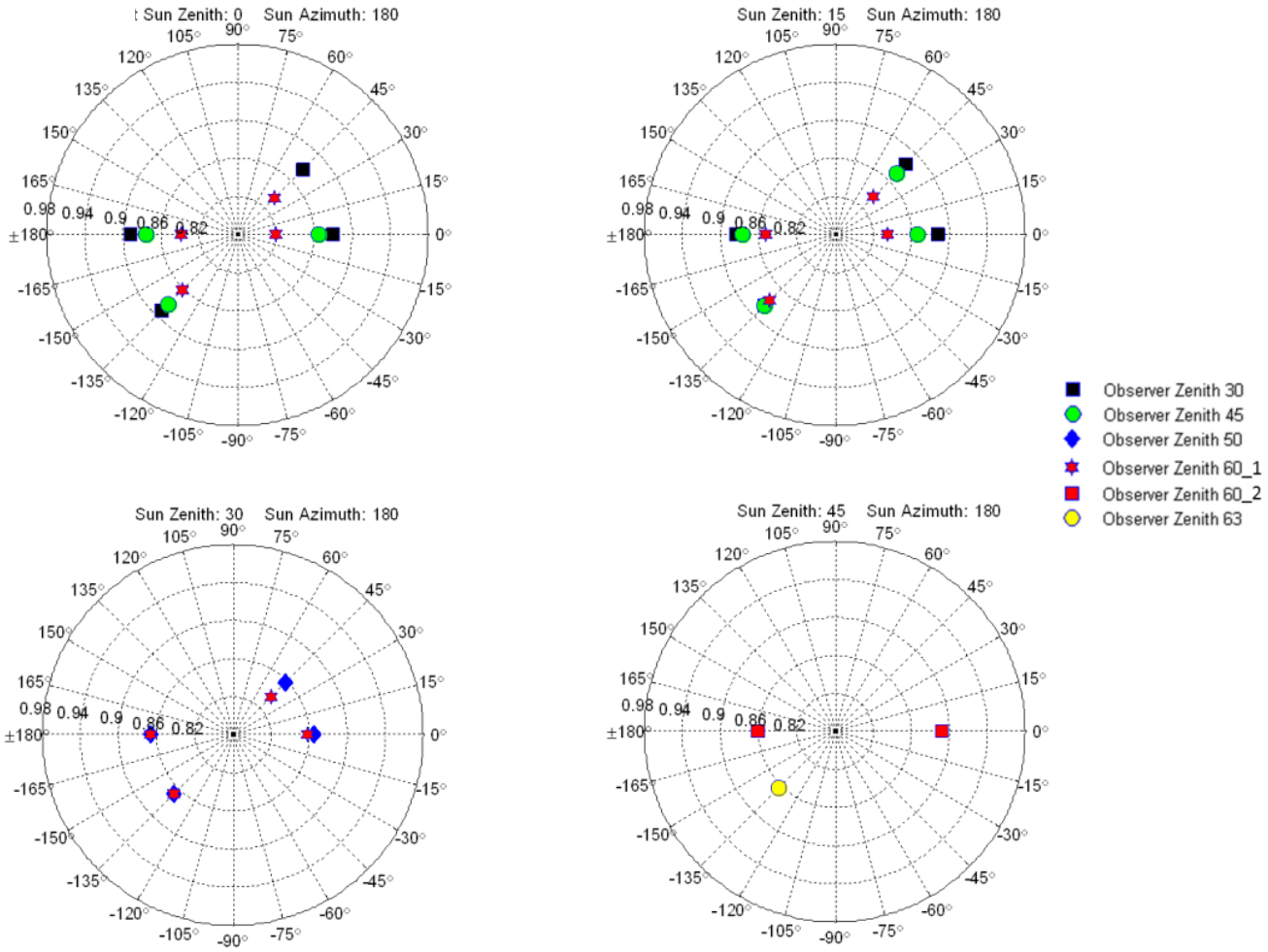


Figure 47. Test 3a 10-24-12. Final form BRF results at a wavelength of 510 nm. Radial value represents BRF while angular value represents viewer azimuth angle.

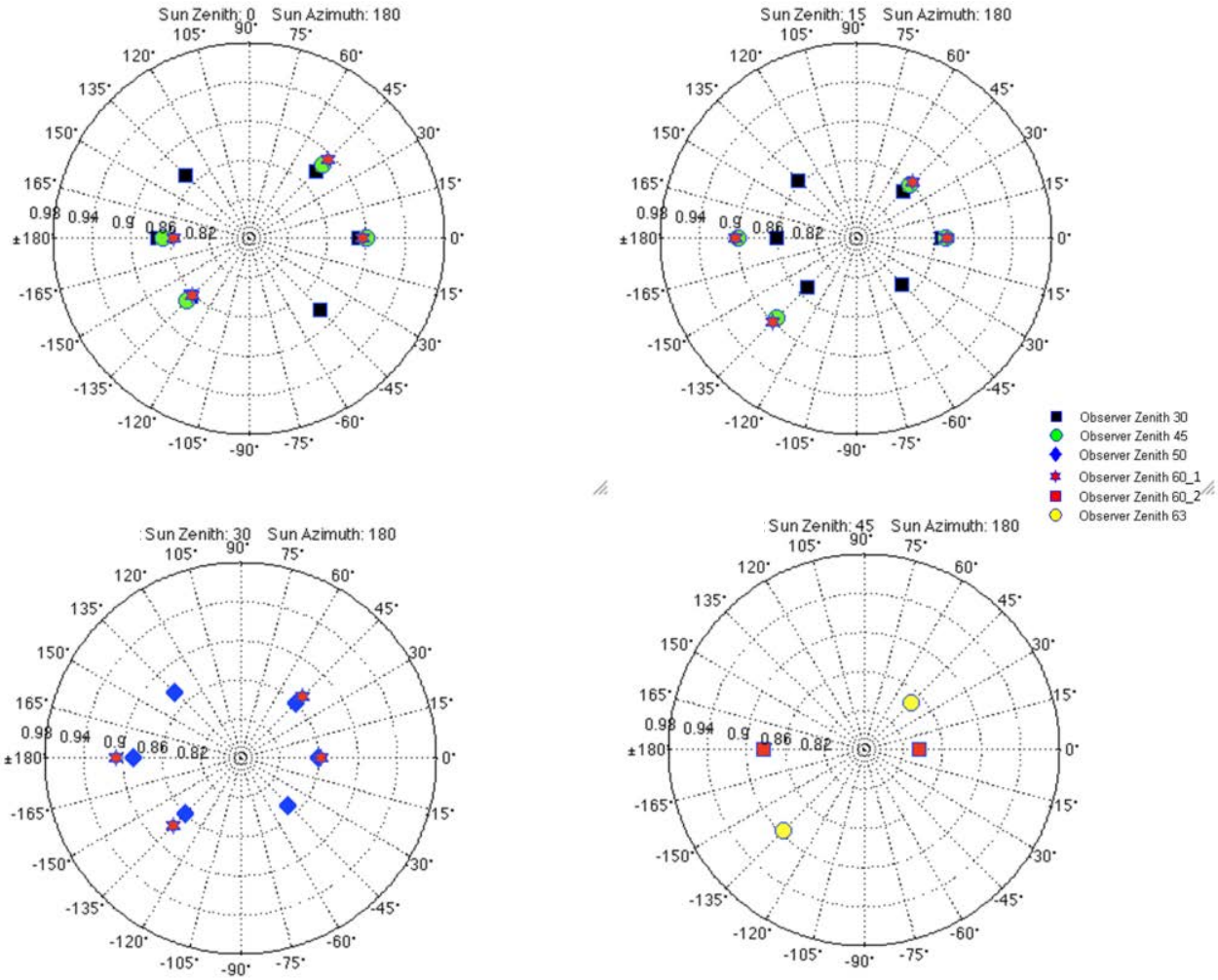


Figure 48. Test 3b 11-15-12. Initial form BRF results at a wavelength of 510 nm. Radial value represents BRF while angular value represents viewer azimuth angle.

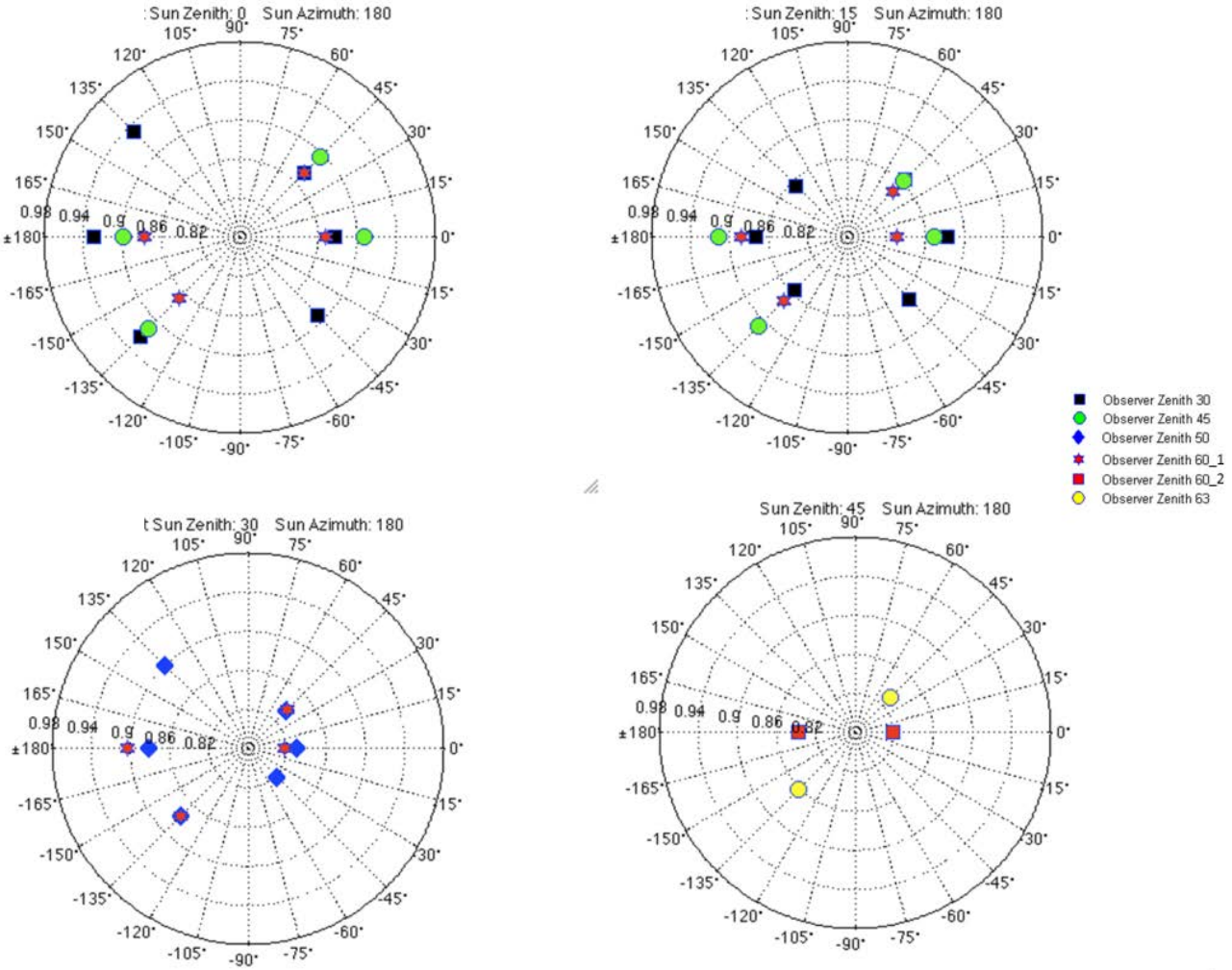


Figure 49. Test 3b 11-16-12. Final form BRF results at a wavelength of 510 nm. Radial value represents BRF while angular value represents viewer azimuth angle.

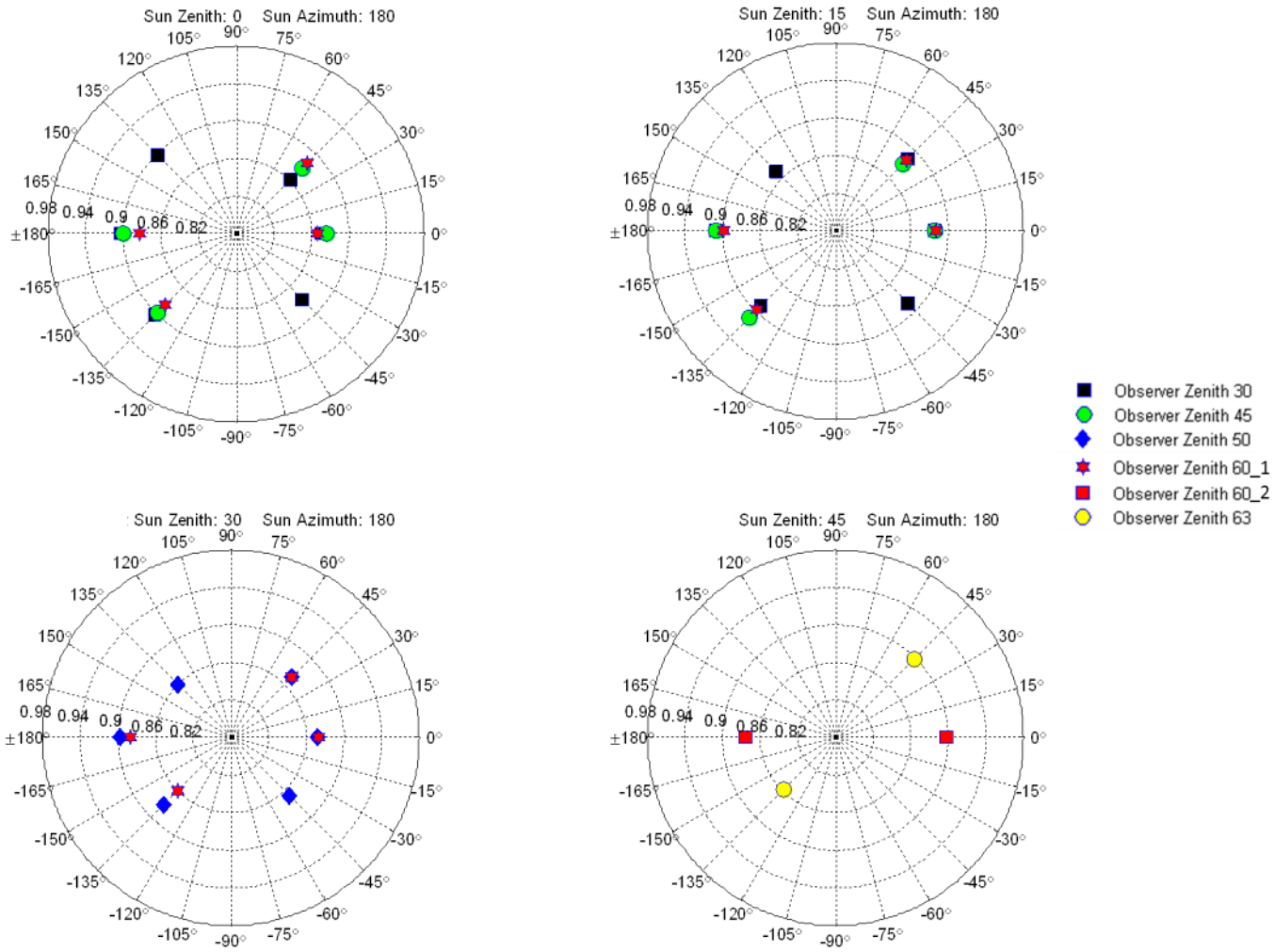


Figure 50. Test 3c 11-28-12. Initial form BRF results at a wavelength of 510 nm. Radial value represents BRF while angular value represents viewer azimuth angle.

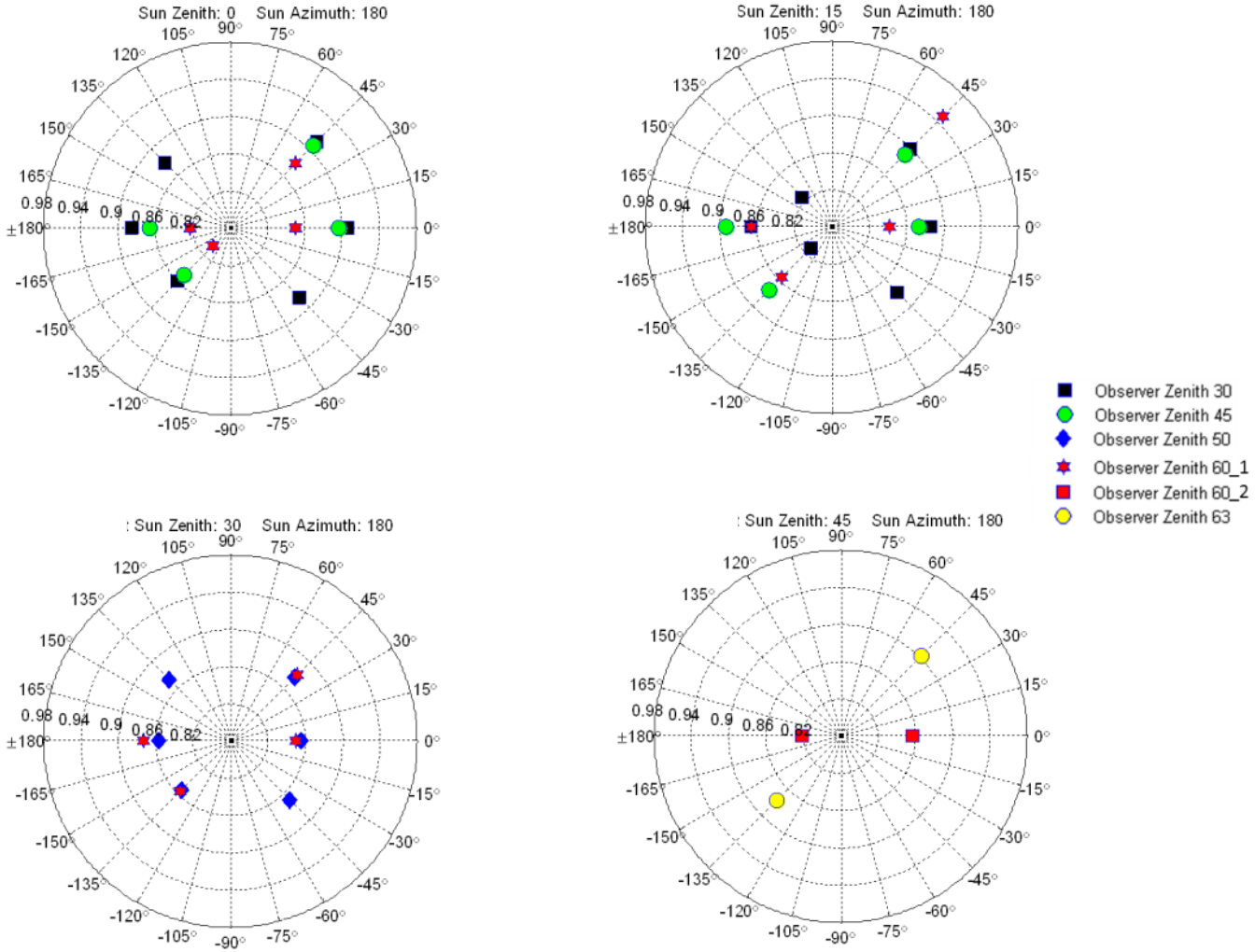


Figure 51. Test 3c 11-30-12. Final form BRF results at a wavelength of 510 nm. Radial value represents BRF while angular value represents viewer azimuth angle.

Discussion: Figure 46 to Figure 51

Conclusion 6. Figure 48 through Figure 51 provide the reader with a general sense of the angular distribution of BRF values. Careful examination shows the maximum and minimum BRF values in each test occur at the geometries indicated in Table 15 and Table 16.

Table 15. Maximum BRF for each test as well as corresponding BRF value and percent change between initial form and final form. A positive sign on the % change indicates an increase in BRF.

Test	Obs Zen	Obs Azm	Sun Zen	Sun Azm	BRF	% Change
3a I.F.	30	0	0	180	0.927	-3.9%
3a F.F.	60	0	45	180	0.892	
3b I.F.	60	180	30	180	0.907	2.8%
3b F.F.	30	135	0	180	0.933	
3c I.F.	45	225	15	180	0.911	4.0%
3c F.F.	60	45	15	180	0.949	

Table 16. Minimum BRF for each test as well as corresponding BRF value and percent change between initial form and final form. A negative sign on the % change indicates an decrease in BRF.

Test	Obs Zen	Obs Azm	Sun Zen	Sun Azm	BRF	
3a I.F.	60	180	45	180	0.863	-5.2%
3a F.F.	60	0	0	180	0.820	
3b I.F.	60	0	45	180	0.837	-2.4%
3b F.F.	60	0	30	180	0.817	
3c I.F.	63	225	45	180	0.858	-6.4%
3c F.F.	60	225	0	180	0.807	

With the notable exception in test 3a in Table 15, which demonstrates a decrease in maximum BRF between rounded grains and surface hoar, the effect of the spreading along the y-axis (i.e. darker darks and lighter lights) can be seen again in the percent change values. The exception in test 3a might be explained by the small amount of

surface hoar growth observed in comparison to the other tests. That is, in Figure 38 the CT scans show significantly less development of surface hoar than in subsequent tests. This single discrepancy aside, the more relevant issue is the random geometries at which these maximum and minimum values occur. That is, there seems to be no discernible pattern predicting where the maximum or minimum bright point will occur spatially. An observer inspecting a field of surface hoar will likely find it brighter or darker at certain viewing angles as compared to rounded snow (which appears more Lambertian), but predicting where those points is not possible with the above data. Nevertheless, a remote sensor mapping BRF values at a variety of angles in the UV/VIS from a field of snow that finds a large range (or standard deviation) in BRF values is likely looking at faceted snow grains.

Conclusion 7. As observed in the upper left hand plot in Figure 46 to Figure 51, i.e. at nadir sun angle, BRF values are lower for observation zenith angles near the horizon ($\theta_r = 60°$) than for observation angles near nadir ($\theta_r = 30°$). In other words, when the data are corrected for the slight breakdown in Lambertian scattering of the Spectralon standard with increasing observer zenith angle, there is a general trend toward darkening at grazing observation angles when the light source is straight overhead. The result is particular apparent in Figure 51. To quantify the effect, Table 17 provides mean BRF values for nadir illumination angle ($\theta_i = 0$) and observer zenith angles moving progressively closer to the horizon ($\theta_r = 30, 45, 60$). The trend toward darkening near large values of observer zenith angle is clear.

Table 17. Mean BRF values for nadir illumination angle θ_i showing darking at grazing observation angles (i.e larger values of θ_r). Initial forms (rounded grains) are shown on the left while finial forms (surface hoar) is shown on the right.

3a Initial Form					3a Final Form			
θ_i	θr	Mean BRF			θ_i	θr	Mean BRF	
0	30	0.903551	Light		0	30	0.885095	Light
0	45	0.897656	↓		0	45	0.869489	↓
0	60	0.886433	Dark		0	60	0.844927	Dark
3b Initial Form					3b Final Form			
θ_i	θr	Mean BRF			θ_i	θr	Mean BRF	
0	30	0.885179	Light		0	30	0.905241	Light
0	45	0.878026	↓		0	45	0.891411	↓
0	60	0.866212	Dark		0	60	0.870778	Dark
3c Initial Form					3c Final Form			
θ_i	θr	Mean BRF			θ_i	θr	Mean BRF	
0	30	0.890872	Light		0	30	0.891979	Light
0	45	0.885928	↓		0	45	0.874903	↓
0	60	0.874625	Dark		0	60	0.834333	Dark

This trend is consistent with Warren (1982) who suggests that, at near nadir sun angles, photons are less likely to escape the snowpack than at grazing incident angles. Dumont et al. (2010) confirmed this prediction postulating that nadir incident light is more likely to penetrate the snow pack. Photons exiting the snowpack from these depths are essentially being fired upward from the bottom of a well that preferentially directs photons. That the effect can be seen in all tests indicates that this is not a function of particle size or shape; rather, it is a general characteristic of the scattering of light by snow. The alignment of the data presented here with previous studies suggests validation of these results.

Conclusion 8. Table 17, above, looks at the change in BRF values as observer angle moves closer to the horizon. This begs the question, what happens as the sun angle moves toward the horizon? Table 18 looks at the directional scatter of light along the

solar principle plane. It provides the mean of all forward-scatter along $\phi_r = 0°$ and all backward-scatter along $\phi_r = 0°$.

Table 18. Mean directional scatter along a in the solar principle plan across all solar zenith angles. In general the trend is for more forward-scatter than backward-scatter with the exception being Test 3c Final Form in which there is almos no difference between forward and backward-scatter.

	Mean Back scatter BRF $\phi_r = 180$	Mean Forward scatter BRF $\phi_r = 0$
3a Initial Form	0.887825765	0.896161501
3a Final Form	0.864744344	0.867937765
3b Initial Form	0.869711208	0.876979881
3b Final Form	0.869280609	0.873298312
3c Initial Form	0.884411503	0.884215748
3c Final Form	0.863136621	0.876282251
	dark →	light

The table shows a general trend toward more forward-scatter than backward-scatter in the solar principle plane in all tests except in test 3c. In this exception to the trend we observer almost no change in BRF between backward- and forward-scatter. No explanation for this exception is readily available. However, the general trend toward more forward-scatter than backward-scatter (as explained on page 56) is reasonably well understood and is consistent with previous studies. Xie et al. (2006) and Mishchenko et al., (1999) suggest that at horizon skimming solar angles, light is less likely to penetrate deeply into the snowpack. Thus, reflection is characterized by single scattering events and heavily dependent upon phase function, which shows a maximum around observer angles equal to zero ($\phi_r = 0$). Dumont et al. (2010) confirmed this with both theoretical and HDRF measurements. In other words, a forward-scatter peak is expected to develop

in the solar principle plane (see page 81) as sun zenith angle increases since the most probable direction that a reflected photon will take is a straight line.

While the data suggests a larger mean BRF in the forward solar principle plane than in the backward principle plan, the exact location of the forward-scatter peak is not apparent. That is, the data does not suggest the maximum BRF occurs at a particular forward reflected zenith angle, nor is there a predictable backward reflected zenith angle for the minimum BRF. In other words, one can expect most of the energy will be scattered in the forward direction of the solar principle plane compared to the backward direction, but the exact geometry of the maximum and minimum zenith angles is unpredictable.

Final Considerations

Anyone who has ever squinted at a field of freshly grown surface hoar on a sunny day is familiar with veritable plethora of crystal faces glinting in the sun light. The observed brightness of the snow is due to the transmissive nature of ice in the UV/VIS and the subsequently high ejection rate of photons from the snow surface. Unobservable to the naked eye, but well documented in previous snow reflectance studies, is the fact that snow is highly absorptive in the NIR and long wavelengths. This trend (conclusion 1), along with a clear dip in BRF values at 1030 nm—a well-known ice absorption line—in all tests (conclusion 2), servers to reinforce observation made in previous studies as well as to provide validation for the data collected in this thesis. Also consistent with previous studies, the BRF values recorded for this thesis varied at most by 17.2% (conclusion 3). This small (relative to NIR and longer wavelengths) variation in BRF

values is consistent with Warren and Wiscombe (1980) and is likely due to multiple scattering events in the snowpack creating Lambertian like appearance.

Conclusions 7 and 8 are also consistent with previous studies and are generally characteristic of snow reflectance regardless of grains size or type. For nadir incident lighting angles, darkening is observed as the viewing angle approaches the horizon (conclusion 7). By way of analogy, this effect is likely explained by imaging a photon fired from the depths of a well (similar to a photon emerging from deep within the snowpack). In this analogy it is easy to imagine the well will preferentially direct photons upward as compared to toward the horizon. Conclusion 8 suggests that there is more energy scattered in the forward direction of the solar principle plane than in the backward direction. This is likely due to the higher probability of specular reflection occurring at grazing incident angles.

Of note are the three remaining conclusions, which suggest an optical signature unique to surface hoar. As surface hoar develops, SSA increases and the reflectance from the snow surface becomes less and less Lambertian (conclusion 4). While there is a slight decrease in overall albedo, likely due to the increase in grain size (conclusion 5), it is not significant enough to account this departure from Lambertian reflectance. Likely grain shape is playing a primary role in the scattering properties of the snow. However, the data suggests that the viewer/incident geometry at which point the BRF value is maximum or minimum cannot be predicted (conclusion 6). That is, while an observer of a field of surface hoar will notice locations at which the snow appears brighter and other locations at which the snow appears darker, the exact positioning of those light and dark

points cannot be predicted. Further, for every dark point observed there will be a corresponding light point somewhere elsewhere in the hemisphere; thus, mean BRF (essentially albedo) changes very little.

CHAPTER 5

CONCLUSIONS AND RECOMMENDATIONS

All truths are easy to understand once they are discovered: the point is to discover them.—Galileo Galilei

Surface Hoar Growth

Significant Findings: Surface Hoar Growth

Central to the natural growth of surface hoar is the cooling of the snow's surface due to longwave energy loss on clear nights. In this study, a methodology for realistically simulating this process was developed in a lab setting. Surface hoar was grown using a temperature controlled cold ceiling to simulate the cold sky. During growth periods, the snow surface temperature averaged ~2-4ºC less than the ambient environmental chamber air temperature, creating the required temperature gradient for vapor deposition and the growth of surface hoar. Protocols for measuring air and snow surface temperature, long- and shortwave energy balance, and vertical temperature profile in the snowpack were established. The onset and growth of surface hoar on an existing snow surface was consistently demonstrated.

In addition, the time history of surface hoar growth at three different snow surface temperatures was documented using both CT and optical microscopic imagery. The results show the three-dimensional development over time of needle like crystals at snow surface temperatures of -8ºC and -29ºC and the development of large feathery crystals at -15ºC. These results are consistent with studies of crystal habits grown using fiber as a

nucleation point. Finally, CT data allowed the tracking of the temporal evolution of SSA during surface hoar growth. This data was compared to optical tests and it was determined that increasing SSA is associated with a departure from Lambertian scattering properties.

Suggestions for Future Work: Surface Hoar Growth

In future studies, it would be useful to incorporate accurate wind speed measurements in the suit of instrumentation recording every thirty seconds. This would improve mass flux calculations. Also, while the CT scanner provides useful information about specific surface area as well as plethora of other information, it might not be the best instrument to measure mass growth rates. A central challenge to this method is the ability to collect relative humidity, snow surface temperature, and air temperature at the exact same point where the CT sample is positioned all without compromising the view factor of the snow to the cold ceiling. If point specific data is need this challenge must be addressed directly. However, if mass flux data is needed as an average across the entire surface of the snow sample, a sensitive scale underlying the box containing the snow sample could more accurately measure the small changes in mass as a result of deposition. Finally, a water heater, with a tighter tolerance than the one used in this study might help to control humidity fluctuations over the snow surface.

With a methodology now in place for growing various surface hoar morphologies, further study could easily build up the work presented in Appendix D which explores the role of parent grain in axial orientation of newly developed surface hoar. Observational evidence suggested that crystal growth in the assumed laminar sublayer behaved

differently than growth extending beyond the 1mm sublayer height. Careful mass flux observations a well as CT scans during and up to the growth of 1mm grains might reveal an accurate mass transfer coefficient as a function of grain size as well as a detailed understanding of the role of parent grain. Additional work in this area has been done by Adams and Miller (2003) and Miller and Adams (2009). Finally, the techniques reported here could be used in other studies examining bulk properties and fracture properties of surface hoar.

Optical Properties of Snow

Significant Findings: Optical Study

Radiative transfer models require accurate bidirectional data against which results can be validated. Bidirectional studies of snow in a natural setting are limited by diffuse atmospheric data and typically report HDRF data. Further, to this author's knowledge, no study has directly addressed surface hoar reflectance. To address this lacuna, bidirectional-reflectance factors (BRF) values were recorded for 42 different forward and backward-scattering lighting and viewing geometries for both rounded grains and surface hoar in a lab setting.

Eight primary conclusions are drawn from the data: 1) BRF values are highest in the UV/VIS and drop off in the NIR for all grain types; 2) There is distinct dip in BRF value at the known ice absorption line at 1030 nm for all grain types; 3) The variation in BRF in the UV/VIS is significantly less pronounced than in the NIR and longer wavelengths; 4) There is a distinct increase in the range (and standard deviation) of BRF values between rounded grains and surface hoar, indicating departure from Lambertian

scatter with the growth of surface hoar; 5) There is a slight decrease in mean BRF (essentially albedo) in the transition from rounded grains to surface hoar; 6) No distinct pattern concerning the geometry of the maximum and minimum BRF value is evident; 7) There is darkening at large viewing angles and nadir incident angles; 8) Forward-scatter in the solar principal plane is brighter than backward-scatter.

Arguably the most important optical finding in this study is that presented in Figure 42 to Figure 44 where, from the initial form (on the left) to the surface hoar form (on the right), there is a distinct spreading of the BRF data along the y-axis. That is, when the data is looked at as a whole, one sees a greater range of BRF values for surface hoar than for rounded grains (conclusion 4). This portends an optical signature unique to surface hoar that is apparent in the visible wavelength. The small decrease in albedo that occurred with the growth of surface hoar is likely attributed to the increase in grain size and does not explain the change in range of BRF values during growth. Rather this effect is likely due to changes in crystal habit. Further, the growth of surface hoar was generally accompanied by a corresponding increase in SSA as seen in Table 8. In general as SSA increase the reflectance of the snow became less and less Lambertian. However, exploration of the directional nature of scatter revealed that the incident/viewing geometry at which the maximum and minimum BRF values were found was not predictable (conclusion 6).

Suggestions for Future Work: Optical Study

Previous optical studies addressing the BRF of surface hoar specifically are not available, likely because, until now, there was no consistent way to grow surface hoar in

a lab setting. Capturing an ephemeral surface hoar event in nature and performing a well-organized study in the variable conditions of atmospheric lighting is difficult at best. There is therefore no study with which these results can be directly compared. Interpretation of the results is thus subjective speculation. Additional experiments rounding out the data set would help to reveal patterns and provide a statistical basis for understanding the observations. The primarily limitation to achieving this in this thesis was the cumbersome process of recording data manually. For accurate, high resolution results, the process outlined in the methodology section needs to be automated. That is, an automated goniometer would allow for the highly repetitions measurements to be made quickly and in bulk without the danger of human error. Additionally, the problem of hoar frost growing onto the cold ceiling and falling into the sample, while solved by hand sweeping the ceiling, meant that each experiment required round the clock supervision during surface hoar growth during the 24 hours of growth typical in each test. Solving this problem would eliminate the possibility of sample contamination and greatly improve the efficiency of the testing process.

In addition, Warren (1982), Xie (2006) and Dumont et al. (2010) demonstrated that much of the optically interesting aspects of snow BRF occur in the wavelengths longer than 1.2 μm, suggesting that directional reflectance in the UV/VIS is close to Lambertian. The small range of BRF values determined in this thesis support this claim. Extending the range of the spectrometer into the farther into long wave will likely provide insight into how surface hoar behaves during single scatter reflectance. Incorporating a hyperspectral camera in the wavelength between 0.2 and 3 μm would

provide a means for capturing the spatial variability of the BRF on a pixel by pixel basis. Finally, the last step is application of BRF data to air and space born remote sensing systems. Obvious questions arise concerning detecting snow grain habit in variable terrain settings with trees, rocks and other obstructions cluttering the FOV.

REFERENCES CITED

Adams, E.E. and D. Miller (2003). "Ice crystals grown from vapor onto an orientated substrate: application to snow depth-hoar development and gas inclusions in lake ice." *Journal of Glaciology* **49:** 8-12.

Adams, E.E., L.R. McKittrick, A.R. Curran, D.S. Levanen, and P. Gauer (2004). "Modeling snow temperature in complex topography." International Symposium on Snow Monitoring Avalanches, Manali, India.

Adams, E.E. and R.L. Brown (1983). "Metamorphism of dry snow as a result of temperature gradient and vapor density differences." *Annals of Glaciology* **4:** 3-9.

Adams, E.E. and R.L. Brown (1988). "On the effect of strong density layering on metamorphism of seasonal snowcover." *Proceeding of the 1988 International Snow Science Workshop*, Whistler, British Columbia, 37-40.

Adams, E.E. and R.L. Brown (1990). "A mixture theory for evaluation heat and mass transport processes in nonhomogeneous snow." *Continuum Mechanics and Thermodynamics* **2:** 31-63.

Ahrens, D.C. (2007). Meteorology today: an introduction to weather, climate, and the environment (8^{th} ed.). Cengage Learning.

Akitaya, E. (1974). "Studies on depth hoar." *Contribution from the Institute of Low Temperature Science, Series A:Physical Sciences* **26:** 1-67.

Anderson, G.P., A. Berk, P.K. Acharaya, L.S. Bernstein, S.M. Alder-Golden, J. Lee, and L. Muratov, (2009). "Reformulated atmospheric band model method for modeling atmospheric propagation at arbitrary fine spectral resolutinoa nd expanded capabilities." U.S. Patent #7593835, issued September 22, 2009.

Aoki, T., T. Aoki, M. Fukabori, A. Hachikubo, Y. Tachibana, and F. Nishio (2000). "Effects of snow physical parameters an spectral albedo and bidirectional reflectance of snow surface." Journal of Geophysical Research **105:**10219-10236.

Arya, Pal S (2001). Introduction to Micrometeorology. San Diego, CA., Academic Press.

Armstrong, R and E. Brun (1985). *Metamorphism in a subfreezing, seasonal snowcover: The role of thermal and vapor pressure conditions*. Ph. D. thesis, University of Colorado.

Armstrong, R. and E. Brun (2008). Snow and climate: physical process, surface energy exchange, and modeling. Cambridge University Press.

Aspen Expeditions. (2011). Figure 1 photo credit. http://www.aspenexpeditions.com/blog/wp-content/uploads/2011/12/Buried-Surface-Hoar.jpg

Atkins, P.W. (1990). Physical Chemistry (4th ed). New York. W.H. Freeman and Company

Babin, S.M. (2000). "Water vapor myths: a brief tutorial." http://www.atmos.umd.edu/~stevenb/vapor/

Barkstrom, B.R. (1972). "Some effects of multiple scattering on the distribution of solar radiation in snow and ice." *Journal of Glaciology* **11:** 357-368.

Barkstrom, B.R. and C.W. Querfeld (1975). "Concerning the effect of anisotropic scattering and finite depth on the distribution of solar radiation in snow." *Journal of Glaciology* **14:** 107-124.

Berger, R.H. (1979). "Snowpack optical properties in the infrared." *CRREL Report* 79-11, U.S. Army Cold Regions Research and Engineering Laboratory, Hanover, N.H.

Birkland, K.W. (1998). "Near-surface faceted crystals formed by diurnal recrystallization: a case study of weak layer formation in the mountain snowpack and its contribution to snow avalanches." *Artic and Alpine Research* **30:** 200-204.

Bohren, C.F. and B.R. Barkstrom (1974). 'Theory of the optical properties of snow." *Journal of Geophysical Research* **79:** 4527-4535.

Bourgeois, C.S., P. Calanca, and A. Ohmura (2006). "A field study of the hemispherical directiona reflectance factor and spectral albedo of dry snow." *Journal of Geophysical Research* **111:** 1-13.

Bruegge, C.J., J.V. Martonchik, and A.H. Strahler (2000). "A review of reflectance nomenclature used in remote sensing." *Remote Sensing Reviews* **19:** 9-20.

Buck, A.L. (1981). "New equations for computing vapor pressure and enhancement factor." *Journal of Applied Meteorology* **20:** 1527-1532.

Chandrasekhar, S. (1960). Radiative transfer. New York, Dover.

Colbeck, S. (1980). "Thermodynamics of snow metamorphism due to variations in curvature." *Journal of Glaciology* **26:**45-61.

Colbeck, S. (1988). "On the micrometeorology of surface hoar growth on snow in mountainous area." *Boundary-Layer Meteorology* **44:** 1-12.

Dalton, John (1808). A new system of chemical philosophy. London. ISBN 1-153-05671-2.

Domine, F. R. Salvatori, L. Legagneux, R. Salzano, M. Fily, R. Cassacchia (2006). "Correlation between the specific surface area and the short wave infrared (SWIR) reflectance of snow." *Cold Regions Science and Technology* **46:** 60-68.

Dozier, J. and T.H. Painter (2004). "Multispectral and hyperspectral remote sensing of alpine snow properties." *Annual Review of Earth and Planetary Science* **32:** 465-94.

Dumont, M., O. Brissaud, G. Picard, B. Schmitt, J.C. Gallet, and Y. Arnaud. (2010). "High-accuracy measurements of snow bidirectional reflectance distribution function at visible and NIR wavelengths—comparison with modeling results." *Atmospheric Chemistry and Physics*. **10:** 2507-2520.

Dunkle, R.V. and J.T. Beavans (1956). "An approximate analysis of the solar reflectance and transmittance of snow cover." *Journal of Meteorology* **13:** 212-216.

Fierz, C., R. Armstrong, Y. Durand, P. Etchevers, E. Greene, D. McClung, K. Nishimura, S. Satyawali and P.K. Sokratov (2009). The international classification for seasonal snow on the ground. Technical documents in Hydrology, 83.

Frei, A. and D.A. Robinson (1999). 'Northern hemisphere snow extent: Regional variability1972-1994." *International Journal of Climatology*, **19:** 1535-1560.

Fukuzawa, T. and E. Akitaya,(1993). "Depth-hoar crystal growth in the near surface layer under high temperature gradient." *Annals of Glaciology* **18:** 39-45.

Gow, A. J. (1965) "On the accumulation and seasonal stratification of snow at the south pole." *Journal of Glaciology* **5:** 467–477.

Gray, D. and D. Male (1981). Handbook of Snow. Pergamon Press Canada.

Greene, E., K. Birkeland, K. Elder, G. Johnson, C. Landry, I. McCammon, M. Moore, D. Sharaf, C. Sterbenz, B. Tremper, and K. Williams (2010). Snow, weather, and avalanches: observational guidelines for avalanche programs in the United States: American. Pagosa Springs, CO., Avalanche Association.

Grenfell, T. and S. Warren (1999). "Representation of a nonspherical ice particle by a collection of independent spheres for scattering and absorption of radiation." *Journal of Geophysical Research* **104:** 18669–18684.

Hachikubo, A. and Akitaya, E. (1997). Effect of wind on surface hoar growth on snow. *Journal of Geophysical Research*. **102:** 4367-4373.

Hallet, J. and B.J. Mason (1958). "The influence of temperature and supersaturation on the habit of ice crystals growth from the vapor." *Proceedings of the Royal Society of London Series A: Mathematical and Physical Science* **247:** 440-453.

Harding, R.J. (1986). Exchanges of energy and mass associated with a melting snow pack. In Modeling Snowmelt-Induced Process (ed Morris, E.M.). IAHs PublicationNo. 155. Wallingford: IAHS Press, pp 3-15.

Hobbs, P.V. (1974). Ice Physics. Oxford: Claredon Press.

Incropera, F. and D. Dewitt (2007). Fundamentals of Heat Transfer (6^{th} ed.). John Wiley & Sons.

Jin, Z., T.P. Charlock, P. Yang, Y. Xie, and W. Miller (2008). "Snow optical properties for different particles shapes with application to snow grain size retrieval and MODIS/CERES radiance comparison over Antarctica." *Remote Sensing of Environment* **112:** 3563–3581.

Kobayashi, T. (1961). "The growth of snow crystals at low supersaturation." *Philosophical Magazine* **6:** 1363-1370.

Kokhanovsky, A.A. and E.P. Zege (2004). "Scattering optics of snow." *Applied Optics* **43:** 1589-1602.

Konstantinov, A.R. (1966). "Isparenie v Prirode." Leningrad: Gidrometeoizdat. Published 1968 as "Evaporation in Nature." (English translation by Israel Programme for Scientific Translation, Jerusalem.)

Kuroda, T. (1983). "Recent developments in theory and experiment of growth kinetics of ice crystals from the vapour phase and their growth forms." *Journal of Crystal Growth* **65:** 27-35.

Kuroda, T. (1986). "Growth forms of snow crystals." *Science on form: proceedings of the first international symposium for science on form*. The Institute of Low Temperature Science, Sapporo, Japan, Hokkaido University

LaChapelle, E.R. and R.L. Armstrong (1977). Temperature patterns in an alpine snowcover and their influence on snow metamorphism. US Army Research Office.

Lang, R., B. Leo, and R. Brown (1984). "Observations on the growth process and strength characteristics of surface hoar." *International Snow Science Workshop Proceedings*. Aspen, CO.

Leroux, C., j.L. Deuze, P. Goloub, C. Sergent, and M. Fily (1998). "Ground measurements of the polarized bidirectional reflectance of snow in the near-infrared spectrum domain: comparison with model results." Journal of Geophysics Research **103:** 19721-19731.

Legagneux, L., A. CAbanes, and F. Domine (2002). "Measurements of the specific surface area of 176 snow samples using methane absorption at 77K." Journal of Geophysical Research, **107:** 1-15.

Li, S., & X. Zhou (2004). "Modeling and measuring the spectral bidirectional-reflectance factor of snow-covered sea ice: An intercomparison study." *Hydrology Processes* **18:** 3559−3581.

Libbrecht, K.G. (1999). "Snowcrystals.com". California Institute of technology. http://www.its.caltech.edu/~atomic/snowcrystals/

Libbrecht, K.G. (2001). "Morphogenesis on ice: the physics of snow crystals." *California Institute of Technology: Engineering and Science* **64:** 10-19.

Libbrecht, K.G. (2005). "The physics of snow crystals." *Reports on Progress in Physics*. Institute of Physics Publishing **68:** 855-895. doi:10.1088/0034-4885/68/4/R03.

Linkletter, G. and J. Warburton (1976). "A note on the contribution of rime and surface hoar to the accumulation of the ross ice shelf, antartica." *Journal of Glaciology* **17:** 351-353.

Magono, C. and C. W. Lee (1966), "Meteorological classification of natural snow crystals." *Journal of the Faculty of Science*. Hokkaido University.

McClung D. and P. Schaerer (2006). The Avalanche Handbook. Seattle, WA., The Mountaineers Books.

Miller, D.A. and E.E. Adams (2009). "A microstructural dry-snow metamorphism model for kinetic crystal growth." *Journal of Glaciology* **55:** 1003-1011.

Mobley, C. (2013). "The Lambertion BRDF." Ocean Optics Web Book. http://www.oceanopticsbook.info/view/radiative_transfer_theory/level_2/the_lambertian_brdf. Accessed Feb11, 2013.

Morstad, B.W. (2004). "Analytical and experimental study of radiation-recrystalized near-surface faces in snow," Ph.d. thesis, Montana State University.

Nakaya, U. (1954). Snow crystals: natural and artificial. Cambridge, Mass., Harvard University Press.

Nicodemus, F.E., J.C. Richmond, J.J. Hsia, I.W. Ginsberg, and T. Limperis (1977). "Geometrical considerations and nomenclature for reflectance." NBS Monograph 160, National Bureau of Standards, US Department of Commerce, Washington, D.C.

Nolin, A.W. and J. Dozier (2000). “A hyperspectral method for remotely sensing the grain size of snow.” *Remote Sensing of Environment* **74:** 207−216.

Nyberg, A. (1939). ‘Temperature measurements in an air layer very close to a snow surface.” *Statens Meteorologik-Hydrografiska Anstalt*, Meddelanden Serien Uppsatser **27:** 234-275.

O’Brien, H.W. and R.H. Munis (1975) “Red and near-infrared spectral reflectance of snow.” *CRREL Resource Report* 332, U.S. Army Cold Regions Research and Engineering Laboratory, Hanover, N.H.

Painter, T. H. and J. Dozier (2004). “Measurements of the hemispherical–directional reflectance of snow at fine spectral and angular resolution.” *Journal of Geophysical Research* 109(D18), D18115. doi:10.1029/2003JD004458.

Pauling, L. (1970). General Chemistry. New York. Dover Publications Inc.

Perrot, P. (1998). A to Z of Thermodynamics. Oxford University Press, USA. ISBN 0198565569.

Perry, R.H. and Green, D.W. (Editors) (1997). Perry's chemical engineers' handbook (7th Edition ed.). McGraw-Hill. ISBN 0-07-049841-5.

Petty, G.W. (2006). A first course in atmospheric radiation. Madison, WI., Sundog Publishing.

Picard, G., L. Arnaud, F. Domine, M. Fily (2008). “Determining snow specific surface area from near-infrared reflectance measurements: numerical study of the influence of grain shape.” *Cold Regions Science and Technology* **56:** 10-17.

Raoult, F.M. (1887). General law of the vapor pressure of solvents. Comptes Rendus **104:** 1430-3 [as translated and published by Henry M. Leicester & Herbert S. Klickstein, A source book in chemistry 1400-1900 (Cambridge, MA: Harvard, 1952)].

Schaepman-Strub, G., M.E. Schaepman, T.H. Painter, S. Dangel, J.V. Martonchik (2006). “Reflectance quantities in optical remote sensing—definitions and case studies.” *Remote Sensing of Environment*. **103:** 27-42.

Schertzer, R.H. (2011). “Fabric tensors and effective properties of granular materials with application to snow”, Ph.D. thesis, Montana State University.

Shaw, J. (2012). Remote Sensing Systems Class Notes. Bozeman, MT. Montana State University. http://www.coe.montana.edu/ee/jshaw/classes/rss_s12.htm

Shea, C. and B. Jamieson (2011). "Sun effect on surface hoar illustrated by three case studies." Cold Regions Science and Technology **68:** 99-105.

Sinnot, R.K. (2005). Chemical engineering design (4th Edition ed.). Butterworth-Heinemann. ISBN 0-7506-6538-6.

Stamnes K. S.C. Tsay, W. Wiscombe, K. Jayaweera (1994). "Numerically stable algorithm for discrete-ordinate-method radiative transfer in multiple scattering and emitting layered media.:" *Applied Optics* 27: 2502-2509.

Stull, R.B. (1988). An introduction to boundary layer meteorology. Dordrecht, The Netherlands, Kluwer Academic Publishers.

Stull, R.B. (1995). Meteorology today for scientists and engineers: a technical companion book. Minneapolis/St. Paul. West Publishing Company.

Sutton, O.G. (1953). Micrometeorology: a study of physical processes in the lowest layers of the Earth's atmosphere. Shrivenham, England. McGraw Hill Book Company, Inc.

Taillandier, A.S., Domine, F., Simpson, W., Sturm, M., Douglas, T. (2007). "The rate of decrease of the specific surface area of dry snow: isothermal versus temperature gradient conditions." *Journal of Geophysical Research* **112** (F03003).

Tester, J.W. and M. Modell (1997). Thermodynamics and its applications (3^{rd} ed). New Jersy, Prentice Hall.

Tremper, B. (2001). Staying alive in avalanche terrain. Seattle, WA, The mountaineers Books.

van de Hulst, H.C. (1963). A new look at multiple scattering. New York, Goddard Institute for Space Studies.

Walters, D.J. and E.E. Adams (2012). "Directional mechanical properties of radiation recrystallized snow layers from experimental testing." International Snow Science Workshop Proceedings.

Wanielsta, M., Kerten, R., Eaglin. R., 1997, Hydrology Water Quality and Quality Control (2^{nd} Edition). John Wiley and Sons.

Warren, SG. (1982). "Optical properties of snow." *Reviews of Geophysics and Space Physics*. **20:** 67-89.

Warren, S. G. (1984). "Optical constants of ice from the ultraviolet to the microwave." *Applied Optics*. **23:** 1206−1225.

Warren, S.G., and W.J. Wiscombe (1980). “A model for the spectral albedo of snow I, snow containing atmospheric aerosols.” *Journal of Atmospheric Science* **37:** 2712-2733.

Warren, S.G., and W.J. Wiscombe (1980). “A model for the spectral albedo of snow II, snow containing atmospheric aerosols.” *Journal of Atmospheric Science* **37:** 111-44.

Wetly, J., C. Wicks, R. Wilson, and G. Rorrer (2008). Fundamentals of momentum, heat, and mass transfer (4^{th} ed.). John Wiley & Sons, Inc.

APPENDICES

APPENDIX A:

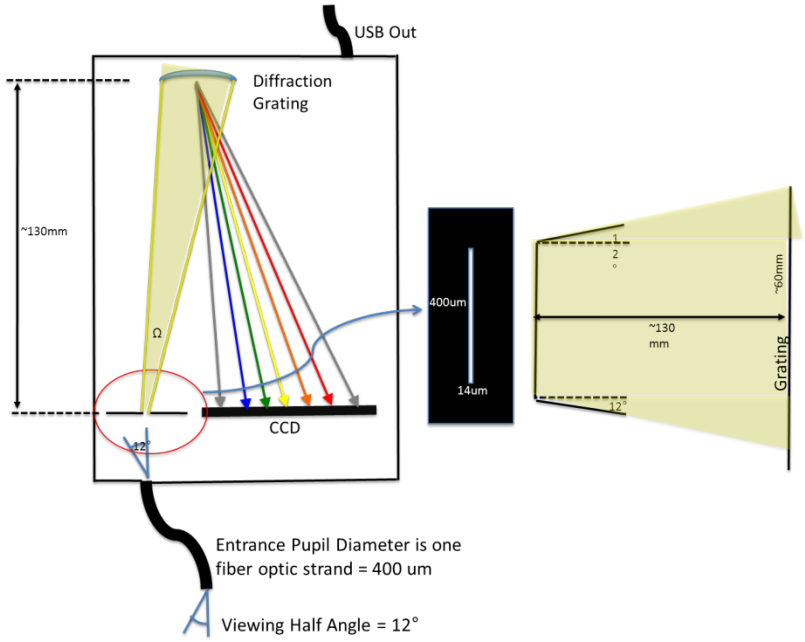
ANALYSIS OF STELLARNET BLACK COMET-HR SPECTROMETER

Black Comet Spectrometer Overview

A spectrometer is a passive sensor designed to take broadband incident light and separate it into power at each wavelength. The diffraction is accomplished via a grooved grating (known as a diffraction grating) and detection of the spectrum is done via a charged-coupled device (CCD). The following paper provides an analysis of a Stellarnet Black Comet Super Range Concave Grating Spectrometer (220 – 1100 nm). The Black Comet's simple design utilizes no mirrors. Light passes an entrance slit, where it then strikes a concave holographic, aberration corrected, dual blaze grating before being refracted onto a Sony ILX511 CCD. The instrument is meant to be compact and robust enough for field use and long life span. A multiband filter provides order sorting and prevents aliasing.

At the Cold Science Laboratory at Montana State University (MSU), the Black Comet is being used in bidirectional reflectance studies of various snow morphologies. A metal halide light source illuminates the snow's surface and reflected light is collected by the spectrometer from various observer angles. Hence, it is important to understand the spectrometer's design features and limitations. The following paper seeks to provide a block diagram and explanation of how the system operates, a radiometric analysis of the light source and throughput of the spectrometer, a brief discussion of atmospheric interference in the lab setting, a calculation of the instrument's signal to noise ratio (SNR), an analysis of the diffraction grating, and a final summary.

System Diagram



Physically, the spectrometer is 150 x 100 x 69 mm. Light enters via a ¼ inch, single strand, multimode fiber optic cable with a SMA905 connecter. Light passes through the cable and enters the housing of the spectrometer through a 14um x 400um slit that acts as the actual entrance pupil for the system. This slit is intended to baffle stray light that would otherwise flood the interior of the housing. Further, its width (14um) is designed to narrow the light to the same width as a single pixel. Spreading of the light between the entrance slit and the grating for the narrow dimension is likely considered nominal or corrected for by the curvature of the diffracting grating, which focuses light onto the CCD. In the 400um slit length direction, the light is assumed to spread at a 12° half angle corresponding the half angle of the fiber optic cable. As illustrated in the diagram above, the projection of the slit using these dimensions suggests that the diffraction grating (likely circular in shape) must have a diameter of approximately 60

mm. This is consistent with the physical dimensions of the housing (69mm x 100mm x 150mm). Once the light is diffracted into its spectral components it is directed via the concave shape of the grating itself onto a Sony ILX511 CCD. The resulting signal is output via a USB cable, which in turn provides power to the spectrometer.

Signal Level and Source Information

The light source used in MSU's Cold Science Laboratory is a Metal-Halide lamp whose output spectrum approximates that of the sun. Additional filters are placed in front of the light to reduce its brightness by 84% for most BRDF measurements. Reducing the radiance of the source helps minimize the likelihood of supersaturating the CCD. Reducing the radiance too much means a longer integration time is required to acquire a signal. This results in a smaller electrical bandwidth (Δf) and thus more noise in the system. However, as per a discussion with the manufacturer, operating at an integration time of 2 ms is the design limit of the instrument. Operating at 10-30 ms or grater provides less likelihood for error in repeated tests. Thus, the light is filtered to provide an adequate response (in raw counts) at 30 ms integration times.

The flux (Φ) incident on the detector can be found by multiplying the radiance of the source (L) by the throughput of the instrument. The throughput is simply the area of the entrance pupil by the solid angle of the field of view (FOV).

$$A_{grating} = \frac{\pi(.06m)^2}{4} = 2.43x10^{-3}m$$

$$\Omega \approx \frac{A_{grating}}{z^2} = \frac{2.42x10^{-3}m}{(0.130m)^2} = 0.14sr$$

Alternatly,

$$\Omega = \pi \sin^2(12^o) = 0.136sr$$

and

$$A_{slit} = 14\mu m \text{ x } 400\mu m = 5600\mu m^2 = 5.6x10^{15}m$$

Therefore, throughput can now be calculated as

$$Throughput = A_{slit}\Omega = 5.6x10^{-9}m^2(0.14sr) = 7.84x10^{-10}m^2sr$$

The radiance of the source (L) can be found by assuming the light source is a perfect black body radiating at T = 5778K (the temperature of the sun). From Planck's function integrated from 220 to 1100 nm (the range of the instrument), we have:

$$L_{BB} = 1.5355e7\frac{W}{m^2sr}$$

However, the specification sheet for the CCD provides a sensitivity curve, which will reduce this value. Figure 1 shows the sensitivity curve on the left and a linear approximation used as a filter function in the integration process on the right.

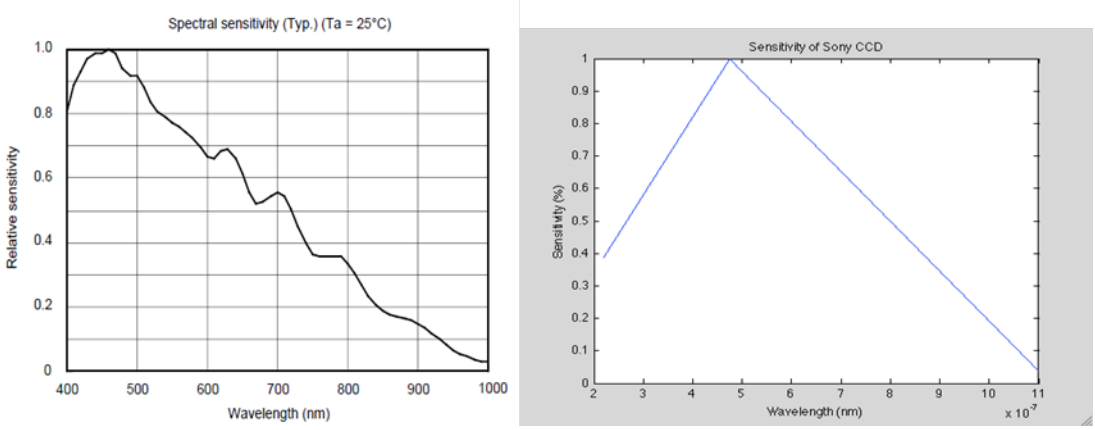


Figure 1: Sensitivity curve on the left from Sony CCD spec sheet and a linear approximation used as a filter function in the integration process.

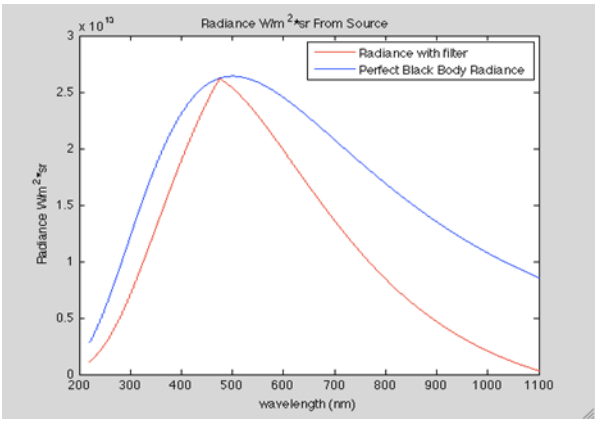


Figure 2: Blackbody curve (blue) and the same curve with the sensitivity filter applied (red).

The resulting blackbody curve (blue) and radiance with filter are shown in Figure 2. The radiance with the sensitivity filter (L_s) is:

$$L_S = 1.0079e7 \frac{W}{m^2 sr}$$

This is multiplied by the contribution of the filters over the light source in the lab to give use the total radiance at the CCD.

$$L = L_S * 0.168 = 1.68x10^6 \frac{W}{m^2 sr}$$

Finally, total flux (Φ) can be calculated as:

$$\phi_s = L * T\square rough\square put = 0.001317\text{W}$$

In addition to the sensitivity curve provided by the manufacturer, a sensitivity value was also provided on the specification sheet for the CCD in photometric units as:

$$S = 1800\frac{V}{lx\cdot s}$$

This value is suspected to be in error for the following reasons. Sensitivity S converted to radiometric units as follows:

$$S = 1800\frac{V}{\frac{lm}{m^2}\cdot s}\left(683\frac{lm}{W}\right)(.061) = 74993\frac{V}{\frac{W}{m^2}\cdot s}$$

This sensitivity can now be used to correct the radiance. Radiance (L = $1.68\text{x}10^6\text{W}/(\text{m}^2\text{sr})$), as determined in the above paper, is conserved throughout the system and represents the total radiance falling on the detector array. The irradiance (E) on just one pixel can be determined by dividing L by the total number of pixels (2048).

$$E_p = \frac{L}{\#\ pixels} = \frac{1.68x10^6\frac{W}{m^2sr}}{2048} = 820\frac{W}{m^2sr}$$

Flux, as a function of integration time (Δt), can be found by multiplying E by the throughput:

$$\phi(\Delta t) = L * Throughput * \Delta t = 820\frac{W}{m^2sr}\left(7.48x10^{-10}m^2sr\right)(\Delta t) = 6.4x10^{-7}W * \Delta t$$

To get this term in units consistent with the sensitivity term, it is advantageous to divide by the area of a single pixel, thus giving us power on a single pixel:

$$\phi(\Delta t)_p = \frac{\phi(\Delta t)}{A_p} = \frac{6.4x10^{-7}W(\Delta t)}{14x10^{-6}m\ x\ 200x10^{-6}m} = 230\frac{W}{m^2}\Delta t$$

Multiplying this by the sensitivity term:

$$S\phi(\Delta t)_p = 74993\frac{V}{\frac{W}{m^2}\cdot s}\left(230\frac{W}{m^2}\Delta t\right) = 1.7x10^7\frac{V}{s}\Delta t$$

Finally, the integration time (Δt) ranges from 2ms to 65s. A typical value, used here, is 0.03s. This is the time it takes to fill one pixel well completely. Plugging this into the above equation yields output signal voltage:

$$i_s = S\phi(\Delta t)_p = 1.7x10^7\frac{V}{s}0.03s = 517452V$$

The specification sheet suggests that the output saturation signal is 0.8V. Thus, the above value is obviously incorrect. In addition to being intuitively too large, we see that it would saturate the instrument. By working backward from the saturation voltage we can calculate a possible S value.

$$i_s = S\phi(\Delta t)_p$$
$$0.8V = S\left(230\frac{W}{m^2}\right)(0.03s)$$
$$\therefore S = 0.12\frac{V}{\frac{W}{m^2}s}$$

This suggests a value of Sensitivity in photometric units of 0.00288V/(lx*s). Thus, it is speculated that the value given for sensitivity in the Sony CCD specification sheet is in error.

Atmospheric Effects

While only two meters of atmosphere lie between the light source and the sensor, it is possible that atmospheric absorption and scattering over this path could further

reduce the signal to the CCD. To determine total transmission and the contributing constituents, a Modtran model was run for a horizontal path, in Bozeman, Montana, with a mid-latitude, summer of 1973 standard atmosphere assumption. The optical path length was set at 2m. As can be seen in Figure 3, there is very little scattering or absorption effect over such a short path length. Total transmission was 99.85%. Only water vapor and oxygen contributed significantly to extinction. It is likely the water content is lower in the cold lab than in this model.

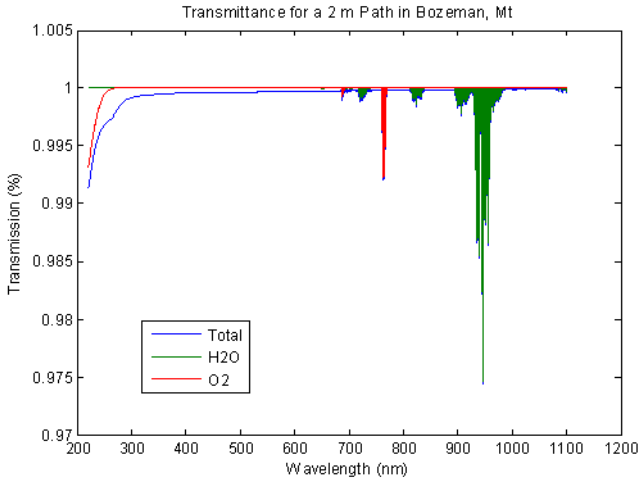


Figure 3: Modtran model of atmospheric transmission in Bozeman, MT for a 2m optical path using a 1973 mid-latitude summer standard atmospheric model. Total transmittance is 99.85%.

Responsivity Calculations

Responsivity expresses how much current is generated by a given number of photons striking the detector. It is a function of the quantum efficiency (η), which describes the likelihood of an electron jumping the quantum band gap. It is also dependent upon the energy per photon (hν) and the charge on an electron (q). Both q and h are constants, $1.6 \times 10^{19} C$ $6.626 \times 10^{-36} Js$ respectively. The optical frequency (ν)

for the Black Comet CCD was estimated from a similar spectrometer that also used a Sony ILX511 CCD. The specification sheet does not provide quantum efficiency. Therefore, the following equations are provided for reference but no values are calculated. Responsivity can be calculated from

$$R = \frac{\eta q}{\square v}.$$

Photocurrent, Noise Current, and SNR

Photocurrent, or the current generated by the photons falling on the CCD, filling the pixel wells, and in turn inducing a current, can be found by multiplying responsivity and flux:

$$i_s = R\phi_s$$

The random arrival rate of photons at the detector gives rise to shot noise, which is essentially the standard deviation from the mean arrival time. A sensor that is shot noise limited (SNL) has the theoretically best signal to noise ratio possible. Additionally, the resistors in the electrical components of the detector heat up, causing a spontaneous flow of electrons called Johnson, or thermal, noise. Only cooling your sensor to 0 K will remove this noise. The calculation of both types of noise requires knowledge of the electrical bandwidth (Δf). Electrical bandwidth is determined by taking 1 over integration time (or time it takes to fill a pixel well). For the Black Comet, the integration time is user controlled from 2ms to 652. However, an integration time of 30 ms is most commonly used. Therefore,

$$\Delta f = \frac{1}{IntegrationTime} = \frac{1}{2\text{ms to }65\text{s}} = 500 \text{ to } 0.0154\text{Hz}$$

$$\Delta f = \frac{1}{.003s} = 333Hz$$

For the Black Comet shot noise and Johnson noise can be calculated as follows:

$$i_{sn} = \sqrt{2qi_s\Delta f}$$

$$i_{jn} = \sqrt{\frac{4kT\Delta f}{R}}$$

where T = 294K (room temp), k = Boltzmann's constant = 1.381×10^{-23}J/K, and R = 250Ω as seen on the spectrometer specification sheet.

Finally, we can calculate the signal to noise ratio (SNR) by dividing the photocurrent (i_s) by the root mean square of the noise current as follows:

$$SNR = \frac{i_s}{\sqrt{i_{sn}^2 + i^2}}$$

This is 4 orders of magnitude larger than the SNR = 1000:1 value given in the specification sheet for the spectrometer, suggesting an error in the values used in the calculation. It is likely the values pulled from the specification sheets were incorrectly used.

Diffracting Grating

One of the first diffraction gratings was constructed using fine hairs strung between two finely threaded screws. Light passing through the hair was found to diffract into its spectrum. Modern gratings function on the same principles but use a finely grooved surface to cause the bending of light (Figure 4).

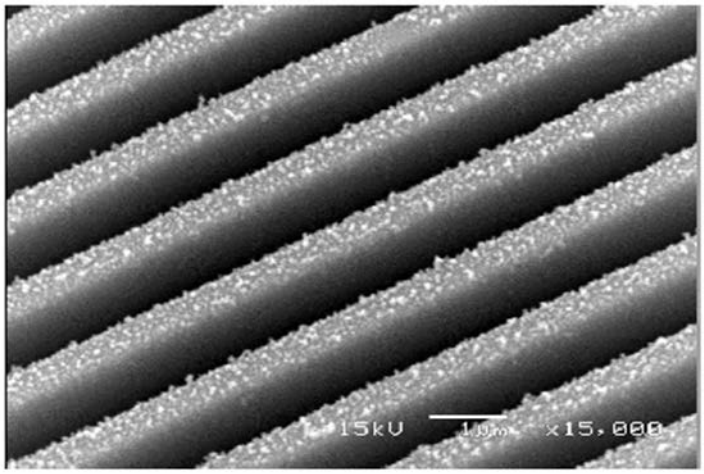


Figure 4: Close up of a diffraction grating from http://www.horiba.com/uploads/media/RE06-04-016.pdf.

As illustrated in Figure 5, when a plane wave strikes a diffracting grating, each wavelength is bent at a slightly different angle. The resulting interaction of all of the waves creates a pattern of signal (a spectrum) labeled m = 1 followed by a null or dark region and then another signal (a spectrum) labeled m = 2 and so on. Each higher order spectrum becomes progressively stretched. Most spectrometers strive to simply capture the first order (m = 1) diffraction pattern.

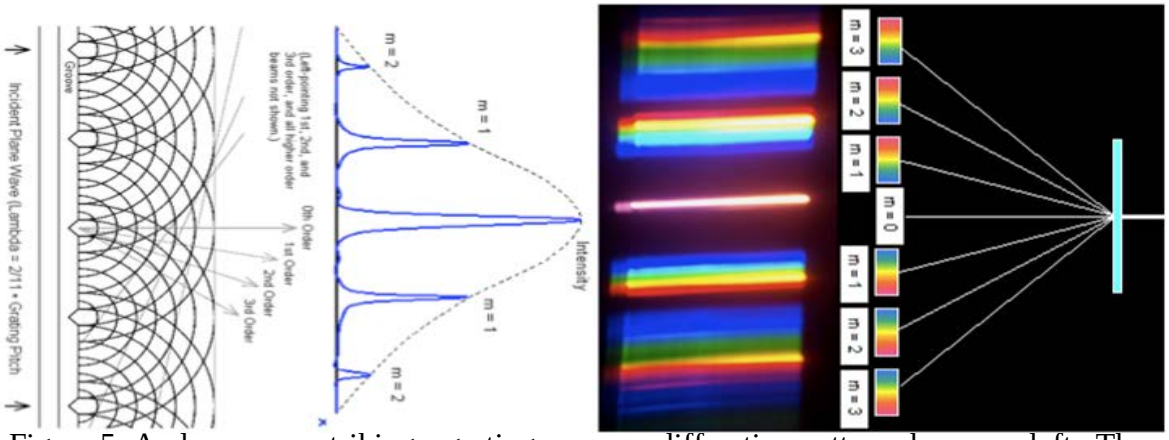


Figure 5: A plane wave striking a grating causes a diffraction pattern shown on left. The interaction of the propagating waves creates null or dark regions followed by a spectrum labeled m = 1, 2, 3, etc. Figure from:

http://www.schoolphysics.co.uk/age16-19/Wave%20properties/Diffraction/text/Diffraction_grating/index.html
http://www.laserholics.com/showthread.php?3115-questions-about-NOVAlasers-diffraction-gratings
http://eastviewchemistry.pbworks.com/w/page/31472408/Cell-Phone%20Spectrometers

The mathematical relationship between groove diameter (d), wavelength (λ), the order of diffraction (m), the angle of incident (θ_i), and exiting light (θ_m), illustrated in Figure 6, is given by the grating equation:

$$m\lambda = d\left[\sin(\theta_m) - \sin(\theta_i)\right]$$

If we assume the angle of incidence (θ_i) is 0, then this equation reduces to:

$$m\lambda = d\sin(\theta_m)$$

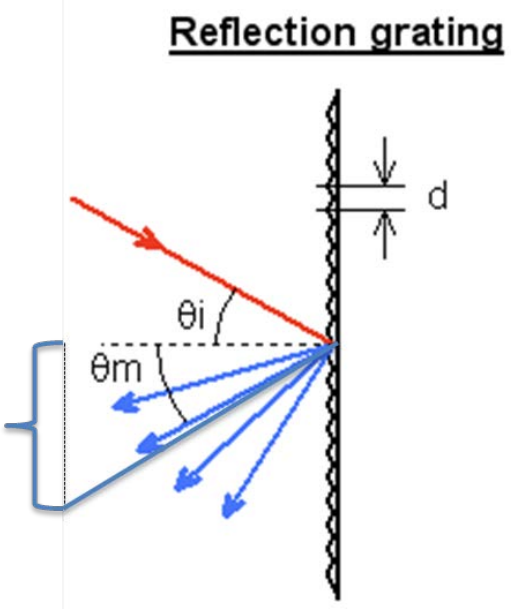


Figure 6: Illustration of terms in diffraction grating equation from: http://www.physicsforums.com/mgc_gloss/201/img_1.gif

This equation can be solved for (θ_m):

$$\theta_m = \sin^{-1}\left(\frac{m\lambda}{d}\right)$$

Additionally, from Figure 6, it can be seen that:

$$y = D\tan(\theta)$$

Finally, resolving power can be calculated from:

$$R = \frac{Nd\sin(\theta_m)}{\lambda}$$

where N = # of grating periods.

To apply these equations to the Black Comet spectrometer, a grating width of 40mm is assumed. Additionally, it is assumed that m = 1 and the distance (D) of the grating from the CCD is 100mm. The specification sheet states the grating has 590 lines/mm.

$$\text{GratingWidth} = 40mm$$
$$\text{LinesPerMilimeter} = 590$$
$$m = 1$$
$$D = 100mm$$

One over the lines per mm value yields d = 1.69×10^{-6}m. Grating width multiplied by lines per millimeter yields N = 2.37×10^{4} grating lines. Plugging these values into the equations for θ_m and y provides the values shown in Figures 7 and 8 below (also, see appendix).

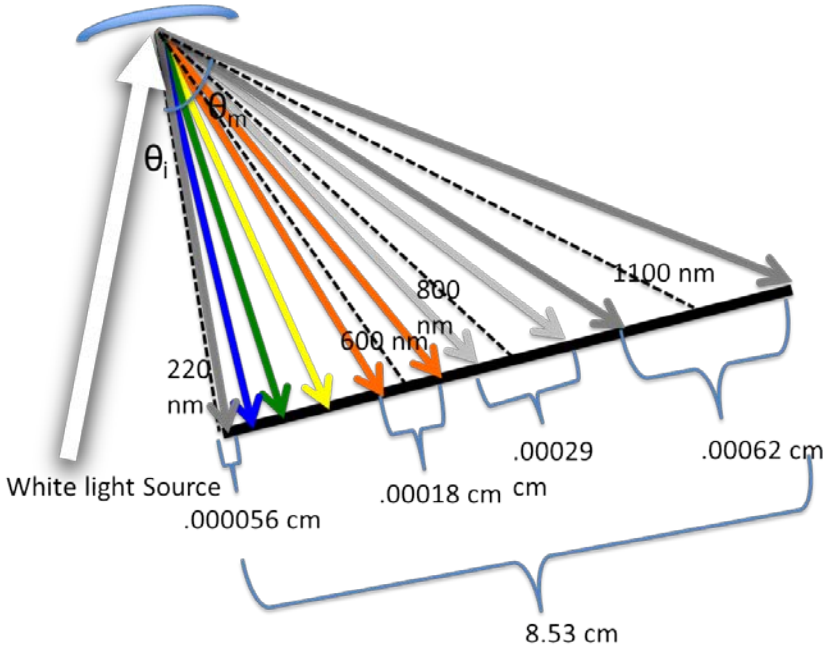


Figure 7: Black Comet values of y and Δy for m = 1. See Appendix A for additional data.

It is interesting to note that the pixel width is 14 um (0.0014 cm). Thus, in Figure 7, even at 1100 nm wavelength, the Δy value (=0.00062cm) is smaller than a single pixel, suggesting the limiting factor in resolution is the CCD, not the grating. Further, the total y value (=8.53 cm) would easily fit within the confines of the spectrometer housing.

However, 85.3mm is still twice the width of the CCD (=40.2mm). This is likely corrected for by curving the grating to focus the 1st order diffraction pattern down to the required width.

Figure 8 shows the effect of increasing m to 2 and repeating the above equations. It can be seen that the y value is larger than the dimensions of the box. Additionally, at 847 nm the Δy value is larger than one pixel. Further, the 850 nm wavelength diffracts over 90°.

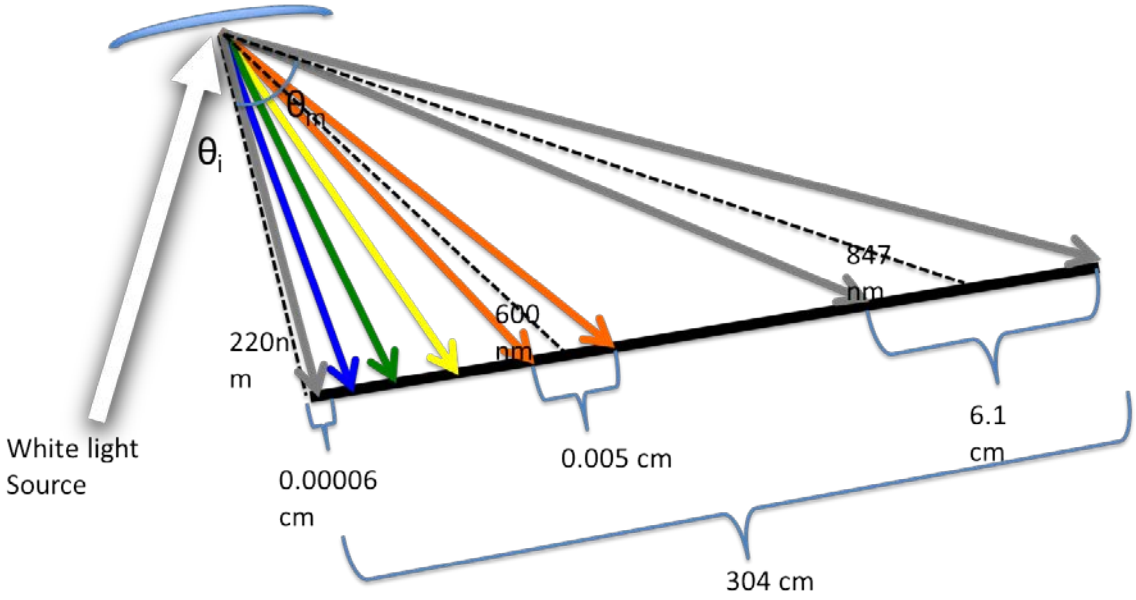


Figure 8: Black Comet values of y and Δy for m = 2. See Appendix A for additional data.

Obviously, the 2nd order diffraction is more difficult to capture and is thus ignored in many spectrometer designs, including those for the Black Comet.

Conclusion

The SNR values calculated are highly suspect due to several major assumptions and to the possible misinterpretation of the information on the specification sheets. A major concern is the use of the sensitivity curve as a filter function in the integration of the Planck function. It is believed that a filter function is the system's overall wavelength dependence. Thus, it can include the sensitivity curve.

Significant assumptions were made about the value of quantum efficiency value (η) and an optical frequency value (ν). The frequency value (ν) was taken from another spectrometer with the same CCD. This value seemed consistent with values in the homework. However, it is unclear what assumptions were made in designing the homework (or if realistic values were used). Additionally, this term is inversely proportional to wavelength. Thus, the singe value used must be an integral form across the wavelengths of the sensor. If the spectrometer from which this data was taken had a different wavelength range, the value could vary considerably from the above calculation.

The grating equation values seem more reasonable. The width of the 1^{st} order spectrum falls within the physical dimensions of the spectrometer housing. Further, the small Δy values calculated suggest that the limiting capability of the instrument is the CCD, not the grating. More accurate optical layout information could improve upon this information.

Spectrometer Spec Sheet

BLACK-COMET-SR *Super Range Models*

BLACK-Comet Model	Wavelength Range (nm)	Grating g / mm	Slit-200 nm res.	Slit-100 nm res.	Slit-50 nm res.	Slit-25 nm res.	Slit-14 nm res.
BLK-C-SR	200-1080	concave	8.0	4.0	2.0	1.5	1.3
BLK-CXR-SR	220-1100	concave	8.0	4.0	2.0	1.5	1.3

Specifications StellarNet Detector Information How to Determine Spectral Resolution

Dynamic Range:	2000:1 with 6 decades	Dimensions:	69 x 100 x 150 mm
Optical Resolution:	see above	Power Consumption:	100 mA @ 5 VDC
Detector Type:	2048 pixel CCD, PDA opt.	Interface:	USB-2
Detector Range:	200-1080 nm or 220-1100 nm	Data Transfer Speed:	3x / 40x faster than USB-1
Pixel Size:	14 um x 200 um	Detector Integration:	1 ms to 65 s
Concave Grating:	Aberration corrected	Slit Size Options:	14, 25, 50, 100, 200 um
Grating Type:	Holographic, 590 g/mm	Stray Light:	0.02% at 435 nm; 0.2% at 200 nm
Spectrograph:	f/2, Flat field - No mirrors	Fiber Optic Input:	SMA905 0.22 na single fiber
Order Sorting Filter:	Integrated multi-band	Operating Systems:	Windows XP/Vista/7
Signal to Noise:	1000:1 CCD, PDA 2000:1	Software Included:	SpectraWiz program & apps
Digitizer:	16-bit	Also Free Programs For:	LabView / VC / VBA / Delphi

see also http://www.stellarnet.us/products_spectrometers_BLACK-Comet-SR.htm

CCD Spec Sheet

Electro-optical Characteristics

(Ta = 25 °C, V_{DD} = 5 V, Clock frequency: 1 MHz, Light source = 3200 K, IR cut filter: CM-500S (t = 1.0 mm), Without S/H mode)

Item	Symbol	Min.	Typ.	Max.	Unit	Remarks
Sensitivity 1	R1	150	200	250	V/(lx • s)	Note 1
Sensitivity 2	R2	—	1800	—	V/(lx • s)	Note 2
Sensitivity nonuniformity	PRNU	—	5.0	10.0	%	Note 3
Saturation output voltage	V_{SAT}	0.6	0.8	—	V	—
Dark voltage average	V_{DRK}	—	3.0	6.0	mV	Note 4
Dark signal nonuniformity	DSNU	—	6.0	12.0	mV	Note 4
Image lag	IL	—	1	—	%	Note 5
Dynamic range	DR	—	267	—	—	Note 6
Saturation exposure	SE	—	0.004	—	lx • s	Note 7
5 V current consumption	I_{VDD}	—	5.0	10.0	mA	—
Total transfer efficiency	TTE	92.0	98.0	—	%	—
Output impedance	Z_O	—	250	—	Ω	—
Offset level	V_{OS}	—	2.8	—	V	Note 8

see also http://www.oceanoptics.com/technical/detectorsonyILX511.pdf

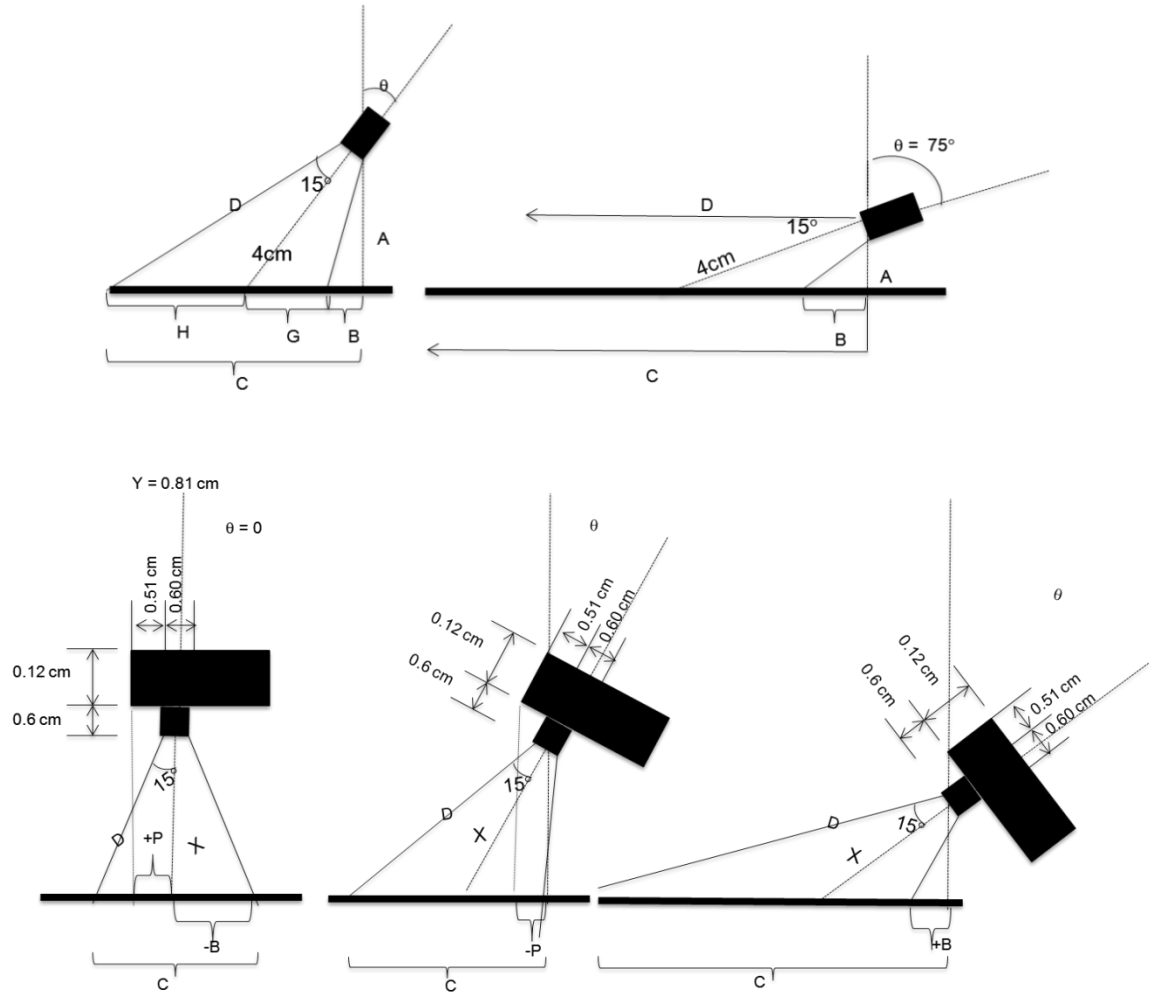
Additional Calculation for Grating

Values			**For m = 1**		
grooves/mm	590	590	590	590	590
d um	1.694	1.694	1.694	1.694	1.694
m	1	1	1	1	1
D (cm)	10	10	10	10	10
N	23718	23718	23718	23718	23718
R	47436	47436	47436	47436	47436
w	220	600	800	847	1100
y (cm)	1.309	3.785	5.35	5.77	8.53
theta	7.458	20.73	28.16	29.98	40.466
del w (nm)	0.0092756	0.0259	0.0337	0.0357	0.0464
del y (cm)	0.0000561	0.0001824	0.00029	0.000324	0.0006214

Values			**For m = 2**		
grooves/mm	590	590	590	590	590
d um	1.694	1.694	1.694	1.694	1.694
m	2	2	2	2	2
D (cm)	10	10	10	10	10
N	23718	23718	23718	23718	23718
R	47436	47436	47436	47436	47436
w	220	600	800	847	1100
y (cm)	2.688	10.02	28.61	304	nan
theta	15.04	45.07	70.73	88.11	nan
del w (nm)	0.0046378	0.0126486	0.0168648	0.01785	0.009322
del y (cm)	0.0000607	0.0004237	0.0055417	6.11	nan

APPENDIX B:

FIELD OF VIEW AND SHADOW GEOMETERY EQUATIONS



Repeat of Figure 29 and Figure 30. Field of View and Shadow Geometry

```
function [C,K] = Probe_Solid_Angle (Theta) %in degrees
format compact

%Inputs (use degrees)
%Theta  = observer zenith angle
Beta    = 15;    %Half angle of scopes view field
X       = 4;     %cm Probe height above snow
R       = 78.74; %cm Radius of bar
tilt    = 24.25; %tilt of bar(same as Theta in special case of Theta=0)
Y       = .81;   %cm Probe Holder width for shadow calculations

%Outputs:
%Lengths cm
A = X.*cosd(Theta);
B = A.*tand(Theta-Beta);%If B = pos then no shadow from probe tip
C = A.*tand(Theta+Beta);
D = sqrt(A.^2+C.^2);
```

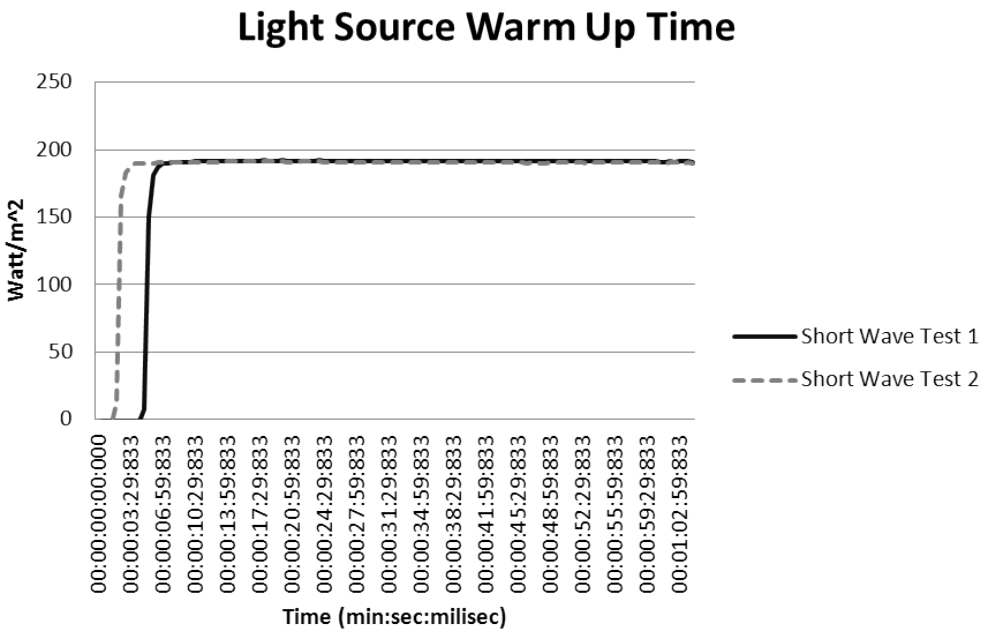
```
E = C-B;                %Length of major axis of ellipse
F = X.*sind(Theta);
G = F-B;
H = C-(G+B);
I = H-(E/2);%Iand J are used to project major axis flat and then find K
J = I.*cosd(90-Theta); %I and J are hard to explain (see diagram)
K = 2.*((X+J).*tand(Beta));  %Length of the minor axis of ellipse

L = X.*sind(tilt); %Length of probe shadow
M = R.*sind(tilt); %Length of bar shadow

N = sqrt((X+0.6).^2+Y.^2);
%O = skipped because it look too much like 0
P = -N.*sind((Theta/2)-(atand(Y./(X+0.6)))); %if P = neg then no shadow
created from bar holder

end

%Note: From experiment
%tilt,beta = ~25,0 with a 4cm probe height is where shadow starts to
%appear.
```



Light source warm up time and temporal consistency. The light reaches full power in less than 10 minutes and stays consistent with time.

APPENDIX C:

MASS FLUX MATLAB CODE

Mass Flux Equations

```
%Mass Flux8_05_12: Equation 6 from Modeling Snow Temp in Complex
Topography by E.
%Adams. For all Data whereas MassFlux is for only certain data scans.
%Updated 8/05/12
format compact
format short g

%-----------------------------------------------------------------
%%IMPORT DATA

%This Script will import data from EXCEL.CSV files created from Data
logger
clear
clc
close all
load Scan

%Load in environmental data
[TheFilename, pathname] = uigetfile( ...
{'*.csv','CSV Data Files (*.csv)';'*.*',  'All Files (*.*)'}, ...
   'Pick a data file',[filesep,'/Users/brad/Dropbox/All Masters
Work/Research/CC5 Data Logger/CC5 Data Logger 1-25-12 to 6-19-
12/MatlabVersion/']);

%Display user selected actions
if isequal(TheFilename,0)
   disp('User selected Cancel')
else
   disp(['User selected ', TheFilename])
end
addpath(pathname)

%Store the Data in a structure. This works for excel files saved as
.csv
%files only!
The_Data = importdata(TheFilename,',',1); %Says filename has CSvalues
with 1 header row

%Pull out the Header from The_Data.textdata
Header = The_Data.textdata(1,:);

%Set Scan Number--for the structure Scan(ScanNum)
for i = 1:length(Scan)
    if 1 == strcmp(TheFilename,Scan(i).filename)
    ScanNum = i;
    break
    end
end
%%
```

```
 %Menu for selecting if you want Large or Small ROI and if you want
result
%from CT scan 1 or 2 displayed.
ROI_Choice = menu('Select Defaults:'   ,cellstr(
num2str((1:length(Scan(ScanNum).Area)).', 'Select ROI Area %d')));
StartTime_Choice = menu('Select Start Time: ',cellstr(
num2str((1:length(Scan(ScanNum).Time)).', 'Select Start Time %d')));
EndTime_Choice = menu('Select End Time: ',cellstr(
num2str((1:length(Scan(ScanNum).Time)).', 'Select End Time %d')));

%Use user defined ROI_Choice, StartTimeChoice, Endtime_Choice to set
%values for equations below
Area = Scan(ScanNum).Area(ROI_Choice);
%StartTime and EndTime are actually a row number.  Thus dividing by 30
converts the time
%to a row number
if StartTime_Choice == 1
    StartTime = 1; %Sets start time to 1st row since row 0 does not
exist.
else
    StartTime = (Scan(ScanNum).Time(StartTime_Choice))/30;
end

EndTime   = (Scan(ScanNum).Time(EndTime_Choice))/30;
Start_Vol = Scan(ScanNum).A(ROI_Choice).Volume(StartTime_Choice);
End_Vol   = Scan(ScanNum).A(ROI_Choice).Volume(EndTime_Choice);

%Display Above Values
display(sprintf('Area (mm^2) = %d',(Scan(ScanNum).Area(ROI_Choice))))
display(sprintf('Start Time (s) =
%d',(Scan(ScanNum).Time(StartTime_Choice))))
display(sprintf('End Time (s) =
%d',(Scan(ScanNum).Time(EndTime_Choice))))
display(sprintf('Start Volume (mm^3) =
%d',Scan(ScanNum).A(ROI_Choice).Volume(StartTime_Choice)))
display(sprintf('Start Volume (mm^3) =
%d',Scan(ScanNum).A(ROI_Choice).Volume(EndTime_Choice)))


%Time step data for plotting (note this does not use the time or data
info
%in the imported data set)
time_s=(StartTime:EndTime).*30;
time_m=time_s./60;
time_h=time_m./60;
Total_time_s = time_s(1,length(time_s));
Total_time_m = time_m(1,length(time_m));
Total_time_h = time_h(1,length(time_h))

%%
%------------------------------------------------------------------
display('------------------------------------------------------')
```

```
%CONSTANTS
K_m             = 2.9e-3; %Unitless turbulent transfer coef for water.
R_air_KJperkgK  = 0.287;  %kJ/(kg*K) ideal gas constant for air
Windspeed_mpers  = 1                        %m/s Measured in Lab
Density_ice      = 916.7;                    %kg/m^3

%The Data
[row,col] = find(ismember(Header,'101 <TC01_a> (C)')==1);
Temp_1    = The_Data.data(StartTime:EndTime,col); %C Temp probe 1 --2cm
above snow.

[row,col] = find(ismember(Header,'102 <TC02_a> (C)')==1);
Temp_2    = The_Data.data(StartTime:EndTime,col); %C Temp probe 2 --1cm
above snow.

[row,col] = find(ismember(Header,'103 <TC03_a> (C)')==1);
Temp_3    = The_Data.data(StartTime:EndTime,col); %C Temp probe 3 snow
surface.

[row,col] = find(ismember(Header,'104 <TC04_a> (C)')==1);
Temp_4    = The_Data.data(StartTime:EndTime,col); %C Temp probe 4 --1cm
below snow.

[row,col] = find(ismember(Header,'105 <TC05_a> (C)')==1);
Temp_5    = The_Data.data(StartTime:EndTime,col); %C Temp probe 5 --2cm
below snow.

[row,col] = find(ismember(Header,'106 <TC06_a> (C)')==1);
Temp_6    = The_Data.data(StartTime:EndTime,col); %C Temp probe 6 --3cm
below snow.

[row,col] = find(ismember(Header,'107 <TC07_a> (C)')==1);
Temp_7    = The_Data.data(StartTime:EndTime,col); %C Temp probe 7 --4cm
below snow.

[row,col] = find(ismember(Header,'108 <TC08_a> (C)')==1);
Temp_8    = The_Data.data(StartTime:EndTime,col); %C Temp probe 8 --5cm
below snow.

[row,col] = find(ismember(Header,'109 <TC09_a> (C)')==1);
Temp_9    = The_Data.data(StartTime:EndTime,col); %C Temp probe 9 --6cm
below snow.

[row,col] = find(ismember(Header,'110 <TC10_a> (C)')==1);
Temp_10   = The_Data.data(StartTime:EndTime,col); %C Temp probe 10 --
7cm below snow.


[row,col]    = find(ismember(Header,'201 <LW_Voltage> (VDC)')==1);
LW_Voltage   = The_Data.data(StartTime:EndTime,col);

[row,col]    = find(ismember(Header,'202 <Rc> (OHM)')==1);
```

```
Rc           = The_Data.data(StartTime:EndTime,col);    %OHM

[row,col]    = find(ismember(Header,'203 <Rd> (OHM)')==1);
Rd           = The_Data.data(StartTime:EndTime,col);    %OHM

[row,col]    = find(ismember(Header,'204 <Surface Temp> (C)')==1);
T_snow_C     = The_Data.data(StartTime:EndTime,col);      %C Temp of
snow surface.

[row,col]    = find(ismember(Header,'205 <Probe_RH> (PCT)')==1);
RH_air       = The_Data.data(StartTime:EndTime,col); %percent

[row,col]    = find(ismember(Header,'206 <Probe_Air Temp> (C)')==1);
T_air_C      = The_Data.data(StartTime:EndTime,col);      %C Temp well
above the snow surface.

[row,col]    = find(ismember(Header,'207 <Probe_Pressure> (MB)')==1);
P_air_hPa    = The_Data.data(StartTime:EndTime,col);

[row,col]    = find(ismember(Header,'208 <Shortwave> (WM2)')==1);
Shortwave    = The_Data.data(StartTime:EndTime,col);

[row,col]    = find(ismember(Header,'211 <TC03_Ceil_SW> (C)')==1);
TC03_Ceil_SW = The_Data.data(StartTime:EndTime,col);

[row,col]    = find(ismember(Header,'212 <TC04_Ceil_NE> (C)')==1);
TC04_Ceil_NE = The_Data.data(StartTime:EndTime,col);

[row,col]    = find(ismember(Header,'218 <A_extra> (C)')==1);
A_extra      = The_Data.data(StartTime:EndTime,col);

[row,col]    = find(ismember(Header,'219 <B_extra> (C)')==1);
B_extra      = The_Data.data(StartTime:EndTime,col);

[row,col]    = find(ismember(Header,'220 <C_extra> (C)')==1);
C_extra      = The_Data.data(StartTime:EndTime,col);

[row,col]    = find(ismember(Header,'301 <HMP60 Temp 1> (C)')==1);
HMP60_Temp_1 = The_Data.data(StartTime:EndTime,col);

[row,col]    = find(ismember(Header,'302 <HMP60 Temp 2> (C)')==1);
HMP60_Temp_2 = The_Data.data(StartTime:EndTime,col);

[row,col]    = find(ismember(Header,'303 <HMP60 RH 1> (PCT)')==1);
HMP60_RH_1   = The_Data.data(StartTime:EndTime,col);

[row,col]    = find(ismember(Header,'304 <HMP60 RH 2> (PCT)')==1);
HMP60_RH_2   = The_Data.data(StartTime:EndTime,col);

%MEAN VALUES:
```

```
Mean_HMP60_RH_1   = mean(HMP60_RH_1)
Mean_HMP60_RH_2   = mean(HMP60_RH_2)
Mean_RH_air       = mean(RH_air)

Mean_HMP60_Temp_1 = mean(HMP60_Temp_1)
Mean_HMP60_Temp_2 = mean(HMP60_Temp_2)
Probe_Mean_T_air_C= mean(T_air_C)

IR_Mean_T_snow_C     = mean(T_snow_C)
Probe_Mean_P_air_hPa = mean(P_air_hPa)

%%
%------------------------------------------------------------------

%CALCULATIONS:

%Select which probe Temp and RH will be used.  Note that for -30 data
the
%probe is not an option
if 1 == strcmp(TheFilename,'3_27_2012 10_18_35 Temp-30.csv')
    display('Only 6hrs of data is available for the 3/27/12 -30C run.
Further, the probe does not work at these temperatures.')
    Selection = 5;
elseif 1 == strcmp(TheFilename,'6_19_2012 09_29_06 Temp -30C.csv')
    Selection = menu('Select Probe (RH and Temp) used for calculations:
','HMP60_Probe_1','HMP60_Probe_2','B_extra_temp and HMP60Probe2RH');
elseif 1 == strcmp(TheFilename,'3_28_2012 11_37_30 Temp-13.csv')||1 ==
strcmp(TheFilename,'3_29_2012 10_40_00 Temp-5.csv')
    Selection = 4;
else
    Selection = menu('Select Probe (RH and Temp) used for calculations:
','HMP60_Probe_1','HMP60_Probe_2','B_extra_temp and
HMP60Probe2RH','Probe');
end

if Selection == 4
    Temperature = T_air_C;
    RelativeHumidity = RH_air./100;
elseif Selection == 1
    Temperature = HMP60_Temp_1;
    RelativeHumidity = HMP60_RH_1./100;
elseif Selection == 2
    Temperature = HMP60_Temp_2;
    RelativeHumidity = HMP60_RH_2./100;
elseif Selection == 3
    Temperature = B_extra;
    RelativeHumidity = HMP60_RH_2./100;
else Selection == 5;
    Temperature = [];
    RelativeHumidity = [];
end
```

```
%Seclect whether snow surface temperature is taken from IR probe or
from
%burried thermocouple array
Selection2 = menu('Select Snow Surface Temperature: ','Infrared
Probe','Thermocouple at surface');
if Selection2 == 1
    SnowSurfaceTemperature = T_snow_C;
else Selection2 == 2
    SnowSurfaceTemperature = Temp_3;
end

%From Ideal Gas Law
density_air_gpercubicm =
((P_air_hPa./10)./(R_air_KJperkgK.*(Temperature+273.15))).*1000; %g/m^3
ideal gas law

%Clausius-Clapeyron Equation from Snow and Climate by Armstrong Equ 2.4
%This equation is valid for T = 0 to -40 C and is the sat vp w/ respect
to
%ice.  Note: T = celcius and P_air and e_sat_ice are in hPa
Probe_e_sat_air_hPa   = (1.0003+(4.8e-
6.*P_air_hPa)).*6.1115.*exp((22.452.*Temperature)./(272.55+Temperature)
); %hPa
% HMP60_1_e_sat_air_hPa = (1.0003+(4.8e-
6.*P_air_hPa)).*6.1115.*exp((22.452.*HMP60_Temp_1)./(272.55+HMP60_Temp_
1)); %hPa

%Multiplying by e_sat_air with RH_air give e_actual_air.
Probe_e_actual_air_hPa = RelativeHumidity .* Probe_e_sat_air_hPa; %THIS
IS e_a IN ED'S MASS FLUX EQUATION (hpa)

%This is CC for snow surface (where T_air = T_snow).  Thus this is
%saturation vapor pressure of surface.  %THIS IS e_s IN ED'S MASS FLUX
%EQUATION
Probe_e_sat_snow_hPa = (1.0003+(4.8e-
6.*P_air_hPa)).*6.1115.*exp((22.452.*SnowSurfaceTemperature)./(272.55+S
nowSurfaceTemperature));%hPa

%MASS FLUX CALCULATON: g/(m^2*s)
Probe_Mass_Flux_gpersqrms =
0.622.*density_air_gpercubicm.*Windspeed_mpers.*K_m.*...
    (Probe_e_actual_air_hPa - Probe_e_sat_snow_hPa)./P_air_hPa;

%Mean Values
Mean_density_air_gpercubicm        = mean(density_air_gpercubicm)
Probe_Mean_e_sat_air_hPa           = mean(Probe_e_sat_air_hPa) %hPa
Probe_Mean_e_actual_air_hPa        = mean(Probe_e_actual_air_hPa) %hPa
Probe_Mean_e_sat_snow_hPa          = mean(Probe_e_sat_snow_hPa)%hPa
Probe_Mean_Mass_Flux_gpersqsrms    = mean(Probe_Mass_Flux_gpersqrms)


%TOTAL MASS ADDED TO SNOW SURFACE (Numerical Method)
%BRAD: The commented code (next 3 lines) provides a method for having a
```

```
%linearly increasing area since the surface area of the sample is
%increasing with time.It is currently set up for only Large ROI and -
13C
%Also, Dr. Miller says the commented code is NOT how mass flux works.
display('-----------------------------------------------------')
% Area_of_Sample_sqrm = linspace(5e-4,6.5e-4,1000);%for -13C/Large
ROI/Short;  %%linspace(3.8059e-04,7.5e-04,length(The_Data.data));%for -
30c/LargeROI  %%linspace(551.9196e-006,910.6673e-006,747);%For -
5C/LargeROI/shortrun
% xxx = Mass_Flux_gpersqrms.*Area_of_Sample_sqrm';
% Calculated_total_mass_added_to_snow_grams = trapz(time_s,xxx)
Calculated_total_mass_added_to_snow_grams =
trapz(time_s,Probe_Mass_Flux_gpersqrms).*(Area.*(1/1000)^2)
%Mean_Total_Mass_added_to_snow_grams =
Mean_Mass_Flux_gpersqsrms*Total_time_s*(Area_of_Sample_sqrm)

%ACTUAL RESULTS FROM CT SCANNER
display('-----------------------------------------------------')

Mass_Added_To_Snow_CTScan_g = ((End_Vol - Start_Vol) *
(1/1000)^3*1000*Density_ice) %mm^3*(1m/1000mm)^3*kg/m^3*1000kg/1g = g
% Percent_Difference = (Calculated_total_mass_added_to_snow_grams -
Mass_Added_To_Snow_CTScan_g/...
%     ((Calculated_total_mass_added_to_snow_grams +
Mass_Added_To_Snow_CTScan_g)/2))*100

display('-----------------------------------------------------')


RH_atsnow = Probe_e_actual_air_hPa./Probe_e_sat_snow_hPa; %Not
displayed or used expect to plot
```

APPENDIX D:

EXAMINATION OF THE DIRECTIONAL GROWTH OF SURFACE HOAR

Abstract

Accurate experimental growth of surface hoar in a lab setting is hindered by difficulty in simulating the long wave coupling of the snow surface and the night sky. Previous experimental attempts simply ignore this process. Montana State University's SubZero Science and Research Facility's cold ceiling provides a unique method for approximating the cooling effects of the night sky. By controlling snow surface temperature (via long wave cooling with the ceiling), air temperature, humidity, and wind speed, it is possible to simulate natural surface hoar growth conditions. This paper examines the process used to grow surface hoar using a cold ceiling. It then turns its attention to the effects of parent grain orientation and wind direction on surface hoar growth. This paper hypothesized that surface hoar would grow with the same orientation as the parent grain regardless of wind direction. This was consistent with field observations that surface hoar orientation is randomly oriented, reflecting the random orientation of the parent grain. In fact, it was found that wind direction plays a central role in creating a random distribution of crystal orientation in well-developed surface hoar, while beneath this lays an ordered substructure reflective of parent grain shape and orientation.

Background

Surface hoar, essentially frozen dew, is the primary weak layer in slab avalanche occurrence (McClung et al., 2010). Its growth orientation could have a significant impact on the layers structural strength once buried. Further, its orientation on the snow surface has significant implications for solar reflectivity and, by extension, for satellite remote sensing models. An accurate model of surface hoar growth orientation could substantially aid in the understanding of the earth's energy balance.

According to McClung et al. (2006), surface hoar forms when "the water-vapor pressure in the air exceeds the equilibrium vapor pressure of ice at the surface." Two conditions are necessary for its formation: 1) sufficient supply of water vapor and 2) a large temperature gradient above a snow surface cooled below the ice point. Previous

lab-grown surface hoar did not utilize a cold ceiling to create the required temperature gradient. Rather, parent crystals were mounted on a plexiglass plate suspended upside down above a vapor source (Adams et al., 2003). This model does not represent the effects of the long wave coupling of the snow surface with the night sky. To address this problem Montana State University (MSU) constructed a cold chamber equipped with a ceiling that can be cooled to -50°C. The ceiling allows surface hoar to be grown under simulated nighttime conditions and distinguishes this study.

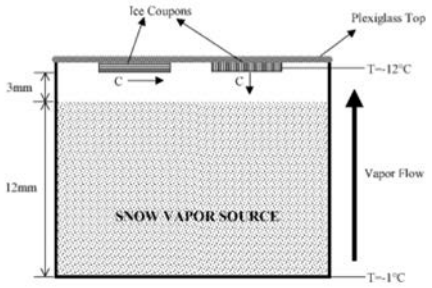


Figure 1: Adams et al. (2003) method for crystal growth. Note, vapor is supplied through diffuse movement of air parallel to c-axis parent grain and no cold ceiling is used.

Additionally, little work has been done investigating the effects of parent grain orientation and wind direction on surface hoar growth. A 2003 study by Adams et al. found surface hoar grown on c-axis oriented parent crystals using diffuse vapor flux perpendicular to the parent grain surface resulted in uniformly oriented surface hoar (Fig. 11).

This paper examines the effect of parent axis orientation using vapor flow parallel to the surface of the parent grain (as opposed to the perpendicular diffusion used in Adams 2003). This more accurately reflects field conditions where wind transport often

influences vapor flux to the snow surface. Further, the cold ceiling more accurately reflects the clear night sky conditions.

Methods

Growing Surface Hoar

Early Montana State University attempts at surface hoar growth, by Andrew Slaughter, consisted of a 30'x30' box of snow exposed to the cold ceiling and an open, above freezing water source left to sublimate and deposit naturally on the snow surface. Due to the relative cold temperature of the ceiling compared to the snow surface, the result was substantial growth on the ceiling, but little growth on the snow surface (Fig. 2).



Figure 2: Hoar frost growth on the cold ceiling. Note swept and un-swept areas.

Therefore, it was concluded that a continuous stream of moist air blown across the snow surface would provide the needed vapor flux, as well as simulate natural conditions. In response, a shroud was constructed to contain the water vapor and three fans were used to direct the moist flow through pliable ducting and across the snow surface. The snow surface was raised to near the ceiling to facilitate temperature coupling between the two surfaces. The final experimental surface hoar set up is pictured in Figure 3.

The variables affecting growth—snow surface temperature, air temperature, relative humidity, long and short wave radiation flux, feed-water temperature, and air speed at the duct outlet—were recorded on thirty second intervals during surface hoar growth trials by an Agilent data logger (Table 1). The dew point temperature (T_D) required to initiate surface hoar growth was calculated, based on air temperature and vent outlet relative humidity readings, using equations outlined in Wanielsta et al. (1997):

$$T_D = \left(\frac{f}{100}\right)^{\frac{1}{8}}(112 + 0.9T) + 0.1T - 112$$

where f is relative humidity (%) and T is air temperature (°C).

Axial Orientation of Surface Hoar Growth

Ice from Lake Bonnie, Antarctica was used to examine the implications of parent grain orientation on surface hoar growth. The lake has no outlet and the only source waters are ephemeral streams in summer resulting in quiescent conditions and the formation of ice with vertically oriented c-axis.



Figure 3. Water source in shroud at lower left. Box of snow upper right.

Axial direction was verified utilizing the polarizing properties of ice. A thin plate like sample of Lake Bonnie ice was placed on a polarizing stage (similar to a Rigsby stage) between two polarized films (Fig. 4 and 5). Polarized light from the first lens passed unaffected through c-oriented ice and was thus extinguished by the upper lens. Conversely, randomly oriented ice re-scattered the polarized light and produced a mosaic of colors when passed through the upper lens. To further verify the axial orientation of the ice, a thin veneer of 0.5% polyvinyal formal (a.k.a Formvar or Vinylec) solution was applied to the surface of the ice. Under a microscope the hexagonal structure of the ice crystals was apparent, confirming axial orientation.

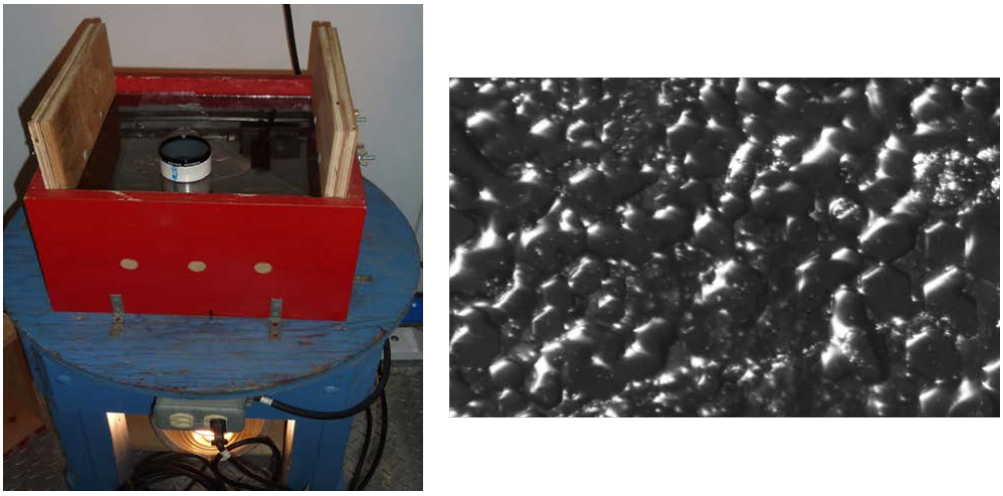


Figure 4: Polarizing stage used to determine crystal orientation (left). Ice sample with polyvinyal formal showing hexagonal crystal structure identifying the c- axis of the ice crystals (right).

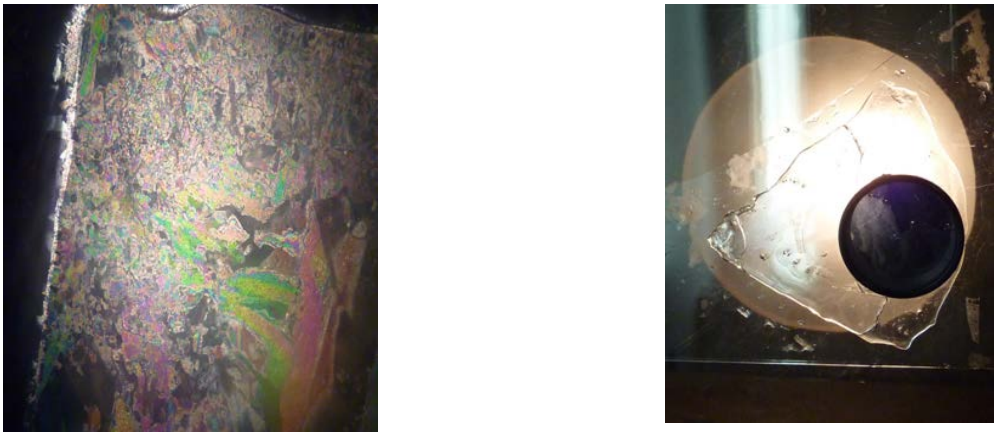


Figure 5: Ice samples on polarizing stage. Ice sample displaying a mosaic of crystal orientations as light passes through upper polarizing lens (left). Ice sample with upper polarizing lens completely extinguishing the light, confirming c-axis orientation (right).

With axial orientation of the ice crystals known, samples were embedded in snow composed of rounded grains as depicted in Figure 6. The known crystal axis was orientated perpendicular to the snow surface in all samples. Surface hoar was grown on the snow and ice surface using techniques explained previously.

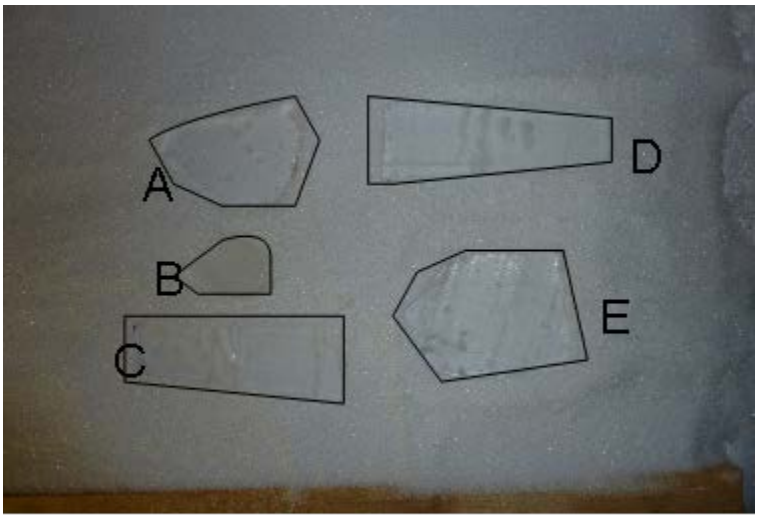


Figure 6: Plane view of parent grain ice embedded in snow surface. Vapor flux from fans was directed from the bottom of the picture toward the top. Sample A and E are oriented with a-axis facing up. Sample C and D are oriented with c-axis facing up. Sample B contains randomly oriented crystals.

In situ photographs of the developed surface hoar were taken at a variety of magnification levels (Fig. 9). Additionally, individual hoar crystals where carefully removed with tweezers and examined individually (Fig. 8). When removed the parent grain crystal orientation was recorded.

Results

Growing Surface Hoar

An Agilent Data Logger recorded snow surface temperature, air temperature, relative humidity, long and short wave radiation flux, feed-water temperature, and air speed at the duct outlet every 30 seconds. Mean values for surface temperature, relative humidity, and air temperature are shown in Table 1. The dew point was calculated using the equation outlined in the methods section. When surface temperatures fall below the dew point, deposition should occur. Therefore, positive values of "T_{surf}—T_{dew}" indicate expected surface hoar formation.

In Test 1, as expected, no surface hoar grew. In Test 2, the snow was moved closer to the cold ceiling to increase long wave radiation loss from snow and decrease snow surface temperature. The snow surface temperature did drop, but no surface hoar formed. In Test 3, the air temperature of the room was decreased by 5°C, the snow was moved closer to the cold ceiling, and the relative humidity of the supplied air was increased. Surface hoar growth occurred as predicted.

Table 1: Surface Hoar Growth Results.

	Snow Surface Temp (°C)	Probe_RH (%)	Probe_Air Temp (C)	Dew Point Temp (°C)	T_{surf}-T_{dew} (neg means growth)	T_{air}-T_{air}	Expected SH Growth?
Test 1: 21hr							**no**
Mean	-11.25	65.86	-8.36	-13.67	2.42	-2.89	
Min	-12.72	56.20	-8.84	-16.07	3.35		
Max	-10.27	79.26	-7.60	-10.61	0.35		
Test 2: 20hr							**no**
Mean	-12.72	62.18	-8.36	-14.38	1.67	-4.36	
Min	-13.80	52.57	-8.84	-16.88	3.08		
Max	-3.57	83.84	-3.03	-5.41	1.84		
Test 3: 33hr							**yes**
Mean	-15.32	67.98	-10.69	-15.51	0.19	-4.63	
Min	-17.81	56.39	-14.28	-21.13	3.32		
Max	-10.81	79.44	-7.73	-10.71	-0.10		

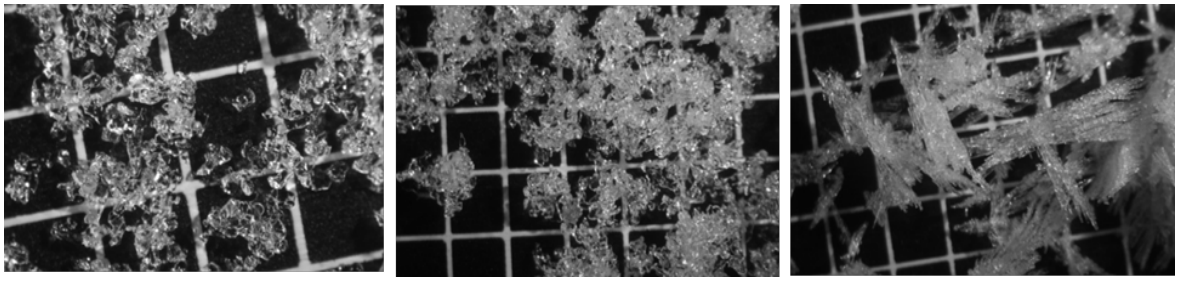


Figure 7: Photos from the three tests in Table 1: 1/24/11 no growth (left), 1/25/11 no growth (middle), 1/26/11 surface hoar (right). All photos on 2mm grid

The surface hoar maker was run for 23 hours in the first trial and for 8 hours in the second. Even though the crystals from the two trials were of different size, the same trends were evident. The growth was examined with the naked eye and with the help of a microscope. With the naked eye, ice with randomly oriented parent crystals displayed the highest crystal distribution density, followed by a-axis oriented parent crystals, and c-axis oriented parent crystals respectively.

Examinations also were conducted under a microscope with 6, 12, 25, and 50 power magnifications. Mean height and width ratios of individual crystals are presented in Table 2. Inspection showed surface hoar grown on randomly oriented parent crystals was tallest, followed by c-axis crystals, then a-axis crystals. Photos of individual crystals are presented in Figure 8. Photos of in situ surface hoar growth are shown in Figure 9.

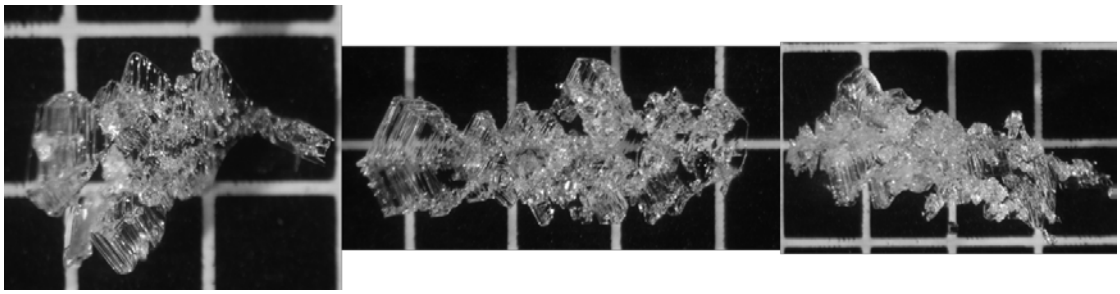


Figure 8: A-axis individual crystal growth (top left), c-axis individual crystal growth (above), and random individual crystal growth (bottom left). Note: All photos are on 2mm grid. The bottoms of all crystals are on the right of the photo with the top of the crystal on the left.

Table 2: Average calculated height to width ratio for each parent grain material (full data in Appendix A).

	Height to Width Ratio
A-axis	1.50
C-axis	2.54
Random	3.78

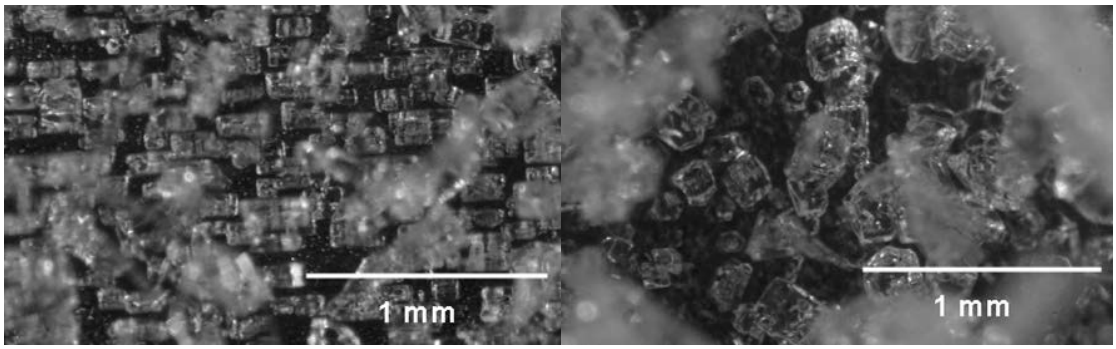


Figure 9: In situ growth on a-axis oriented parent grain (left). In situ growth on c-axis oriented parent grain (right). Note the uniform columns on left and uniform hexagonal plates on right. These features lie below the randomly oriented larger grains apparent shown in Figure 10. Note: Photos taken parallel to the parent grain crystals orientation.

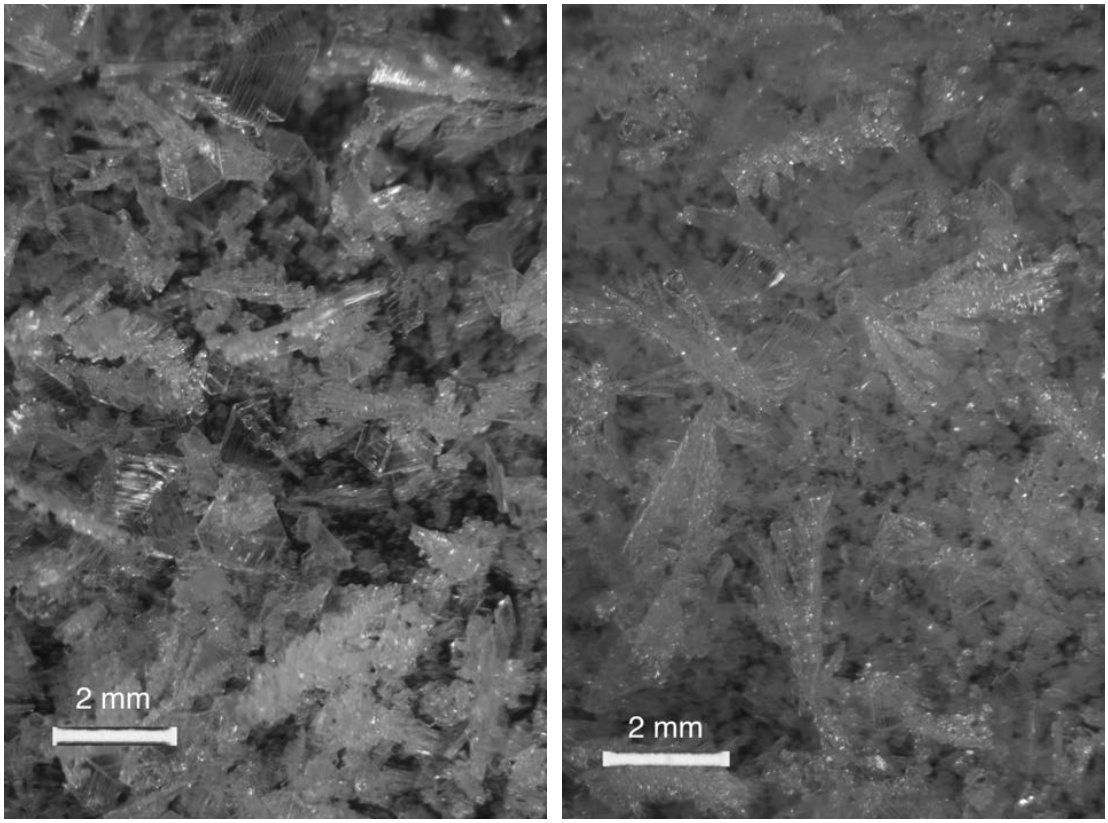


Figure 10: In situ growth on c-axis parent grain (left). In situ growth on a-axis parent grain (right). Note the higher crystal distribution density in a-axis growth.

Discussion

Surface Hoar Growth

Every thirty seconds, the data logger recorded a variety of parameters (detailed in the methods section). Table 1 shows the mean, minimum, and maximum recorded surface temperature of the snow, relative humidity at the duct outlets, and the air temperature from three separate tests. Some variation in these parameters is expected through the course of the experiment as researchers open and close doors (affecting air temperature), the cold ceiling becomes covered with hoar frost (affecting snow surface temperature), and the water heater cycles on and off (affecting relative humidity).

Nevertheless, it can be seen in Test 1 that the average snow surface temperature never fell below the average dew point temperature of the air (i.e. T_{surf}-T_{dew} never became negative). Further, inspection of the full data set shows at no point in the duration of the experiment did this occur. In line with expectations, no surface hoar formed. In Test 2, with the snow surface closer to the cold ceiling (≈0.5 m), long wave coupling decreased the average snow surface temperature by 1.47°C compared to test one. Average values of T_{surf}-T_{dew} also decreased (meaning conditions were closer to producing surface hoar than in Test 1). Inspection of the full data set (20 hrs) shows a two-hour stretch and one-hour stretch where T_{surf}-T_{dew} was negative; however, no surface hoar formed, suggesting conditions were not quite conducive to deposition. In Test 3, the overall room temperature was dropped by 5°C, the snow surface was positioned approximately 0.5 meters from the ceiling, and the relative humidity of the outlet fans was increased by increasing the feed water temperature. The result was significant surface hoar formation.

The average T_{surf}-T_{dew} was 0.19°C (< 0°C indicates surface hoar growth). Most importantly, inspection of the full data set shows nearly 11 (of 30) hours during which conditions were conducive to growth (T_{surf}-T_{dew} was negative). Final snow grain forms from each of the three tests can be seen in Figure 7.

In Test 1, where the snow surface was approximately 1.5 meters from the ceiling, coupling with the cold ceiling allowed the snow surface temperature to average 2.89°C colder than the surrounding air temperature. In Tests 2 and 3, with the snow within 0.5 meters of the ceiling, the average snow surface temperature was 4.36°C and 4.63°C less than the surrounding air respectively. The cold ceiling's effect on the snow surface was strongest at the start of the experiment and dropped off as hoar frost condensed on the ceiling. Similar to clouds in the sky, the frost in the ceiling absorbed incoming radiation from the snow surface and reflected it back to the snow, keeping it warmer than when the ceiling was dry.

Axial Orientation of Surface Hoar Growth

The initial hypothesis guiding the experimental design was that surface hoar would pick up the axial orientation of the parent grain regardless of wind direction. This experiment used a 2-3 m/s wind directed perpendicular to the parent grain's c-axis. It was speculated that growth would be uniform, similar to the results from Adams et al. (2003), in which vapor diffusion occurred parallel to the parent grain's c-axis (Fig. 1). A cursory examination of the two photos in Figure 11 suggests this hypothesis is invalid. In fact, wind direction appears to play a significant role in creating the random distribution of surface hoar orientation once the grains have established a certain size. When vapor is

supplied, as in Adams et al., through diffusion from a source parallel to the c-axis of the parent grain, crystal growth is observed to be uniform (left photo), while turbulent flow perpendicular to the parent grain's c-axis (this study) produced randomly oriented surface hoar (right photo).

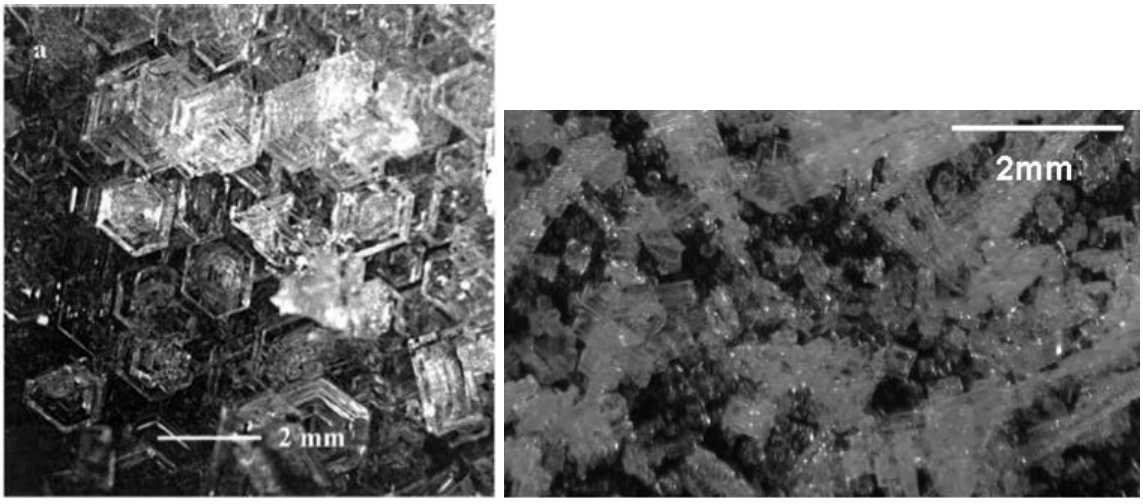


Figure 11: Left: In situ uniform crystal growth on c-axis oriented parent grain (diffuse vapor flux parallel to c-axis) (Adams et al., 2003; see also Fig. 1). Right: In situ randomly oriented crystal growth on c-axis oriented parent grain (2-3 m/s wind perpendicular to c-axis). Note the turbulent wind blown across the parent sample created random crystal growth (left) while diffuse vapor movement parallel to the parent grain created uniformly oriented crystals. Substrate c-axis points out of the page.

What is less obvious in Figure 11 is the underlying crystal orientation. Below the large grained surface hoar, readily apparent in Figure 11, lie smaller crystals that appear to have a uniform orientation and shape. Figure 9 focuses on these smaller crystals, which lie closer to the parent grain surface. In particular, Figure 9-left illustrates a uniform pattern of rectangular columns lined up like cars on a freeway. The parent grain in this photo is oriented with the a-axis pointing toward the camera. The right photo,

taken at the same magnification, of the c-axis oriented parent grain shows uniformly distributed hexagonal plate like crystals.

One speculative reason for this behavior is illustrated in Figure 12. The larger surface hoar crystals block the wind, growing quickly and randomly in response to the turbulent air current. Meanwhile, below the upper reaches of the surface hoar, the air is less turbulent. Vapor flux is mostly dominated by diffusion downward in a process similar to that utilized by Adams et al. (2003). Under these conditions crystal growth picks up the underlying parent grain orientation. Further, less vapor flux means slower growth rates and smaller crystals.

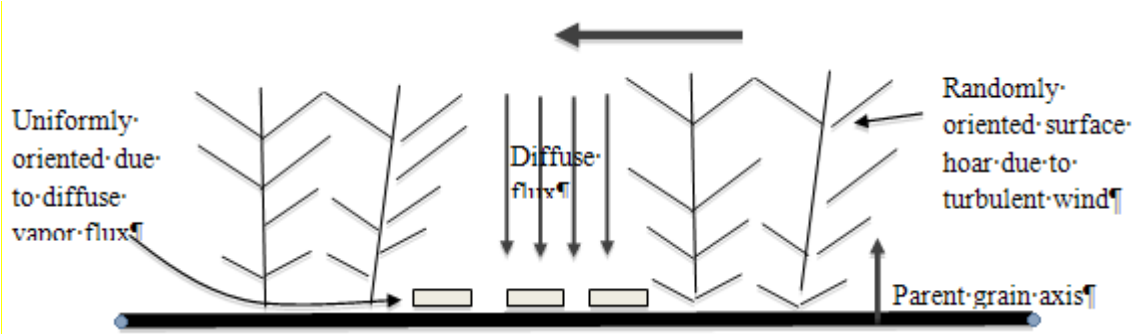


Figure 12: Turbulent wind across the top of the surface hoar creates random large crystals, while diffuse vapor flux downward through the larger grains causes the growth of small uniform crystals displaying parent grain orientation.

However, this hypothesis does not explain the initial stages of growth before the large crystal structures develop. Several questions remain. Does initial growth involve crystals oriented along parent grain axis? If so, which crystals are selected for preferential growth and why? Further study is needed of the initial growth conditions.

While orientation with respect to wind direction of the large surface hoar grains (greater than 2 mm) appears random, there are observable patterns in the width to height

ratios of individual crystals. Table 2 provides average height to width ratios of crystals from respective parent grain orientations. Low ratios imply a preference for crystals to be wide and short. Thus, a-axis parent grain crystals tend to be wide and short while c-axis parent grain crystals tend to be tall and thin. This is consistent with previous observation that subsurface crystals on a-axis parent grains are also wider than they are tall. If these tiny crystals act as nucleation surfaces for subsequent larger grain growth, it is expected that a-axis parent grains will grow wide short crystals, while the opposite is true for c-axis parent grains. Thinnest of all were the randomly oriented parent grain crystals. These crystals also displayed the highest crystal distribution density. It is speculated that the crystals were close enough to each other the tops were the only locations with the appropriate surface pressure gradient to facilitate growth. Figure 13 illustrates the three cases.

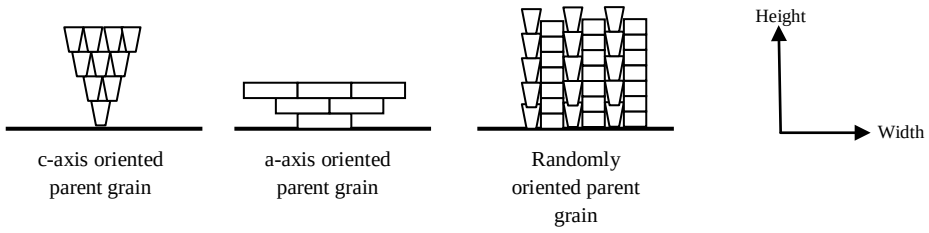


Figure 13: Illustration of typical width to height ratios based on respective parent grain orientation. It is speculated that the tall skinny nature of the randomly oriented grains is due to its high density whereas the other two are reflective of parent grain orientation.

Finally, the crystal distribution density of a-axis growth was higher than c-axis growth (Fig. 10). This is likely a product of growing the surface hoar at -15°C, a temperature favorable to a-axis growth (Nakaya, 1954).

Conclusion

Montana State University's cold ceiling provided a unique resource for simulating the cooling effects of the night sky on surface hoar formation. Three tests were conducted varying air temperature, relative humidity, and the distance of the snow surface from the ceiling. It was demonstrated that the ceiling produced an average snow surface temperature between 2.89°C and 4.63°C cooler than the surrounding air. Further, it was shown that surface hoar could be predictably grown in a lab setting. With this ability researchers are no long limited to field studies of surface hoar, nor are they at the whim of weather conditions.

Attention was then turned to the effects of wind direction and parent grain orientation on surface hoar growth. Ice samples with known axial orientation were used as a substrate for surface hoar growth. It was found that fully developed surface hoar crystals were randomly distributed when a turbulent wind was blown perpendicular to the parent grain surface. However, beneath the large grains, near the parent grain surface, crystal growth becomes more predictable. C-axis parent grains produced hexagonal plates, while a-axis parent grains produced columns in uniform order. It is speculated that these smaller crystals are shrouded from turbulent wind by their taller neighboring crystals leaving vapor to be supplied primarily through diffusion. Additional research needs to be conducted concerning the initial phases of surface hoar growth. With the ability to selectively grow surface hoar with known orientation, optical testing of varying growth patterns can be conducted pinpoint an optical signature unique to differing orientations and morphologies. This, in turn, could allow accurate remote sensing of

surface hoar type. Further implications include the ability to explore the anisotropic characteristics of surface hoar (stronger in compression than in sheer) for varying orientations and morphologies.

Table 3: Supplemental information: size of individual surface hoar crystal

Trial 1				Trial 2			
	Individual	Height (mm)	Width (mm)		Individual	Height (mm)	Width (mm)
A-axis front	1	3	2	A-axis front	1	5	3
	2	4	1		2	4	2
	3	4	3		3	3	3
A-axis back	1	5	3	A-axis back	1	5	3
	2	2	3		2	5	3
	3	1	2		3	4	2
A-axis avg		**3.17**	**2.33**	**A-axis avg**		**4.33**	**2.67**
C-axis front	1	6	2	C-axis front	1	2	2
	2	7	2		2	6	2
	3	5	2		3	4	2
C-axis back	1	7	2	C-axis back	1	3	2
	2	5	2		2	6	2
	3	6	2		3	4	2
C-axis avg		**6.00**	**2.00**	**C-axis avg**		**4.17**	**2.00**
Random	1	8	3	Random	1	4	1
	2	8	2		2	5	1
	3	6	1		3	3	1
Random avg		**7.33**	**2.00**	**Random avg**		**4.00**	**1.00**

.

APPENDIX E:

METEORLOGICAL CONDITIONS DURING SURFACE HOAR GROWTH

Meteorlogical Conditions During Surface Hoar Growth

The following figures represent the environmental chamber conditions recorded every 30 seconds by and Agilent data logger (as detailed in the methodology chapter) during the course of each test. A detail of the instrumentation location is reproduced below and also given in the main text (see Figure 21). The results are presented in reverse order (test 3c to test 1a) so that data from the tests with optical properties are presented first. Note that during test 1a the single Campbell Scientific, Inc CS215 Relative Humidity and Temperature Probe used failed to work at the -30°C temperature of the experiment and no weather data is presented. Additionally, during test 1, no thermocouple array was buried in the snow and thus is not presented. Finally, for tests subsequent to test 1, three different probes were used to measure temperature and humidity. The location of the probes are shown in the diagram below. The Campbell Scientific, Inc CS215 Relative Humidity and Temperature Probe is called T air or simple Probe in the following figure, while the two Vaisala INTERCAP Humidity and Temperature Probe HMP60 are labeled HMP60 in the legend. Note that calculated values utilized measurements from HMP60_1 in tests 2 and 3 and the Campbell Scientific probe (labeled RH Probe below) for tests 1.

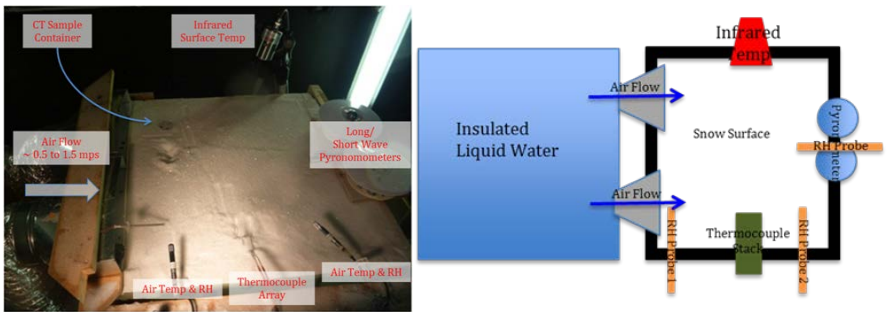
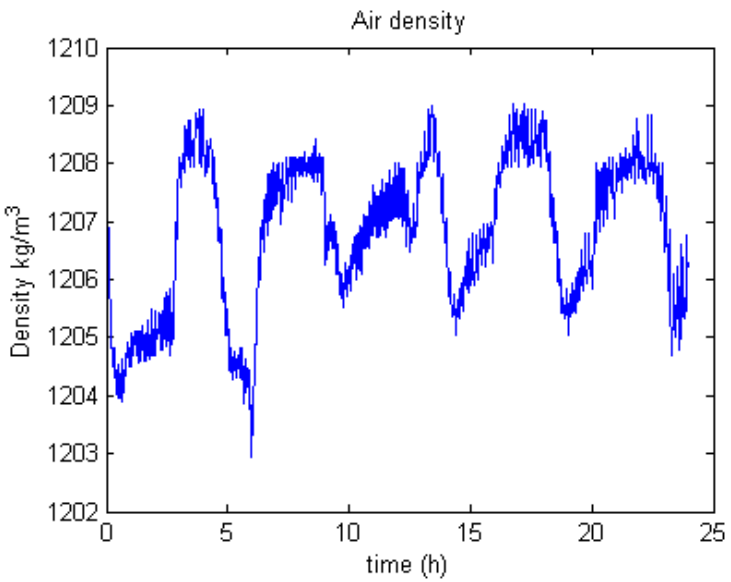
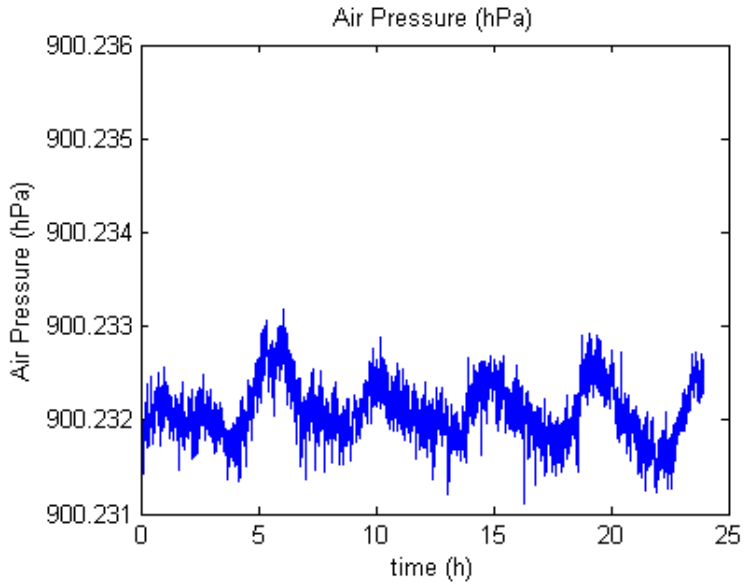
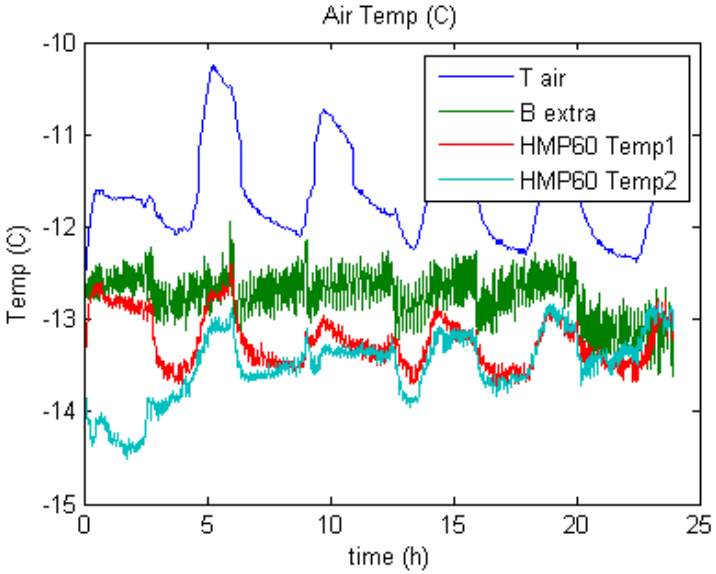
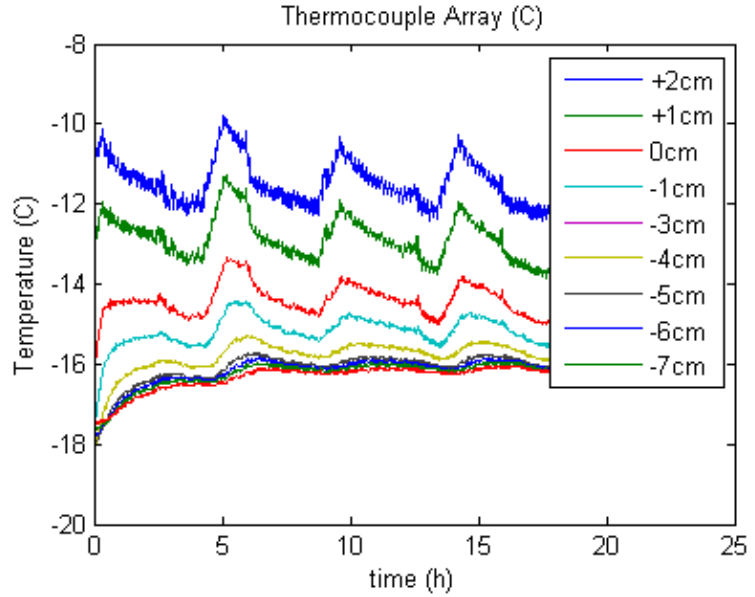


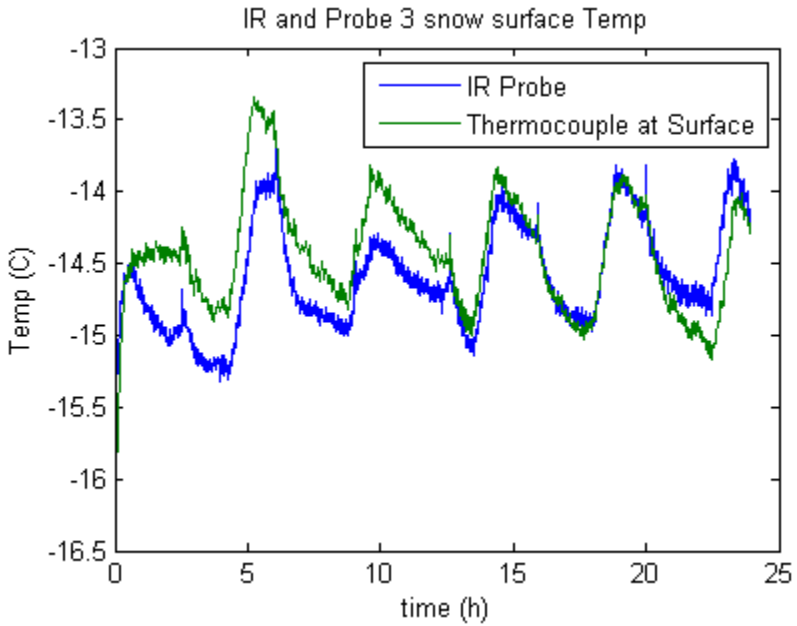
Figure 1 A) Detail of experimental set up and instrumentation. B) Functional diagram of experimental set up.

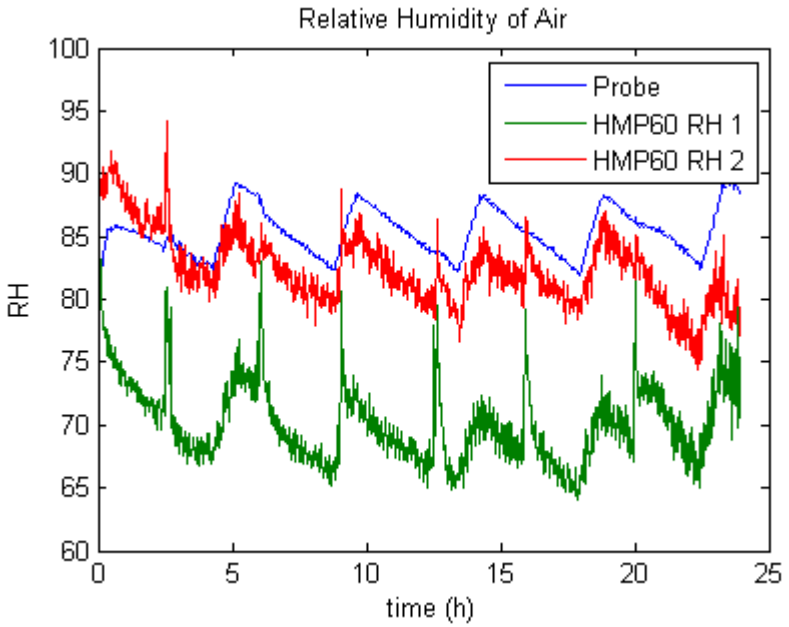

Air density
Density kg/m3
time (h)

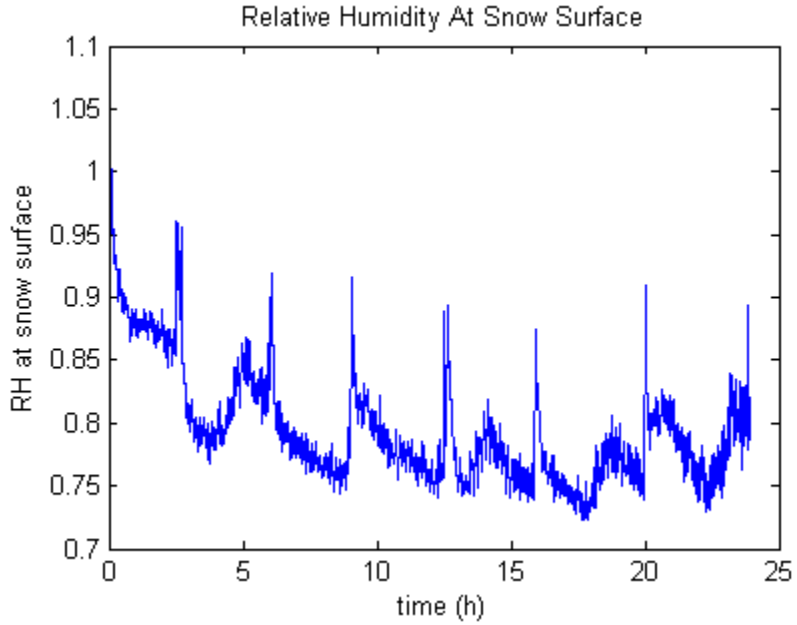

Air Pressure (hPa)
Air Pressure (hPa)
time (h)

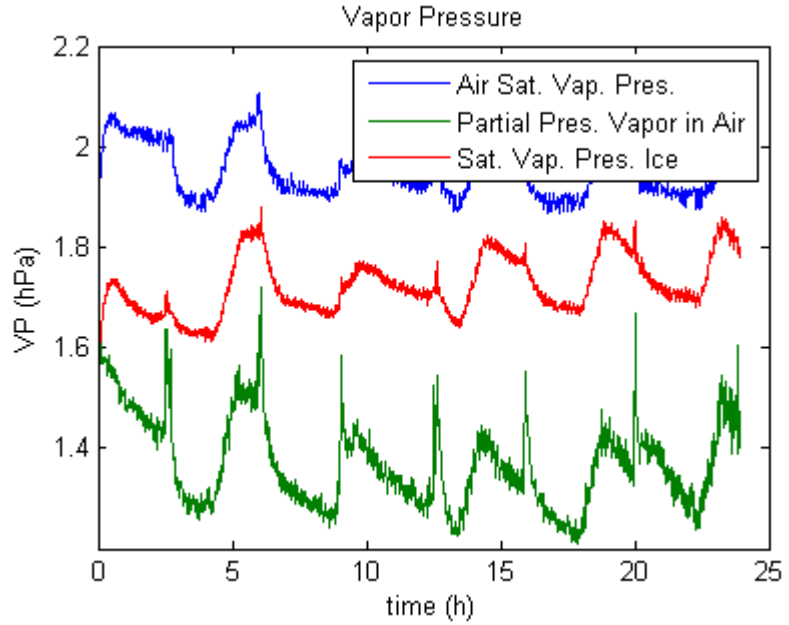

Air Temp (C)
T air
B extra
HMP60 Temp1
HMP60 Temp2
Temp (C)
time (h)


Thermocouple Array (C)
+2cm
+1cm
0cm
-1cm
-3cm
-4cm
-5cm
-6cm
-7cm
Temperature (C)
time (h)


IR and Probe 3 snow surface Temp
IR Probe
Thermocouple at Surface
Temp (C)
time (h)


Relative Humidity of Air
Probe
HMP60 RH 1
HMP60 RH 2
RH
time (h)


Relative Humidity At Snow Surface
RH at snow surface
time (h)


Vapor Pressure
Air Sat. Vap. Pres.
Partial Pres. Vapor in Air
Sat. Vap. Pres. Ice
VP (hPa)
time (h)

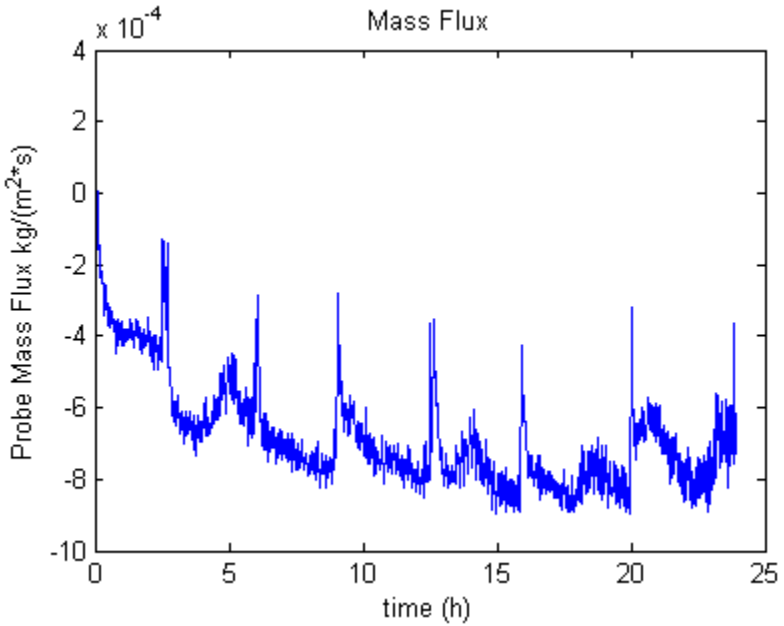
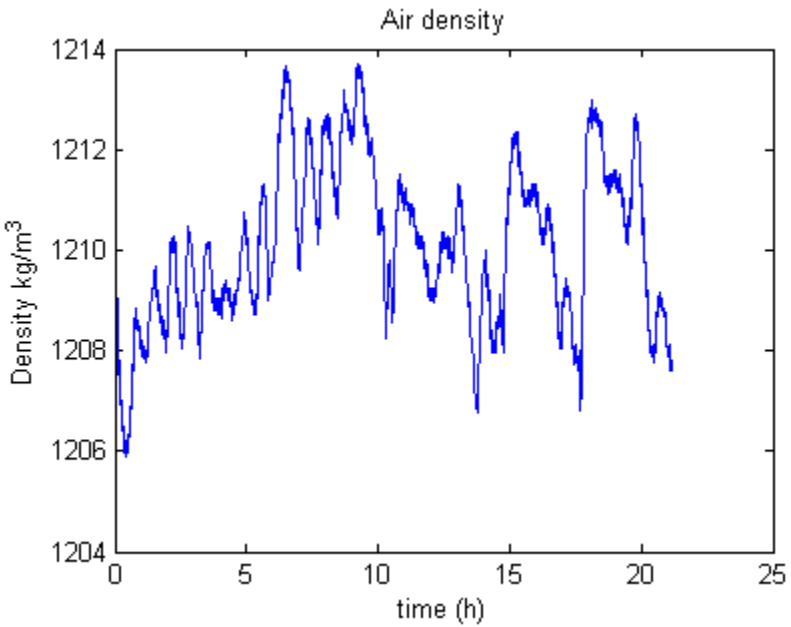
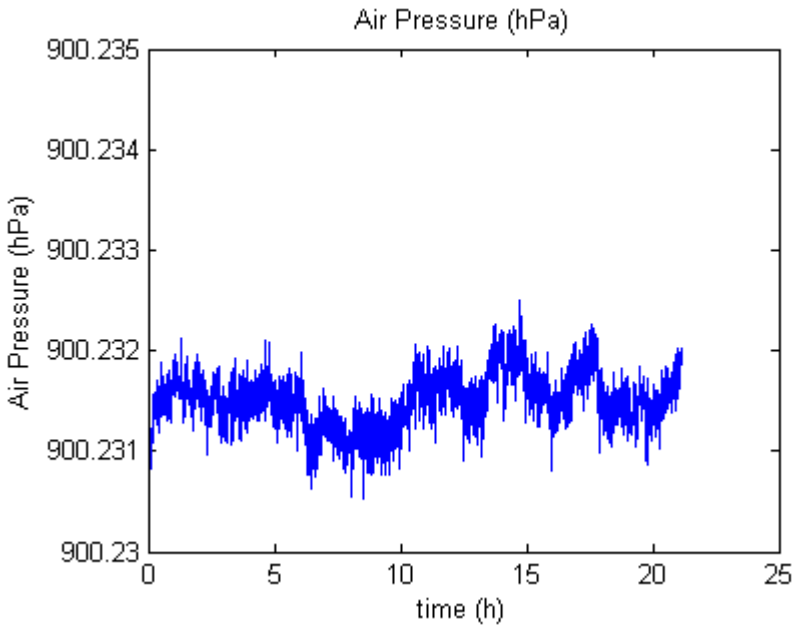
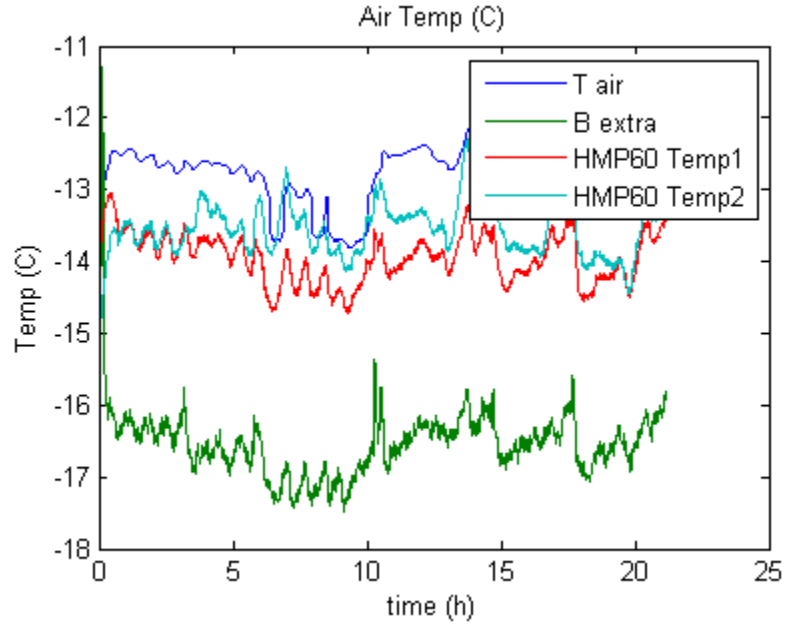
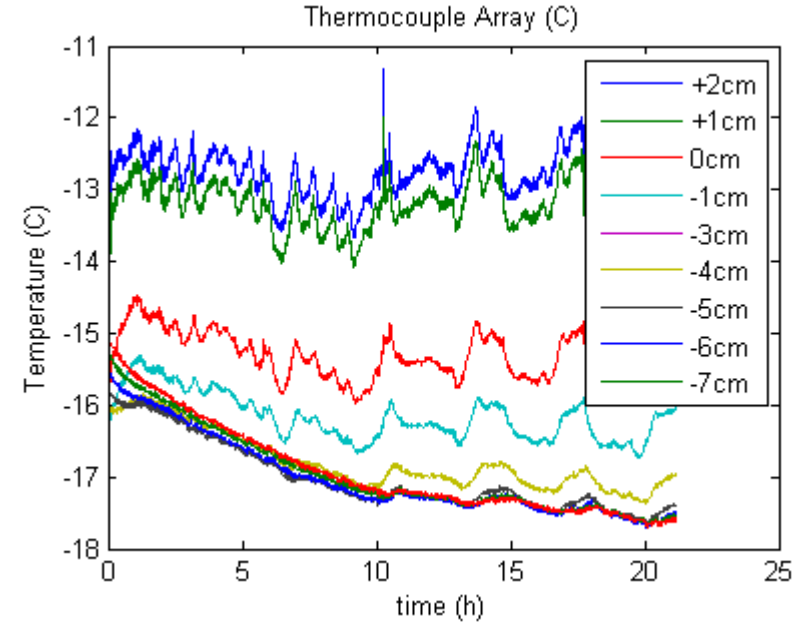


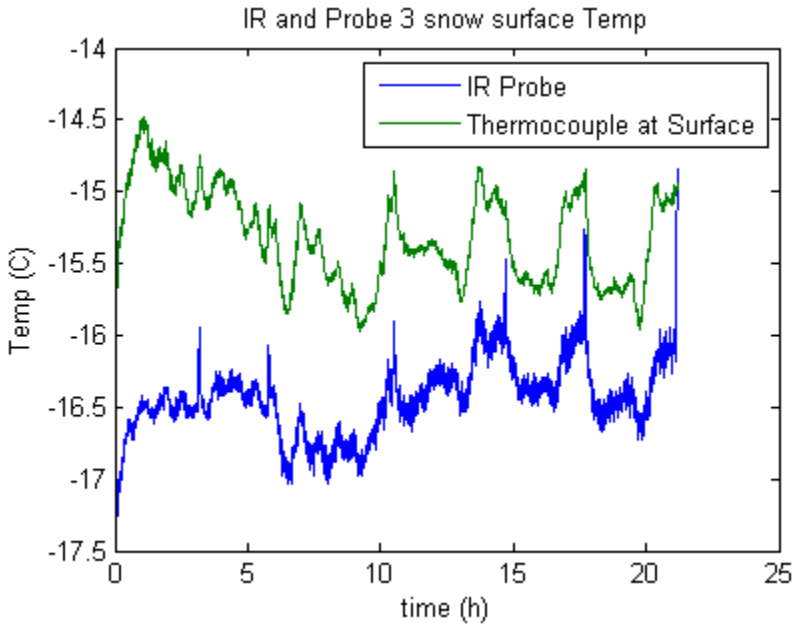
Figure 2. Test 3c 11/29/12. Environmental chamber data recorded during surface hoar growth experiments showing: air density, air pressure, air temperature, thermocouple array in snowpack, snow surface temperature as recorded by IR sensor as well as a thermocouple sensor (#3 at 0cm) on the snow surface, relative humidity several centimeters above the snow surface, relative humidity at the snow surface (calculated using snow surface temperature from IR sensor), vapor pressure with respect to ice from Equation (5), and mass flux as calculated from Equation (17).

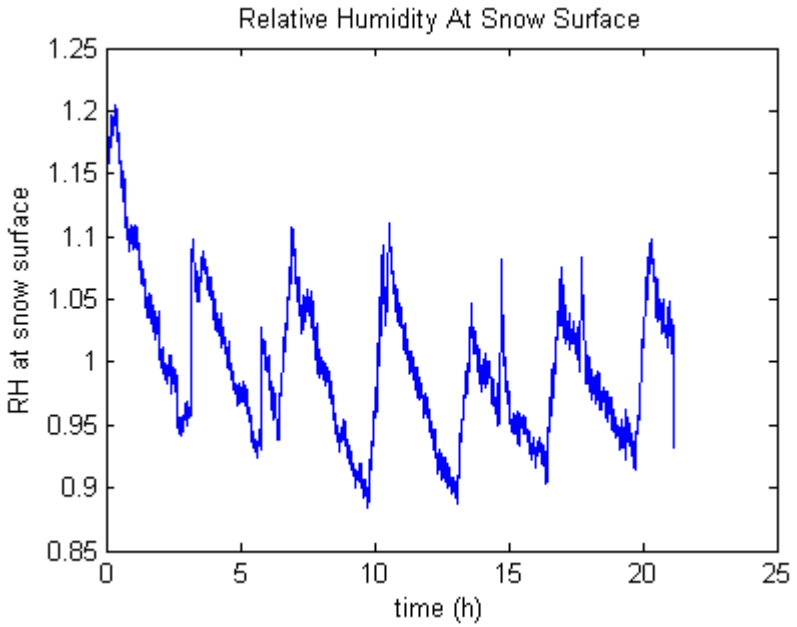

Air density
Density kg/m3
1214
1212
1210
1208
1206
1204
0
5
10
15
20
25
time (h)

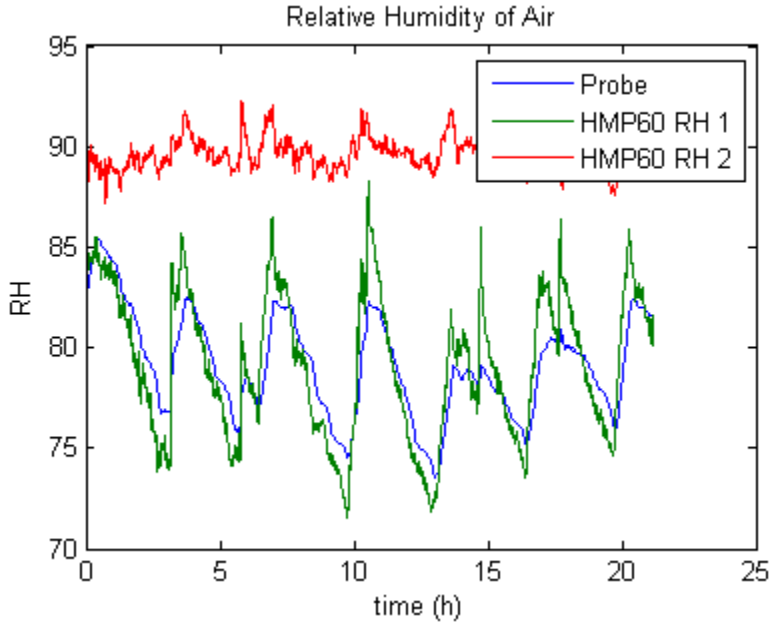

Air Pressure (hPa)
Air Pressure (hPa)
900.235
900.234
900.233
900.232
900.231
900.23
0
5
10
15
20
25
time (h)

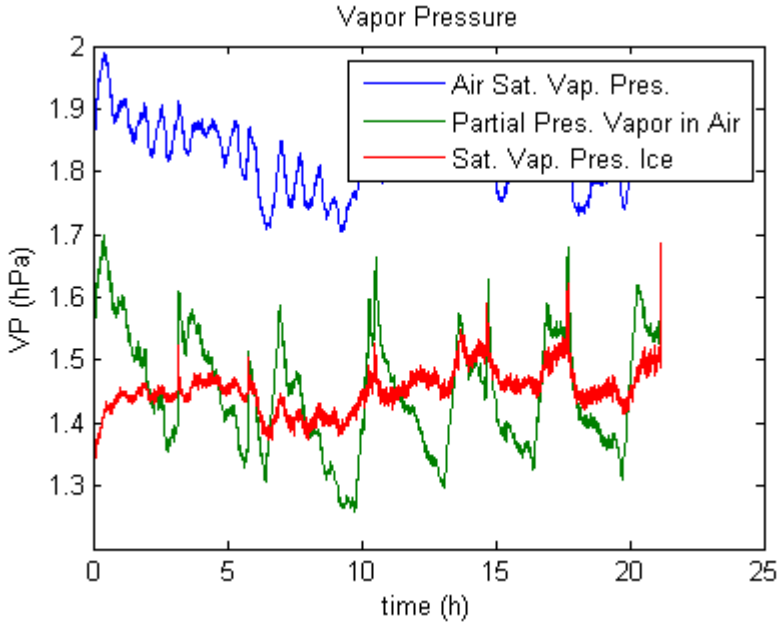

Air Temp (C)
Temp (C)
-11
-12
-13
-14
-15
-16
-17
-18
0
5
10
15
20
25
time (h)
T air
B extra
HMP60 Temp1
HMP60 Temp2


Thermocouple Array (C)
Temperature (C)
-11
-12
-13
-14
-15
-16
-17
-18
0
5
10
15
20
25
time (h)
+2cm
+1cm
0cm
-1cm
-3cm
-4cm
-5cm
-6cm
-7cm


IR and Probe 3 snow surface Temp
IR Probe
Thermocouple at Surface
Temp (C)
time (h)


Relative Humidity At Snow Surface
RH at snow surface
time (h)


Relative Humidity of Air
Probe
HMP60 RH 1
HMP60 RH 2
RH
time (h)


Vapor Pressure
Air Sat. Vap. Pres.
Partial Pres. Vapor in Air
Sat. Vap. Pres. Ice
VP (hPa)
time (h)

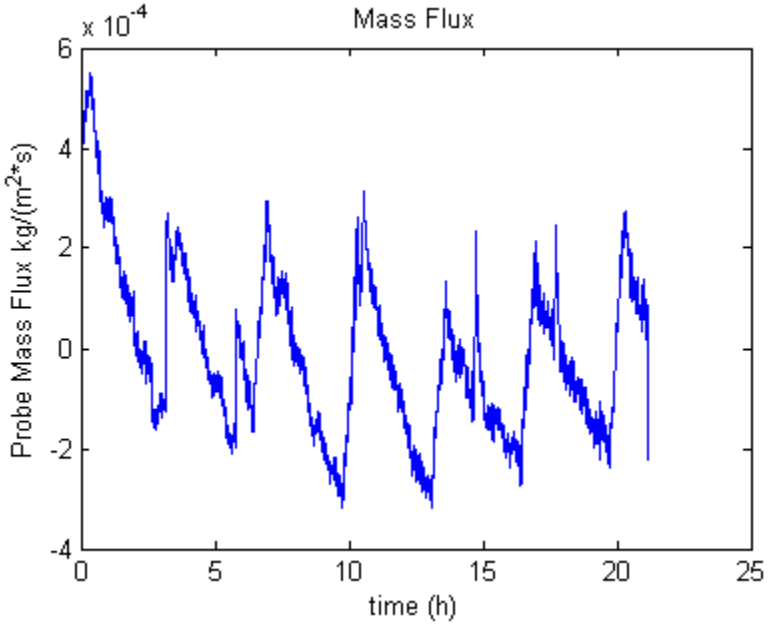
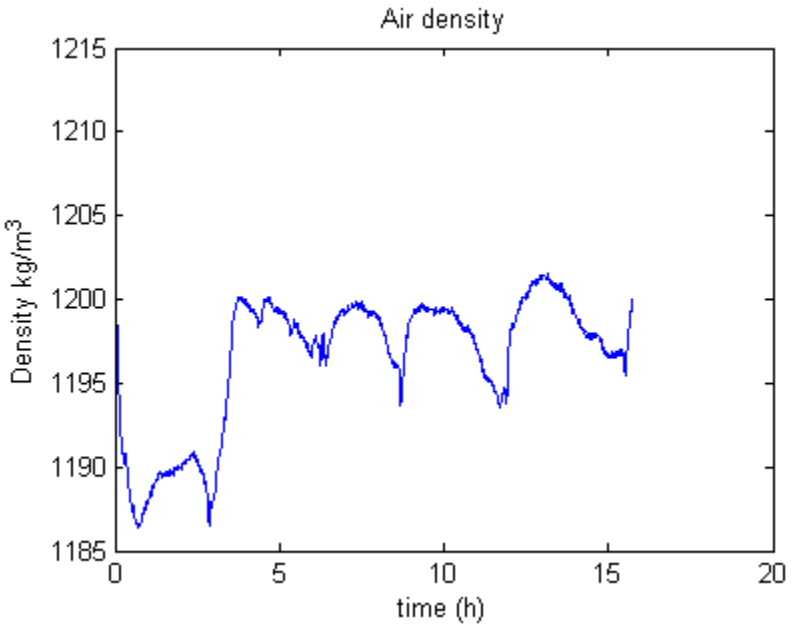
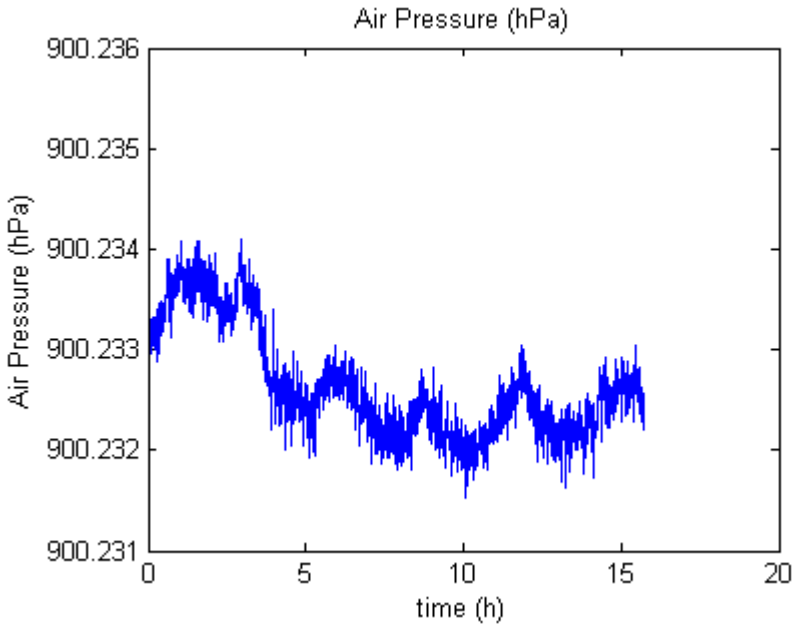
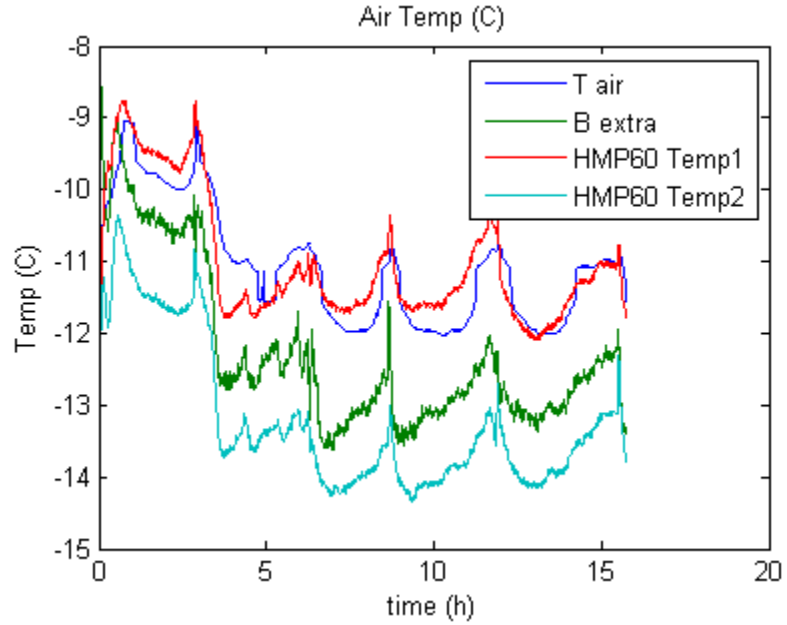
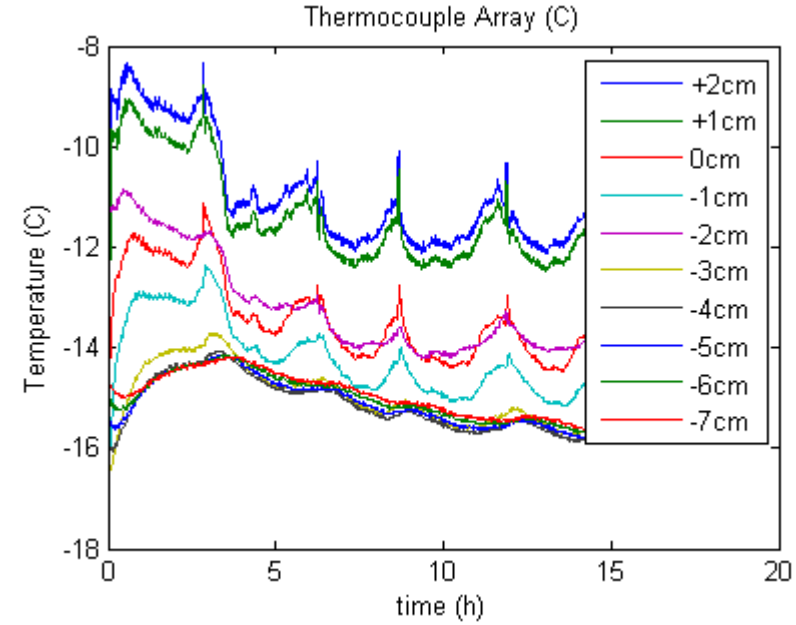


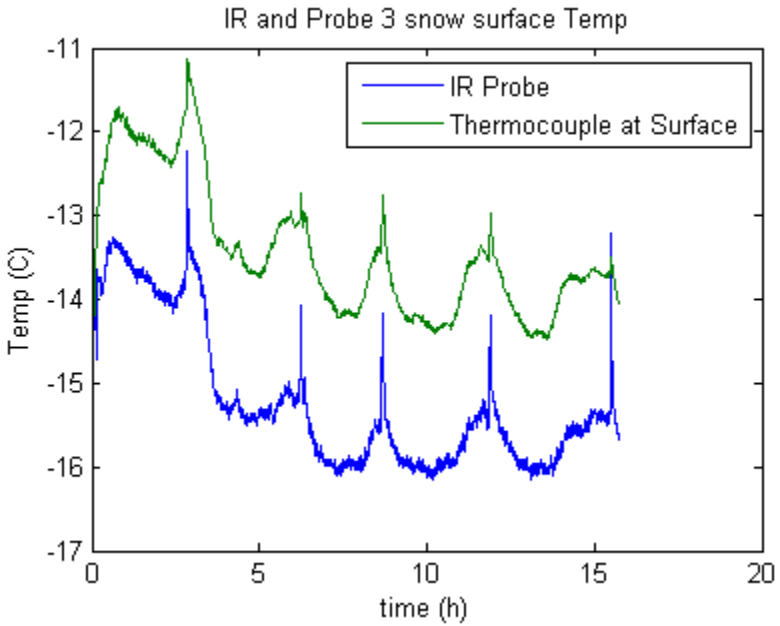
Figure 3. Test 3b 11/15/12. Environmental chamber data recorded during surface hoar growth experiments showing: air density, air pressure, air temperature, thermocouple array in snowpack, snow surface temperature as recorded by IR sensor as well as a thermocouple sensor (#3 at 0cm) on the snow surface, relative humidity several centimeters above the snow surface, relative humidity at the snow surface (calculated using snow surface temperature from IR sensor), vapor pressure with respect to ice from Equation (5), and mass flux as calculated from Equation (17).

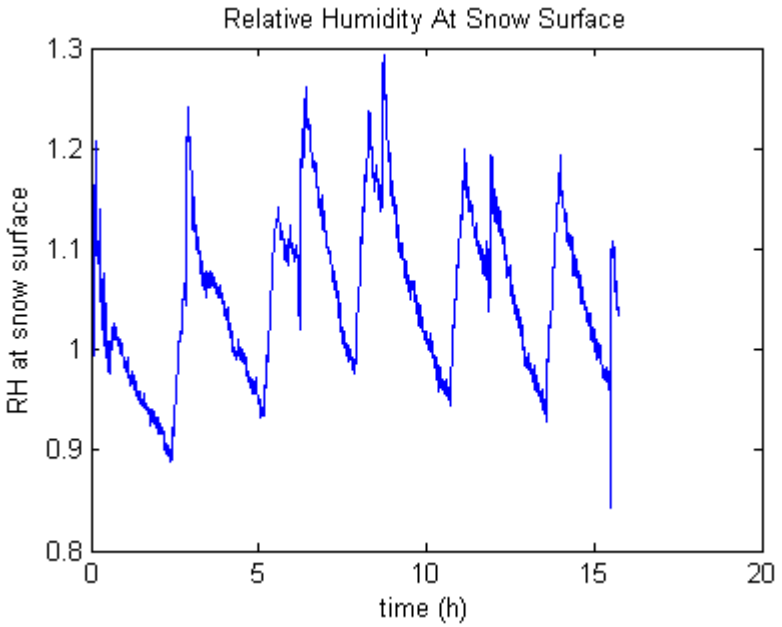

Air density
Density kg/m3
1215
1210
1205
1200
1195
1190
1185
0
5
10
15
20
time (h)

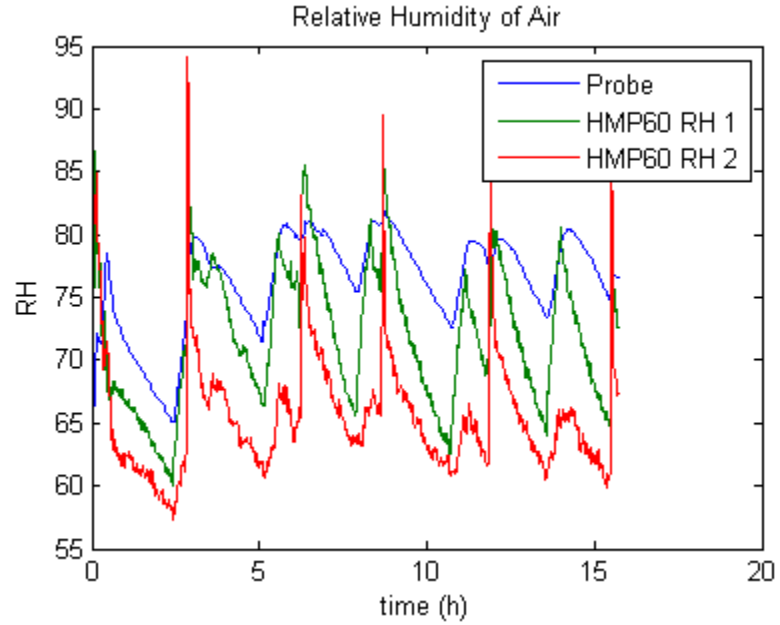

Air Pressure (hPa)
Air Pressure (hPa)
900.236
900.235
900.234
900.233
900.232
900.231
0
5
10
15
20
time (h)

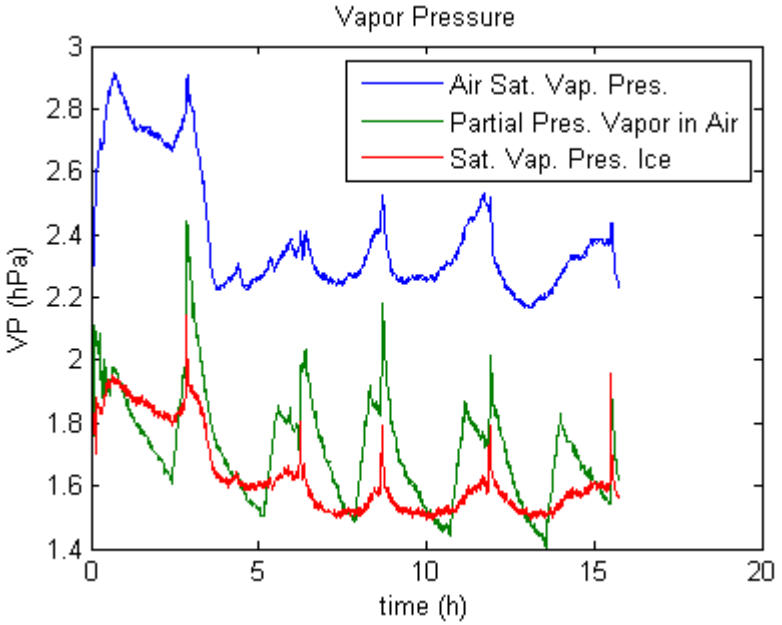

Air Temp (C)
Temp (C)
-8
-9
-10
-11
-12
-13
-14
-15
0
5
10
15
20
time (h)
T air
B extra
HMP60 Temp1
HMP60 Temp2


Thermocouple Array (C)
Temperature (C)
-8
-10
-12
-14
-16
-18
0
5
10
15
20
time (h)
+2cm
+1cm
0cm
-1cm
-2cm
-3cm
-4cm
-5cm
-6cm
-7cm


IR and Probe 3 snow surface Temp
IR Probe
Thermocouple at Surface
Temp (C)
time (h)


Relative Humidity At Snow Surface
RH at snow surface
time (h)


Relative Humidity of Air
Probe
HMP60 RH 1
HMP60 RH 2
RH
time (h)


Vapor Pressure
Air Sat. Vap. Pres.
Partial Pres. Vapor in Air
Sat. Vap. Pres. Ice
VP (hPa)
time (h)

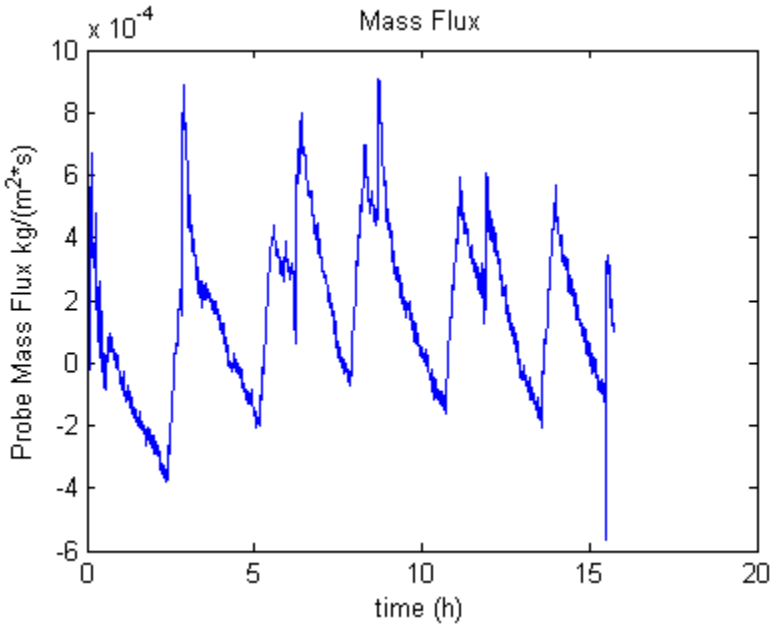
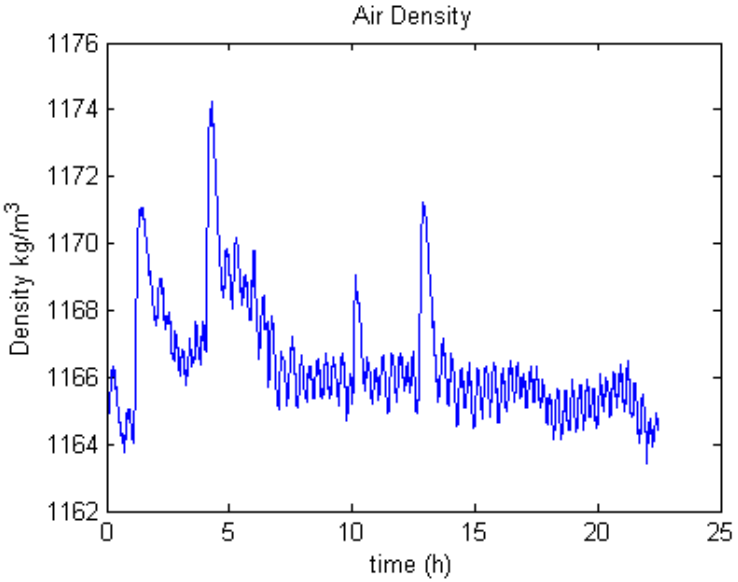
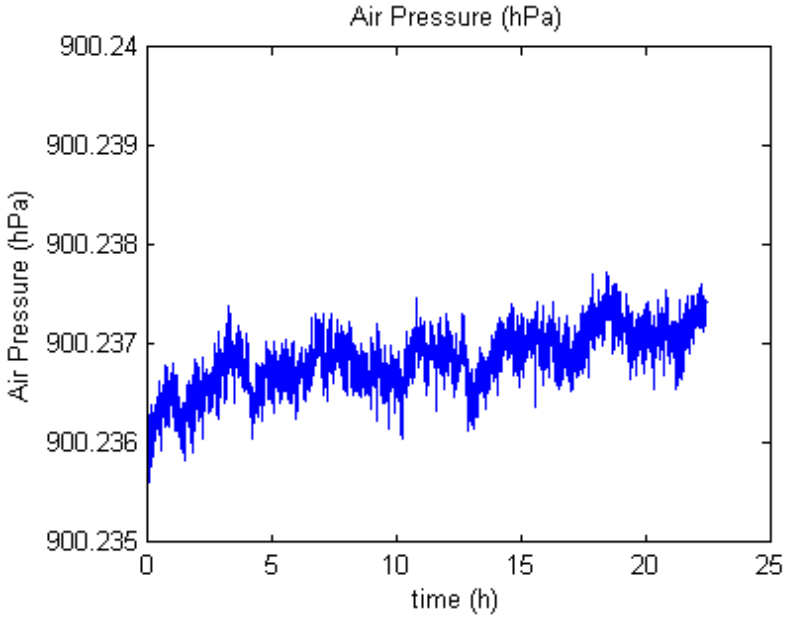
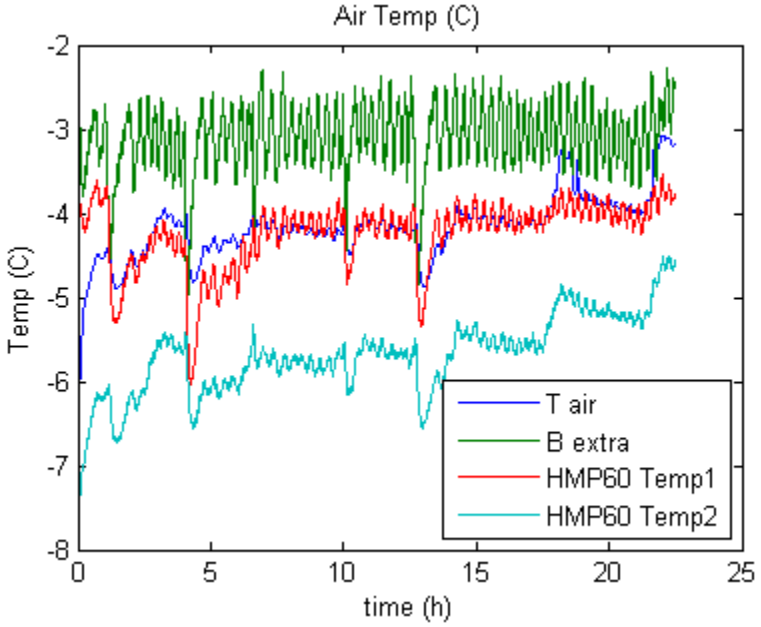
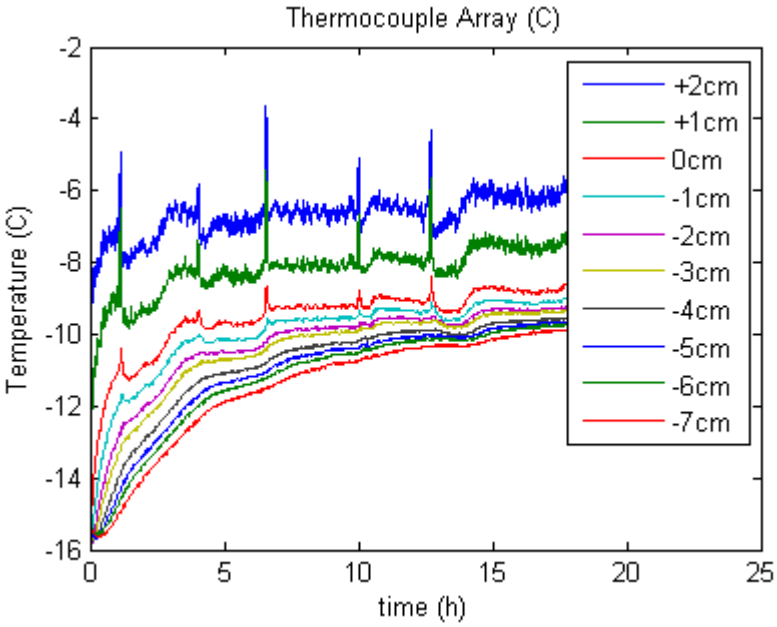


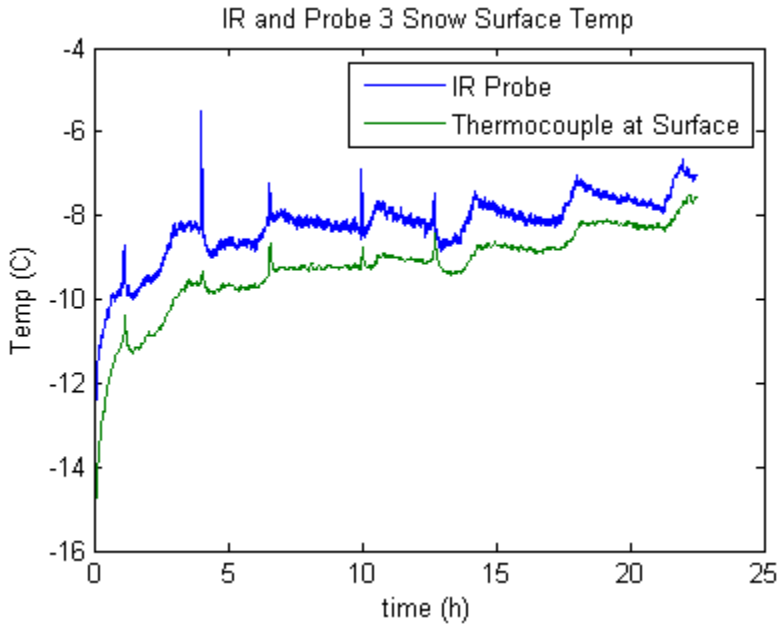
Figure 4. Test 3a 10/25/12. Environmental chamber data recorded during surface hoar growth experiments showing: air density, air pressure, air temperature, thermocouple array in snowpack, snow surface temperature as recorded by IR sensor as well as a thermocouple sensor (#3 at 0cm) on the snow surface, relative humidity several centimeters above the snow surface, relative humidity at the snow surface (calculated using snow surface temperature from IR sensor), vapor pressure with respect to ice from Equation (5), and mass flux as calculated from Equation (17).

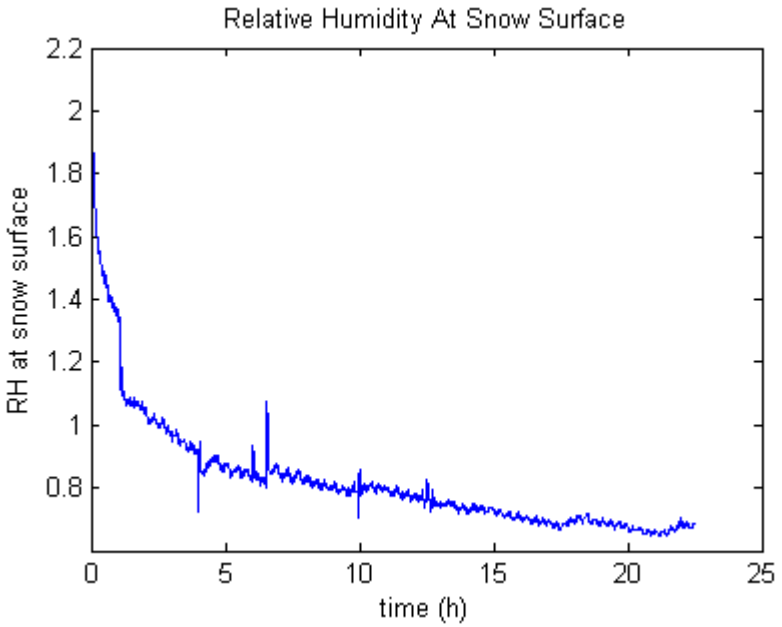

Air Density
Density kg/m3
1176
1174
1172
1170
1168
1166
1164
1162
0
5
10
15
20
25
time (h)

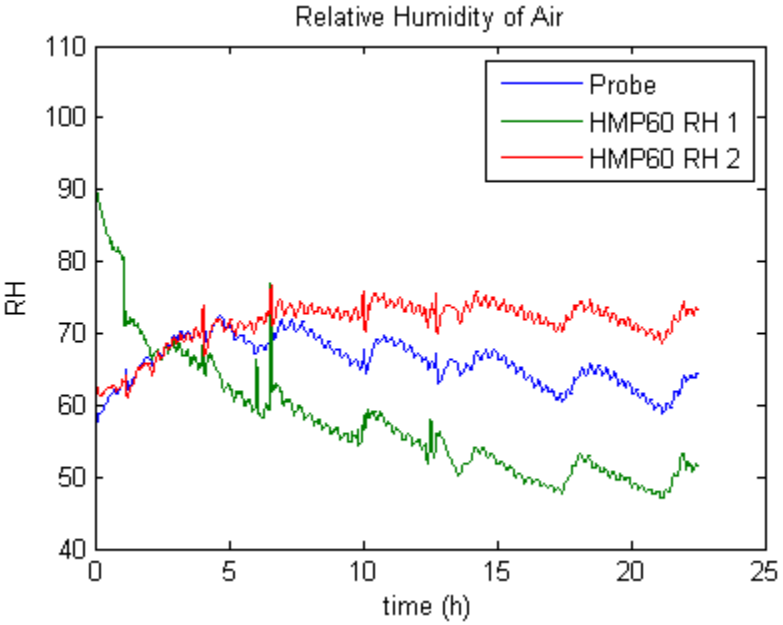

Air Pressure (hPa)
Air Pressure (hPa)
900.24
900.239
900.238
900.237
900.236
900.235
0
5
10
15
20
25
time (h)

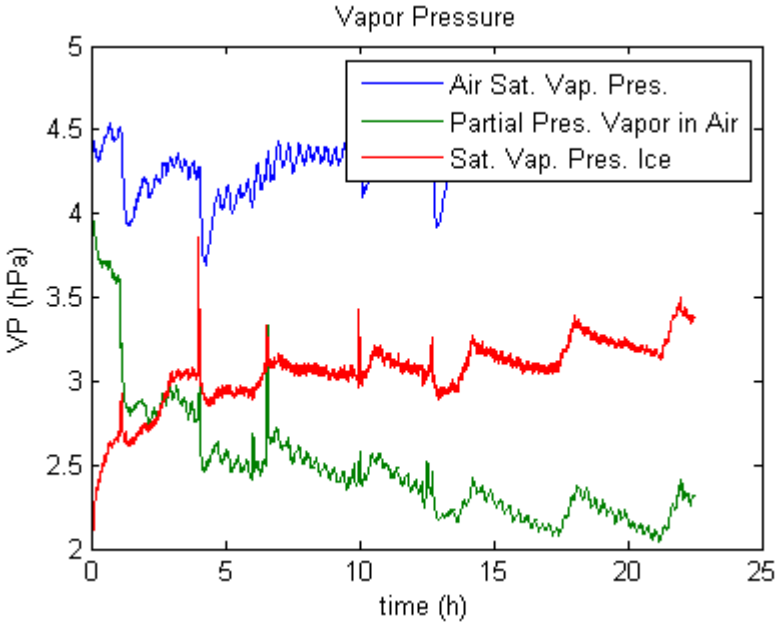

Air Temp (C)
Temp (C)
-2
-3
-4
-5
-6
-7
-8
0
5
10
15
20
25
time (h)
T air
B extra
HMP60 Temp1
HMP60 Temp2


Thermocouple Array (C)
Temperature (C)
-2
-4
-6
-8
-10
-12
-14
-16
0
5
10
15
20
25
time (h)
+2cm
+1cm
0cm
-1cm
-2cm
-3cm
-4cm
-5cm
-6cm
-7cm


IR and Probe 3 Snow Surface Temp
IR Probe
Thermocouple at Surface
Temp (C)
time (h)


Relative Humidity At Snow Surface
RH at snow surface
time (h)


Relative Humidity of Air
Probe
HMP60 RH 1
HMP60 RH 2
RH
time (h)


Vapor Pressure
Air Sat. Vap. Pres.
Partial Pres. Vapor in Air
Sat. Vap. Pres. Ice
VP (hPa)
time (h)

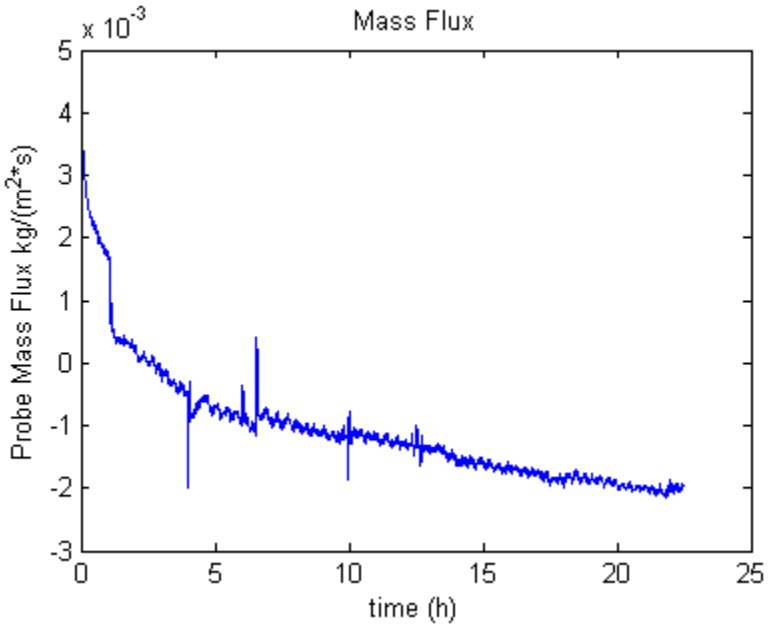
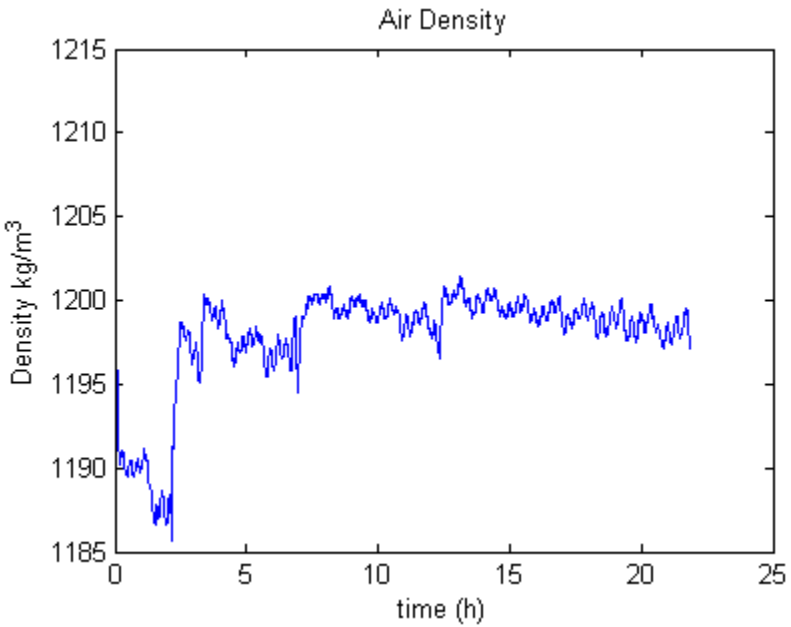
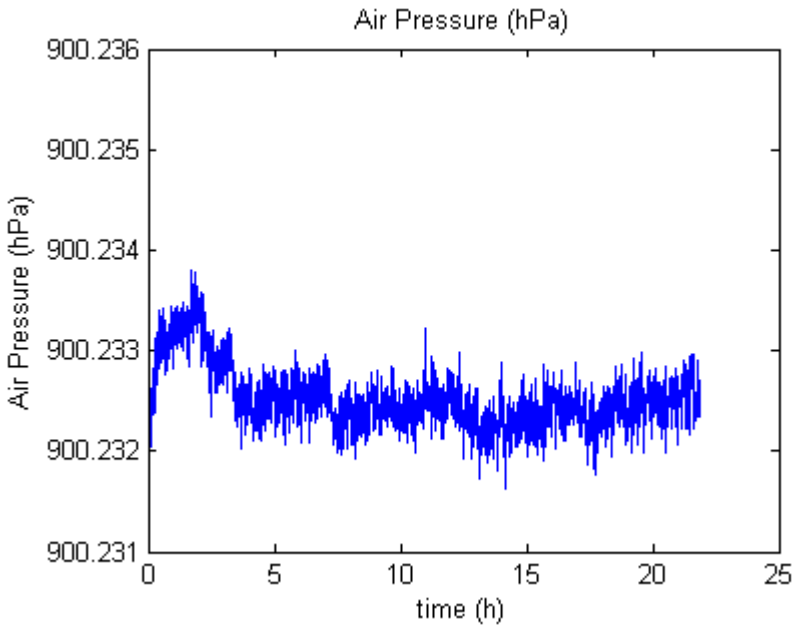
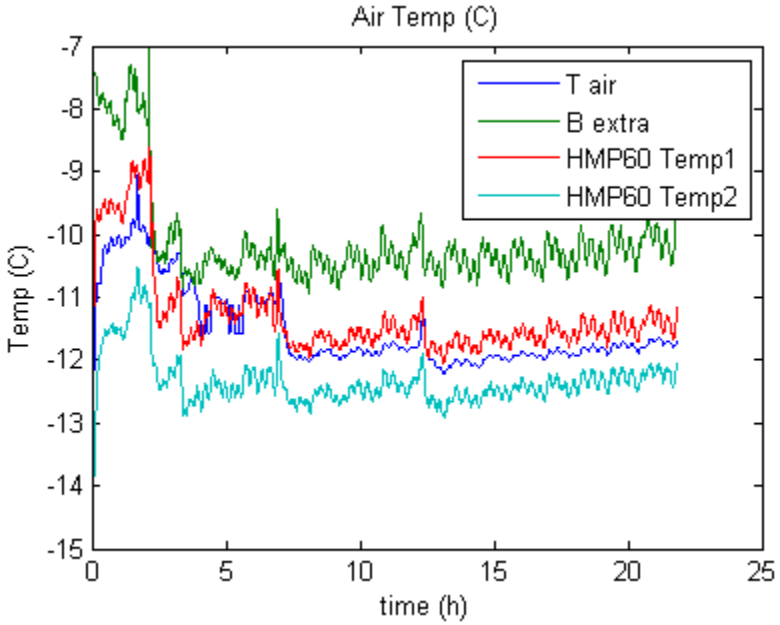
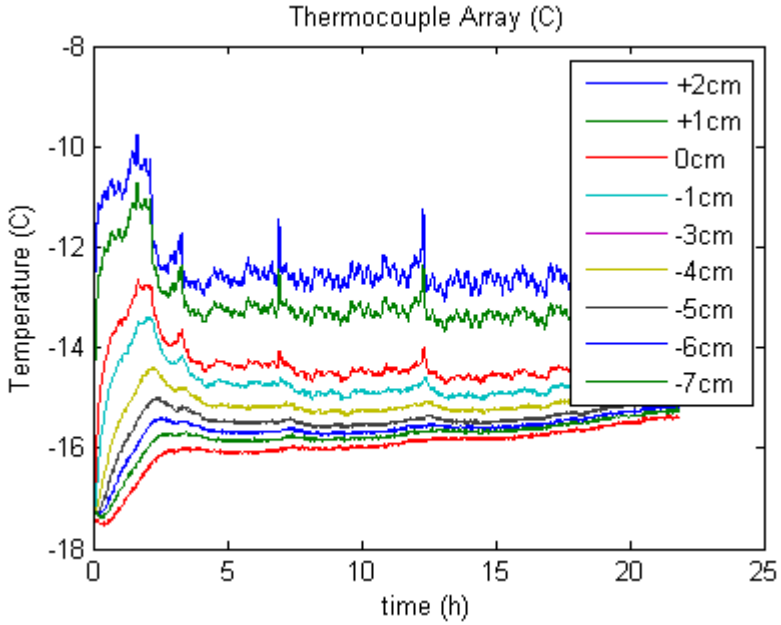


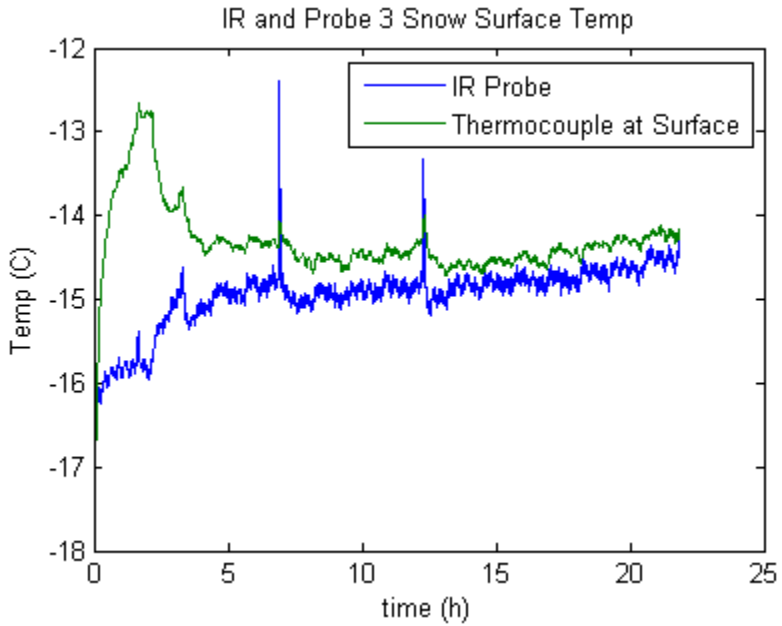
Figure 5. Test 2c 6/26/12. Environmental chamber data recorded during surface hoar growth experiments showing: air density, air pressure, air temperature, thermocouple array in snowpack, snow surface temperature as recorded by IR sensor as well as a thermocouple sensor (#3 at 0cm) on the snow surface, relative humidity several centimeters above the snow surface, relative humidity at the snow surface (calculated using snow surface temperature from IR sensor), vapor pressure with respect to ice from Equation (5), and mass flux as calculated from Equation (17).

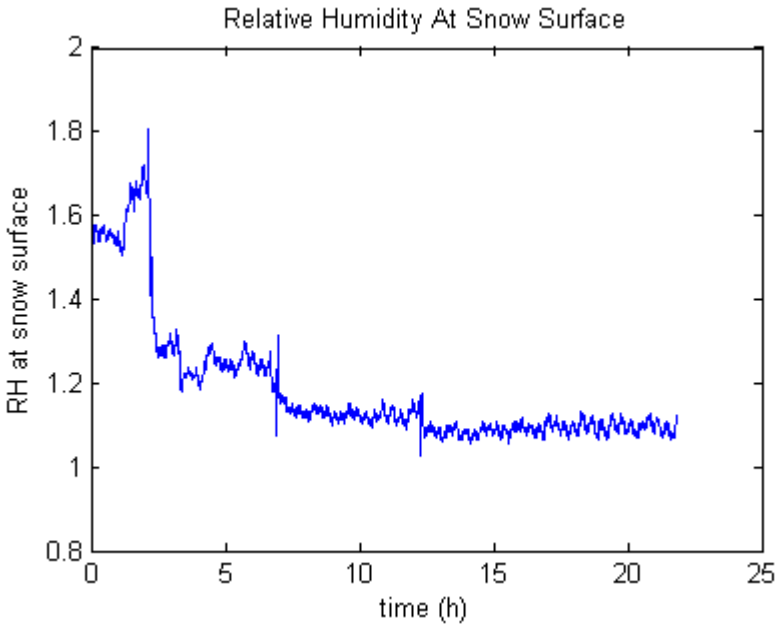

Air Density
Density kg/m3
time (h)

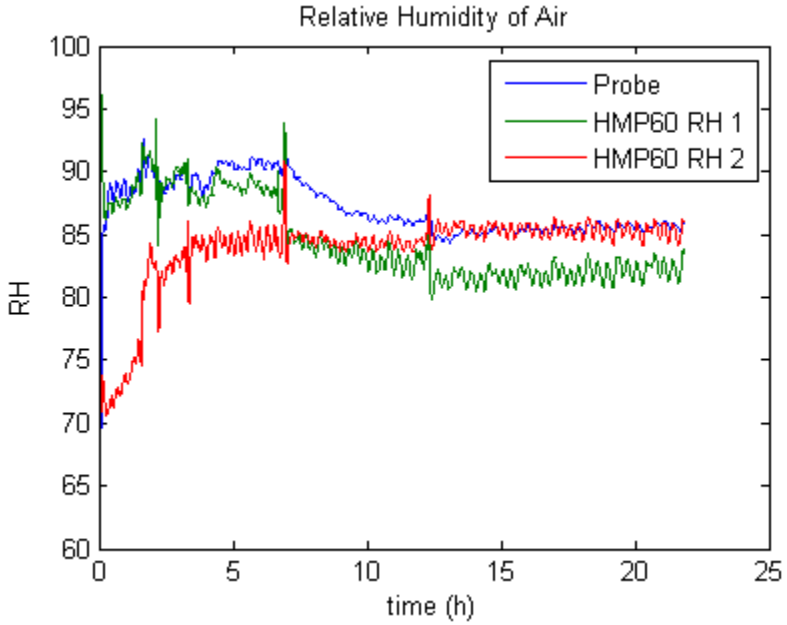

Air Pressure (hPa)
Air Pressure (hPa)
time (h)

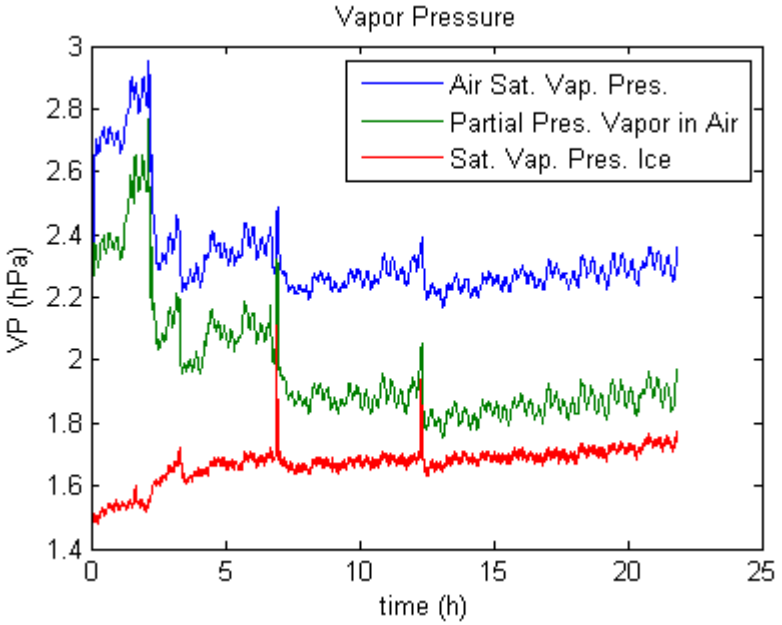

Air Temp (C)
Temp (C)
time (h)
T air
B extra
HMP60 Temp1
HMP60 Temp2


Thermocouple Array (C)
Temperature (C)
time (h)
+2cm
+1cm
0cm
-1cm
-3cm
-4cm
-5cm
-6cm
-7cm


IR and Probe 3 Snow Surface Temp
IR Probe
Thermocouple at Surface
Temp (C)
time (h)


Relative Humidity At Snow Surface
RH at snow surface
time (h)


Relative Humidity of Air
Probe
HMP60 RH 1
HMP60 RH 2
RH
time (h)


Vapor Pressure
Air Sat. Vap. Pres.
Partial Pres. Vapor in Air
Sat. Vap. Pres. Ice
VP (hPa)
time (h)

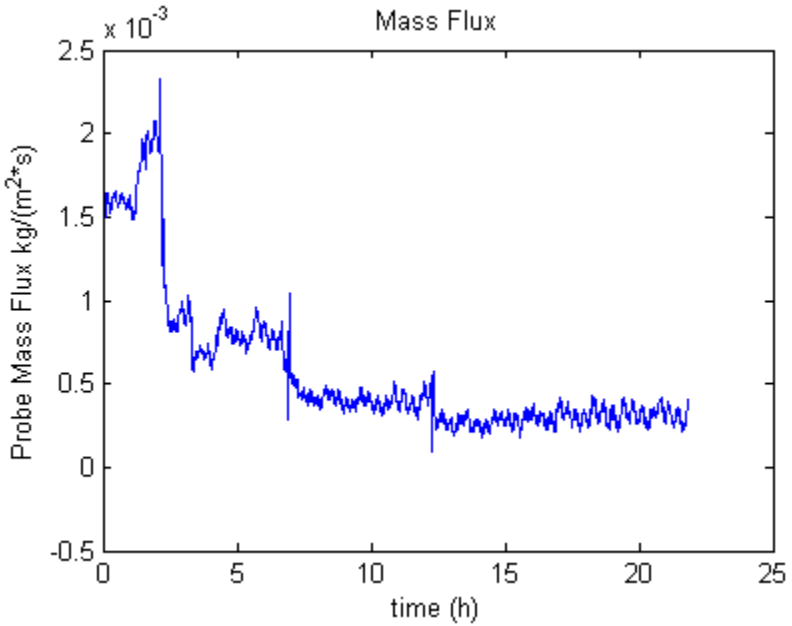
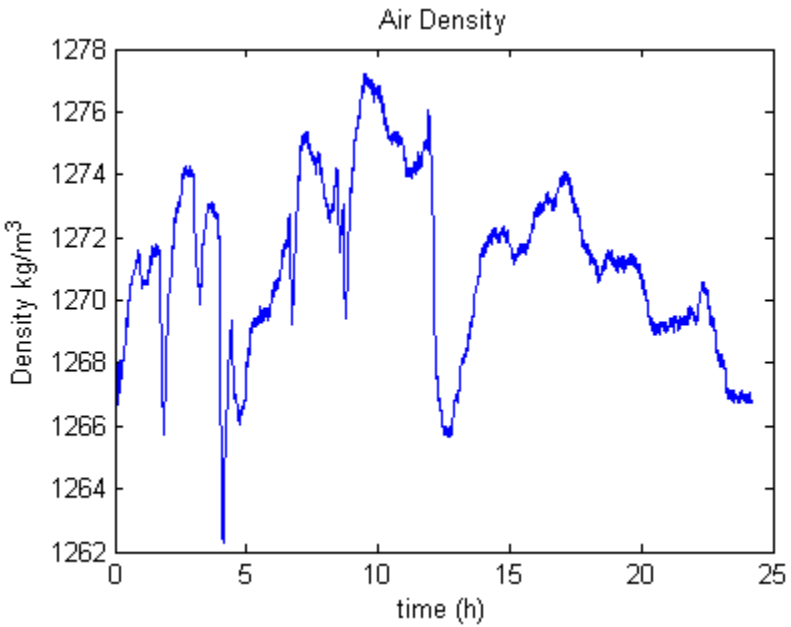
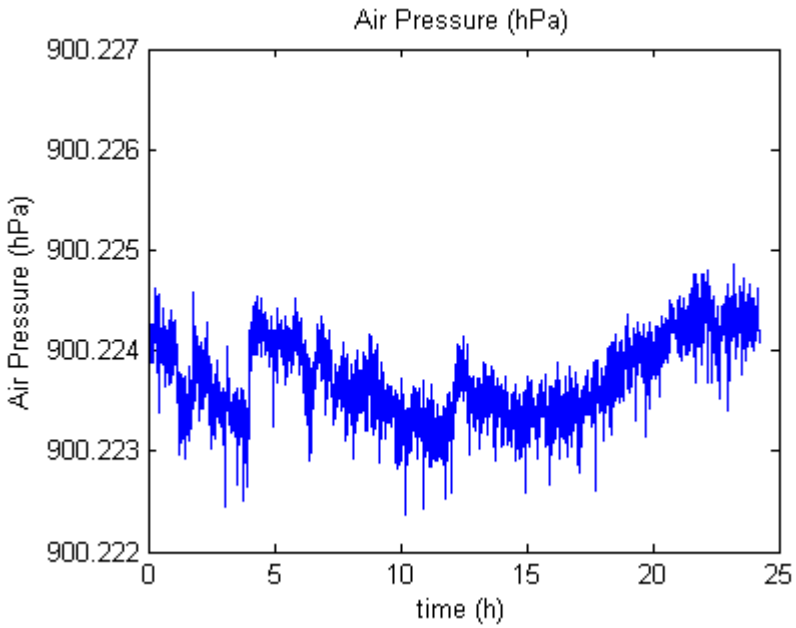
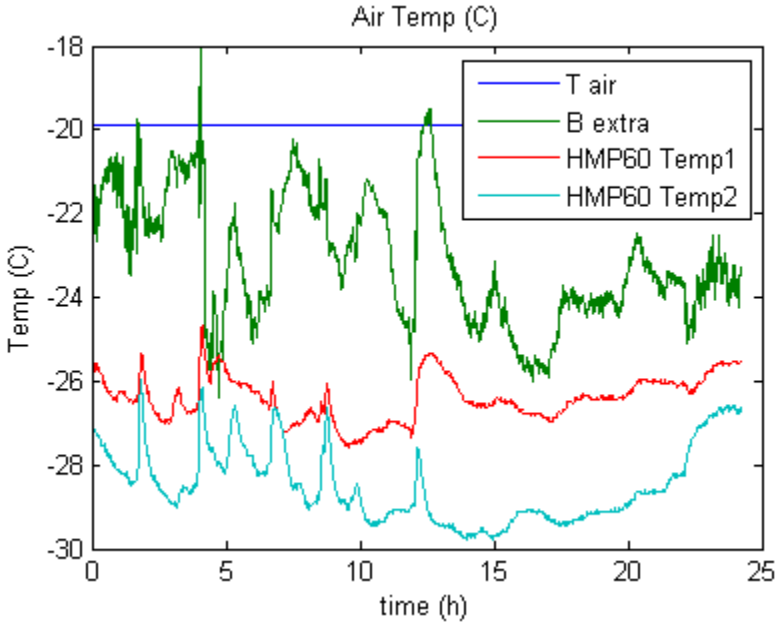
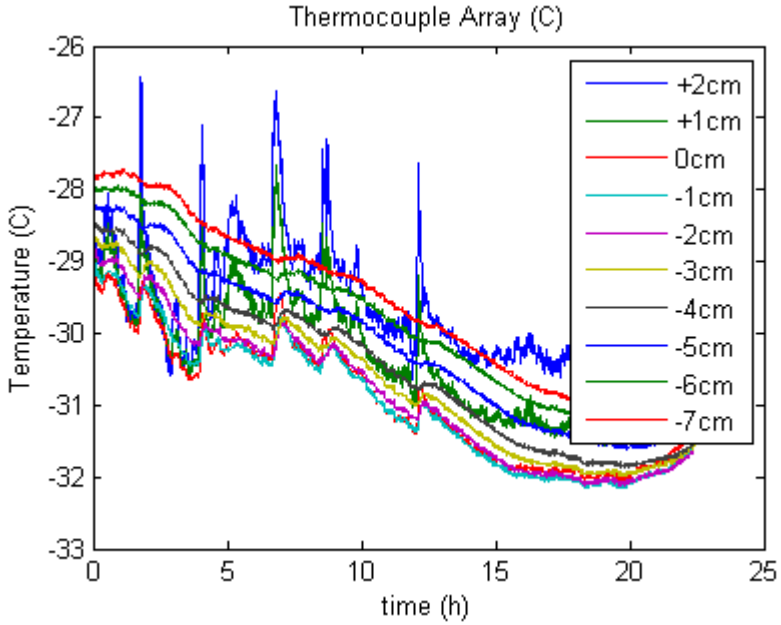


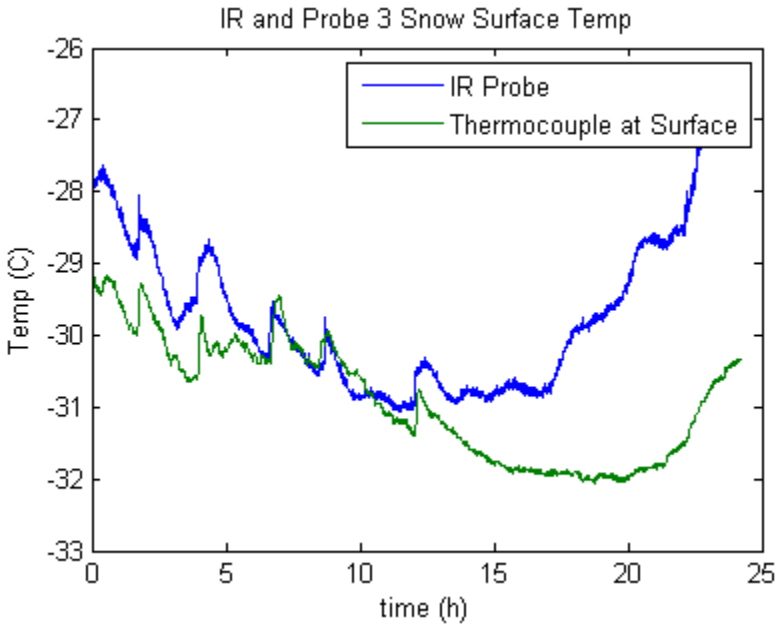
Figure 6. Test 2b 6/21/12. Environmental chamber data recorded during surface hoar growth experiments showing: air density, air pressure, air temperature, thermocouple array in snowpack, snow surface temperature as recorded by IR sensor as well as a thermocouple sensor (#3 at 0cm) on the snow surface, relative humidity several centimeters above the snow surface, relative humidity at the snow surface (calculated using snow surface temperature from IR sensor), vapor pressure with respect to ice from Equation (5), and mass flux as calculated from Equation (17).

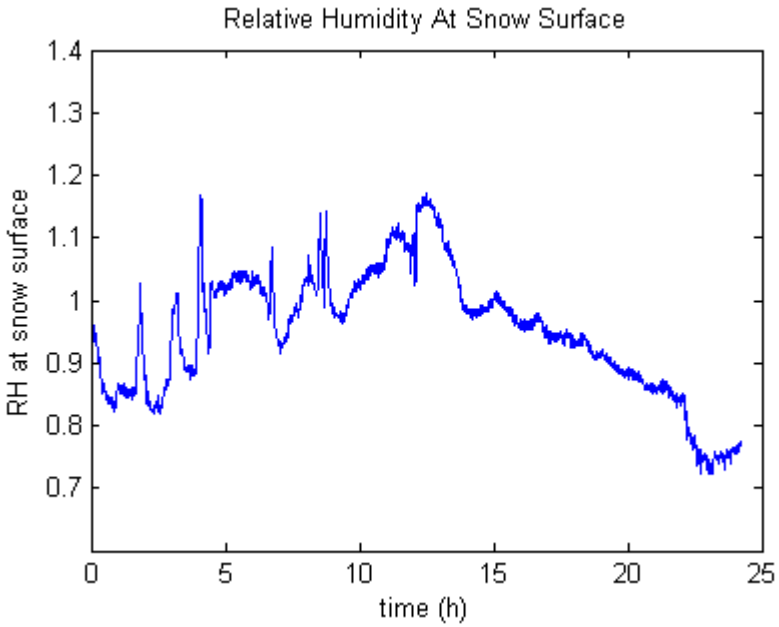

Air Density
Density kg/m3
time (h)

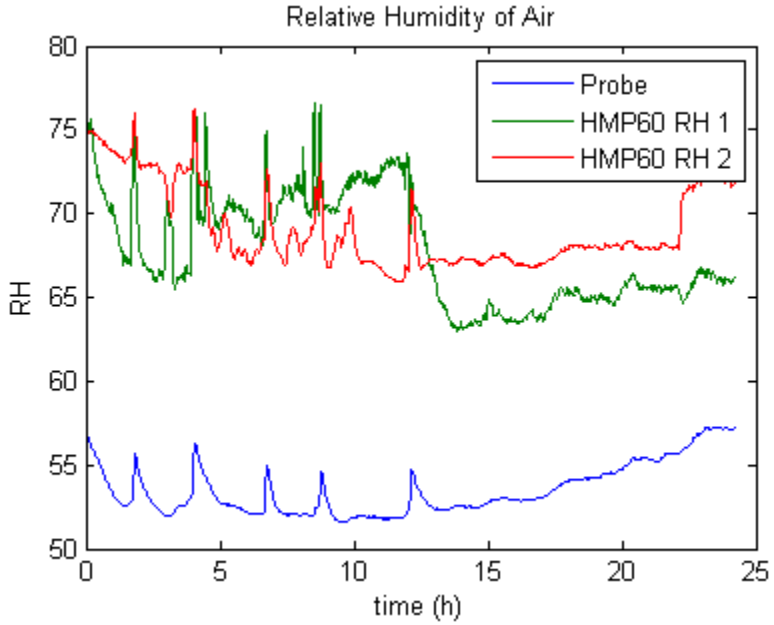

Air Pressure (hPa)
Air Pressure (hPa)
time (h)

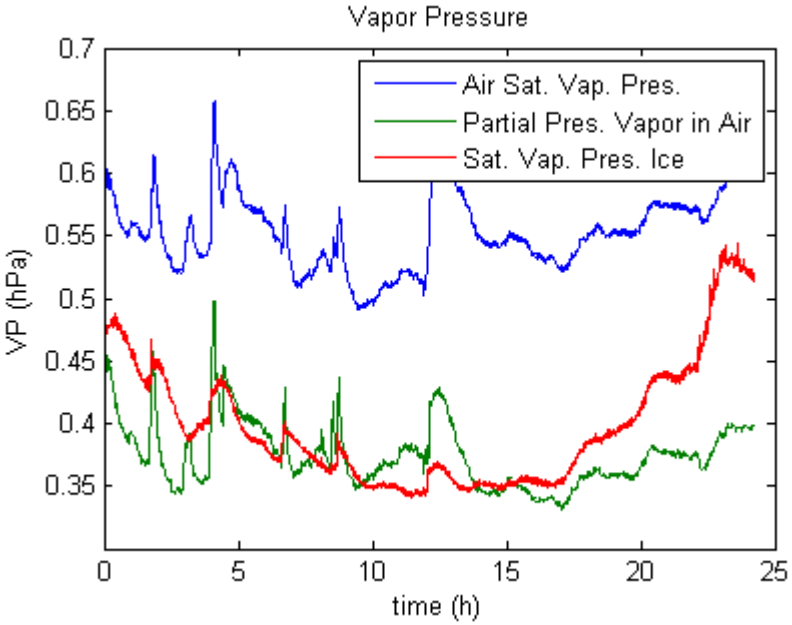

Air Temp (C)
T air
B extra
HMP60 Temp1
HMP60 Temp2
Temp (C)
time (h)


Thermocouple Array (C)
+2cm
+1cm
0cm
-1cm
-2cm
-3cm
-4cm
-5cm
-6cm
-7cm
Temperature (C)
time (h)


IR and Probe 3 Snow Surface Temp
IR Probe
Thermocouple at Surface
Temp (C)
time (h)


Relative Humidity At Snow Surface
RH at snow surface
time (h)


Relative Humidity of Air
Probe
HMP60 RH 1
HMP60 RH 2
RH
time (h)


Vapor Pressure
Air Sat. Vap. Pres.
Partial Pres. Vapor in Air
Sat. Vap. Pres. Ice
VP (hPa)
time (h)

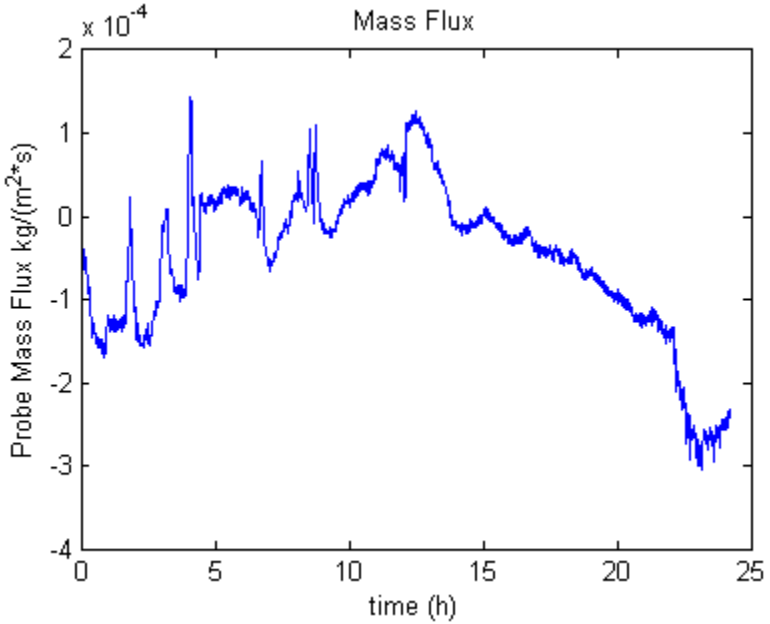
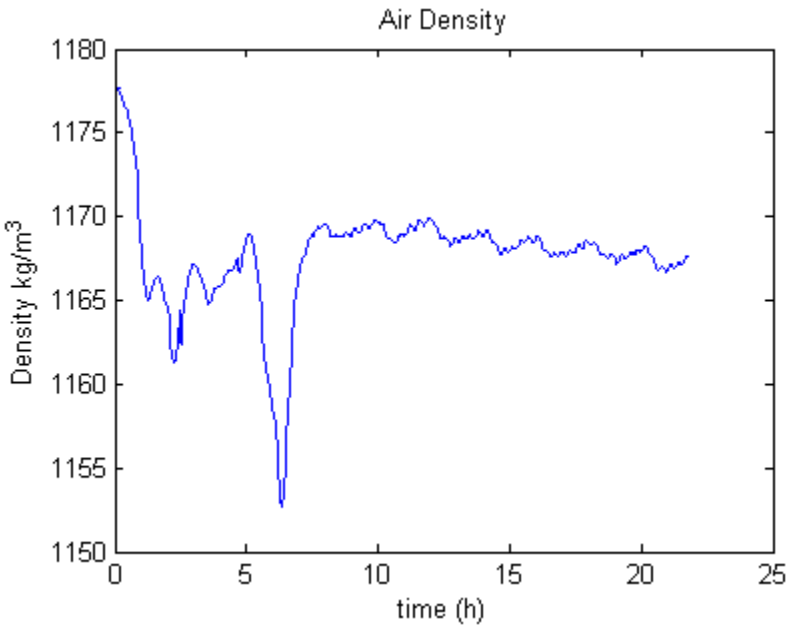
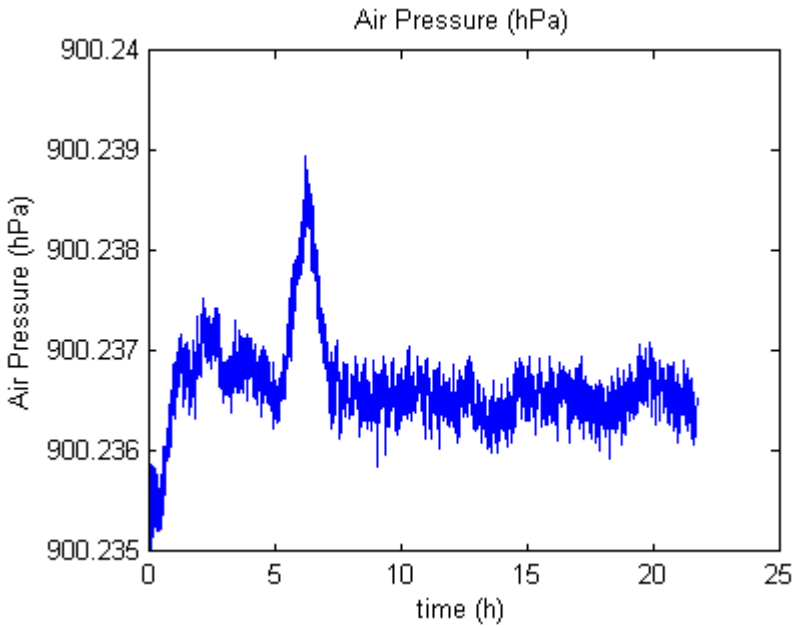
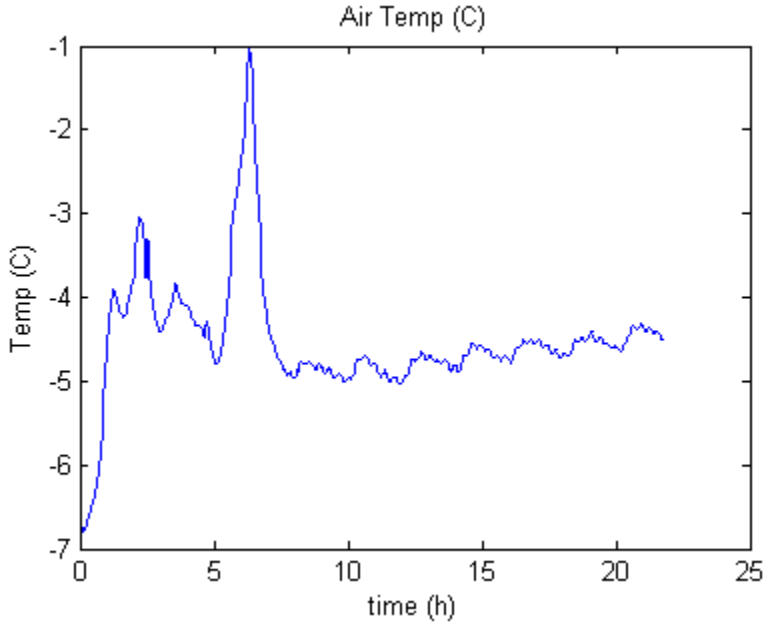
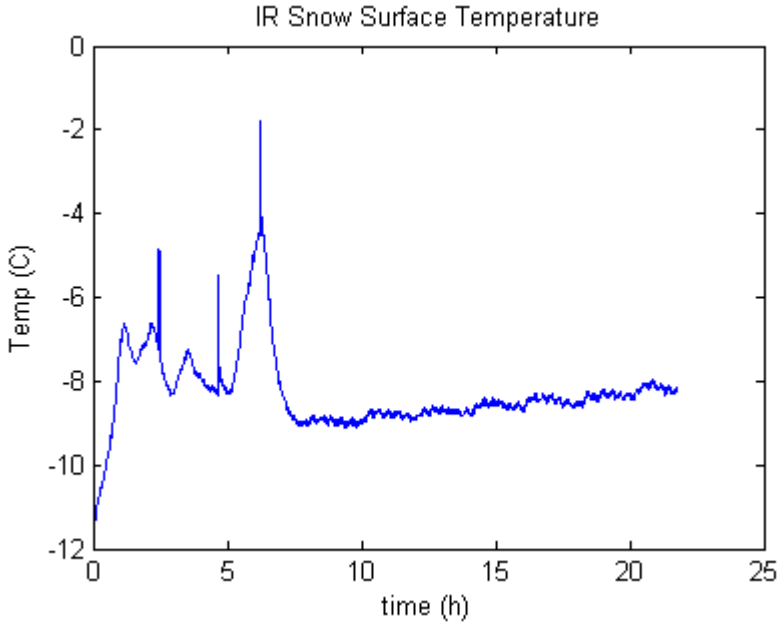


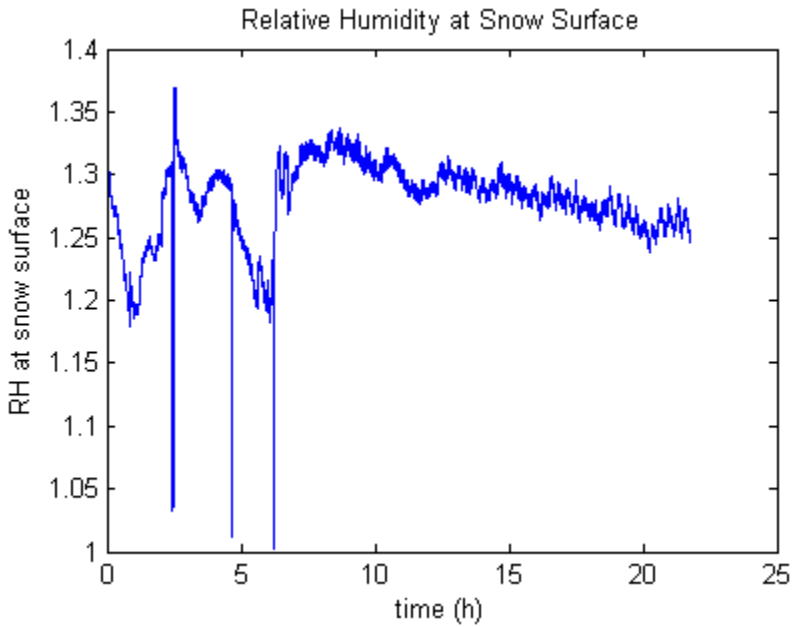
Figure 7. Test 2a 6/19/12. Environmental chamber data recorded during surface hoar growth experiments showing: air density, air pressure, air temperature, thermocouple array in snowpack, snow surface temperature as recorded by IR sensor as well as a thermocouple sensor (#3 at 0cm) on the snow surface, relative humidity several centimeters above the snow surface, relative humidity at the snow surface (calculated using snow surface temperature from IR sensor), vapor pressure with respect to ice from Equation (5), and mass flux as calculated from Equation (17). Note the the Campbell Scientific, Inc CS215 Relative Humidity and Temperature Probe (labeled T air) was not capable or recording air temperatures below $-30°C$ and thus reports only a flat line in the above figure. Additionally, B extra represents an additional air temperature measurement made using a single thermocouple.

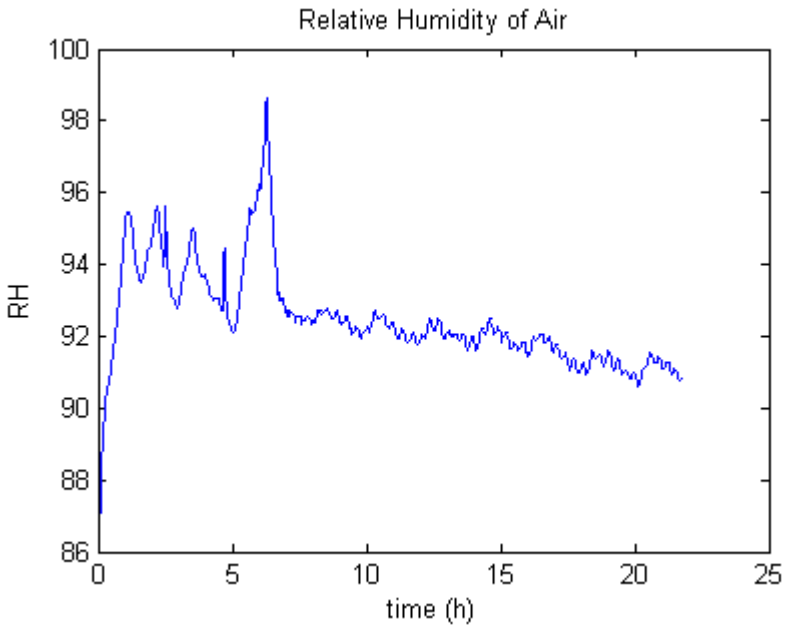

Air Density
Density kg/m3
1180
1175
1170
1165
1160
1155
1150
0
5
10
15
20
25
time (h)

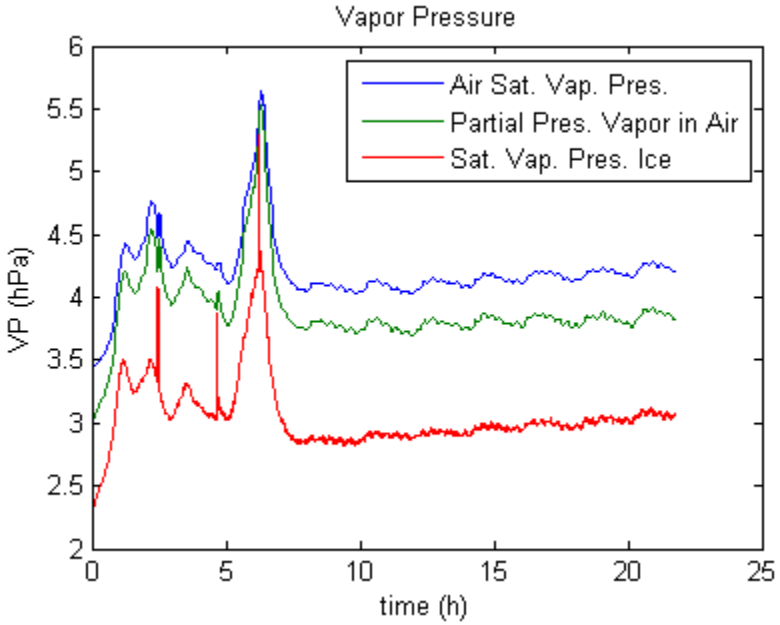

Air Pressure (hPa)
Air Pressure (hPa)
900.24
900.239
900.238
900.237
900.236
900.235
0
5
10
15
20
25
time (h)

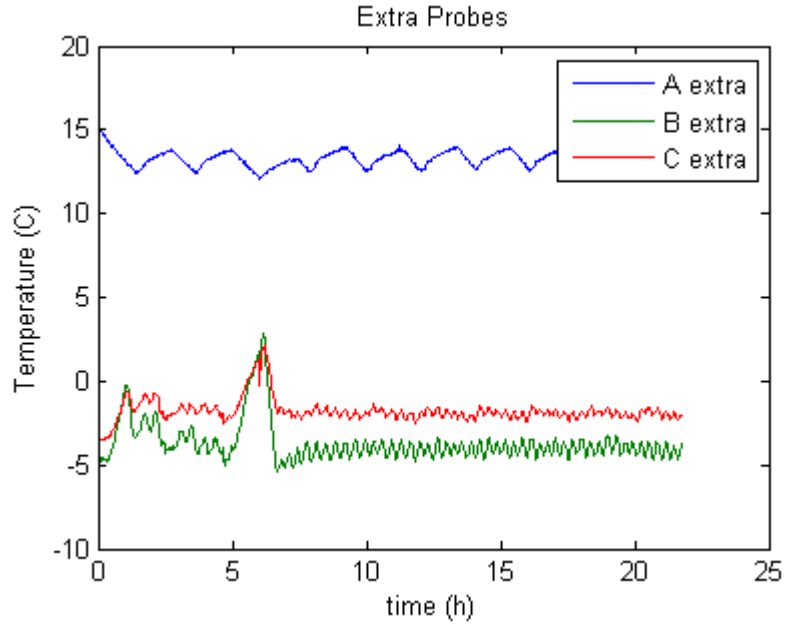

Air Temp (C)
Temp (C)
-1
-2
-3
-4
-5
-6
-7
0
5
10
15
20
25
time (h)


IR Snow Surface Temperature
Temp (C)
0
-2
-4
-6
-8
-10
-12
0
5
10
15
20
25
time (h)


Relative Humidity at Snow Surface
RH at snow surface
time (h)


Relative Humidity of Air
RH
time (h)


Vapor Pressure
Air Sat. Vap. Pres.
Partial Pres. Vapor in Air
Sat. Vap. Pres. Ice
VP (hPa)
time (h)


Extra Probes
A extra
B extra
C extra
Temperature (C)
time (h)

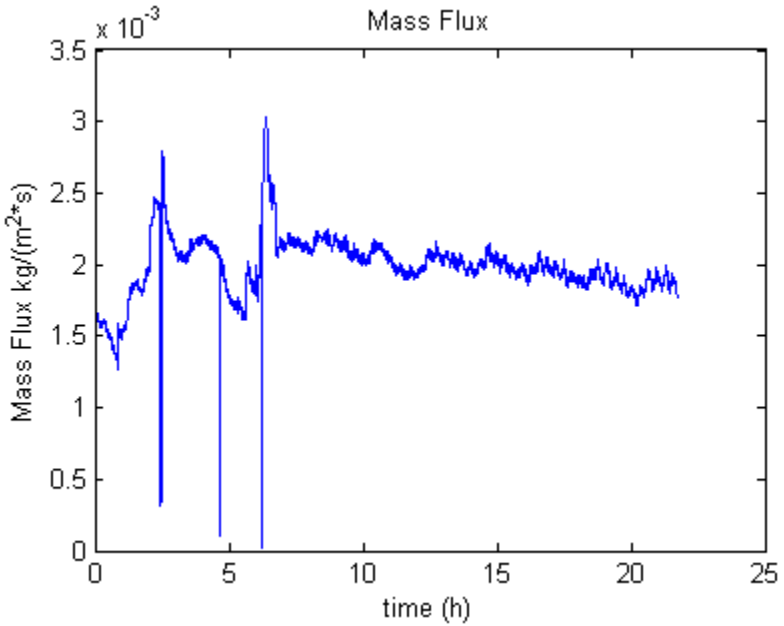
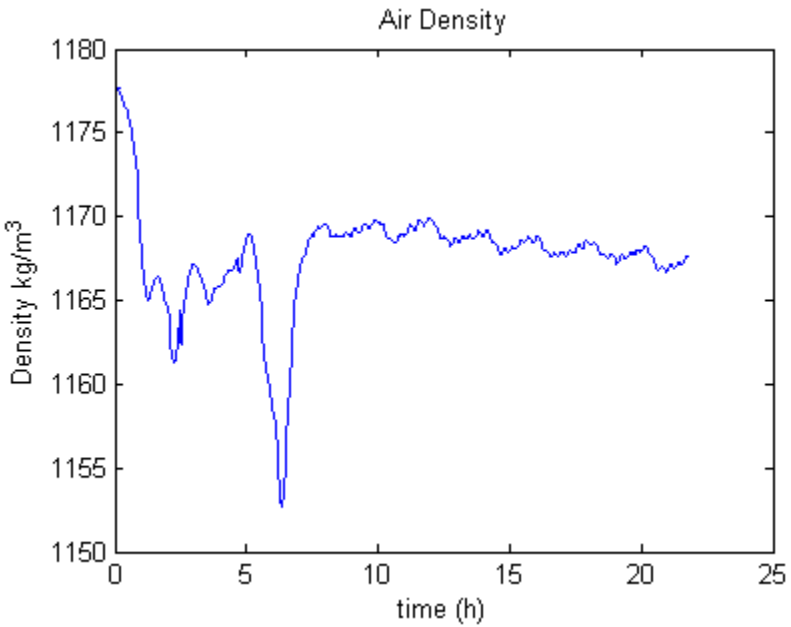
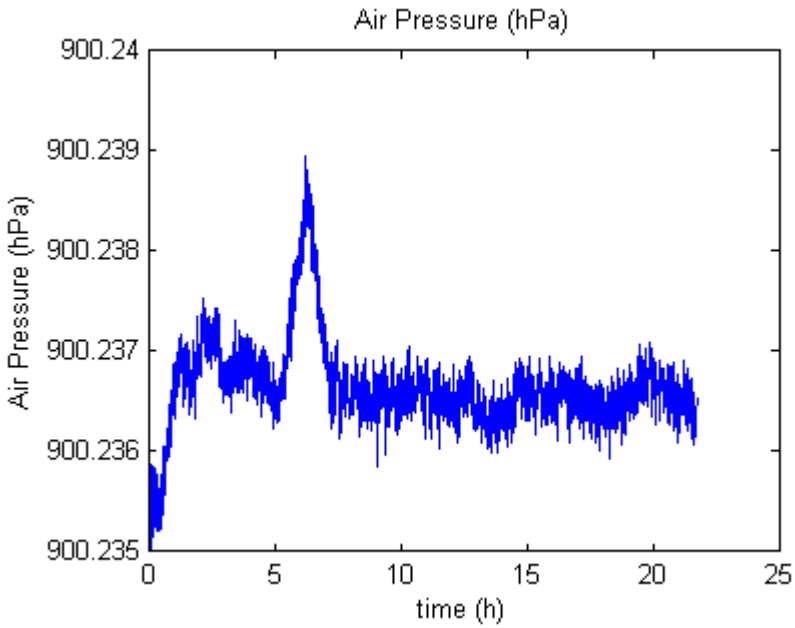
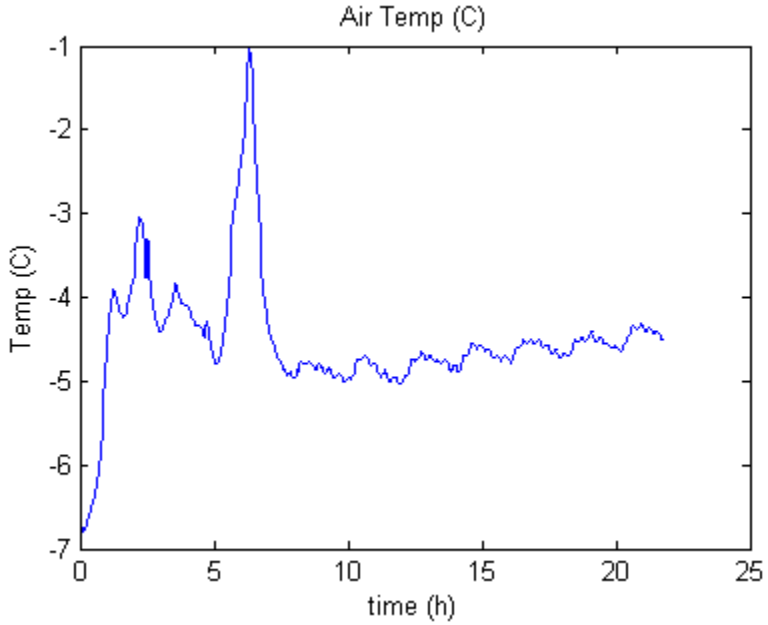
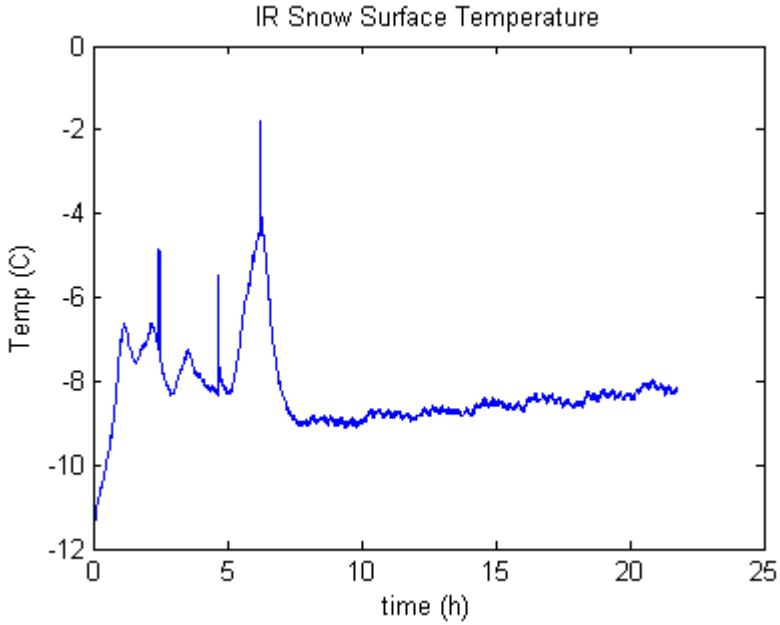


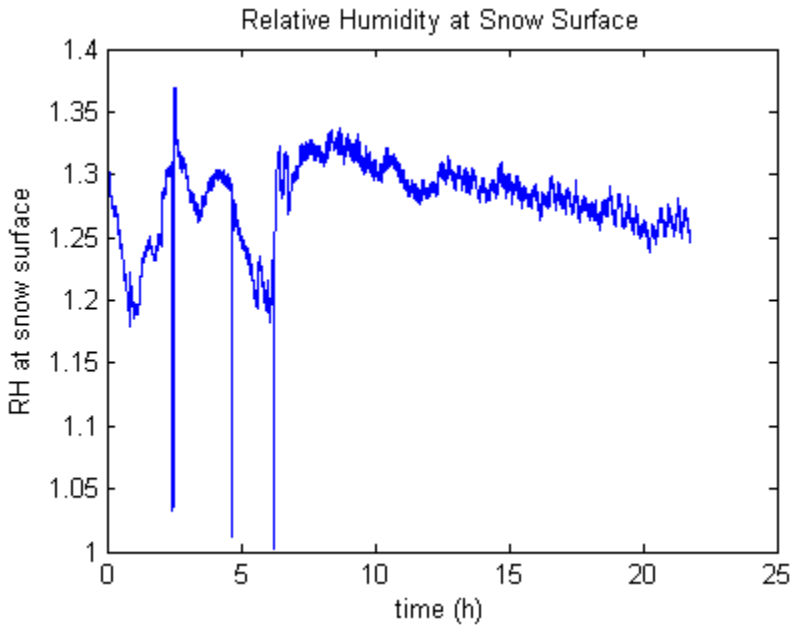
Figure 8. Test 1c Environmental chamber data recorded during surface hoar growth experiments showing: air density, air pressure, air temperature, snow surface temperature as recorded by IR sensor, relative humidity several centimeters above the snow surface, relative humidity at the snow surface (calculated using snow surface temperature from IR sensor), vapor pressure with respect to ice from Equation (5), and mass flux as calculated from Equation (17). A extra, B extra, C extra represent the temperature of liquid water in the holding tank feeding the ducting, temperature at the exit of the ducting, and temperature at the entrance to the ducting respectively. Note that test 1 did not include a thermocouple array.

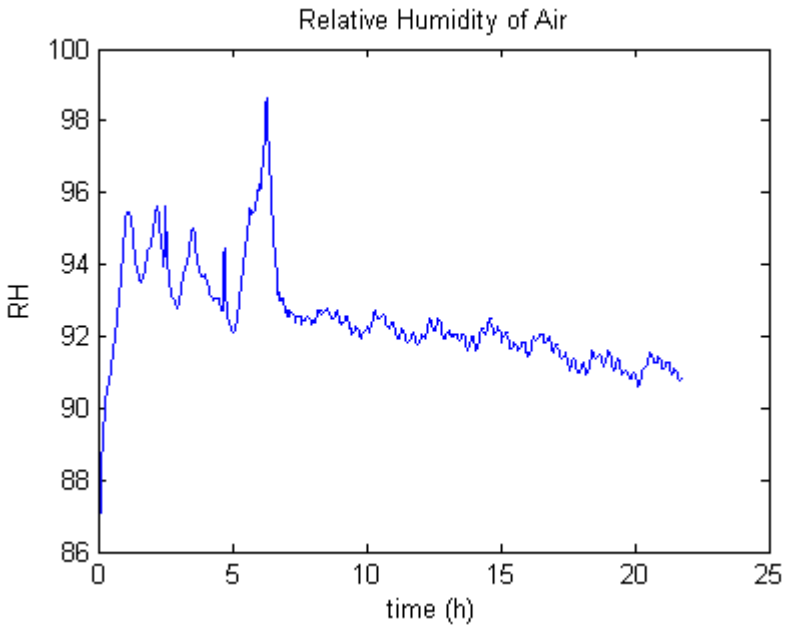

Air Density
Density kg/m3
1180
1175
1170
1165
1160
1155
1150
0
5
10
15
20
25
time (h)

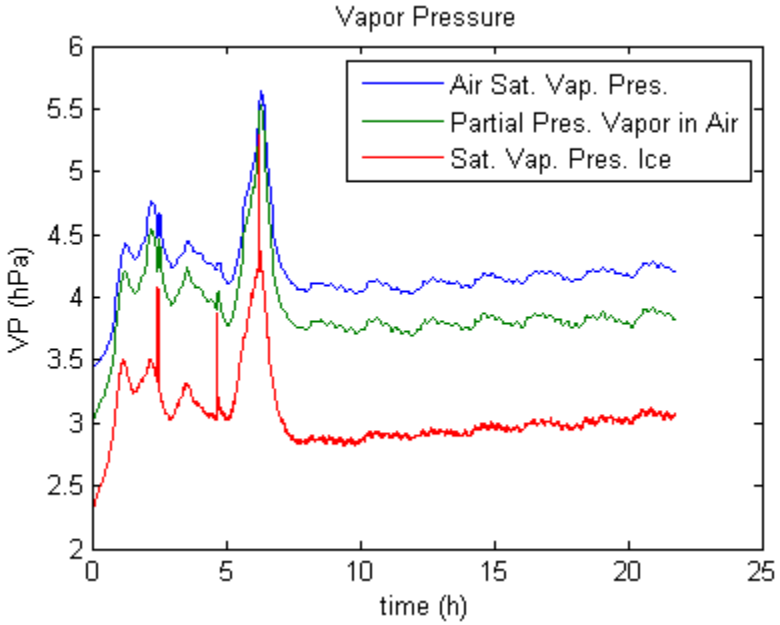

Air Pressure (hPa)
Air Pressure (hPa)
900.24
900.239
900.238
900.237
900.236
900.235
0
5
10
15
20
25
time (h)

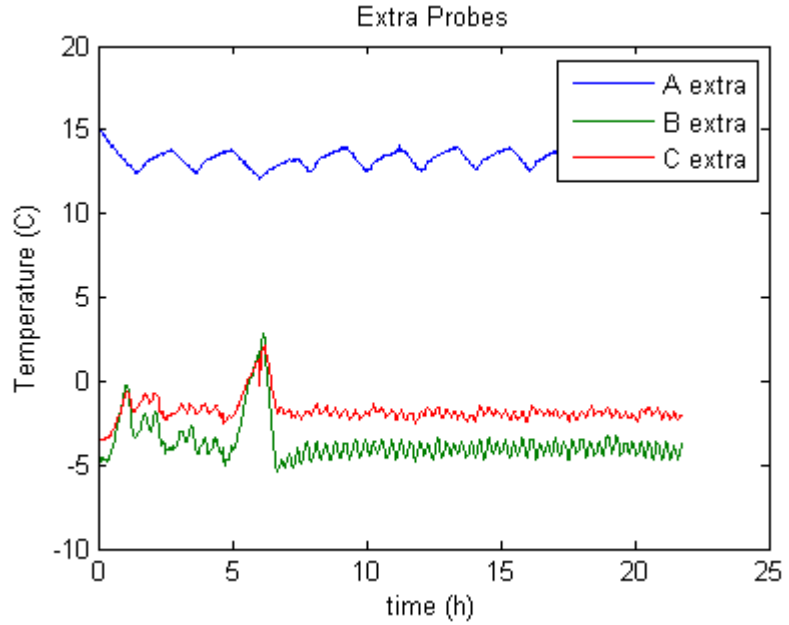

Air Temp (C)
Temp (C)
-1
-2
-3
-4
-5
-6
-7
0
5
10
15
20
25
time (h)


IR Snow Surface Temperature
Temp (C)
0
-2
-4
-6
-8
-10
-12
0
5
10
15
20
25
time (h)


Relative Humidity at Snow Surface
RH at snow surface
time (h)


Relative Humidity of Air
RH
time (h)


Vapor Pressure
Air Sat. Vap. Pres.
Partial Pres. Vapor in Air
Sat. Vap. Pres. Ice
VP (hPa)
time (h)


Extra Probes
A extra
B extra
C extra
Temperature (C)
time (h)

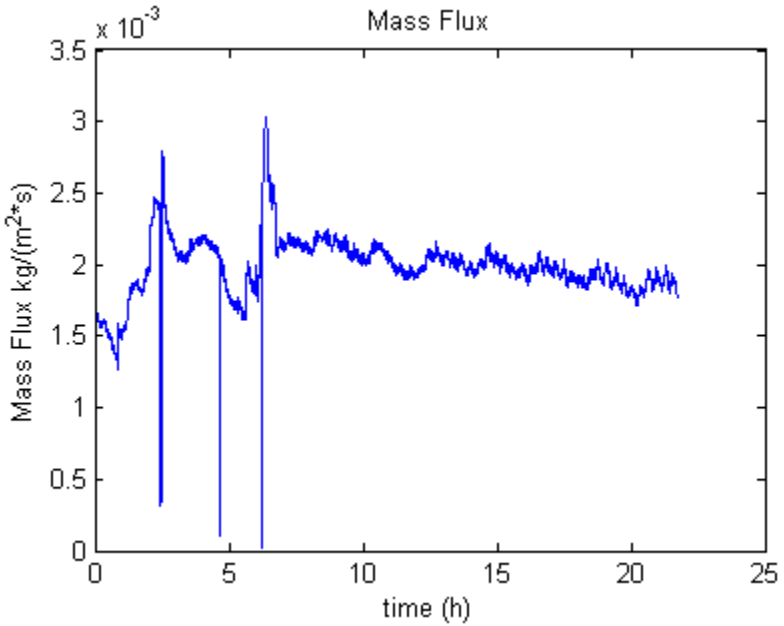


Figure 9. Test 1b Environmental chamber data recorded during surface hoar growth experiments showing: air density, air pressure, air temperature, snow surface temperature as recorded by IR sensor, relative humidity several centimeters above the snow surface, relative humidity at the snow surface (calculated using snow surface temperature from IR sensor), vapor pressure with respect to ice from Equation (5), and mass flux as calculated from Equation (17). A extra, B extra, C extra represent the temperature of liquid water in the holding tank feeding the ducting, temperature at the exit of the ducting, and temperature at the entrance to the ducting respectively. Note that test 1 did not include a thermocouple array buried in the snow.

APPENDIX F:

BRF VALUES AND GEOMETRIES

Test 3a Initial Form

θ_r ¤	ϕ_r ¤	θ_i ¤	ϕ_i ¤	BRF ¤
30¤	0¤	0¤	180¤	0.926754343860996¤
30¤	180¤	0¤	180¤	0.905429965245672¤
30¤	225¤	0¤	180¤	0.899625326658481¤
30¤	45¤	0¤	180¤	0.882395724630807¤
45¤	0¤	0¤	180¤	0.906262478370824¤
45¤	180¤	0¤	180¤	0.901692236781458¤
45¤	225¤	0¤	180¤	0.905140141280641¤
45¤	45¤	0¤	180¤	0.877529531769274¤
60¤	0¤	0¤	180¤	0.894847676540783¤
60¤	180¤	0¤	180¤	0.884203249222261¤
60¤	225¤	0¤	180¤	0.890974753841436¤
60¤	45¤	0¤	180¤	0.875706608974806¤
30¤	0¤	15¤	180¤	0.902295851813201¤
30¤	180¤	15¤	180¤	0.892023277269179¤
30¤	225¤	15¤	180¤	0.890198178896626¤
30¤	45¤	15¤	180¤	0.893404310568683¤
45¤	0¤	15¤	180¤	0.895180642580989¤
45¤	180¤	15¤	180¤	0.897748592870544¤
45¤	225¤	15¤	180¤	0.900641355420654¤
45¤	45¤	15¤	180¤	0.919706807684584¤
60¤	0¤	15¤	180¤	0.889603207521084¤
60¤	180¤	15¤	180¤	0.891204993869134¤
60¤	225¤	15¤	180¤	0.891707494102704¤
60¤	45¤	15¤	180¤	0.875308942806419¤
50¤	0¤	30¤	180¤	0.891639871382637¤
50¤	180¤	30¤	180¤	0.887848203471942¤
50¤	225¤	30¤	180¤	0.885388331777029¤
50¤	45¤	30¤	180¤	0.892320076104058¤
60¤	0¤	30¤	180¤	0.889309400230681¤
60¤	180¤	30¤	180¤	0.884073261309926¤
60¤	225¤	30¤	180¤	0.886665296897473¤
60¤	45¤	30¤	180¤	0.883566963790361¤
60¤	0¤	45¤	180¤	0.902645290581162¤
60¤	180¤	45¤	180¤	0.862796833773087¤
63¤	225¤	45¤	180¤	0.867247701546474¤
63¤	45¤	45¤	180¤	0.889417966923175¤

Test 3a Final Form

θ_r ¤	ϕ_r ¤	θ_i ¤	ϕ_i ¤	BRF ¤
30¤	0¤	0¤	180¤	0.880515823493648¤
30¤	180¤	0¤	180¤	0.892006504479801¤
30¤	225¤	0¤	180¤	0.892131859828091¤
30¤	45¤	0¤	180¤	0.876260949309047¤
45¤	0¤	0¤	180¤	0.864900838546519¤
45¤	180¤	0¤	180¤	0.876045301902943¤
45¤	225¤	0¤	180¤	0.883069110322602¤
60¤	0¤	0¤	180¤	0.819984557068651¤
60¤	180¤	0¤	180¤	0.839370895264431¤
60¤	225¤	0¤	180¤	0.861197233484379¤
60¤	45¤	0¤	180¤	0.835682880870961¤
30¤	0¤	15¤	180¤	0.887522828072006¤
30¤	180¤	15¤	180¤	0.883897523241786¤
30¤	225¤	15¤	180¤	0.884153339964802¤
30¤	45¤	15¤	180¤	0.884088548428979¤
45¤	0¤	15¤	180¤	0.865851219837355¤
45¤	180¤	15¤	180¤	0.876832742686401¤
45¤	225¤	15¤	180¤	0.885276262990020¤
45¤	45¤	15¤	180¤	0.871711627284289¤
60¤	0¤	15¤	180¤	0.835303470206000¤
60¤	180¤	15¤	180¤	0.853156467134842¤
60¤	225¤	15¤	180¤	0.876283796044275¤
60¤	45¤	15¤	180¤	0.836007936784210¤
50¤	0¤	30¤	180¤	0.865130403715613¤
50¤	180¤	30¤	180¤	0.866572466693581¤
50¤	225¤	30¤	180¤	0.868052454224351¤
50¤	45¤	30¤	180¤	0.858622077494420¤
60¤	0¤	30¤	180¤	0.857879181084198¤
60¤	180¤	30¤	180¤	0.865715732613099¤
60¤	225¤	30¤	180¤	0.867844668173413¤
60¤	45¤	30¤	180¤	0.836076487776011¤
60¤	0¤	45¤	180¤	0.892144288577154¤
60¤	180¤	45¤	180¤	0.860912174896344¤
63¤	225¤	45¤	180¤	0.863740234893979¤

Test 3b Initial Form

θ_r ¤	ϕ_r ¤	θ_i ¤	ϕ_i ¤	BRF ¤
30¤	0¤	0¤	180¤	0.892112252407923¤
30¤	135¤	0¤	180¤	0.870954831332190¤
30¤	180¤	0¤	180¤	0.872760896597902¤
30¤	225¤	0¤	180¤	0.863146626365669¤
30¤	315¤	0¤	180¤	0.882467716982919¤
30¤	45¤	0¤	180¤	0.877443632798912¤
45¤	0¤	0¤	180¤	0.900918408092640¤
45¤	180¤	0¤	180¤	0.867366826891420¤
45¤	225¤	0¤	180¤	0.869507470946320¤
45¤	45¤	0¤	180¤	0.887677272876839¤
60¤	0¤	0¤	180¤	0.895739154850484¤
60¤	180¤	0¤	180¤	0.857324576564120¤
60¤	225¤	0¤	180¤	0.862675888385404¤
60¤	45¤	0¤	180¤	0.894249424244539¤
30¤	0¤	15¤	180¤	0.868066788416384¤
30¤	135¤	15¤	180¤	0.863413376546848¤
30¤	180¤	15¤	180¤	0.860953800298063¤
30¤	225¤	15¤	180¤	0.849850791950417¤
30¤	315¤	15¤	180¤	0.845897925499207¤
30¤	45¤	15¤	180¤	0.847649961049078¤
45¤	0¤	15¤	180¤	0.872230369284096¤
45¤	180¤	15¤	180¤	0.899742894864846¤
45¤	225¤	15¤	180¤	0.894550193778510¤
45¤	45¤	15¤	180¤	0.858772340852801¤
60¤	0¤	15¤	180¤	0.872991842942071¤
60¤	180¤	15¤	180¤	0.902924237357411¤
60¤	225¤	15¤	180¤	0.899452005080748¤
60¤	45¤	15¤	180¤	0.861363873707662¤
50¤	0¤	30¤	180¤	0.859321186137906¤
50¤	135¤	30¤	180¤	0.876081258191350¤
50¤	180¤	30¤	180¤	0.889479208720226¤
50¤	225¤	30¤	180¤	0.859177459299257¤
50¤	315¤	30¤	180¤	0.848818557813343¤
50¤	45¤	30¤	180¤	0.859368482675350¤
60¤	0¤	30¤	180¤	0.862182814302192¤
60¤	180¤	30¤	180¤	0.906794395678596¤
60¤	225¤	30¤	180¤	0.877435792069036¤
60¤	45¤	30¤	180¤	0.869268040093206¤
60¤	0¤	45¤	180¤	0.836929859719439¤
60¤	180¤	45¤	180¤	0.882795756825158¤
63¤	225¤	45¤	180¤	0.897241855768720¤
63¤	45¤	45¤	180¤	0.848875472981591¤

Test 3b Finial Form

θ_r ¤	ϕ_r ¤	θ_i ¤	ϕ_i ¤	BRF ¤
30¤	0¤	0¤	180¤	0.876688745960129¤
30¤	135¤	0¤	180¤	0.933276157804460¤
30¤	180¤	0¤	180¤	0.928686669004878¤
30¤	225¤	0¤	180¤	0.923503668020528¤
30¤	315¤	0¤	180¤	0.892413096328103¤
30¤	45¤	0¤	180¤	0.873933529393163¤
45¤	0¤	0¤	180¤	0.907240782643418¤
45¤	180¤	0¤	180¤	0.899104497267400¤
45¤	225¤	0¤	180¤	0.912445066571178¤
45¤	45¤	0¤	180¤	0.896133723799809¤
60¤	0¤	0¤	180¤	0.867099536712060¤
60¤	180¤	0¤	180¤	0.877200138264777¤
60¤	225¤	0¤	180¤	0.867445742904841¤
60¤	45¤	0¤	180¤	0.872510293809757¤
30¤	0¤	15¤	180¤	0.883133315940517¤
30¤	135¤	15¤	180¤	0.853174720094284¤
30¤	180¤	15¤	180¤	0.872805336739763¤
30¤	225¤	15¤	180¤	0.856354732573265¤
30¤	315¤	15¤	180¤	0.868649470856662¤
30¤	45¤	15¤	180¤	0.864139184627370¤
45¤	0¤	15¤	180¤	0.868930809225437¤
45¤	180¤	15¤	180¤	0.911660065318602¤
45¤	225¤	15¤	180¤	0.908406214631135¤
45¤	45¤	15¤	180¤	0.862286632304706¤
60¤	0¤	15¤	180¤	0.831411585787364¤
60¤	180¤	15¤	180¤	0.888804666889607¤
60¤	225¤	15¤	180¤	0.871580475412811¤
60¤	45¤	15¤	180¤	0.847126396769590¤
50¤	0¤	30¤	180¤	0.829310468024294¤
50¤	135¤	30¤	180¤	0.900040956749672¤
50¤	180¤	30¤	180¤	0.881849010900283¤
50¤	225¤	30¤	180¤	0.876878730055621¤
50¤	315¤	30¤	180¤	0.820802014026254¤
50¤	45¤	30¤	180¤	0.834963960338078¤
60¤	0¤	30¤	180¤	0.817091983852365¤
60¤	180¤	30¤	180¤	0.903798109385550¤
60¤	225¤	30¤	180¤	0.877107047462503¤
60¤	45¤	30¤	180¤	0.836794023005511¤
60¤	0¤	45¤	180¤	0.818372745490982¤
60¤	180¤	45¤	180¤	0.837187012007969¤
63¤	225¤	45¤	180¤	0.861316894297710¤
63¤	45¤	45¤	180¤	0.830423876535862¤

Test 3c Initial Form

θ_r ¤	ϕ_r ¤	θ_i ¤	ϕ_i ¤	BRF ¤
30¤	0¤	0¤	180¤	0.892112252407923¤
30¤	135¤	0¤	180¤	0.870954831332190¤
30¤	180¤	0¤	180¤	0.872760896597902¤
30¤	225¤	0¤	180¤	0.863146626365669¤
30¤	315¤	0¤	180¤	0.882467716982919¤
30¤	45¤	0¤	180¤	0.877443632798912¤
45¤	0¤	0¤	180¤	0.900918408092640¤
45¤	180¤	0¤	180¤	0.867366826891420¤
45¤	225¤	0¤	180¤	0.869507470946320¤
45¤	45¤	0¤	180¤	0.887677272876839¤
60¤	0¤	0¤	180¤	0.895739154850484¤
60¤	180¤	0¤	180¤	0.857324576564120¤
60¤	225¤	0¤	180¤	0.862675888385404¤
60¤	45¤	0¤	180¤	0.894249424244539¤
30¤	0¤	15¤	180¤	0.868066788416384¤
30¤	135¤	15¤	180¤	0.863413376546848¤
30¤	180¤	15¤	180¤	0.860953800298063¤
30¤	225¤	15¤	180¤	0.849850791950417¤
30¤	315¤	15¤	180¤	0.845897925499207¤
30¤	45¤	15¤	180¤	0.847649961049078¤
45¤	0¤	15¤	180¤	0.872230369284096¤
45¤	180¤	15¤	180¤	0.899742894864846¤
45¤	225¤	15¤	180¤	0.894550193778510¤
45¤	45¤	15¤	180¤	0.858772340852801¤
60¤	0¤	15¤	180¤	0.872991842942071¤
60¤	180¤	15¤	180¤	0.902924237357411¤
60¤	225¤	15¤	180¤	0.899452005080748¤
60¤	45¤	15¤	180¤	0.861363873707662¤
50¤	0¤	30¤	180¤	0.859321186137906¤
50¤	135¤	30¤	180¤	0.876081258191350¤
50¤	180¤	30¤	180¤	0.889479208720226¤
50¤	225¤	30¤	180¤	0.859177459299257¤
50¤	315¤	30¤	180¤	0.848818557813343¤
50¤	45¤	30¤	180¤	0.859368482675350¤
60¤	0¤	30¤	180¤	0.862182814302192¤
60¤	180¤	30¤	180¤	0.906794395678596¤
60¤	225¤	30¤	180¤	0.877435792069036¤
60¤	45¤	30¤	180¤	0.869268040093206¤
60¤	0¤	45¤	180¤	0.836929859719439¤
60¤	180¤	45¤	180¤	0.882795756825158¤
63¤	225¤	45¤	180¤	0.897241855768720¤
63¤	45¤	45¤	180¤	0.848875472981591¤

Test 3c Final Form

θ_r ¤	ϕ_r ¤	θ_i ¤	ϕ_i ¤	BRF ¤
30¤	0¤	0¤	180¤	0.905667018655403¤
30¤	135¤	0¤	180¤	0.879105520614955¤
30¤	180¤	0¤	180¤	0.885470139973855¤
30¤	225¤	0¤	180¤	0.860300368376311¤
30¤	315¤	0¤	180¤	0.884286300634610¤
30¤	45¤	0¤	180¤	0.912500395281915¤
45¤	0¤	0¤	180¤	0.895847198189804¤
45¤	180¤	0¤	180¤	0.866629354052808¤
45¤	225¤	0¤	180¤	0.850060223314561¤
45¤	45¤	0¤	180¤	0.905695765193643¤
60¤	0¤	0¤	180¤	0.849922785343254¤
60¤	180¤	0¤	180¤	0.822329761493260¤
60¤	225¤	0¤	180¤	0.806786821573371¤
60¤	45¤	0¤	180¤	0.879649661525578¤
30¤	0¤	15¤	180¤	0.885924863031568¤
30¤	135¤	15¤	180¤	0.824690630524455¤
30¤	180¤	15¤	180¤	0.865836349442907¤
30¤	225¤	15¤	180¤	0.811997857525442¤
30¤	315¤	15¤	180¤	0.879510663775527¤
30¤	45¤	15¤	180¤	0.898889898727603¤
45¤	0¤	15¤	180¤	0.873083588854819¤
45¤	180¤	15¤	180¤	0.893231881036759¤
45¤	225¤	15¤	180¤	0.875261515245053¤
45¤	45¤	15¤	180¤	0.890621862239775¤
60¤	0¤	15¤	180¤	0.842458177796212¤
60¤	180¤	15¤	180¤	0.866532902314867¤
60¤	225¤	15¤	180¤	0.855380148793323¤
60¤	45¤	15¤	180¤	0.949037490862255¤
50¤	0¤	30¤	180¤	0.855448374419436¤
50¤	135¤	30¤	180¤	0.872501638269987¤
50¤	180¤	30¤	180¤	0.857287040775131¤
50¤	225¤	30¤	180¤	0.853883317770290¤
50¤	315¤	30¤	180¤	0.869411976263262¤
50¤	45¤	30¤	180¤	0.876477260253924¤
60¤	0¤	30¤	180¤	0.849877450980392¤
60¤	180¤	30¤	180¤	0.873860567184335¤
60¤	225¤	30¤	180¤	0.856585165399630¤
60¤	45¤	30¤	180¤	0.880829973739690¤
60¤	0¤	45¤	180¤	0.857314629258517¤
60¤	180¤	45¤	180¤	0.821280491088256¤
63¤	225¤	45¤	180¤	0.877929531806345¤
63¤	45¤	45¤	180¤	0.902087496279920¤